

**INVESTIGATION OF HORIZONTAL METEOROLOGICAL
STRUCTURES IN COMPARISON TO TURBULENT STRUCTURES
AT A FOREST EDGE**

A dissertation submitted to the
FACULTY OF BIOLOGY, CHEMISTRY AND GEOSCIENCES
AT THE UNIVERSITY OF BAYREUTH

to attain the academic degree of

DR. RER. NAT.

presented by

JÖRG HÜBNER

Diplom-Geoökologe

born 25 February 1984

in Ulm, Germany

Bayreuth, September 2014

supervised by

PROF. DR. THOMAS FOKEN

**INVESTIGATION OF HORIZONTAL METEOROLOGICAL
STRUCTURES IN COMPARISON TO TURBULENT STRUCTURES
AT A FOREST EDGE**

presented by
JÖRG HÜBNER, DIPL.-GEOÖKOL.

supervised by
PROF. DR. THOMAS FOKEN



DEPARTMENT OF MICROMETEOROLOGY
UNIVERSITY OF BAYREUTH

Die vorliegende Arbeit wurde in der Zeit von Juli 2010 bis September 2014 an der Abteilung Mikrometeorologie der Universität Bayreuth unter Betreuung von Herrn Prof. Dr. Thomas Foken angefertigt.

Vollständiger Abdruck der von der Fakultät für Biologie, Chemie und Geowissenschaften der Universität Bayreuth genehmigten Dissertation zur Erlangung des akademischen Grades eines Doktor der Naturwissenschaften (Dr. rer. nat.).

Dissertation eingereicht am: 09. September 2014

Zulassung durch die Prüfungskommission: 17. September 2014

Wissenschaftliches Kolloquium am: 15. Dezember 2014

Amtierender Dekan:

Prof. Dr. Rhett Kempe

Prüfungsausschuss:

Prof. Dr. Thomas Foken (Erstgutachter)

Prof. Dr. Andreas Held (Zweitgutachter)

Prof. Dr. Cyrus Samimi (Vorsitz)

Prof. Dr. Anke Jentsch-Beierkuhnlein

Contents

Contents	III
Acknowledgements	VII
Summary	IX
Zusammenfassung	XI
1. Introduction	1
1.1. Motivation: The role of forest ecosystems	1
1.2. Scope of the research topic	2
1.2.1. Exchange processes of forest ecosystems	2
1.2.2. Characteristics of exchange processes at a forest edge	5
1.2.3. Measuring techniques	6
1.3. Objectives of the thesis	8
2. Materials and methods	11
2.1. The EGER project	11
2.1.1. Site description	11
2.1.2. Intensive observation periods 1 & 2 (IOP1 & IOP2)	13
2.1.3. Intensive observation period 3 (IOP3)	14
2.2. Measurements	15
2.2.1. General set-up of the measurements	15
2.2.2. Measurements of turbulent fluxes	17
2.2.3. Profile measurements	19
2.2.4. Additional measurements	20
2.3. The Horizontal Mobile Measuring System (HMMS)	22
2.3.1. HMMS design and power supply	23
2.3.2. Train control, position detection and data acquisition system	25
2.3.3. Sensor system	27

2.3.4.	Individual sensor response times and the dynamical error	30
2.3.5.	Variability of run duration	34
2.3.6.	Radiation-induced error in CO ₂ measurements	35
2.4.	Post-field data processing	35
2.4.1.	Correction of dynamical errors in HMMS measurements	36
2.4.2.	Analysis of turbulent fluxes	39
2.4.3.	Analysis of coherent structures	41
2.4.4.	Analysis of storage heat flux within forest biomass	43
2.4.5.	Modelling of energy and matter exchange	43
3.	Results and discussion	47
3.1.	Metrological assessment of the HMMS	47
3.2.	Characterisation of horizontal structures at the forest edge	51
3.2.1.	Horizontal gradients of typical meteorological parameters	52
3.2.2.	Horizontal distribution of turbulent structures	58
3.2.3.	Horizontal distribution of coherent structures and coupling regimes	63
3.2.4.	Stand-scale modelling of the energy and matter exchange	69
3.3.	Characterisation of vertical structures at the forest edge	72
3.3.1.	Vertical CO ₂ profile	72
3.3.2.	Vertical temperature and wind profile	74
3.4.	Linkage of vertical structures and horizontal fields	79
3.4.1.	Energy balance closure and secondary circulations	79
3.4.2.	Influence on horizontal profiles by low-level jet	86
3.4.3.	Nocturnal drainage caused by a long decoupling situation	90
3.4.4.	Inflow of fresh air caused by convergence line	96
4.	Conclusions	101
	References	109
A.	Analysis of vertical wind velocity	131
B.	Parameter for ACASA Tile Approach	139
C.	Detailed overview of horizontal structures	141
C.1.	Meteorological gradients measured with the HMMS	141
C.1.1.	Variation regarding different wind directions	142

C.1.2. Variation regarding different wind directions and stability parameters	143
C.1.3. Variation regarding different wind directions and friction velocities	148
C.2. Energy and trace gas fluxes measured with the eddy-covariance method	152
C.2.1. Percentage distribution of energy fluxes at the forest edge	152
D. List of publications	155
E. Individual contribution to the joint publication	157
List of Figures	159
List of Tables	163
List of abbreviations and symbols	165
Abbreviations	165
Latin symbols	166
Greek symbols	169
Versicherungen und Erklärungen	171

Acknowledgements

Many persons supported me during the last few years in the development and completion of this thesis in many ways. I would like to thank all of them, in particular:

- My supervisor Prof. Dr. Thomas Foken for his guidance through all stages of this thesis, for many fruitful discussions and his continuous support in countless ways.
- Prof. Dr. Andreas Held for having agreed to be the second assessor of my thesis.
- All co-authors for their contribution to my manuscript, in particular Dr. Franz X. Meixner (Max Planck Institute for Chemistry, Mainz), Dr. Hubert Falke (GAF mbH, Zwickau) and Johannes Olesch
- Fabian Eder and Dr. Andrei Serafimovich for providing their analyses of coherent structures and coupling regimes, as well as their teamwork during EGER IOP3. Kathrin Gatzsche for providing the ACASA results.
- All other participants of the EGER IOP3 project for their great work and the unforgettable time, in particular Linda Voß and Dr. habil. Eva Falge (Max Planck Institute for Chemistry, Mainz), Dr. Matthias Sörgel (Atmospheric Chemistry, University of Bayreuth), Henrique F. Duarte (University of Georgia, Griffin, USA), Dr. Peter Werle[†], Dr. Stanislaw Cieslik (Joint Research Centre, Ispra, Italy), Gordon Dowler and Prof. Dr. Heping Liu (Washington State University Pullman, USA), Qianqian Liu (Graduate University of the Chinese Academy of Sciences, Beijing, China), Farah Kanani-Süring and Prof. Dr. Siegfried Rasch (Leibniz University, Hannover), all staff members of the Department of Micrometeorology, and Gerhard Müller (BayCEER).
- All other people, who make the full functionality and the fast construction of the HMMS possible. In particular: The technical workshops of the University of Bayreuth, Harald Franke and Christoph Klaus (enviscope GmbH), Marc Clement (Sick Vertriebs-GmbH), Dr. Lutz Heymann (Chair of Applied Mechanics and Fluid Dynamics, University of Bayreuth).

- All other current and former staff members of the Department of Micrometeorology for their support, helpful programs and scripts, discussions and comments, especially Dr. Rafael Eigenmann for his help on the data analysis of all eddy-covariance tower measurements. But also Dr. Wolfgang Babel, Dr. Tobias Biermann, Dr. Michael Riederer, Dr. habil. Johannes Lüers, Carsten Schaller, Dr. Lukas Siebicke, Lisa Dirks, Kilian Huber, Dr. Peng Zhao, Dr. Doojdao Charuchittipan and Johannes Olesch.
- Dr. William Hornsby and Robert Krug for proofreading my thesis.
- My family, my friends and Daniela for supporting me all the time. My colleagues from the riding club for hundreds of great rides.

This thesis was embedded in the EGER IOP3 project (ExchanGE processes in mountainous Regions - Intense Observation Period 3), funded by the German Research Foundation (DFG) under the contract numbers DFG projects: PAK 446 (FO 226/21-1, ME 2100/5-1, RA 617/23-1 and HE 5214/4-1). The funding of the Horizontal Mobile Measuring System (HMMS) presented in this thesis was realised by the University of Bayreuth and the Max Planck Institute for Chemistry, but not within PAK 446.

Summary

Forest ecosystems play a key role in the Earth's carbon cycle, as their uptake of carbon dioxide is largest in the terrestrial biospheres (CO₂ sink). Despite a vast number of ecological studies about forest ecosystem, there are still outstanding issues about prevailing meteorological conditions, turbulent and coherent structures and exchange processes of heterogeneous forest ecosystems. Therefore, this thesis is related to the joint research project EGER IOP3 (ExchanGE processes in mountainous Regions - Intensive Observation Period 3), aimed at the investigation of diurnal cycles of energy, matter and (non-)reactive trace compounds in the soil-vegetation-boundary-layer-system at a forest edge within a heterogeneous forest ecosystem in a very complex terrain in mid Europe.

Well established measurement techniques were used, such as the eddy-covariance method for determination of turbulent/coherent fluxes and for detection of different vertical and horizontal coupling regimes. SODAR/RASS systems were used to investigate boundary layer phenomena. Additionally, a novel, fully automatic Horizontal Mobile Measuring System (HMMS) was successfully developed, applied and assessed within this thesis. The HMMS was installed on a 150 m long transect perpendicular to the forest edge, to obtain higher information density about horizontal gradients of eight quantities (short/long-wave down/upwelling radiation, temperature, humidity, CO₂ and O₃ concentration). The experimental design, with 3D installation of the towers/masts, HMMS and profiling systems was ideal for the investigation of the research issues mentioned above.

By combination of all measurement techniques, significant differences could be observed along the transect forest-forest edge-clearing (three locations), with strong distinctions in the vicinity of the forest edge. The highest gradients in the HMMS measurements occurred near the forest edge. Furthermore, it could be observed that the turbulence influenced quantities in the HMMS measurements (temperature, humidity and trace gases) were mainly affected by the prevailing vertical structures at the forest edge, while the influence decreased, the further away from the forest edge. These findings coincide with the findings for coherent structures, where only at the forest edge a significant daily variation could be observed for ejections and sweeps, with strong ejection motions during daytime (updraft) and strong sweep motions during nighttime (downdraft).

The thermal updraft during daytime could be attributed to the highest temperatures occurring near the forest edge (1.5 K warmer than at the clearing and within the forest) and the advective transport of energy towards the forest edge. The reverse was also apparent, where energy was transported off the forest edge towards the clearing. Nevertheless, highest energy and CO₂ fluxes, as well as highest variation could be observed at the forest edge. This leads to a better energy balance closure at the forest edge (Residual *Res* = 17 %), compared to both other locations (*Res* = 25 – 30 %). These findings indicate the facilitation of quasi-stationary secondary circulations above the observation site, which could be confirmed to some extent by further experimental observations. During times of horizontal energy exchange, there was a horizontal coupled regime and an inflow of O₃-depleted (decrease in concentration of approximately 20 ppb), and slightly colder air along the transect perpendicular to the forest edge, originating from the atmosphere above the site. Additionally, the ACASA model showed discrepancies between modelled and measured fluxes which could be attributed to horizontal advective flow and secondary circulations.

The investigation of boundary layer phenomena, such as low-level jets (LLJ) and strong winds showed considerable different impacts on exchange processes above the heterogeneous forest ecosystem. During LLJ there was a coupled regime (C/Cs), with good mixing and enhanced CO₂ fluxes, while during strong wind situations wave motions (Wa; uncoupled regimes) occurred with no mixing and reduced CO₂ fluxes. True, effects could be observed at every location, due to changes in vertical coupling regimes and coherent transport. However, coherent transport was found to be largest above the forest and decreasing towards the clearing, and thus the CO₂ fluxes were also most affected above the forest and less affected towards the clearing. During LLJ events the CO₂ fluxes were enhanced by approximately 100 % above the forest, 70 – 100 % at the forest edge, while above the clearing the fluxes were only marginally enhanced. During uncoupled situations (Wa) the fluxes were reduced by approximately 100 % above the forest and again, the changes were less at the forest edge and marginal above the clearing. The different CO₂ fluxes led to significant gradients of CO₂ concentration along the transect, resulting even to a drainage of CO₂-enriched air out off the forest onto the clearing (during strong wind situation).

The continuous horizontal transect measurements of the HMMS in combination with tower measurements provided a new understanding of exchange processes of heterogeneous forest ecosystems. Such an overview of prevailing gradients, inflows, outflows, accumulations, depletions, as well as insights on coherent/turbulent transport, coupling regimes, secondary circulations and boundary layer phenomena over spatial and temporal terms would have not been possible if only static tower measurements were used.

Zusammenfassung

Der Wald spielt eine sehr wichtige Rolle im Kohlenstoffkreislauf der Erde, denn er nimmt global gesehen das meiste Kohlenstoffdioxid der gesamten terrestrischen Biosphäre auf (CO₂-Senke). Trotz einer Vielzahl bestehender Untersuchungen gibt es ungelöste Fragen über die vorherrschenden horizontalen Gradienten meteorologischer Messgrößen, die turbulenten und kohärenten Strukturen und die Austauschprozesse von heterogenen Wäldern. Diesen offenen Fragen widmete sich das EGER IOP3 Projekt (Austauschprozesse in Gebirgsregionen - Intensive Observationsperiode 3), welches Energie-, Stoff- und (nicht-)reaktive Spurengasflüsse an einer Waldkante innerhalb eines heterogenen Waldes in einem mitteleuropäischen Mittelgebirge untersucht.

Für die Untersuchung der turbulenten und kohärenten Flüsse, sowie für die Bestimmung der vertikalen und horizontalen Kopplungszustände wurde die sehr gebräuchliche Eddy-Kovarianz-Methode verwendet. SODAR/RASS Systeme wurden verwendet, um Besonderheiten in der Grenzschicht zu erkennen. Neben den üblichen Messmethoden, wurde im Rahmen dieser Dissertation ein neues, vollautomatisches Horizontal Mobiles Messsystem (HMMS) entwickelt, mit anderen Messsystemen verglichen und damit gemessen. Das HMMS war orthogonal zur Waldkante auf einem 150 m langen Transekt aufgebaut, um sehr detaillierte horizontale Profile von Globalstrahlung, Reflexstrahlung, Gegenstrahlung, Ausstrahlung, Temperatur, Luftfeuchte, CO₂- und O₃-Konzentration (insgesamt acht Messgrößen) zu erhalten. Der experimentelle Aufbau aller Messmasten/-türme, des HMMS und der Profilanlagen wurde optimal für die oben genannten Fragestellungen gewählt.

Erhebliche Unterschiede konnten entlang des Profils Wald – Waldkante – Lichtung (drei Messstandorte) beobachtet werden, mit deutlichen Auffälligkeiten in der Nähe der Waldkante. Diese Erkenntnisse waren erst möglich durch die Kombination einer Vielzahl von Messsystemen. So haben die HMMS-Messungen ergeben, dass sich die deutlichsten Gradienten für alle Messgrößen an der Waldkante befinden, und diese sehr stark durch die turbulenten Bedingungen dort beeinflusst werden (gilt nur für Temperatur, Luftfeuchte und Spurengaskonzentrationen). Je weiter entfernt von der Waldkante, desto weniger ist ein Einfluss messbar. Dies kann durch die Untersuchungen der kohärenten Strukturen bestätigt werden, bei denen ausschließlich an der Waldkante ein Tagesgang für die Verteilung

von aufwärtsgerichteten (Auftrieb) und abwärtsgerichteten (Böen) Strukturen beobachtet wurde. Am Tag dominiert an der Waldkante der Auftrieb und in der Nacht die Böen.

Der Auftrieb tagsüber an der Waldkante kann durch die dort höchsten Temperaturen (1.5 K wärmer als im Wald und auf der Lichtung) und durch den advektiven Transport von Energie von den beiden anderen Standorten in Richtung Waldkante erklärt werden. Es gibt zwar auch den umgekehrten Transport von Energie von der Waldkante in Richtung Lichtung, dieser ist aber geringer, sodass die höchsten Energie- und CO₂-Flüsse, sowie die größten Schwankungen in den Flüssen, an der Waldkante gemessen werden konnten. Die erhöhten Energieflüsse führen an der Waldkante zu einer besser geschlossenen Energiebilanz (Residuum $Res = 17\%$) im Vergleich zu den beiden anderen Standorten ($Res = 25 - 30\%$). Diese Untersuchungsergebnisse suggerieren eine quasi-stationäre, sekundäre Zirkulation über der Messfläche, welche durch weitere Messungen ansatzweise bestätigt und gezeigt werden konnte. So zeigten die horizontalen Kopplungszustände, zu Zeiten des horizontalen Energieaustausches, ein teilweise oder komplett gekoppeltes System. Zur gleichen Zeit war ein Eintrag von O₃-ärmeren (ungefähr 20 ppb geringere Konzentration), leicht kälteren Luftmassen entlang des gesamten HMMS-Transektes messbar, welche von oben nach unten transportiert wurden. Auch die Modellierungen mit ACASA zeigten Unterschiede beim Vergleich der modellierten und gemessenen Flüsse, welche auf einen horizontal advektiven Transport und sekundäre Zirkulation hinweisen.

Die Untersuchung von Phänomenen in der atmosphärischen Grenzschicht hat gezeigt, dass zum Beispiel ein Starkwindband (Low-level Jet, im Folgenden LLJ genannt; verursacht durch Bodeninversion) deutlich unterschiedliche Auswirkungen auf die Austauschprozesse über einem heterogenen Wald haben kann, als eine stark ausgeprägte Inversionsschicht (Starkwinde treten häufig oberhalb der Inversionsschicht auf). Während des LLJ kam es zu einem gekoppelten System (C/Cs) mit guter Durchmischung und erhöhten CO₂-Flüssen, wohingegen es bei der Inversionsschicht mit Starkwinden zu einem entkoppelten System (Wa) mit schlechter Durchmischung und verringerten CO₂-Flüssen kam. Bei beiden Phänomenen waren zwar die Auswirkungen an allen Standorten messbar, aber am deutlichsten über dem Waldbestand und abnehmend in Richtung Waldkante und Lichtung. Dies kann durch den kohärenten Transport erklärt werden, welcher über dem Waldbestand ebenfalls am größten ist und in Richtung Lichtung abnimmt. Der CO₂-Fluss wurde während des LLJ um 100 % über dem Wald, um 70 – 100 % an der Waldkante und nur minimal über der Lichtung erhöht, wohingegen bei dem entkoppelten System (Wa) eine Reduzierung um etwa 100 % oberhalb des Waldes gemessen wurde. Die Reduzierung an der Waldkante und über der Lichtung war deutlich weniger ausgeprägt. Die Unterschie-

de in den CO_2 -Flüssen führten auch zu erheblichen Gradienten in der CO_2 -Konzentration entlang des Transektes. Im Falle des entkoppelten Systems kam es zu einem nächtlichen Kaltluftabfluss mit hohen CO_2 -Konzentrationen aus dem Wald auf die Lichtung.

Die kontinuierlichen horizontalen Transektmessungen des HMMS lieferten in Kombination mit den Eddy-Kovarianz-Turmmessungen ein neues, besseres Verständnis über die Austauschprozesse eines heterogenen Waldes. Ein solcher Überblick in räumlichen und zeitlichen Skalen von vorliegenden Gradienten, Zuflüssen, Ausströmungen, An- und Abreicherungen von Spurengaskonzentrationen, sowie Einblicke in den turbulenten und kohärenten Transport, in Kopplungszustände, in sekundäre Zirkulationen und in Grenzschichtphänomene war erst durch die Kombination aller Messmethoden möglich und wäre niemals in diesem Umfang zu realisieren gewesen, wenn ausschließlich die wie sonst üblichen Fixpunkt-Messungen verwendet worden wären.

1. Introduction

1.1. Motivation: The role of forest ecosystems

Forest ecosystems cover 31 % of the total land surface (as of 2010), largely in the temperate, boreal zones and in the tropics (FAO, 2010). Due to the high biomass and the resulting high level of photosynthesis and respiration, forests play a key role in the Earth's carbon cycle. They, as well as the oceans, are the most important sink for atmospheric carbon dioxide (CO_2), and it is widely considered to be the prime sink of the terrestrial biosphere. CO_2 is a greenhouse gas like methane (CH_4), nitrous oxide (N_2O), and the halocarbons – a group of gases containing fluorine, chlorine and bromine; e.g. chlorofluorocarbons (CFCs) – they are all responsible for a temperature increase in the atmosphere. Because of human activities the CO_2 concentration in the atmosphere has risen rapidly since the industrialisation (pre-industrial value of about 280 to 391 ppm in 2011), primarily because of fuel combustion and land-use changes, and is therefore the most important anthropogenic greenhouse gas with a radiative forcing of about 1.68 W m^{-2} (IPCC, 2013). However, this anthropogenic induced increase of CO_2 affects not only the atmosphere (global warming), there is also an interaction between the atmosphere and the other earth's spheres (biosphere, hydrosphere, lithosphere) observable, disturbing the global carbon cycle. The biosphere reacts the fastest to changes in the atmosphere with a short time delay, followed by the hydrosphere and then by the lithosphere. Having a closer look at the terrestrial biosphere, mainly in forest ecosystems, an increased uptake of CO_2 is observable. This is related to an anthropogenic induced enhancement in the atmosphere (e.g. Prentice et al., 2001; Schimel et al., 2001; Houghton, 2003; House et al., 2003; Le Quéré et al., 2003; Schulze, 2006; Wolf, 2008; Luysaert et al., 2010; Ballantyne et al., 2012; IPCC, 2013). Despite the increased carbon uptake of the biosphere and the hydrosphere, CO_2 concentrations in the atmosphere will continue to increase, because anthropogenic discharge is higher than the uptake by plants and oceans (IPCC, 2013).

These insights illustrate the need to investigate the terrestrial biosphere, particularly forest ecosystems, in order to understand the processes there in detail (e.g. prevailing turbulent exchange processes above plants, photosynthesis and respiration rates, plant

growth, etc). With the understanding of the processes, together with the investigation of the total CO₂ balance of an ecosystem, the so called Net Ecosystem Exchange (*NEE*), an overall evaluation of an ecosystem can be created.

The majority of investigations performed until today were conducted in homogeneous parts of forests. If one looks at the terrestrial earth's surface, it reveals a patchy, or in other words a heterogeneous surface. The heterogeneity increases more and more. Especially forest ecosystems are particularly affected by an increasing heterogeneity due to wind throws, forest fires, pests, and human activities, like deforestation (fragmented land use). It is presumed that the heterogeneity of forest ecosystems, or rather forest edges has greater effects on exchange processes between atmosphere, vegetation and soil. Up to now relatively little is known about the influence of the heterogeneity on the exchange processes (Knohl et al., 2002).

Based on the latest state of knowledge about forest ecosystems and the prevailing exchange processes an overview of the work already done is given in Section 1.2. This current study addresses the investigation of horizontal as well as vertical structures in a heterogeneous part of a forest ecosystem, with the focus on a forest edge. Here, issues are considered to achieve a better understanding of the influences of a forest edge on the exchange processes within a forest ecosystem (Section 1.3).

1.2. Scope of the research topic

1.2.1. Exchange processes of forest ecosystems

As already mentioned, a large portion of the earth's surface is covered by forest ecosystems and due to that, this is a very active area of research. With a large focus on exchange processes between the (forest) ecosystem and the atmosphere, which differs substantially from those in the 'standard' surface layer (Finnigan, 2000). Garratt (1978, 1980) as well as Cellier and Brunet (1992) considered the roughness sublayer (RSL, extent: approximately 3 times the canopy height), where the turbulent diffusivity is larger than in the unaffected atmospheric surface layer due to an increased vertical mixing. Within forest ecosystems the turbulent exchange is extremely intermittent and restricted to distinct, mainly short periods (Shaw et al., 1983; Finnigan, 2000). An additional special phenomenon for forest ecosystems has been discussed by Denmead and Bradley (1985, 1987), the so-called counter-gradients, where turbulent fluxes in the canopy do not follow local gradients. Counter-gradients can also be observed in the RSL above the canopy (Fazu and Schwerdtfeger, 1989). Furthermore, in forest ecosystems advection can also be observed (Aubinet et al., 2003). In

addition to small-scale random turbulent motions, there are large-scale, organised, quasi-deterministic, but non-periodic eddy structures observable (Cantwell, 1981), which play a key role in the exchange processes of forest ecosystems, so called coherent structures (Holmes et al., 2012). Coherent structures appear as ramp structures in scalar time series and were described by Bergström and Högström (1989) and Gao et al. (1989) within and above the forest. Ramp structures can also be found in trace gas fluctuations (Rummel et al., 2002). According to the mixing layer analogy (Raupach et al., 1996; Finnigan, 2000), coherent structures are caused by Kelvin-Helmholtz instabilities, which develop by high shear forces above the rough forest canopy. Harman and Finnigan (2007, 2008) developed a theory combining the mixing layer analogy with the RSL. Another reason for the development of coherent structures within forest canopies are thermal plumes, rising up and bursting through the canopy (Thomas et al., 2006), or larger coherent structures in the lower boundary layer impinging down to the ground (Inagaki et al., 2012). Additionally, low-level jets (LLJ) exist, which have a substantial effect on the night-time exchange in forests (increasing the turbulence and mixing near the ground due to an increased shear; Karipot et al., 2006, 2008; Foken et al., 2012b).

The investigation of coherent structures has been an integral part in a variety of laboratory (e.g. Kline et al., 1967; Wallace et al., 1972; Lu and Willmarth, 1973; Raupach, 1981) and experimental studies (e.g. Finnigan, 1979; Shaw et al., 1983; Bergström and Högström, 1989). These have shown that coherent structures mainly consist of a weak ejection transporting warm and/or moist air out of the forest and a strong burst (sweep) of cool and/or dry air penetrating into the canopy. Nevertheless, the contribution to the total flux of sensible and latent heat lies more on the side of the ejections than on the sweeps (Bergström and Högström, 1989). The contribution under near-neutral conditions is higher for sweeps and under unstable conditions higher for ejections (Maitani and Ohtaki, 1987). Wavelet analyses were also used for the investigation of large datasets, to determine the time scales and flux contributions of coherent structures in forest ecosystems (Collineau and Brunet, 1993a,b). Thomas and Foken (2005, 2007a,b) improved the wavelet analysis technique by estimating the mean temporal scales of coherent structures via the fitting of a normal Gaussian distribution function to the probability density function of the results from individual 30-min intervals. Thomas and Foken (2007b) defined different coupling (exchange) regimes along the vertical profile by investigating the flux distribution, caused by coherent structures, in different heights. This classification scheme is based on the conditional sampling and averaging technique (Antonia, 1981) in combination with wavelet analysis (Thomas and Foken, 2005) and was extended to the horizontal profile by Serafimovich et

al. (2011b) to investigate the lateral contribution of coherent structures in the sub-canopy layer (trunk space) of the forest. Thomas et al. (2013) introduced an additional coupling regime in the vertical profile.

A variety of experimental studies have been conducted in homogeneous parts of forest ecosystems in order to describe coherent structures prevailing there, with the following results: (i) the persistence of coherent structures typically ranges from tens of seconds to a few minutes, (ii) the contribution is higher to scalar fluxes than to the momentum flux (Collineau and Brunet, 1993b; Thomas and Foken, 2007b; Serafimovich et al., 2011b; Steiner et al., 2011), (iii) ejections are dominating the coherent structures in the RSL, whereas the sweeps are dominating the canopy layer (valid for a dense crown layer; Finnigan, 1979; Bergström and Högström, 1989; Poggi et al., 2004; Katul et al., 2006). In the ejection phase, the motions can be directly linked to ecosystem responses such as sub-canopy respiration events (Zeeman et al., 2013). And as a further result: (iv) the vertical coupling is usually stronger during daytime than at night (Thomas and Foken, 2007b; Serafimovich et al., 2011b), whereas the horizontal coupling is not influenced by diurnal or nocturnal differences, but rather controlled by topography, vegetation structure and mean wind direction (Serafimovich et al., 2011b).

Another observed phenomenon within forest ecosystems and also for other complex (heterogeneous) terrain, is an energy balance which can not be closed (the so-called energy balance closure problem; Foken, 2008b; Mahrt, 2010; Foken et al., 2012b). Theoretically, the available energy at the Earth's surface – sum of net radiation (Q_S^*), ground heat flux (Q_G) and storage heat flux (Q_B), which is only relevant for the forest – should be the same as the sum of sensible (Q_H) and latent heat flux (Q_E). The investigations of Aubinet et al. (2000) and Wilson et al. (2002) showed an underestimation of sensible and latent heat in eddy-covariance measurements, which resulted in a residual (Res) of the energy balance. The residual is in the order of about 20 % of the available energy:

$$Res = Q_S^* - (Q_G + Q_B + Q_H + Q_E) \quad (1.1)$$

Possible reasons for an unclosed energy balance have been discussed in a number of former studies. They have shown that (i) the eddy-covariance method as well as the measurements of the net radiation are accurate and a careful application, in order to minimise measuring errors, only have a small effect on the energy balance closure (e.g. Foken, 2004; Moncrieff, 2004; Mauder and Foken, 2006; Mauder et al., 2006, 2007b), (ii) most energy storage terms can be determined with high accuracy and the storage terms can not close the energy balance (e.g. Culf et al., 2004; Liebethal and Foken, 2007; Oncley et al., 2007; Foken,

2008b), and (iii) the surface heterogeneity generated larger time scale turbulent structures (low-frequency part of the spectra up to about 2 h) which are close to measuring towers can be captured by the eddy-covariance method (Thomas and Foken, 2007b; Zhang et al., 2007) and therefore the relevance for the energy balance closure is small. Nevertheless, it is assumed that the surface heterogeneity plays a substantial role for the unclosed energy balance, because, in landscapes without heterogeneities, a closure of the energy balance could be observed (e.g. Heusinkveld et al., 2004; Mauder et al., 2007a; Foken, 2008b). The surface heterogeneity generates large-scale turbulence structures, which can not be captured adequately by the eddy-covariance method and therefore they have a substantial influence on the energy balance closure (Foken, 2008b; Mahrt, 2010; Foken et al., 2012b). So, there is an indication that the residual *Res* is transported within advective and low-frequency flux contributions (e.g. Sakai et al., 2001; Finnigan et al., 2003; Malhi et al., 2005; Foken et al., 2006; Mauder and Foken, 2006) and within quasi-stationary circulations (e.g. Kanda et al., 2004; Inagaki et al., 2006; Steinfeld et al., 2007; Foken et al., 2010; Stoy et al., 2013). Such secondary circulation systems are mainly buoyancy-driven due to differences in thermal heating of the land surface. Possible ways to close the energy balance are long-time averaged fluxes (Sakai et al., 2001; Finnigan et al., 2003; Mauder and Foken, 2006) or spatially averaged fluxes (Kanda et al., 2004; Inagaki et al., 2006; Steinfeld et al., 2007), via Laser-Scintillometer or airborne measurements. There is another approach for a closed energy balance available, which divides the available residual to the sensible (Q_H) and latent (Q_E) heat flux (Twine et al., 2000; Charuchittipan et al., 2014)

1.2.2. Characteristics of exchange processes at a forest edge

Investigation of surface heterogeneities of forest ecosystems (mainly forest edges) and the presumed impact on the exchange processes is becoming more and more the focus of the community. Here, the forest edge with the prevailing driving forces, which are in detail differences of up- and downwelling radiation, temperature, moisture, and the resulting wind regime (Murcia, 1995; Matlack and Litvaitis, 1999; Davies-Colley et al., 2000; Klaassen et al., 2002), has a strong impact on the atmospheric boundary layer (ABL) flow structure (Mahrt et al., 1994; Weaver and Avissar, 2001). A possible consequence is the facilitation to develop quasi-stationary secondary circulations near the forest edge, caused by different surfaces. A secondary circulation is defined as an 'organized flow superimposed on a larger-scale mean circulation' (Glickman, 2000). Additionally, at the forest edge an enhancement of vertical turbulent fluxes in the downwind region is observable (Klaassen et al., 2002; Leclerc et al., 2003), which might be explainable by an increased number of

coherent structures there (Zhang et al., 2007; Eder et al., 2013).

Forest edges and prevailing gradients were targeted in a variety of micrometeorological studies (e.g. Dawson and Sneddon, 1969; McDonald and David, 1992; Chen et al., 1993, 1995; Davies-Colley et al., 2000; Newmark, 2001). Sogachev et al. (2005, 2008) investigated the effects of forest edges and source distribution on fluxes, estimated by eddy-covariance measurements above forests. Also numerical studies, like large-eddy simulations (LESs), in many cases also combined with experimental measurements have been performed (e.g. Yang et al., 2006a,b; Cassiani et al., 2008; Dupont and Brunet, 2008, 2009; Finnigan et al., 2009; Huang et al., 2011; Belcher et al., 2012; Dupont et al., 2012; Schlegel et al., 2012; Kanani et al., 2014). However, the micrometeorological community lacks sufficient experimental data and because of this, there still exists a knowledge gap about turbulent exchange processes, as well as properties of coherent structures directly around roughness heterogeneities (forest edges).

1.2.3. Measuring techniques

Measurements of turbulent fluxes of sensible heat, momentum, water vapour, carbon dioxide (CO_2), and further trace gases are performed with the fast-response (measuring frequency: 10 – 20 Hz) and direct eddy-covariance method, which is state-of-the-art. Therefore, the eddy-covariance method is also appropriate for the quantification of long-term flux measurements (Baldocchi et al., 2001; Moncrieff, 2004; Baldocchi, 2014) and for the detection of forest typical phenomena (see sections above).

Despite the relatively easy applicability and the high temporal resolution of the eddy-covariance method, it lacks an adequate spatial resolution, as well as the representativeness of measurements (Thomas et al., 2006). A high spatial resolution needed for the interpretation of huge investigation areas can be achieved either by a large number of locally fixed sensors at various locations or by (fast moving) mobile measuring systems (Oncley et al., 2009). The application of mobile systems makes sense if the number of locally fixed sensors is not sufficient and/or the accuracy of different, independent sensors of the same measured quantity is not guaranteed (Oncley et al., 2009). For a highly spatially resolved investigation of the ABL, in order to determine coherent structures and LLJ for example, there are (radio-)acoustic sounding systems available (SODAR/RASS; e.g. Taconet and Weill, 1982, 1983; Thomas et al., 2006; Karipot et al., 2006, 2008; Duarte et al., 2012).

In former studies, mobile measuring systems mostly carried radiometers above and under forest canopies to measure the areal distribution of upwelling and/or downwelling radiation (e.g. Leonard and Eschner, 1968; Mukammal, 1971; Brown, 1973; Baldocchi et al.,

1984a; Baldocchi et al., 1984b; Péch, 1986; Lee and Black, 1993; Chen et al., 1997; Privette et al., 1997; Blanken et al., 2001). Rodskjer and Kornher (1967, 1971) did comparable measurements above grasslands. To study wind velocity and tower-induced errors of its measurements, Dabberdt (1968) built a mobile system which carried an anemometer. The ‘Asa-Shuttle’ of Örlander and Langvall (1993) and Langvall and Löfvenius (2002) measured, in addition to radiation, the air temperature along a horizontal transect of decreasing shelterwood density of Norway spruce. The mobile system of Gamon et al. (2006) carried a dual-detector spectrometer to measure ecosystem spectral reflectance. A mobile system, moving in the vertical and horizontal direction, was invented by Singh et al. (2008). They used their system for the study of river and lake aquatic systems. The TRAM (Transect Measurement) system of Oncley et al. (2009) measured wind velocity (high frequency via ultrasonic anemometer), carbon dioxide concentration, air temperature and humidity. They were able to run their TRAM within a closed measurement track (loop) through a forest ecosystem and over a creek (AmeriFlux site at Niwot Ridge) through the use of steel cables and masts, which allowed mobile measurements over a long horizontal distance and also changing of the vertical measurement height. Besides the mobile platforms mentioned above, there are investigations with mobile measurements in aircrafts, balloons, lifts, and other mobile platforms (e.g. Lenschow, 1972; Kaimal et al., 1976; Ogawa and Ohara, 1982; Balsley et al., 1992, 1998; Friehe and Khelif, 1992; Muschinski et al., 2001; Mayer et al., 2009), as well as temporally and spatially high resolved measurements of temperature with fibre-optic (Thomas et al., 2012).

Most sensors used on mobile measuring systems are low frequency measuring sensors – except of the wind velocity measurements of the TRAM from Oncley et al. (2009), some high frequency airborne measurements and the fibre-optic measurements from Thomas et al. (2012) – and due to that, mobile systems are not performing the eddy-covariance method and consequently no fluxes are measured (to provide a comprehensive view of flux measurements within large investigation areas the eddy-covariance method has to be applied at a variety of locations). Mobile systems are rather used for the investigation of gradients along transects. But there exists a common problem when low frequency sensors are in use. The input signal of every low frequency sensor will follow a very sudden change in the measured quantity with certain delay and damping effects. These effects are commonly characterised by an individual sensor response time, or time constant τ . The bias is usually due to (i) the sensor itself, (ii) the sensor’s housing, and/or (iii) the sensor’s inlet system, particularly for gas analysers (see Mayer et al., 2009). The time constant influences the measurements of mobile measuring systems in such a way that because of

the movement, the time constant can result in an error in time, but also in space. The total error of a measuring system is referred to as the dynamical error.

There are possibilities named in the literature to correct dynamical errors mathematically and these corrections were done mainly for temperature sensors in aircraft (e.g. Rodi and Spyers-Duran, 1972; McCarthy, 1973; Friehe and Khelif, 1992; Inverarity, 2000; Saggin et al., 2001). Correction algorithms also exist for the temperature and humidity measurements with radiosondes (e.g. Miloshevich et al., 2004), while another simple linear correction algorithm for temperature sensors in a vertical moving platform was developed by Mayer et al. (2009). Comparable corrections for measurements with horizontal measuring systems (mentioned above) have not yet been made, because of (i) an averaging along the measuring track (especially for radiation measurements in more homogeneous measuring sites), (ii) a non-moving system while measurements are conducted, to guarantee a full adaptation of the sensor input signal to the prevailing environmental conditions and (iii) the application of high-frequency sensors for which the dynamical errors are negligible.

1.3. Objectives of the thesis

This thesis investigates horizontal structures at a forest edge within a heterogeneous forest ecosystem during the EGER IOP3 project (ExchanGE processes in mountainous Regions - Intense Observation Period 3, see Section 2.1 for an overview of the EGER project). Several studies already exist in heterogeneous forest ecosystems (see Section 1.2.2), however not all turbulent exchange processes around roughness heterogeneities are completely understood. To better understand the impact of forest edges (equivalent to a roughness change) on the exchange processes of a forest ecosystem, the following research issues have been addressed:

1. Application of a new mobile measuring system to investigate horizontal gradients and implementation of a correction algorithm for dynamical errors.
2. Investigation of the interaction between forest and clearing, including the influence of the forest edge on the temporal and spatial variability (heterogeneity) of micro-meteorological parameters, turbulent structures and energy balance closure.
3. Investigation of vertical structures and their influence on horizontal structures considering the prevailing coherent structures and coupling regimes (Eder et al., 2013).
4. Consideration of other influencing factors on horizontal structures, like boundary layer dynamics, in particular low-level jets, nocturnal strong winds or bursts.

In Section 2 the objectives of the EGER project, and the project site, as well as all used methods of measurement, and post-field data analyses needed for the processing of the research issues are presented. The EGER project was conducted in three different IOPs. In IOP1 (autumn 2007) and IOP2 (summer 2008) the focus was on the investigation of exchange processes within a homogeneous part of a heterogeneous spruce forest (see Section 2.1.2), while in IOP3 the focus changed to the investigation of exchange processes caused by roughness heterogeneity (forest edge) within this forest (see Section 2.1.3). As previously mentioned, this study mainly addresses IOP3, and therefore, known measurement techniques were used. Such as the eddy-covariance method, SODAR/RASS systems and additional vertical gradient measurements of temperature, wind velocity and CO₂ concentration. The measurements were positioned in such a way to obtain best representativity of the heterogeneous forest ecosystem. Measurements were taken within and above the forest (which can be compared to the results gained in IOP1 & IOP2 and presented in Foken et al., 2012b), at the forest edge and at the clearing and additionally another transect along the forest edge. This 3D installation of the fixed tower measurements was like a cross, with a transect perpendicular and another parallel to the forest edge, with SODAR measurements on both sides (Section 2.2).

Beside the fixed tower measurements, a new Horizontal Mobile Measuring System (HMMS; Hübner et al., 2011, 2014 and Section 2.3) was designed, built and applied to investigate horizontal gradients along a 150 m long transect perpendicular to the forest edge. The HMMS is equipped with long-wave and short-wave radiation sensors (with individual sensors for up- and downwelling radiation), a sensor for air temperature and relative humidity, and analysers for the carbon dioxide (CO₂) and ozone (O₃) concentration. In particular, the O₃ analyser used on such a small system is an innovation in mobile measuring techniques. It was installed because trace gases are good tracers for different coupling regimes (Foken et al., 2012b). Here, low frequency sensors are used to measure gradients and not turbulent fluxes. To my knowledge, dynamical errors caused by the individual response times of the sensors have not been considered in near-ground horizontal mobile measuring systems up to now (in contrast to vertical systems and aircrafts). A linear correction algorithm to correct dynamical errors was applied and results presented, showing the necessity of this application (see Hübner et al., 2014 and Section 2.4.1).

Comparison of the HMMS results with fixed tower measurements show, in essence, a very good agreement (Section 3.1) and therefore a successful realisation of the new mobile system. This allows an interpretation of the prevailing gradients of typical meteorological parameters near the forest edge (Section 3.2.1), which have never been possible with fixed

tower measurements. This enables the interpretation of energy fluxes and the energy balance closure (Section 3.2.2), which are investigated along the same transect perpendicular to the forest edge. The same is also true for the interpretation of the horizontal and vertical coupling regimes and the distribution of coherent structures. At and in the vicinity of the forest edge discrepancies are expected, caused by the roughness change (landscape heterogeneity) and thereof induced secondary circulations, which affect the closure of energy balance (Foken, 2008b) and the exchange of the soil-vegetation-boundary-layer system. There is already a good indication for secondary circulations at the forest edge of the EGER site. Such as the findings of Eder et al. (2013), which are presented in Section 3.2.3, with a daily cycle of coherent structures only at the forest edge as well as the ACASA modelling results, produced by Gatzsche (2013) in the scope of her master thesis (Section 3.2.4), show a better agreement by closing the energy balance by the buoyancy flux (Charuchittipan et al., 2014). Their results are now linked with all other measurement results (mainly turbulent fluxes, vertical temperature and CO₂ profiles and the HMMS measurements) to validate their assumptions. To clarify if discrepancies are mainly caused by changing weather conditions or alternating wind directions, the coherences were, in addition to averaged periods, also considered in individual cases (Section 3.4.1).

In addition, other influencing factors on horizontal structures are considered, such as atmospheric boundary layer dynamics, which were investigated with the aid of SODAR systems. Here especially, low-level jets (LLJ; Section 3.4.2) are very interesting, since they enhance the mixing and nocturnal fluxes (e.g. Karipot et al., 2006, 2008; Foken et al., 2012b) due to changes of coherent transport. But also, nocturnal strong winds change the conditions significantly. Longtime decoupling situations, and the accumulation of trace gas concentrations and nocturnal drainage are the result (Section 3.4.3). Other boundary layer dynamics can change the vertical and horizontal conditions directly by for example inflow of fresh air reaching the ground (Section 3.4.4).

2. Materials and methods

2.1. The EGER project

The EGER project (ExchanGE processes in mountainous Regions) investigates the diurnal cycles of energy, matter, reactive and non-reactive trace compounds in the soil-vegetation-boundary layer-system of a heterogeneous forest ecosystem in a very complex terrain (see Section 2.1.1). Therefore, a total of three intensive observation periods (IOPs) have been conducted. In IOP1 & IOP2 (Section 2.1.2; Foken et al., 2012b) the measurements were conducted in a more homogeneous part of the forest ecosystem in autumn 2007 and summer 2008, where footprint analyses have shown that the results are mainly unaffected by the heterogeneity (Siebicke, 2008). In IOP3 (see Section 2.1.3) the focus of the investigations changed to a more heterogeneous part of the forest and due to that, measurements were conducted at a transition from the forest to the clearing ‘Köhlerloh’ (forest edge with roughness change), in summer 2011. As previously mentioned, this work addresses the results found during IOP3.

2.1.1. Site description

The experimental field work was conducted at a research site of the Bayreuth Center of Ecology and Environmental Research (BayCEER), namely the ‘Waldstein-Weidenbrunnen’ site (50°31′11″ N, 11°52′1″ E, 775 m a.s.l.). The site is situated within a very complex terrain in the upper ‘Lehstenbach’ catchment (4.5 km²; 695 – 877 m a.s.l.) part of the ‘Fichtelgebirge Mountains’ (northeastern Bavaria, Germany, see Figure 2.1). The ‘Fichtelgebirge Mountains’ are located in the climate zone Dc (Classification by Köppen according to Hendl, 1991). The annual precipitation at the site is 1162.5 mm and the mean annual temperature is 5.3 °C (1971-2000; Foken, 2003). The upper ‘Lehstenbach’ catchment is surrounded by the hilltops of ‘Großer Waldstein’ (879 m a.s.l.) in the south-west and ‘Bergkopf’ (857 m a.s.l.) in the north-east. The wind flow regime at the site is dominated by westerly winds (west to south-west) due to the synoptic prevailing wind direction and the channelling function of both hills, ‘Großer Waldstein’ and ‘Bergkopf’. Furthermore, there are

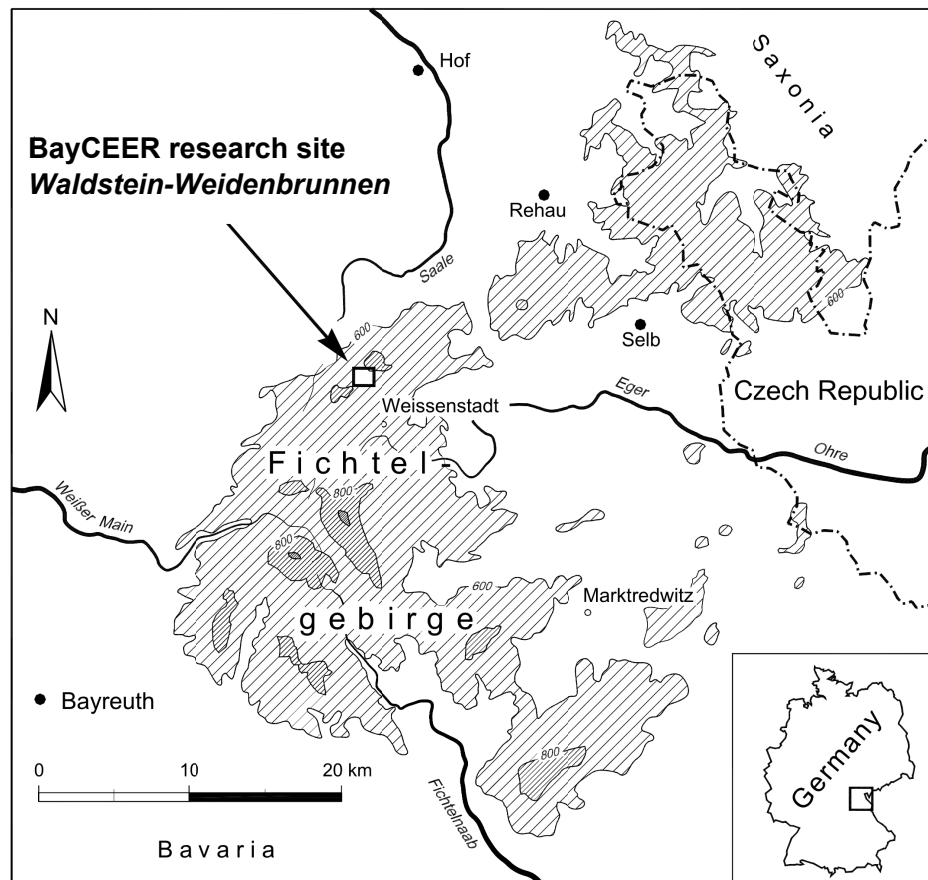


Figure 2.1. Location of the investigation site of the EGER project within the ‘Fichtelgebirge Mountains’ (Gerstberger et al., 2004 modified). Hatchings indicates elevations > 500 m a.s.l. and > 750 m a.s.l., respectively.

Table 2.1. Representativeness of the vegetation at the clearing ‘Köhlerloh’ with ground cover (%), height (m) and PAI ($m^2 m^{-2}$) (Serafimovich et al., 2011a).

Vegetation form	Ground cover	Height	PAI
<i>Deschampsia flexuosa</i>	21.7	0.17 ± 0.05	2.65 ± 1.08
<i>Picea abies</i>	21.4	1.21 ± 0.50	8.67 ± 2.29
<i>Vaccinium myrtillus</i>	15.9	0.27 ± 0.10	3.46 ± 1.05
<i>Calamagrostis, Agrostis, Poaceae</i>	9.0	0.42 ± 0.11	3.43 ± 1.07
<i>Juncaceae, Cyperaceae</i>	3.1	0.74 ± 0.13	1.77 ± 0.60
other herbaceous*	1.6	-	-
mosses	0.9	-	-
dead grass, bare soil	7.2	-	-
dead wood	18.8	-	-
leats	0.2	-	-

* I.a. *Digitalis purpurea*, *Epilobium angustifolium*, *Urtica dioica*

anabatic winds which originate from the ‘Lehstenbach’ valley, hitting the site in the south-east and katabatic drainage following the slope from north-east to south-west. A more detailed description of the surrounding topography can be found in Thomas and Foken (2007b). The site is also a FLUXNET site (DE-Bay, Baldocchi et al., 2001) featuring CO₂ flux measurements above the dense spruce forest since 1996.

The research site is dominated by Norway Spruce (*Picea abies*) with a mean canopy height h_c of 27 m (as of 2011) and a stage age of approximately 55 years. The plant area index (PAI) is 5.6 m² m⁻² (leaf area index (LAI): 4.8 m² m⁻²) for the overstorey and 3.5 m² m⁻² (LAI: 0.5 m² m⁻² and less) for the understorey (Foken et al., 2012a), characterising a forest with an open trunk space and a dense crown space. The understorey covers about 60 to 80 % of the forest floor (Gerstberger et al., 2004) and consists of grasses, ferns, bushes (mainly blueberries), young spruces (h_c : 1 – 2 m), and deadwood. On 18 January 2007, the ‘hurricane like’ low pressure system ‘Kyrill’ destroyed large areas of the dense spruce forest close to the research site and enlarged the ‘Köhlerloh’ clearing to its present dimensions (in southern direction of research site). Furthermore, the northern border of the clearing was artificially straightened. Meanwhile, the clearing’s vegetation is similar to the understorey of the forest, with a heterogeneous distribution of vegetation cover and species. The plant height ranges from 0.2 to 4.5 m. See Table 2.1 for an overview of the representativeness of the clearing’s vegetation. For a detailed ecological description of the site, see Gerstberger et al. (2004) and reference data on climate, meteorology, vegetation structure and soil properties can be found in Staudt and Foken (2007).

2.1.2. Intensive observation periods 1 & 2 (IOP1 & IOP2)

The focus of IOP1 & IOP2 was the analysis of coupling regimes between the trunk space, the canopy and the above-canopy atmosphere and their consequences (Foken et al., 2012a), as well as the interaction between turbulent transport and chemical processes within the dense spruce forest. The used methods for flux observation were vertical gradient flux measurements via the eddy-covariance method, direct advection measurements in the trunk space and remote sensing with SODAR/RASS and miniSODAR to extend the vertical profile to a height of several hundreds of metres. The experimental field observations were combined with flux modelling using the multi-layer model ACASA (Advanced Canopy-Atmosphere-Soil Algorithm, Pyles, 2000). A detailed documentation of the micro-meteorological and chemical instrumentation and their location in the homogeneous part of the forest ecosystem during IOP1 is given in Serafimovich et al. (2008a), which was conducted from 6 September to 7 October 2007 (mainly wet autumn weather conditions), and

in Serafimovich et al. (2008b) for IOP2, which took place from 1 June to 15 July 2008 (sunny summer weather conditions). An overview of the results of IOP1 & IOP2 is presented in Foken et al. (2012a).

2.1.3. Intensive observation period 3 (IOP3)

In IOP3 the former research topic was modified and the focus changed to the investigation of energy and matter exchanges around surface heterogeneities in a disturbed forest ecosystem. It is assumed that heterogeneities will substantially impact exchange processes between atmosphere, vegetation and soil, because of (i) the formation of secondary circulations at roughness changes (like forest edges) and (ii) the enhancement of coherent structures near the forest edge (Section 1.2.2). To achieve answers for the issues of IOP3, comparable micrometeorological and chemical measurements like in IOP1 & IOP2 were performed, but the focus is the investigation of exchange and coupling processes at and near the forest edge (see Section 2.2). Afterwards, the measurements (mainly surface-near fluxes) are combined with adequate modelling approaches (large-eddy simulation, LES). IOP3 was conducted from 13 June to 26 July 2011 (Serafimovich et al., 2011a).

During the measuring campaign there were some bad weather conditions but three periods with mainly good weather conditions (so-called ‘Golden Day’ periods, GDP) were selected. These are presented with prevailing weather conditions in Table 2.2. For a detailed documentation of instrumentation and location of the measurements see the text below.

Table 2.2. ‘Golden Day’ periods and corresponding weather conditions during EGER IOP3 in June/July 2011 (Serafimovich et al., 2011a). The acronym LLJ stands for low-level jet.

No.	Period	Conditions	Wind	Occurrences
1	26 – 29 June DOY: 177 – 180	best conditions on 27 th , 28 th and 29 th up to 2 p.m.	moderate from east (26 th /27 th), respectively west (28 th /29 th) (1.0 – 4.5 m s ⁻¹)	LLJ in the night of 27 th /28 th and 28 th /29 th
2	4 – 8 July DOY: 185 – 189	best conditions on 6 th and 7 th , other days partly cloudy	low from west (4 th /7 th /8 th), respectively east (5 th /6 th) (0.5 – 3.5 m s ⁻¹)	Small amount of precipitation on 4 th /8 th
3	14 – 17 July DOY: 195 – 198	best conditions on 15 th and 16 th , other days partly cloudy	moderate from south-west (1.5 – 6.0 m s ⁻¹)	Small amount of precipitation on 17 th

2.2. Measurements

2.2.1. General set-up of the measurements

The exact positions of all measuring points during the EGER IOP3 project within the heterogeneous forest ecosystem are shown in Figure 2.2 (coordinates of the towers are in Serafimovich et al., 2011a). The so-called ‘main tower’ (M1, walk-up type) with a height of 32 m is located in the forest and measurements of vertical profiles of standard meteorological parameters (e.g. wind velocity, dry and wet bulb temperature) as well as trace gas concentrations and trace gas fluxes at the top height were conducted. At the 35 m tall so-called ‘turbulence tower’ (M2, slim tower type), also located in the forest, turbulent flux measurements at different heights were performed. Directly at the forest edge, another walk-up tower (M3) was installed, the ‘forest edge tower’ with a height of 42 m. The tower was equipped to measure vertical profiles of standard meteorological parameters (as for M1), vertical CO₂ profile and vertical profiles of trace gas concentrations and trace gas fluxes. In addition to the canopy protruding towers there were some small turbulence masts installed at various positions in the forest (near M2 & M8) below the forest canopy (in the trunk space), at the forest edge (M6 & M7) and at the clearing (M4). At M5 the modified Bowen ratio method was performed. In addition, at a total of four locations (M1, north and south of M3, near M4), measurements of net radiation as well as ground heat fluxes were conducted and in conjunction with the turbulence flux measurement of latent and sensible heat, the energy balance could be determined. For a detailed overview of the measurements of turbulent fluxes see Section 2.2.2, for vertical profile measurements see Section 2.2.3, and for further measurements see Section 2.2.4.

As already performed during IOP1 & IOP2, the structures in the atmospheric boundary layer were monitored via remote sensing with SODAR/RASS (METEK GmbH, Elmshorn, Germany) and miniSODAR (Scintec AG, Rottenburg, Germany) and the 482 MHz wind profiler (Vaisala Oyj, Vantaa, Finland) of the German Meteorological Service (DWD, Deutscher Wetterdienst) about 25 km south of the field site. The horizontal mobile measuring system (HMMS, for more details see Section 2.3 and Hübner et al., 2011, 2014) performed profile measurements on a 150 m long transect perpendicular to the forest edge. The necessity of the ozone monitor ‘49i’ (located in the forest near the HMMS track) is explained in Section 2.3.3. The Laser-Scintillometer SLS-40 (Scintec AG, Rottenburg, Germany) was used for determining momentum and sensible heat flux along a horizontal path parallel to the forest edge. Some chemical measurements of ozone, NO_x and nitrous acid (HONO) on a vertical lift (0.1 – 1.6 m), as well as wet and dry bulb temperature, leaf wetness and

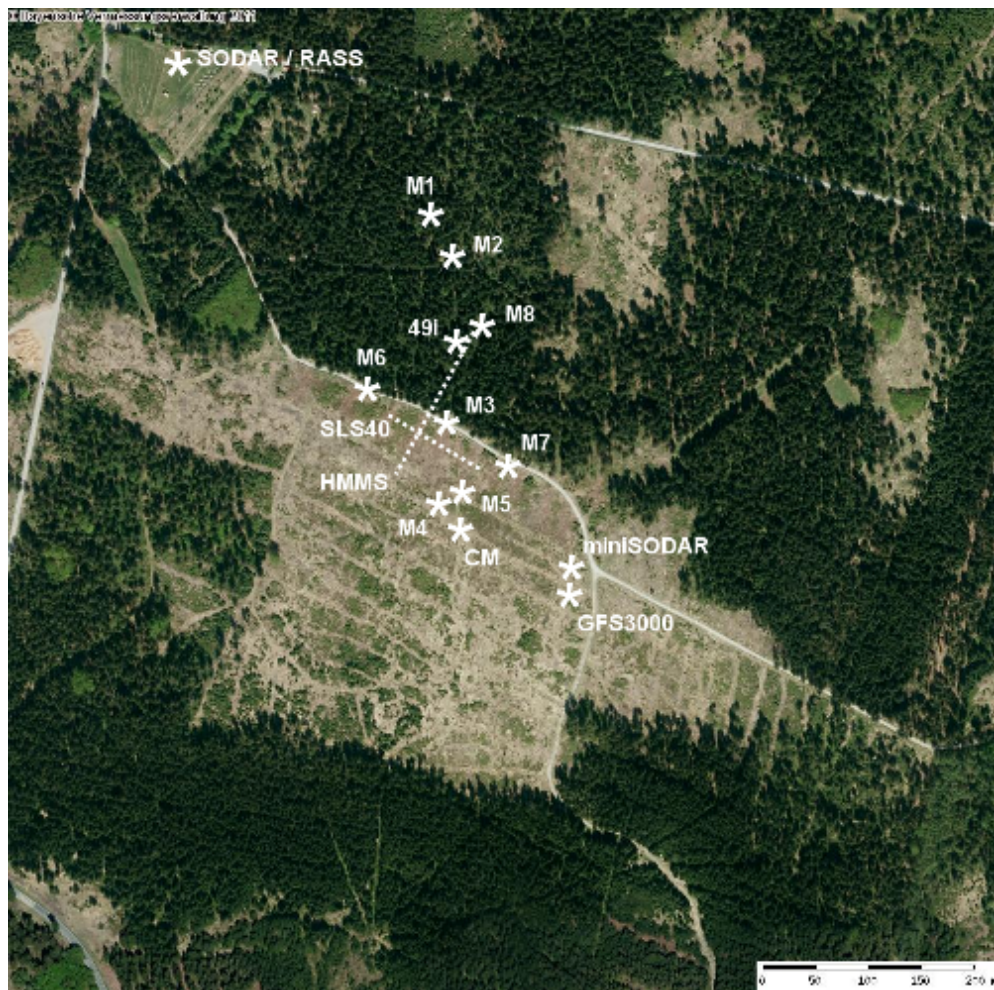


Figure 2.2. Aerial view of the investigation site of the EGER IOP3 project in summer 2011 with all measuring points and exact positions of the main tower M1 (32 m), the turbulence tower M2 (36 m), the forest edge tower M3 (41 m), the turbulence mast M4 (5.5 m), the mast for the modified Bowen ratio Method M5 (3.1 m), the turbulence masts M6-M8 (5.5 m), the mast for chemical measurements CM (2 m), the Laser-Scintillometer SLS-40, the horizontal mobile measuring system HMMS, the ozone monitor ‘49i’, SODAR/RASS, miniSODAR, and the GFS3000 (leaf gas exchange measurements). The map is orientated to the north. Image taken from Bayerische Vermessungsverwaltung, URL: <http://geoportal.bayern.de/bayernatlas?base=910>

photolysis frequency of NO_2 were performed at the mast CM (chemical measurements). Lastly the GFS3000 (Walz GmbH, Effeltrich, Germany) served for the investigation of plant photosynthesis and respiration (here: six representative species were investigated). For a detailed documentation of measurement instrumentation of turbulent fluxes, vertical profiles and other parameters see text below (some of the measurements named in this section, which are not used in this study, are not described in detail) and for further information on

experiment set-up, geographic coordinates of the measurements, calibration parameters, and data acquisition, see Serafimovich et al. (2011a).

2.2.2. Measurements of turbulent fluxes

As mentioned in Section 2.2.1 a total of 7 turbulence towers/masts were installed during EGER IOP3. The instrumentation of all towers is shown in Table 2.3. The towers/masts were equipped with 3D sonic anemometers (USA-1, METEK GmbH, Elmshorn, Germany; CSAT3, Campbell Scientific Inc., Logan, Utah, USA) to measure the three wind components (u , v and w) and the sonic temperature T_s . In most cases, the 3D sonic anemometers performed their measurements in conjunction with high-frequency optical gas analysers for the carbon dioxide (c) and water vapour (q) concentration (LI-7000, LI-7200, LI-7500, LI-7500A, LI-COR Biosciences Inc., Lincoln, Nebraska, USA) and at some points additionally with fast-response ozone (O_3) analysers (Enviscope fast ozone detector, cooperation between Karlsruhe Institute of Technology, Karlsruhe, Germany and enviscope GmbH, Frankfurt Germany; GFAS OSG-2, Immenstaad, Germany (dissolved); both analysers based on the solid-phase chemiluminescence technique from Güsten and Heinrich, 1996). All time series of turbulent fluxes were recorded with a high acquisition frequency (20 Hz, except at M3 at 27 m, where the acquisition frequency was 10 Hz). In the case of the ozone analysers, measured raw signal is provided only in relative units (counts s^{-1} , or voltages), and additionally the analysers' sensitivity is not temporally constant (due to the influence of relative humidity on the chemiluminescent dye, the sensor's disc ages within two days; Zahn et al., 2012). Therefore, absolute ozone concentrations were simultaneously measured side-by-side of each fast-response ozone analyser by commercial state-of-the-art slow response UV-absorption based ozone analysers (Model 205, 2B Technologies, an InDevR company, Boulder, Colorado, USA). Based on this data, the fast-response ozone signals could be converted to ozone concentrations and the turbulent ozone fluxes calculated.

The measurements within the forest were conducted at M1 in one level above the canopy ($z/h_c = 1.2$) and at M2 in three levels: above forest canopy ($z/h_c = 1.3$), around canopy height ($z/h_c \approx 1$) and 2.25 m above ground ($z/h_c = 0.1$). At the forest edge (M3) the measurements were also conducted in the three different levels ($z/h_c = 1.5$, $z/h_c \approx 1$, $z/h_c = 0.1$). At the clearing the measurements were taken at 2.25 m above the ground ($z/h_c = 1.2$) and at 5.5 m above the ground ($z/h_c = 6.1$). Additionally three 3D sonic anemometers (without gas-analysers) were installed at 2.25 m above the ground ($z/h_c = 0.1$) at various locations around the forest edge in order to investigate horizontal coherent exchange. Locations of the towers were west of M3 (M6) and east of M3 (M7) leading to a transect parallel to the forest

Table 2.3. Turbulent flux measuring instrumentation of towers/masts M1 – M4 and M6 – M8 during EGER IOP3 ($h_{c,forest} = 27$ m; $h_{c,clearing} = 0.9$ m)

Tower	z (m)	z/h_c	Measured variables	Instrument	Period of measurement		
M1	32	1.2	Wind vector, T_s	USA-1	13 June – 26 July 2011		
			c, q	LI-7000	13 June – 26 July 2011		
			O ₃ (sensor)	Enviscope*	13 June – 26 July 2011		
			O ₃ (monitor)	Model 205 [†]	13 June – 26 July 2011		
M2	36	1.3	Wind vector, T_s	USA-1	13 June – 26 July 2011		
			c, q	LI-7500	13 June – 26 July 2011		
	26	1.0	Wind vector, T_s	USA-1	18 June – 26 July 2011		
M3	2.25	0.1	Wind vector, T_s	USA-1	18 June – 26 July 2011		
			41	1.5	Wind vector, T_s	CSAT3	13 June – 26 July 2011
	27	1.0	c, q	LI-7500	13 June – 26 July 2011		
			Wind vector, T_s	USA-1	13 June – 05 July 2011		
			c, q	LI-7500	13 June – 26 July 2011		
			O ₃ (sensor)	GFAS*	13 June – 05 July 2011		
	2.25	0.1	O ₃ (monitor)	Model 205 [†]	13 June – 05 July 2011		
			Wind vector, T_s	CSAT3	20 June – 26 July 2011		
M4	5.5	6.1	c, q	LI-7500A	27 June – 01 July 2011		
			Wind vector, T_s	CSAT3	13 June – 26 July 2011		
			c, q	LI-7500	13 June – 26 July 2011		
			O ₃ (sensor)	Enviscope*	13 June – 26 July 2011		
	2.25	2.5	O ₃ (monitor)	Model 205 [†]	13 June – 26 July 2011		
			Wind vector, T_s	CSAT3	13 June – 26 July 2011		
			c, q	LI-7000	13 June – 21 June 2011		
				LI-7200	21 June – 26 July 2011		
M6	5.5	6.1	Wind vector, T_s	CSAT3	20 June – 26 July 2011		
			c, q	LI-7500A	20 June – 26 July 2011		
M7	5.5	6.1	2.25	0.1	Wind vector, T_s	USA-1	20 June – 26 July 2011
			Wind vector, T_s	CSAT3	20 June – 26 July 2011		
M8	2.25	0.1	c, q	LI-7500A	20 June – 26 July 2011		
			Wind vector, T_s	CSAT3	20 June – 26 July 2011		
	2.25	0.1	Wind vector, T_s	USA-1	13 June – 26 July 2011		

* All fast-response O₃-analysers based on solid-phase chemiluminescence technique (Güsten and Heinrich, 1996)† The measured raw signals of the fast-response O₃-analysers in relative units were recalculated via side-by-side O₃-monitor measurements (see text for more information).

edge (M6 – M3 – M7). A third tower was installed north of M3 in the sub-canopy layer of the forest (M8) leading to a transect perpendicular to the forest edge (M8 – M3 – M4). At M6 and M7 additional flux measurements were conducted in 5.5 m above the ground ($z/h_c = 6.1$).

2.2.3. Profile measurements

In the forest, at the ‘main tower’ (M1), measurements of vertical profiles of wind velocity at nine different levels and dry and wet bulb temperature at six levels (for height of different levels see Table 2.4) were performed since 1997 in a continuously running monitor programme, which is maintained by the Department of Micrometeorology, University of Bayreuth. The wind velocity is measured with cup anemometers, characterised by a low distance constant of approximately 3 m (Theodor Friedrichs & Co. Meteorologische Geräte & Systeme GmbH, Schenefeld, Germany) and dry and wet bulb temperature with aspirated Frankenberger type psychrometer (Frankenberger, 1951), all equipped with high precision sensors. At the forest edge, at the tower M3, a vertical profile of wind velocity at six levels and dry and wet bulb temperature at five levels was installed (height of different levels are given in Table 2.4).

Additionally, a vertical profile of CO₂ concentration was measured at eight levels at M3 (Ruppert, 2005). The CO₂ concentration from the different levels have been measured sequentially by one absolute, non-dispersive infrared gas analyser (LI-820, LI-COR Biosciences Inc., Lincoln, Nebraska, USA) in order to exclude deviations due to the limited absolute accuracy of gas analysers. The ambient air was drawn continuously from all eight heights through Dekabon lines (3.9 mm inner diameter; opaque; length: 55 m each) into buffer volumes of 2.5 L each. Every minute the system switched to another height, including 15 s of flushing time, in order to purge the system with ambient air of the ‘active’ level, followed by afterwards 45 s of measurements (averaging time). The time period required to ‘scan’ the full vertical profile was 8 min. The LI-820 was calibrated twice a day (12 a.m. and 12 p.m.), using a defined CO₂ standard and nitrogen zero gas.

At the mast CM at the clearing a further vertical profile of dry and wet bulb temperature (two levels), as well as trace gas concentrations on a vertical lift (five levels between 0.1 – 1.6 m and occasionally only in three levels) were measured. The lift was equipped with a moving platform, carrying inlet tubes for different trace gas analysers (O₃, NO_x, HONO). In the current study only the O₃ concentration from the lift is used. The ozone analyser was a dual-cell, UV photometric analyser Model 49i (Thermo Scientific, Part of the Thermo Fisher Scientific Inc., Waltham, Massachusetts, USA). Approximately every

Table 2.4. Instrumentation of vertical profile measurements of meteorological parameters as well as trace gases at towers M1 and M3 and at mast CM during EGER IOP3

Tower	z (m)	Measured variables	Instrument	Period of measurement
M1	2, 4.6, 10, 16.5, 18, 21, 25, 31	Wind velocity	Cup anemometer	continuously
	0.05, 2, 5, 13, 21, 31	Dry & wet bulb temperature	Ventilated psychrometer	continuously
M3	5, 13, 18, 21, 25, 39	Wind velocity	Cup anemometer	15 June – 19 July 2011
	1, 5, 18, 25, 39	Dry & wet bulb temperature	Ventilated psychrometer	15 June – 19 July 2011
	0.5, 1, 2.25, 5, 8, 13, 26, 36	CO ₂	CO ₂ profile system with Li-820	01 July – 25 July 2011
CM	0.1, 1.4	Dry & wet bulb temperature	Ventilated psychrometer	14 June – 26 July 2011
	0.1, 0.2, 0.4, 0.8, 1.6	O ₃ , NO _x and HONO [*]	Vertical lift	14 June – 08 July 2011 [†]
	0.1, 0.4, 1.6	O ₃ , NO _x and HONO [*]	Vertical lift	08 July – 23 July 2011 [†]
	0.1, 0.2, 0.4, 0.8, 1.6	O ₃ , NO _x and HONO [*]	Vertical lift	23 July – 26 July 2011 [†]

^{*} Ozone concentration measurement at the vertical lift were the only considered in the current study

[†] No continuous measurements during indicated period

6.5 to 7 min the lift changed the position in the following order: 1.6 → 0.8 → 0.4 → 0.2 → 0.1 → 1.6 → ... (five levels), or 1.6 → 0.4 → 0.1 → 1.6 → ... (three levels).

2.2.4. Additional measurements

The net radiation measurements (short-wave downwelling radiation: K_{\downarrow} ; short-wave upwelling radiation: K_{\uparrow} ; long-wave downwelling radiation: I_{\downarrow} ; long-wave upwelling radiation: I_{\uparrow}) were conducted at M1 at 29.5 m, north of M3 (in the forest) at 2 m, south of M3 (on the clearing) at 2 m, and near M4 (at the clearing) at 2 m. The measurement devices were CM14, CG2, CNR1, CNR4, CM24 (Kipp & Zonen, Delft, The Netherlands), PIR (Eppley Laboratory Inc., Newport, Rhode Island, USA). At all four locations measurements of soil temperature with PT100 (4-wire connection), soil moisture with TDR probes (IMKO GmbH, Ettlingen, Germany) and heat fluxes with heat flux plates (REBS, Campbell Scientific Inc., Logan, Utah, USA; CN3, Middleton Solar, Victoria, Australia; RIMCO HP3,

Table 2.5. Instrumentation of net radiation measurements (short-wave downwelling radiation: K_{\downarrow} ; short-wave upwelling radiation: K_{\uparrow} ; long-wave downwelling radiation: I_{\downarrow} ; long-wave upwelling radiation: I_{\uparrow}) as well as soil temperature, soil moisture and ground heat flux measurements at towers M1, M3 and M4 during EGER IOP3.

Tower	z (m)	Measured variables	Instrument	Period of measurement	
M1	29.5	$K_{\downarrow}, K_{\uparrow}$	CM14	continuously	
		$I_{\downarrow}, I_{\uparrow}$	CG2	continuously	
	-0.02, -0.05, -0.1, -0.2, -0.5, -0.7, -1.0, -2.0	Soil temperature	PT100	continuously	
	-0.1, -0.5	Soil moisture	TDR IMKO	continuously	
	2 x -0.1	Soil Heat flux	REBS	continuously	
M3 (north)	2	$K_{\downarrow}, K_{\uparrow}$ & $I_{\downarrow}, I_{\uparrow}$	CNR1	13 June – 26 July 2011	
		-0.02, -0.05, -0.1, -0.2	Soil temperature	PT100	13 June – 26 July 2011
		-0.1, -0.2	Soil moisture	TDR IMKO	13 June – 26 July 2011
		2 x -0.1	Soil Heat flux	CN3	13 June – 26 July 2011
M3 (south)	2	$K_{\downarrow}, K_{\uparrow}$ & $I_{\downarrow}, I_{\uparrow}$	CNR4	13 June – 26 July 2011	
		-0.02, -0.05, -0.1, -0.2	Soil temperature	PT100	13 June – 26 July 2011
		-0.1, -0.2	Soil moisture	TDR IMKO	13 June – 26 July 2011
		2 x -0.1	Soil Heat flux	CN3	13 June – 26 July 2011
M4	2	$K_{\downarrow}, K_{\uparrow}$ & $I_{\downarrow}, I_{\uparrow}$	CNR4	13 June – 26 July 2011	
		$K_{\downarrow}, K_{\uparrow}$	CM24	13 June – 26 July 2011	
	2	$I_{\downarrow}, I_{\uparrow}$	PIR	13 June – 26 June 2011	
	-0.02, -0.05, -0.1, -0.2, -0.5, -0.7, -1.0	Soil temperature	PT100	13 June – 26 July 2011	
	-0.1, -0.2	Soil moisture	TDR IMKO	13 June – 26 July 2011	
	2 x -0.15	Soil Heat flux	CN3	13 June – 26 July 2011	

McVan Instruments Ltd., Victoria, Australia; HFP01, Hukseflux Thermal Sensors B.V., Delft, The Netherlands) were measured at different depths. The setup of the measurements and the measurement heights/depths are listed in Table 2.5.

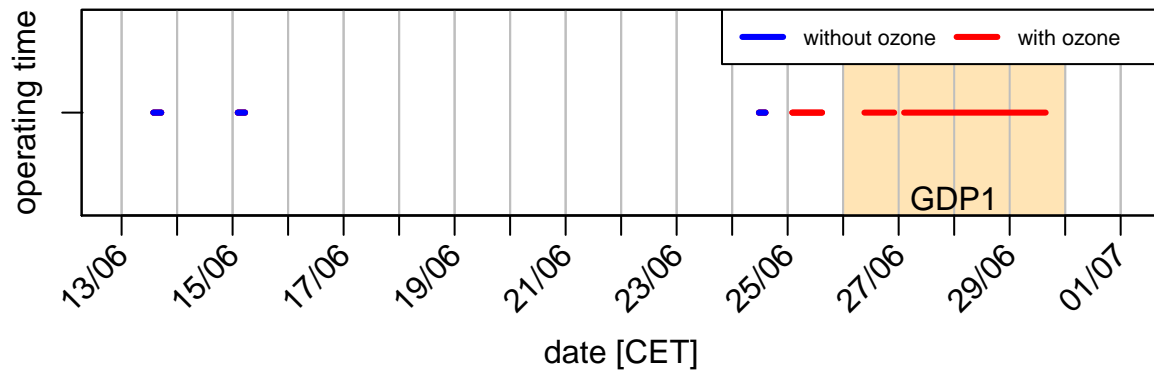
At the ‘small’ clearing northwest of M1 (‘Pflanzgarten’), where the SODAR/RASS was installed (see Figure 2.2), another continuously running monitoring programme was installed. Measurements of air temperature and relative humidity (HMP45a, Vaisala Oyj,

Vantaa, Finland), air pressure (Ammonit Measurement GmbH, Berlin, Germany), precipitation (OMC 212 heated rain gauge, Observator (Belfort), Ridderkerk, The Netherlands) and some air chemistry measurements were conducted since 1994. The air chemistry measurements included concentration measurements of O₃ and SO₂ (Model 49i and Model 43C, Thermo Scientific, Part of the Thermo Fisher Scientific Inc., Waltham, Massachusetts, USA), NO₂ and NO (CLD-700, ECO PHYSICS GmbH, Munich, Germany).

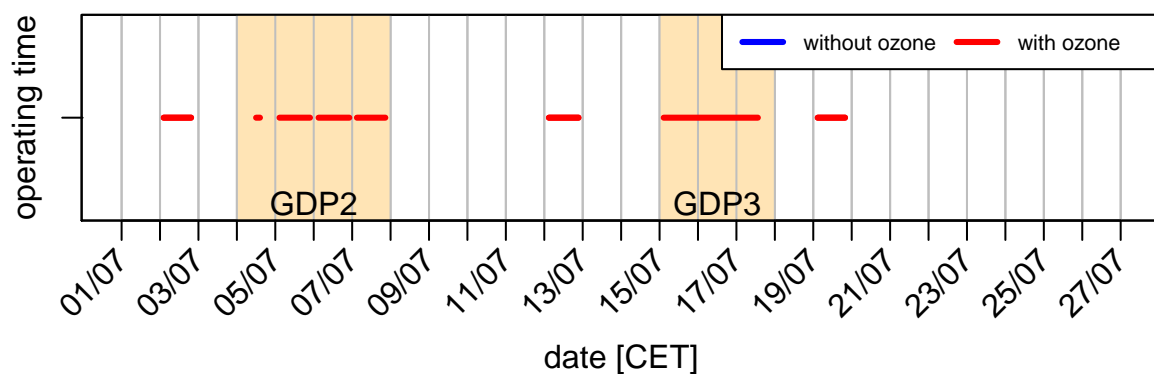
2.3. The Horizontal Mobile Measuring System (HMMS)

In addition to all measurements at fixed locations (towers and masts named above), a fully automatic Horizontal Mobile Measuring System (HMMS) was installed. The HMMS is based on the drive mechanism of a garden railway system (moving on rails) and is equipped with state-of-the-art measuring devices. In addition to meteorological quantities, in detail long-wave and short-wave radiation (individual sensors for up- and downwelling radiation), air temperature and relative humidity, the HMMS was equipped with trace gas analysers for CO₂ and O₃ concentrations. The chosen measuring track during EGER IOP3 was a straight line with a length of 150 m, installed perpendicular to the forest edge in a NE to SW direction (75 m in the forest and the clearing, respectively). The track is marked by the dotted line (labelled 'HMMS') in Figure 2.2. The elevation difference between start (forest) and end (clearing) point of the HMMS track was approximately -8 m (slope of -5% , or -3°). Applying a sampling frequency of 1 Hz, the HMMS was running with a quasi-constant speed of 0.5 m s^{-1} approximately 1 m above ground. The measurements of the HMMS were usually started in the forest and for a complete return run (300 m; forest–clearing–forest) the HMMS needed approximately 10 min. Within the EGER IOP3 measuring period (13 June – 26 July 2011) no continuous measurements were conducted with the HMMS. Taking account of appropriate weather conditions and the main project aims, almost 250 h of data was collected during various day- and night-time periods, mainly in the 'Golden Day' periods (cf. Table 2.2 and see Figure 2.3 for the operating time of the HMMS during EGER IOP3).

In the following sections, the technical description of the HMMS is presented, comprising details of drive mechanism and carrier design (see Section 2.3.1), train and position control, as well as data acquisition (see Section 2.3.2) and sensor systems (see Section 2.3.3). The front and lateral view of the HMMS are shown in Figure 2.4, with the corresponding descriptions listed in Table 2.6. For more technical details of the HMMS, including technical drawings, pictures and the detailed wiring plan, see Hübner et al. (2011). Besides the tech-



(a) Operating time of the HMMS during June



(b) Operating time of the HMMS during July

Figure 2.3. Operating time of the HMMS during EGER IOP3. Blue lines indicate measurements of the HMMS without the ozone analyser from enviscope GmbH and red lines with the ozone analyser. The three ‘Golden Day’ periods (GDP) are highlighted in colour.

nical description of the HMMS, some results of laboratory tests for the individual sensor response times (see Section 2.3.4), variabilities in the run duration (see Section 2.3.5) and problems with the CO₂ sensor (see Section 2.3.6) are also presented. The application of a simple correction algorithm to correct the measurements for the response-time-induced dynamical error are introduced in Section 2.4.1. A majority of the HMMS description is also presented in Hübner et al. (2014).

2.3.1. HMMS design and power supply

The HMMS is based on two major components: a rail system and a fully automatic railcar. Therefore components of a commercial garden railway system were used (*‘Lehmann-Groß-Bahn’*, LGB, since 2007 part of Gebr. Märklin & Cie. GmbH, Göppingen, Germany). The rails used are made of brass with a track gauge of 45 mm and a rail segment length of 2 m. The segments are connected with brass connecting clamps. Two DC engines were re-

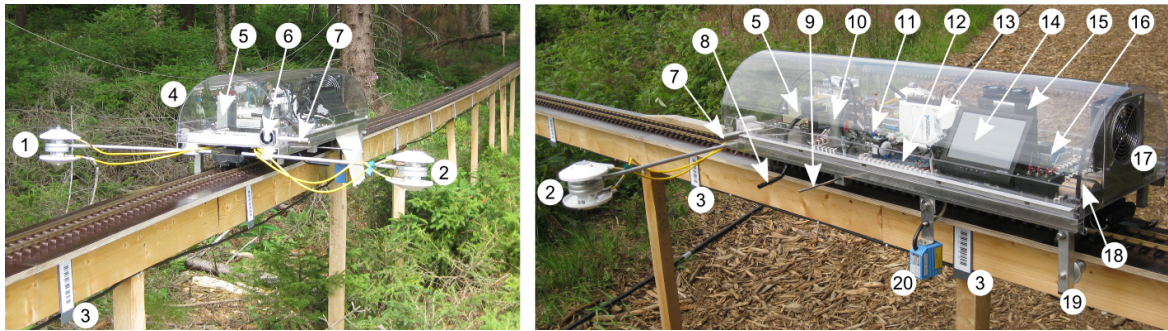


Figure 2.4. Front and lateral view on the HMMS. Specifications of the numbers are in Table 2.6.

Table 2.6. Specification of numbers from Figure 2.4.

No.	Description
1	Short-wave radiation sensors on a 0.4 m long boom
2	Long-wave radiation sensors on a 0.4 m long boom
3	Code 39 bar code
4	Makrolon [®] cover to protect the HMMS for rain and dirt
5	Enviscope O ₃ analyser
6	Fan for ventilation of the HMP 155
7	Inlet for HMP 155, double shielded
8	Inlet for O ₃ analyser, made of PTFE
9	Inlet for CO ₂ analyser, made of aluminium
10	Pump for O ₃ analyser
11	Pump for CO ₂ analyser
12	Edinburgh Instruments Ltd. Gascard [®] NG CO ₂ analyser
13	National Instruments DAQ device
14	7" TFT monitor
15	Micro PC
16	LGB Analog throttle with potentiometer
17	Fan for cooling the entire system
18	On-board storage battery
19	Lateral holder to protect the HMMS for downfalls
20	Sick CLV412-1010 bar code scanner

moved from a replica Diesel hydraulic locomotive and mounted under an aluminium plate (300 mm × 1000 mm) with a downward-facing U-profile to increase mechanical stability. This plate serves as the carrier platform of the (i) speed and position control system as well as data acquisition via a Nettop (see Section 2.3.2) and (ii) sensors (see Section 2.3.3). A removable transparent cover, made of Makrolon[®] was constructed to protect HMMS electronics and sensors against dirt and moisture (i.e. drizzle and short showers, but not

prolonged wet conditions). To avoid heat accumulation inside the cover a fan was installed (No. 17 in Figure 2.4). Four lateral holders at each corner of the carrier platform (No. 18 in Figure 2.4) prevent the HMMS falling from heights (measuring height during EGER IOP3: 1 m).

Due to the high electrical conductivity of brass, electrical power for the entire system was supplied through the rails (infeed: 24 V DC, 5 A). This infeed covers the total use of the HMMS, which is approximately 3 A for all devices and the rest is used for the drive mechanism, which differs depending on speed and/or inclination. The power was fed in continuously every 25 m starting in the middle of the HMMS track (forest edge) and going in both directions (feed points were at positions: 25 m, 50 m, 75 m, 100 m, 125 m) to avoid power loss over long distances. Spring-mounted pick-up shoes (sliding contacts) on both sides of the engines tapped the power from the rails. Whereas the working voltage of the engines is between 0 V DC (motor standstill) and 24 V DC (full throttle) with an alternating polarity (+: forward direction, -:backward direction), the sensors – except of the radiation sensors, which do not have an external power supply and the heating of the ozone analyser, which was supplied with 24 VDC – and the Nettop of the HMMS need a 12 V DC supply with constant polarity. This is realised by a DC/DC-converter which reduces the 24 V DC of the first electrical circuit to 12 V DC in the second electrical circuit of the HMMS. The DC/DC-converter has a programmable and stabilised output and occasional breakdowns of electrical power are buffered by an on-board storage battery (12 V DC, 0.8 A h).

2.3.2. Train control, position detection and data acquisition system

On the HMMS, a Nettop (Quanmax QBOX-1010, Quanmax Inc., Taipei, Taiwan) is used as a central control unit for the train control, position detection and for data acquisition. The Quanmax QBOX-1010 is a very small, light-weight, and low-power BOX PC with a sufficient number of ports to connect all parts of the HMMS with an input voltage of 12 V and a current of approximately 1 A. A small 7" TFT display (MM400, e.g. CarTFT.com e.K., Reutlingen, Germany; No. 14 in Figure 2.4) and a compact wireless keyboard with trackball (CTFWIKE-2, e.g. CarTFT.com e.K., Reutlingen, Germany) are used for operational control of the Quanmax QBOX-1010.

A second central unit on the HMMS is a 16 bit data acquisition (DAQ) device (USB-6211, National Instruments, Austin, USA) which is connected via USB to the Nettop. The DAQ device, a very compact box with 16 analogue input and two analogue output channels

Table 2.7. The influence of the analogue output of the DAQ device on the HMMS speed and direction.

DAQ output [VDC]	Analogue throttle output [VDC]	Direction and speed of HMMS
0	-24	Backward direction with max. speed
0 to < 2.5	-24 to < 0	Backward direction with decreasing speed
2.5	0	Stop of the HMMS
2.5 to < 5	0 to < 24	Forward direction with increasing speed
5	24	Forward direction with max. speed

(with an additional four digital inputs/outputs), which contains a low pass filter, a multiplexer (MUX), a sample and hold circuit (SH) and an analogue-to-digital converter (A/D). All analogue signals of the used sensors on the HMMS (the two pyranometers, the two pyrgeometers, two extra PT100 temperature sensors for the pyrgeometers, and the temperature and humidity sensor) are sampled one after the other by the multiplexer and only the CO₂ and O₃ analysers are connected via serial ports directly to the Quanmax QBOX-1010. For a detailed overview of all applied sensors see Section 2.3.3. The sensors' sampling rate can be set in the range from 1 to 5 Hz, with a 200 times higher internal oversampling rate to improve resolution and reduce potential (although highly unlikely) aliasing effects, caused for example by noise (signal frequencies occur that are greater than half of the sampling frequency, or Nyquist frequency) of the power frequency (Bentley, 2005). Oversample mode is a common practice also used in data loggers. Because of the movement of the HMMS, only the first 10 % of the internal sampling rate were used for linear averaging in order to allocate the measured values to an exact position, without having blurring effects. The A/D converter converts the analogue signals which it receives from the SH and transfer it as digital via USB to the Quanmax QBOX-1010. Via an analogue output of the DAQ device a potentiometer of an analogue throttle (provided by LGB) can be controlled, in order to change speed and driving direction of the HMMS. The influence of the analogue output on speed and driving direction is shown in Table 2.7.

For determination of position and speed, the HMMS is equipped with a commercial raster bar code scanner (CLV412-1010, SICK Vertriebs GmbH, Düsseldorf, Germany; No. 20 in Figure 2.4). This is absolutely necessary in order to link the collected measuring data with the exact position along the transect. The applied 'Code 39' bar codes (No. 3 in Figure 2.4) contain information of the distance in metres from the starting point, as well as a check digit (digit sum in hexadecimal). Beside the determination of position and speed, it is possible to program distinct speed profiles along the measuring track. Additionally, each

bar code can be used as a turning point for reversing the driving direction of the HMMS.

The specifically developed HMMS software (Gesellschaft für Akustik und Fahrzeugmeßwesen mbH (GAF), Zwickau, Germany) is installed on the Nettop Quanmax QBOX-1010. It is responsible for a failure-free regulation of the train control system (position, speed and change of driving direction), as well as the handling of the DAQ device USB-6211, including the storage of a comma-separated datafile on the internal hard disk drive (HDD). Depending on the chosen sampling rate, data files are updated automatically.

During the EGER IOP3 project, three new updates of the HMMS software were released. The first was released because of incorrect measurements of the PT100 temperature of the radiation sensors and the second release was a bug-fix for a fatal exception error caused by the previous update. Both updates were during the testing phase of the HMMS (13 to 24 June 2011) and before the effective measurements, which started shortly before the first ‘Golden Day’ period (GDP1) on 25 June 2011 (Figure 2.3). The third update was released on the 4 July 2011 to fix a bug in the HMMS software, causing a communication failure in the RS-232 signal reception of the CO₂ and the O₃ analyser. This resulted in a loss of data up to the restart of the HMMS software. The measurements during GDP1 and 2 July 2011 were affected. All update releases can be found in Hübner et al. (2011).

2.3.3. Sensor system

The selection of appropriate sensors was a major challenge due to (i) the limited power of the drive mechanism, leading to payload restrictions for sensors and electronics, (ii) the space on the carrier platform restricting the size of sensors, analysers, and electronics, and (iii) the requirement for short response times in order to capture true spatial variations of meteorological quantities and trace gas concentrations (with the highest variations occurring mainly at the forest edge) within an acceptable time. So the final selection resulted in a compromise between their weight/size and acceptable response times. The latter may be described by the time constant, which is a sensor/analyser specific quantity. Generally, the smaller the time constant, the smaller are dynamical errors and consequently spatially smoothing effects of the measurements. An overview of the HMMS sensors and analysers is shown in Table 2.8, and more detailed information, particularly of their individual time constants τ_{63} , which have been determined by laboratory tests (see Section 2.3.4), are given in Table 2.9.

For air temperature and relative humidity measurements the HMMS was equipped with a HMP155 temperature (PT100 RTD Kl. F0.1 IEC 60751) and a humidity (HUMICAP[®] 180R) probe (Vaisala Oyj, Vantaa, Finland). A PT100 sensor for ‘true’ air temperature measure-

ments should be protected against the incidence of direct sunlight. Additional ventilation of the sensor prevents heat accumulation and the turbulent exchange of heat. A common practice to realise both requirements is to place the sensor in an aspirated radiation shield tube. For that, both sensors of the HMP155 were detached from the original sensor housing and the sintered PTFE filter. Then, the sensors have been mounted in a double thermal radiation shield tube according to Assmann (Assmann, 1887, 1888) and Frankenberger (Frankenberger, 1951). Aspiration has been facilitated by a small PC fan maintaining a constant air flow of approximately 4 m s^{-1} within the tube. According to the manufacturers' information, the time constant of the temperature sensor could be reduced from $<20 \text{ s}$ to approximately 12 s because of these modifications, while there was no change in the relative humidity sensor's time constant ($<20 \text{ s}$). The time constants have been measured in laboratory tests (see Section 2.3.4). Since the sintered PTFE filter was removed from the HMP155 probe, the relative humidity sensor was changed approximately every 70 operating hours during EGER IOP3, to minimise potential problems of humidity measurements caused by the accumulation of dust on the sensor. When comparing measurements by locally fixed (aspirated) sensors close to the HMMS track, no increasing deviation in the humidity measurements between the HMMS and the locally fixed measurements was observed, even after more than 250 operating hours.

A total of four radiation sensors were applied on the HMMS, two pyranometers (CMP3, short-wave radiation, $0.3 - 2.8 \mu\text{m}$) and two pyrgeometers (CGR3, long-wave radiation, $4.5 - 42 \mu\text{m}$) to measure down- and upwelling radiation (Kipp & Zonen, Delft, The Netherlands). The sensor housing temperature of the pyrgeometer was measured with a PT100 temperature sensor (replacing the original thermistor sensor). The conducted laboratory tests for determination of the individual time constant of each sensor (see Section 2.3.4) confirmed the time constants given in the manufacturer's information. The output signal of the thermopile-type radiation sensors (μV -range) was amplified (home-built amplifiers, electronic workshop, University of Bayreuth) to match the input sensitivity of the applied National Instruments DAQ device (range $0 - 1 \text{ V}$). The amplification factors are given in Table 2.8. Each pair of radiation sensors is mounted on 40 cm long booms, which in turn are fixed to the front side of the HMMS's carrier platform, pointing in opposite directions but perpendicular to the driving direction (see No. 1 & 2 in Figure 2.4). This lateral installation minimises 'shadowing' effects caused by the HMMS itself and/or by the track's construction elements and guarantees a rather free hemispheric view.

The carbon dioxide concentration was measured on the HMMS with a closed-path, single cell, non-dispersive infrared gas analyser (OEM Gascard[®] NG CO₂, Edinburgh Instru-

Table 2.8. Sensors mounted on the HMMS are two pyranometers (down- and upwelling, $K_{\downarrow}, K_{\uparrow}$), two pyrgeometers (down- and upwelling, $L_{\downarrow}, L_{\uparrow}$), a temperature (T) and relative humidity sensor (RH), a CO_2 analyser (CO_2), and an O_3 analyser (O_3). The accuracies are taken from the manufacturers' information.

Parameter	Instrument	Accuracy	Remark
K_{\downarrow}	CMP3	$<15 \text{ W m}^{-2}$	Amplifier used (Factor: 50-fold)
K_{\uparrow}	CMP3	$<15 \text{ W m}^{-2}$	Amplifier used (Factor: 100-fold)
L_{\downarrow}	CGR3	$<15 \text{ W m}^{-2}$	Amplifier used (Factor: 500-fold); optional PT100 temperature sensor
L_{\uparrow}	CGR3	$<15 \text{ W m}^{-2}$	Amplifier used (Factor: 500-fold); optional PT100 temperature sensor
T	HMP155	$\pm 0.1 \text{ K}$	Radiation shield and ventilated with 4 m s^{-1}
RH	HMP155	$\pm 11 \%$	Radiation shield and ventilated with 4 m s^{-1}
CO_2	Gascard [®] NG	$\pm 40 \text{ ppm}$	Vacuum pump DC24/16F (Flow rate: 1.2 L s^{-1})
O_3	Enviscope	$\sim 0.09 \text{ ppbv}^*$	Vacuum pump DC24/80L (Flow rate: 3.0 L s^{-1})

* Accuracy at a measuring frequency of 1 Hz and a mixing ratio of 50 ppbv (1 ppbv = mixing ratio of $10^9 \text{ mol mol}^{-1}$)

ments Ltd., Edinburgh, United Kingdom) with a measurement range of 0 – 1000 ppm. The Gascard[®] NG is a very lightweight (300 g) and small (160 mm × 100 mm × 40 mm) sensor, an OEM version, which (i) has no housing (sheltered by the HMMS's Makrolon[®] cover only), and (ii) is supplied by a small vacuum pump (12 V DC, 1.2 L min^{-1} ; model DC24/16F, Fürgut GmbH, Tannheim, Germany). The inlet tubing of the CO_2 analyser consists of an aluminium tube (inner diameter 3 mm; outside of HMMS) and a flexible tube of polyethylene aluminium composite structure (Dekabon, inner diameter 3 mm; inside of HMMS). The overall length of inlet tubing is 50 cm, which translates to a time delay $t_d = 0.2 \text{ s}$. This time delay has to be added to the delay caused by the time constant of the sensor. According to the manufacturer, the Gascard[®] NG's standard (optimised) response time should be 10 s (τ_{90}). In laboratory tests, a time constant (τ_{63}) of approximately 1 s was determined for the Gascard[®] NG, including the delay time caused by inlet tubing length.

To measure the ozone concentration on the HMMS, a fast response chemiluminescence ozone detector was used (developed by a cooperation between Karlsruhe Institute of Technology, Karlsruhe, Germany and the company enviscope GmbH, Frankfurt, Germany; Zahn et al., 2012). Here, a fast-response photomultiplier (up to 50 Hz) measures the chemiluminescence originating from a surface reaction of O_3 with a coumarin dye layer on a

small aluminium disc, which is in contact with the sample air stream. For the EGER IOP3 project, enviscope GmbH provided an OEM version (without housing and front panel control elements), resulting in a 53 % reduction of weight and 81 % of volume. For operation, the analyser itself needs 12 VDC, while the heating within the reaction chamber needs an operating voltage in a range of 15 – 60 VDC. Therefore, 24 VDC were tapped directly from the engines of the HMMS. A small vacuum pump (12 VDC, 3 L min⁻¹; model DC24/80L; Fürgut GmbH, Tannheim, Germany) is used to draw ambient air through the O₃ analyser. Inlet tubing consisted of a 30 cm long black PTFE tube (inner diameter 6.35 mm), like the first 10 cm of the outlet tubing. Another 20 cm of Dekabon tube (inner diameter 3 mm) lengthens the output. In- and outlet tubing have to be black (lightproof), otherwise the (chemiluminescence) detection of O₃ in the reaction chamber would be affected by incident sunlight. The chemiluminescence analyser, was developed for aircraft and eddy-covariance measurements at up to 50 Hz; consequently its time constant is negligible and only the delay time of 0.5 s, caused by the inlet tubing, has to be considered.

The (multiplier) raw signal of the enviscope O₃ analyser (counts s⁻¹) can be calibrated by a suitable O₃ source. However, the sensitivity of the O₃ analyser has a considerable temporal variability caused by the ageing of the sensor's disc (it is recommended to change the sensor's disc approximately every 48 h; Zahn et al., 2012). In the case of the EGER IOP3 project, the signal of the HMMS O₃ analyser was adjusted in situ by simultaneous O₃ concentration measurements performed on a fixed location 0.5 m aside the HMMS track at the turning point of the HMMS in the forest (see Figure 2.2, label '49i'). Every time the HMMS passed this turning point, the fast-response O₃ analyser at the HMMS was adjusted to the O₃ monitor (approximately every 10 min). These measurements were performed by a commercial state-of-the-art UV-absorption O₃ analyser (Model 49i, Thermo Scientific, Part of the Thermo Fisher Scientific Inc., Waltham, Massachusetts, USA).

To assess the HMMS measurements, whether to check if there are influences of the movement and/or the chosen design, the used components or the realised modifications, a side-by-side comparison with fixed tower measurements was made. This field-site comparison was preferred over laboratory tests because the changing conditions caused by the movement of the HMMS, or the changing position of the sun, etc. could not be simulated adequately in the laboratory. This comparison is shown in Section 3.1.

2.3.4. Individual sensor response times and the dynamical error

As mentioned in Section 1.2.3 the input signal of most sensors will follow a very sudden change in the measured quantity with certain delay and damping effects, characterised by

an individual sensor response time, or time constant τ . The signal's temporal adaptation of so-called first-order measuring systems to a sudden temporal change of the quantity to be measured can be described in the following form (e.g. Brock and Richardson, 2001; Foken, 2008a)

$$X_o(t) = X_i(t) + \tau \frac{dX_i}{dt}, \quad (2.1)$$

where τ is the time constant and t stands for the time. The time constant τ characterises the dependency between the input signal X_i and the output signal X_o , in other words, the inertia of the sensor and/or the measuring system, respectively. By definition τ represents the time required for the measuring system to reach 63 % of its final or equilibrium value. Equation (2.1) has the following exponential solution

$$X(t) = X_\infty \left(1 - e^{-\frac{t}{\tau}}\right) \quad (2.2)$$

where X_∞ is the final value of $X(t)$ after final adaptation to new conditions.

Section 1.2.3 refers to the much greater importance of the time constant for mobile measuring systems than it is for standard tower and other stationary measuring systems. The movement of the measuring system means that the time constant can result in a temporal and also a spatial error. The total error of a measuring system is referred to as the dynamical error. A linear change in a measured quantity is achieved when

$$X_i(t) = 0 \quad \text{for} \quad t \leq 0 \quad (2.3)$$

and

$$X_i(t) = at \quad \text{for} \quad t > 0 \quad (2.4)$$

with a as a constant and $X(0) = 0$ as the initial condition. This leads to a change of Eq. (2.1) to

$$a \cdot t = X_i(t) + \tau \frac{dX_i}{dt}. \quad (2.5)$$

The exponential solution is

$$X(t) = a \cdot t - a \cdot \tau \left(1 - e^{-\frac{t}{\tau}}\right) \quad (2.6)$$

with the dynamical error as the second term in the right-hand side.

Mathematical corrections for the dynamical error exist and these were calculated mainly

Table 2.9. Results of calculation of the sensor response time with the given signal differences ΔX_i in the laboratory test and its consequences (in some cases additional delay time t_d has to be taken into account) on the location of the measured data. The spatial relocation (for HMMS speed of 0.5 m s^{-1}) is shown for a positive or negative signal difference, with the possible effect of hysteresis. For the sensors used see Table 2.8.

Parameter	ΔX_i	τ_{63}	t_d	Hysteresis	Spatial relocation	
					$+\Delta X_i$	$-\Delta X_i$
$K_{\downarrow}, K_{\uparrow}$	350 W m^{-2}	4 s^*	-	no	12 m	12 m
$L_{\downarrow}, L_{\uparrow}$	150 W m^{-2}	4 s^*	-	no	14 m	14 m
T	5 K	12 s^{\dagger}	-	yes	21 m	19 m
RH	15 %	20 s^*	-	yes	23 m	20 m
CO_2	480 ppm	$<1 \text{ s}^*$	0.2 s^{\S}	no	3 m	3 m
O_3	-	$<0.1 \text{ s}^{\ddagger}$	0.5 s^{\S}	no	0.5 m	0.5 m

* In agreement with the data given by the manufacturer.

† 8 s shorter than data given by the manufacturer due to sensor modification.

‡ Developed for high frequency measurements (50 Hz), τ_{63} is negligible (no laboratory test conducted).

§ Delay time t_d caused by the inlet length.

for temperature and humidity sensors in radiosondes and aircraft measurements, but up to now were not applied to near-ground horizontal mobile measuring systems (see Section 1.2.3 for the reasons). The measured values of the HMMS had to be corrected because of (i) a heterogeneous measuring site, with the focus on a forest edge (not suitable for averaging the measured quantities along the total measuring track), (ii) measurements during movement in order to achieve a higher temporal resolution of the investigation site and (iii) weight and money restrictions, which made the application of high-frequency sensors impossible (apart from the O_3 analyser).

To correct the response time induced dynamical errors in the HMMS measurements, it is necessary to have a detailed knowledge about the individual sensor response time. Therefore, laboratory tests have been conducted, where the HMMS or rather the sensor was rapidly positioned ($<1 \text{ s}$) between two different environmental conditions. Those were for temperature and humidity, a big cold chamber with moist conditions and a room with constant ambient conditions (warmer and dryer). Long-wave radiation was tested above two water bodies with different temperatures and the short-wave radiation with and without short-wave light. The CO_2 analyser was tested between nitrogen and a CO_2 calibration gas. A laboratory test for the O_3 analyser was not conducted because of the high frequency multiplier, resulting in a very low time constant.

Table 2.9 gives the exact numbers of the realised sudden change of environmental conditions. The signal differences (ΔX_i) were used for the calculation of the time constant

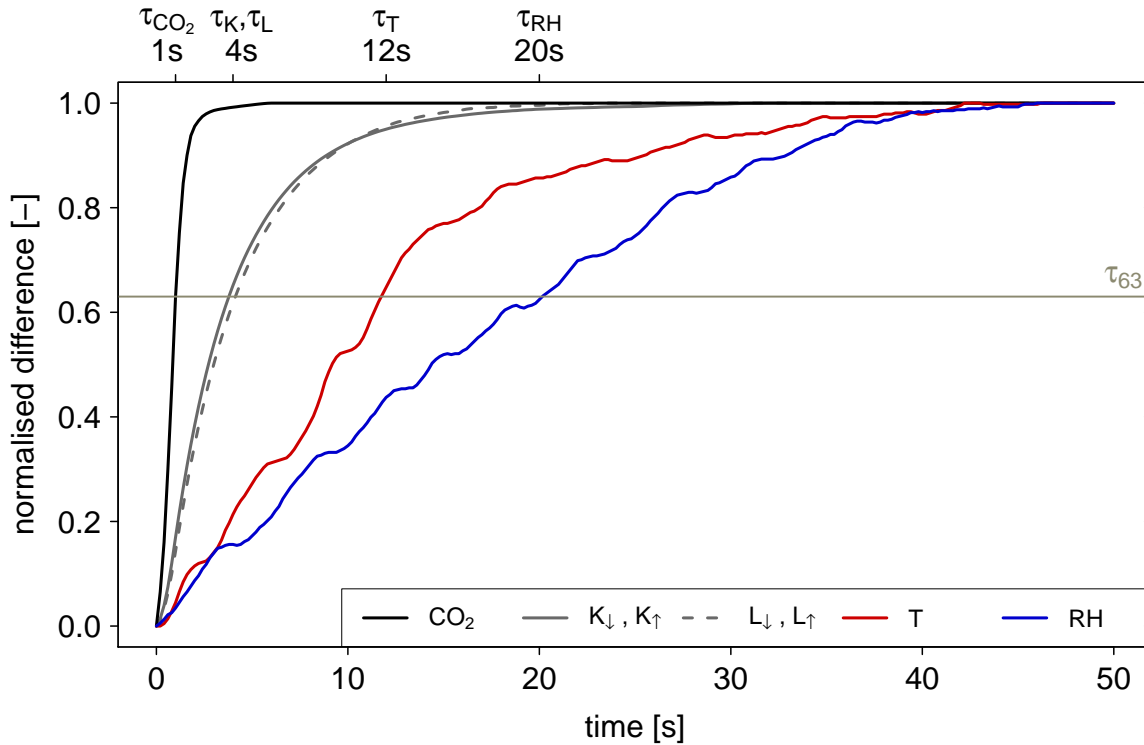


Figure 2.5. Measurement results of the laboratory tests conducted for the short-wave radiation (K_{\downarrow} , K_{\uparrow}), long-wave radiation (L_{\downarrow} , L_{\uparrow}), temperature (T), relative humidity (RH) and CO_2 concentration to determine the individual time constant τ_{63} . The small fluctuations of the temperature and humidity signal are caused due to the turbulence under room conditions. An overview of all sensors is shown in Table 2.8 and Table 2.9.

τ_{63} , which indicating a signal change of 63 % of the final value (Figure 2.5). For a better comparison, the signal differences are presented as the normalised difference between the initial value (0.0) and the final value (1.0). The calculation served also for the identification of possible hysteresis effects, which were found in the temperature and humidity sensor. For both sensors, the adjustment to changes in the input signal was faster for a positive signal difference (T : cold \rightarrow warm; RH : dry \rightarrow wet).

The final signal is nearly reached after a sudden change of the input signal beyond five times the time constant (Foken, 2008a). This delay causes, together with the speed of the HMMS (0.5 m s^{-1}) – and in the case of the CO_2 and O_3 analyser an additional time delay t_d caused by the inlet length – a spatial relocation of the measurement signal (Table 2.9). The relocation for the sensors with a hysteresis can vary, depending on the way the change in the input signal occurred. This relocation can be corrected for (see Section 2.4.1) or must be taken into account during the interpretation of the data.

2.3.5. Variability of run duration

The application of the LGB drive mechanism was uncomplicated in terms of system integration and control by the HMMS software. Nonetheless, there occurred problems with the rail system and the driving mechanism (especially with the inner workings of the engines) during the EGER IOP3 project. In wet conditions, the HMMS was not operational because of a grave reduction in climbing ability. This was not a big loss, because the focus was on the ‘Golden Day’ periods with dry conditions. The HMMS measurements had to be stopped in wet conditions anyway, because of an insufficient waterproofness. Additionally, the relatively high coefficient of thermal expansion of brass caused problems in the smooth driving of the HMMS. While during temperatures above 20 °C wave formations in the total rail system could be observed, leading to a halting system, there were during night/early morning (cold temperatures, $T < 10$ °C) gaps between the 2 m long rail segments. If the gap occurred in the first 25 m (Position: 0 to 25 m) or in the last 25 m (Position: 125 to 150 m), this led to powerless rail segments and a stationary HMMS, due to the chosen feed points for the power (Section 2.3.1).

Those problems led to a high variability in the durations for a single run of the HMMS. Figure 2.6 shows the mean run duration with the standard deviation (arrows) for all three ‘Golden Day’ periods, broken down in the two different driving directions. The dashed line shows the intended run duration of 5 min (corresponding to a speed of 0.5 m s^{-1}). In GDP1 the run duration was in both directions lower than the intended duration, especially in case of the ‘Backward Direction’ (BD), but the variability was very low. So in other words, the system was faster than the intended 0.5 m s^{-1} but consistent. During GDP2 the mean run duration in the ‘Forward Direction’ (FD) was similar to GDP1, whereas the run duration in BD had increased by approximately 1 min. For both cases a substantial increase in the variability is observable. The reason for this is the ageing of the engines and their inner workings (gearboxes), leading to an increase of the run duration in general and because of the named problems above, the HMMS had more stops and halted runs. This trend continued in GDP3, where both driving directions had longer run durations than the intended one with also high variability. The differences in the run duration (respectively speed) must be considered for the corrections of the dynamical errors, which is exemplarily shown in Section 2.4.1. After 250 h of operating time and more than 3500 runs (corresponding to more than 500 km distance) during EGER IOP3, a maintenance and a change of the engines was necessary. This is not surprising since the total weight of the HMMS was almost 10 times greater than the original weight of the garden railway locomotive, resulting in a higher axial load and consequently more stress for the engines.

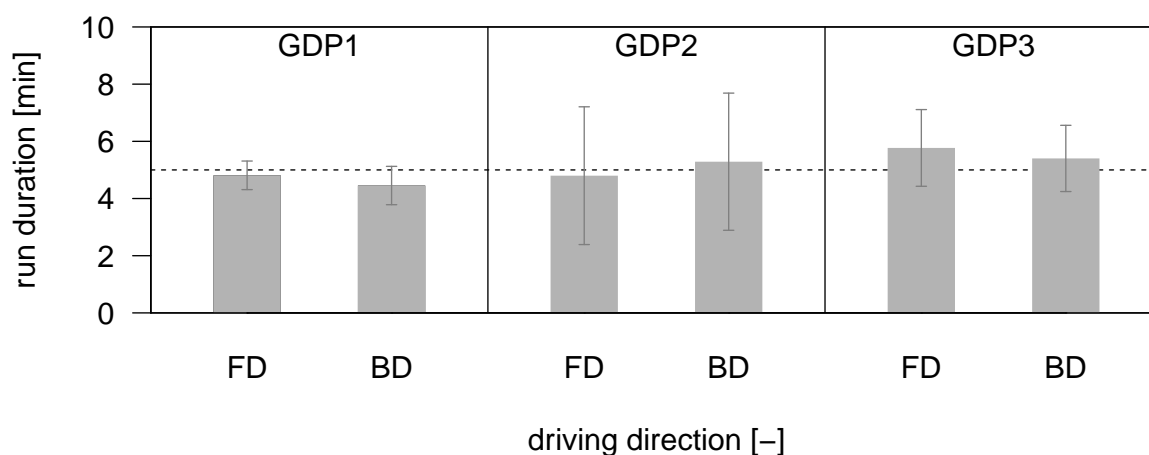


Figure 2.6. Mean run duration of the HMMS for all three ‘Golden Day’ periods (GDP) depending on the driving direction, with ‘Forward Direction’ (FD) and ‘Backward Direction’ (BD). Arrows indicates the standard deviation. Dashed line shows the intended run duration of 5 min (HMMS speed of 0.5 m s^{-1}).

2.3.6. Radiation-induced error in CO_2 measurements

Due to the small time constants of the CO_2 and O_3 analysers ($\tau_{63} < 1 \text{ s}$, see Table 2.9 and Figure 2.5), there is no need for a response-time-induced error correction. Whereas the O_3 measurements were – with the exception of the connection problems between the analyser and the HMMS software up to 4 July 2011 (see Section 2.3.2) – of high accuracy, some substantial problems in the CO_2 measurements were observable during daytime. Because of the late delivery of the Gascard[®] NG CO_2 analyser shortly before the start of the EGER IOP3 project, there was not enough time to check properly the analyser against different influences. Laboratory tests after the project have shown that the CO_2 concentration can be kept at a constant level as long as the analyser was shadowed (no direct sunlight), and immediately drifts down when the analyser was exposed to direct sunlight. A development of a temperature compensation was considered, but investigations showed a complicated dependence of the errors on temperature and radiation, which made a correction impossible for daytime measurements. Because of this, the CO_2 measurements were discarded during daytime, whereas the measured values recorded during nighttime were in acceptable agreement with other CO_2 measurements near the HMMS track.

2.4. Post-field data processing

This section is about post-field data processing. Details are given of the correction algorithm to correct the dynamical errors in the HMMS measurements, caused by the move-

ment and the sensor time constants (see Section 2.4.1), the analysis of turbulence fluxes, using micrometeorological standards for data processing (see Section 2.4.2), analysis and classification of coupling situations (see Section 2.4.3) and the modelling of energy and matter exchange using the model ACASA (see Section 2.4.5).

2.4.1. Correction of dynamical errors in HMMS measurements

The HMMS measurements during the EGER IOP3 were performed on a transect from the dense spruce forest to the open clearing ‘Köhlerloh’ (see Section 2.3). The main focus of the HMMS measurements during EGER IOP3 lay on the forest edge: the relative distinct transition area. Here, an abrupt change in the input signals of all quantities is observable mostly within a few metres. Because of the individual sensor response times τ , the sensors were not able to adapt to sudden changes adequately in a short time and through the movement of the HMMS, the measured input signals lag behind the ‘real’ input signal. To correct this lag in the input signals, or to be more precise, the dynamical errors in the measurements of the HMMS sensors, a correction algorithm was applied.

For the correction of the dynamical errors in the recorded signal X_i of the HMMS measurements, a linear adjustment after Eq. (2.6) was used, a first-order differential equation. The correction algorithm only considers a linear gradient along a defined distance, ignoring the influence of turbulent structures and small-scale heterogeneities, which can affect the prevailing gradient within a short time. Especially at the forest edge, the prevailing gradients are significantly influenced by turbulence, with an increased number of coherent structures like sweeps and ejections (Eder et al., 2013). Nevertheless, the application of a generalised dynamic performance model (e.g. Brock and Richardson, 2001), which considers – beside a steady-state solution – a transient solution, was neglected, since (i) the changes in the quantities caused by the transition from the forest to the clearing are significantly higher than the changes caused by fluctuations of small-scale structures, which have a purely random character and (ii) analysis effort is considerably higher.

The data of every single run was examined and properly corrected on a case-by-case basis (forest \rightarrow clearing: ‘Forward Direction’; clearing \rightarrow forest: ‘Backward Direction’). The starting point and endpoint (distance of linear gradient) and the gradient itself (variable for every measured quantity) were determined and afterwards the correction algorithm was applied. After that, the final value of the signal will be reached earlier in time and also spatially. This procedure was seen to be the best way to correct the measured values at the forest edge adequately after the investigation of many runs. The disadvantage of this procedure is the greater effort, required to an automatism and therefore only data of

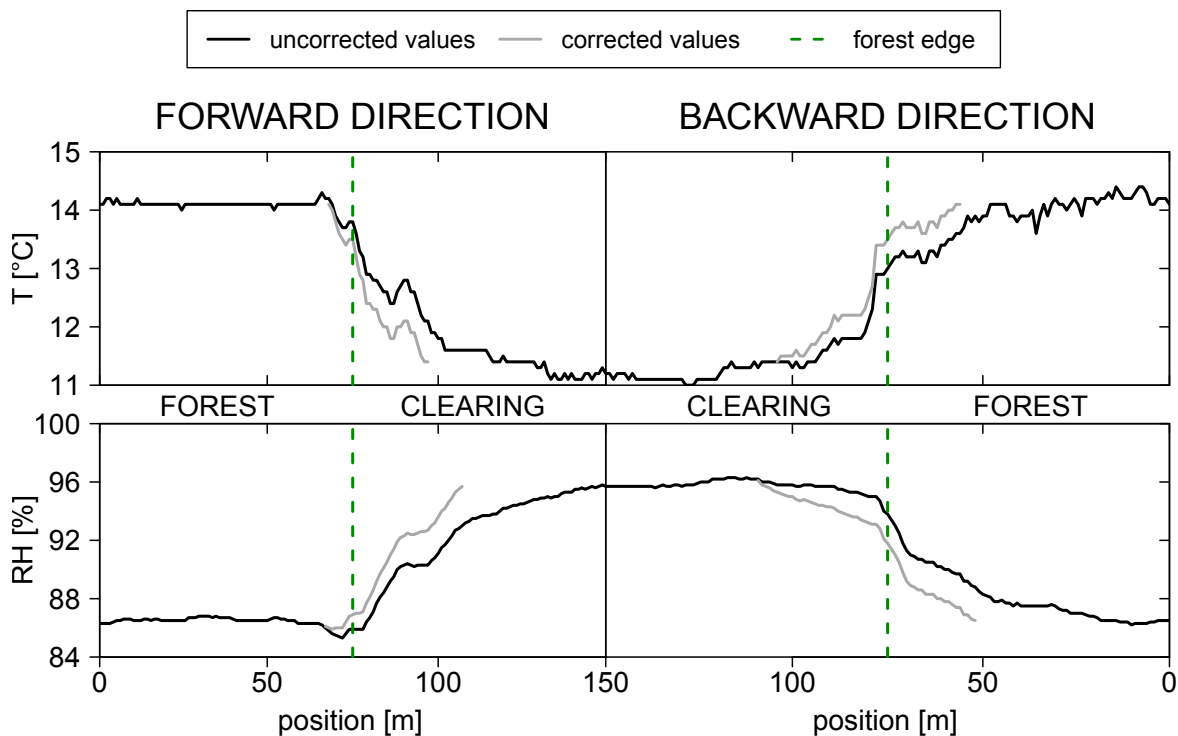


Figure 2.7. Example time series of temperature T (top) and relative humidity RH (bottom) for one complete run of the HMMS during night-time of 28 June 2011. The runtime was 02:53 – 02:58 CET in forward direction and 02:58 – 03:03 CET in backward direction. The forest edge is indicated by the vertical green dotted line. The time series shows the uncorrected measured values (black solid line) and, at the forest edge, the corrected gradient (grey solid line).

measurements which are used for detailed studies of the micrometeorological phenomena near the forest edge would be corrected in the following sections.

The application of the correction algorithm and results with a pre-post comparison are exemplarily shown for the 28 June 2011 (DOY: 179). Figure 2.7 shows a night-time series for air temperature T (top) and relative humidity RH (bottom) of one complete run of the HMMS. The run led from the forest to the clearing ('Forward Direction' – 02:53 - 02:58 CET) and from the clearing back to the forest ('Backward Direction' – 02:58 - 03:03 CET). The measured (equivalent to uncorrected) values (black solid lines) were almost constant in the forest and at the clearing, while an obvious steep gradient near the forest edge was observed. The grey lines indicate the corrected data of air temperature and relative humidity at the forest edge. In both cases, the final value of the gradient was reached earlier in time and spatial terms, and the relocation of the measured signal compared to the corrected measured signal is obvious and corresponds to the calculated relocation in Table 2.9. After the correction, the 'real' measured values for air temperature have almost the same val-

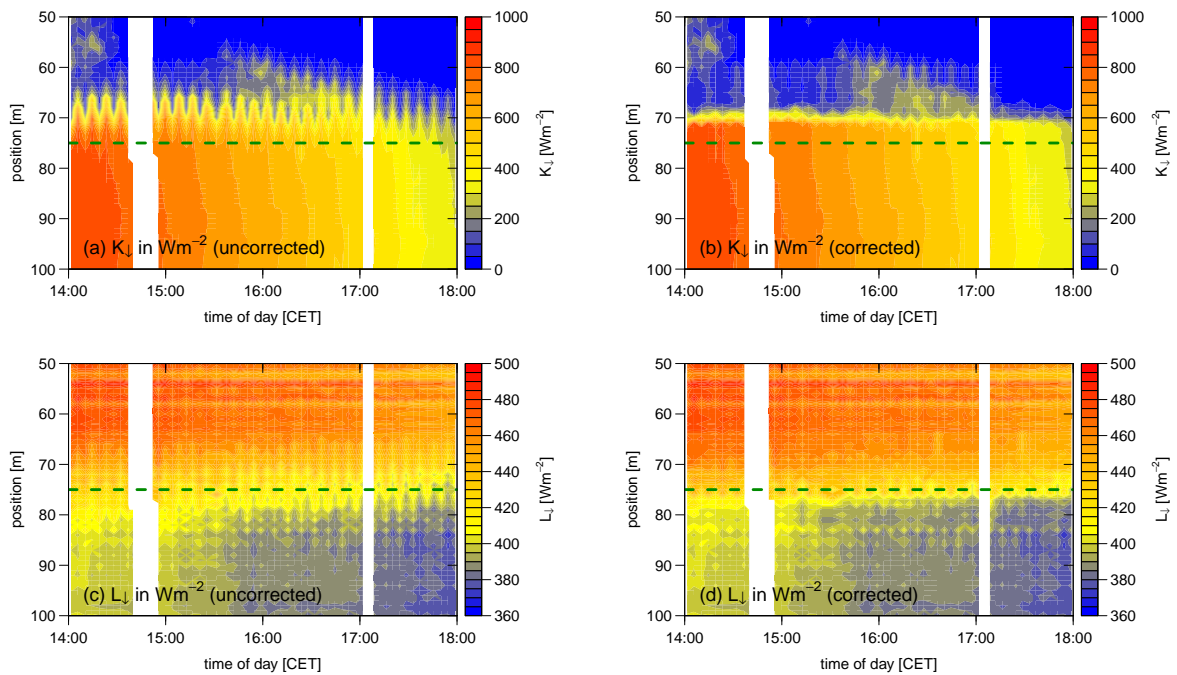


Figure 2.8. Detailed horizontal profiles during daytime of 28 June 2011 at the forest edge (horizontal green dotted line), uncorrected profiles for short-wave downwelling radiation K_{\downarrow} (a) and long-wave downwelling radiation L_{\downarrow} (c), and in both cases response time corrected profiles (b, d). Position shows distance from starting point in metres, starting in the forest (50 m) and ending at the clearing (100 m).

ues at the forest edge, while the gradient for the relative humidity starts in the backward direction much later than in the forward direction. Possible reasons include (i) an effect caused by the hysteresis, outlined in Section 2.3.4 or (ii) an abrupt change of the gradient affected by turbulent structures, or (iii) a combination of both effects.

Figure 2.8 shows horizontal profiles of short-wave downwelling radiation (K_{\downarrow}) and long-wave downwelling radiation (L_{\downarrow}) during the daytime on the 28 June around the forest edge. The profiles in Figure 2.8a and 2.8c show the uncorrected measurements for K_{\downarrow} and L_{\downarrow} , respectively. Time constants of the sensors and the different driving direction of the HMMS led to the zigzag pattern of the uncorrected measurement data. To correct radiation measurements between 14:00 and 18:00 CET of 28 June 2011, the corresponding response times (4 s, see Table 2.9) were used to calculate the ‘real’ measured values assuming a linear gradient between the defined starting and end point. The dynamical error corrected horizontal radiation profiles, shown in Figure 2.8b (K_{\downarrow}) and 2.8d (L_{\downarrow}), are nearly free of the zigzag pattern. The correction made it easier to discern the significant change of K_{\downarrow} (top), which occurred approximately 5 m north of the forest edge (position measured from

starting point: 70 m). This is caused by the angle of incidence of the sun's radiation and the open forest's trunk space. In contrast, the significant change of L_{\downarrow} (bottom) lies exactly on/slightly south to the forest edge (position measured from starting point: 75 – 77 m).

2.4.2. Analysis of turbulent fluxes

The turbulent fluxes measured during the EGER IOP3 project were post-processed and quality controlled with the comprehensive software package TK3b, an updated version of the TK3 (Mauder and Foken, 2011), based on more than 20 years of experiences with eddy-covariance data. An inter-comparison study of the former software package TK2 with other EC-flux software packages, like EddySoft or ECPack was done by Mauder et al. (2008) and the TK3b has the same micrometeorological post-field data processing standards, including some enhancements (e.g. Mauder et al., 2006; Mauder et al., 2013). The applied flux corrections in TK3b follow the recommendations of Foken et al. (2012a) and Rebmann et al. (2012). Quality tests implemented in TK3b consist of a stationarity test and a test on the fulfilment of integral turbulence characteristics (ITC) for each 30 min interval (according to Foken and Wichura, 1996; Foken et al., 2004). According to this, the planar-fit method was applied to all towers/masts (Wilczak et al., 2001). While the mean vertical wind for the complete period is set to zero by this method ($\bar{w} = 0$), the individual 30 min averages do not vanish completely. Siebicke et al. (2012) recommends for the very complex terrain at the EGER site (surrounding hilltops and tall vegetation) a sector-wise planar-fit rotation, which was applied to the measurements at the towers/masts where needed (sector-wise planar-fit proposed by Foken et al., 2004). An overview of the applied method for each individual tower/masts is given in Table 2.10. For the tower M1 ($z = 32$ m), as well as for the tower M2 ($z = 26$ m; $z = 36$ m) an analysis of the vertical wind velocity was performed to determine the different sectors for the sector-wise planar-fit rotation. For the towers/masts influenced by the forest edge (in particular M3, M6, M7) a sector-wise planar-fit considering the angle of the forest edge was applied (direction of forest edge is NW to SE: 300 to 120°). A schematic drawing of the sectors is shown in Figure 2.9. The four sectors comprise two planes with different land surfaces (forest & clearing) and two planes for the transition areas (this rotation procedure is suggested for complex terrain e.g. by Paw U et al., 2000; Finnigan et al., 2003). At the forest edge tower M3 at 27 m height, data is only available up to 2 July 2011, so that there is only data for the first 'Golden Day' period available. For a reliable planar-fit, this quantity of data is insufficient. The analysis of the vertical wind velocity for the mast M4 at the clearing, as well as for the masts M2 ($z = 2.25$ m) and M8 ($z = 2.25$ m) within the trunk space of the forest showed that

Table 2.10. Angles of sectors with their quantity in brackets behind used for (sector-wise) planar-fit rotation at towers/masts M1 – M4 and M6 – M8 during EGER IOP3. For the measurements with the quantity indicated by ‘-’ no sector-wise planar-fit rotation was applied. \bar{w} -analysis (95 %) shows the ranges which contains 95 % of the vertical wind velocity data.

Tower	z (m)	Sector(s)	\bar{w} -analysis (95 %)
M1	32 m	30 – 90°; 90 – 150°; 150 – 190°; 190 – 310°; 310 – 30° (5)	$\pm 0.09 \text{ m s}^{-1}$
M2	36 m	20 – 100°; 100 – 150°; 150 – 240°; 240 – 20° (4)	$\pm 0.1 \text{ m s}^{-1}$
	26 m	20 – 100°; 100 – 150°; 150 – 240°; 240 – 20° (4)	$\pm 0.08 \text{ m s}^{-1}$
	2.25 m	0 – 360° (-)	$\pm 0.02 \text{ m s}^{-1}$
M3	41 m	90 – 150°; 150 – 270°; 270 – 330°; 330 – 90° (4)	$\pm 0.16 \text{ m s}^{-1}$
	2.25 m	90 – 150°; 150 – 270°; 270 – 330°; 330 – 90° (4)	$\pm 0.06 \text{ m s}^{-1}$
M4	5.5 m	0 – 360° (-)	$\pm 0.06 \text{ m s}^{-1}$
	2.25 m	0 – 360° (-)	$\pm 0.04 \text{ m s}^{-1}$
M6	5.5 m	90 – 150°; 150 – 270°; 270 – 330°; 330 – 90° (4)	$\pm 0.08 \text{ m s}^{-1}$
	2.25 m	90 – 150°; 150 – 270°; 270 – 330°; 330 – 90° (4)	$\pm 0.04 \text{ m s}^{-1}$
M7	5.5 m	90 – 150°; 150 – 270°; 270 – 330°; 330 – 90° (4)	$\pm 0.04 \text{ m s}^{-1}$
	2.25 m	90 – 150°; 150 – 270°; 270 – 330°; 330 – 90° (4)	$\pm 0.07 \text{ m s}^{-1}$
M8	2.25 m	0 – 360° (-)	$\pm 0.02 \text{ m s}^{-1}$

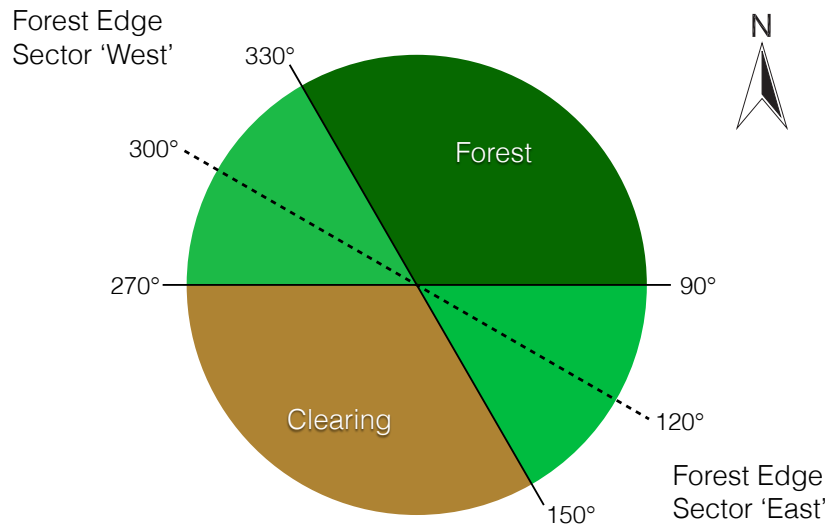


Figure 2.9. Schematic drawing of used sectors for the sector-wise planar-fit rotation at towers/masts at the forest edge (M3, M6, M7). Dashed line indicates the forest edge.

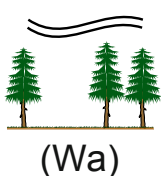
there was no sector-wise planar-fit necessary. After the (sector-wise) rotation, most of the vertical wind velocity vanishes. The ranges which contain 95 % of the vertical wind velo-

city data, are given for each tower/mast in Table 2.10. The effect of (sector-wise) coordinate rotation approaches on vertical wind velocity w compared to the case before coordinate rotation, are presented in Appendix A for each tower/mast. The figures show the vertical wind velocity versus the wind direction.

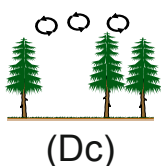
2.4.3. Analysis of coherent structures

For the analysis of coherent structures and coupling, some data quality assessment and quality control (QA/QC) presented by Thomas and Foken (2007a) were performed in order to filter out inappropriate data. Additionally despiking, planar-fit rotation, cross-correlation between sonic anemometer and gas analysers, as well as an averaging from 20 Hz to 2 Hz to reduce computing time and a low-pass filtering was conducted. Afterwards a wavelet transform was performed to extract coherent structures from the time series of turbulent data (Thomas and Foken, 2005, 2007a). For a more detailed description of the post-field data processing and wavelet analysis see Eder et al. (2013), who presented the results of analysis of coupling for the EGER IOP3 project.

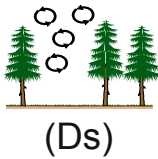
To detect the coupling in the forest of the EGER IOP3 project by coherent structures, turbulence tower measurements at three different levels (above canopy, top of the forest canopy, and sub-canopy) were performed (see Section 2.2.2). In detail, the method examines the coherent portion of the sensible heat of the canopy and can identify characteristic exchange regimes. Considering the portion of coherent structures at each level allows the definition of the coupled states between the sub-canopy, canopy and layer above the canopy. Foken et al. (2012b) describes this method as a good tool for the investigation of tall vegetation, which also comprises night time situations with sudden coupling/decoupling events. Five exchange regimes were proposed by Thomas and Foken (2007b):



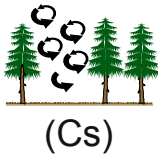
Wavemotion (Wa): The flow above the canopy is dominated by linear wave motions (gravity waves), resulting in a greatly reduced scalar transport (Cava et al., 2004). The sub-canopy layer and forest canopy are decoupled from the layer above the canopy.



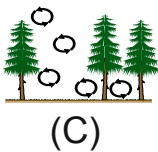
Decoupled canopy (Dc): The air above the canopy is decoupled from the sub-canopy layer and forest canopy (analogous to Wa regime).



Decoupled sub-canopy layer (Ds): The forest canopy layer is coupled to the air above the canopy, but the sub-canopy layer is still decoupled.

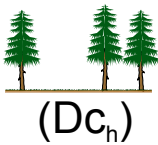


Coupled sub-canopy layer by sweeps (Cs): The canopy layer is coupled to the region above the canopy, but the sub-canopy layer is only coupled to the air above the canopy by strong sweep motions

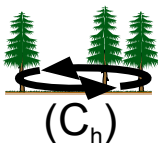


Fully coupled canopy (C): All layers are completely coupled and in all layers, both ejections and sweeps contribute to the exchange of energy and matter.

Regarding the exchange in tall vegetation the coherent exchange in horizontal direction has also been taken into account. Serafimovich et al. (2011b) introduced an approach based on the assumption that coherent structures dominate the exchange in the sub-canopy layer. They used the horizontal sensible heat flux $\overline{u'T'_s}$ for the investigation and proposed two further coupling regimes:



Horizontal decoupled regime (Dc_h): The different measuring locations are horizontally decoupled. The vertical coupling into the sub-canopy can be either absent (Wa, Dc, or Ds) or present (only by sweeps Cs or fully coupled C).



Horizontal coupled regime (C_h): The sub-canopy is coupled by coherent structures and also a vertical coupling with the air above the forest canopy is present.

Vertical and horizontal coupling were investigated during the EGER IOP3 project at various locations. Towers for the investigation of vertical coupling were M2, M3 and M4 (see Figure 2.2 for locations and Section 2.2.2 for description). Horizontal coupling was investigated along two different transects, one perpendicular to the forest edge (M8 – M3 – M4) and one parallel (M6 – M3 – M7). Besides a fully coupled and decoupled situation along the transect, there is also the possibility to distinguish the coupling situation between the different towers (first two towers are coupled, while tower two and three are decoupled and vice versa).

2.4.4. Analysis of storage heat flux within forest biomass

To determine the residual Res of the energy balance in a proper way, in addition to the measured net radiation (Q_S^*) and heat fluxes (Q_H , Q_E , Q_G), the storage heat flux Q_B of the biomass has to be considered. This was calculated only for the forest, as the heat storage capacity in the forest is significantly higher than in the vegetation of the clearing. Haverd et al. (2007) and Lindroth et al. (2010) reveal the necessity of a correct analysis of the storage heat flux for tall vegetation. The storage heat flux can be calculated in the following way:

$$Q_B = m_w \cdot c_w \cdot \frac{T(t) - T(t - \Delta t)}{\Delta t} \quad (2.7)$$

where m_w is the biomass of the forest (biomass for research site ‘Waldstein-Weidenbrunnen’ is $m_w = 12.7 \text{ kg m}^{-2}$; Mund et al., 2002), c_w is the specific heat capacity for wood ($c_w = 1702.8 \text{ J kg}^{-1} \text{ K}^{-1}$) and T the air temperature. It is assumed, that the trunk temperature correlates with the air temperature and therefore air temperature can be used as a proxy for the calculation.

2.4.5. Modelling of energy and matter exchange

The energy and matter exchange within and above the canopy was modelled using the multi-layer model ACASA (Advanced Canopy-Atmosphere-Soil Algorithm, Pyles, 2000; Pyles et al., 2000), which incorporates a third-order closure method (Meyers, 1985; Meyers and Paw U, 1986, 1987). Implemented features of the ACASA model are (i) long- and short-wave radiative transfer within the canopy (Meyers, 1985), (ii) calculation of leaf, stem and soil surface temperatures using the fourth-order polynomial of Paw U and Gao (1988), (iii) plant physiological response to ambient conditions by a combination of the Ball-Berry stomatal conductance approach (Leuning, 1990; Collatz et al., 1991) and photosynthesis equation (Farquhar and von Caemmerer, 1982), following Su et al. (1996), and (iv) a model for soil moisture and soil temperature adapted from MAPS (Mesoscale Analysis and Prediction System; Smirnova et al., 1997, 2000).

The ACASA model requires half-hourly meteorological input data (precipitation, relative/specific humidity, mean wind velocity, downward short- and long-wave radiation, air temperature, air pressure and CO_2 concentration), as well as an initial soil profile (temperature, moisture). Measurements were used from M1 and from the small clearing ‘Pflanzgarten’ for the forest and for the clearing from the mast M4. A parametrisation and validation of the ACASA model for EGER project site ‘Waldstein-Weidenbrunnen’ was performed by Staudt et al. (2010) for IOP1 & IOP2 and these parameters were also used for

IOP3. Because the investigation focus lay at the clearing ‘Köhlerloh’ during IOP3, it was necessary to adapt the plant physiology sub models in the ACASA model to the altered conditions, compared to the used parameters in Staudt et al. (2010). The ACASA model was adapted for a tile approach of the clearing within the scope of the master thesis of Gatzsche (2013). The used ACASA model for EGER IOP3 (release date April 2013) was corrected by the author for the deficits found by Staudt et al. (2010) and due to that, the model has a significant enhanced performance regarding the energy balance closure, compared to the ACASA model used in EGER IOP1 & IOP2 (Staudt et al., 2010). Enhancements include a parametrisation to close the energy and matter exchanges for every single model layer, without the utilisation of further assumptions, this facilitates a nearly closed energy balance, with a residual Res not more than 20 W m^{-2} at the clearing during EGER IOP3 (Gatzsche, 2013). Plant physiological parameters used in the ACASA model during EGER IOP3 are given in the Tables B.1 and B.2 in Appendix B.

Since the modelled energy fluxes have an almost closed energy balance (very low residual Res , see Equation 1.1), the measured fluxes have to have also a closed energy balance. Therefore, two different approaches were used/compared in order to close the measured energy fluxes. Both spread the available residual to the sensible (Q_H) and latent (Q_E) heat flux. The two methods are:

- (i) Bowen ratio correction (EBC-Bo) method after Twine et al. (2000):

With the Bowen ratio

$$Bo = \frac{Q_H}{Q_E} \quad (2.8)$$

and for $Bo > 0$ the energy fluxes can be corrected as follows:

$$Q_H^{EBC-Bo} = Q_H + Res \cdot \frac{Bo}{1 + Bo} \quad (2.9)$$

$$Q_E^{EBC-Bo} = Q_E + Res \cdot \frac{1}{1 + Bo}. \quad (2.10)$$

- (ii) Buoyancy flux correction (EBC-HB) method of Charuchittipan et al. (2014):

With the ratio of the sensible heat flux Q_H to buoyancy flux Q_{HB}

$$\begin{aligned} f_{HB} &= \frac{Q_H}{Q_{HB}} \\ &= \left(1 + 0.61 \bar{T} \cdot \frac{c_p}{\lambda \cdot Bo}\right)^{-1} \end{aligned} \quad (2.11)$$

where c_p is the specific heat of air and λ is the heat of evaporation for water. For

$Bo > 0$ the energy fluxes can be corrected:

$$Q_H^{EBC-HB} = Q_H + f_{HB} \cdot Res \quad (2.12)$$

$$Q_E^{EBC-HB} = Q_E + (1 - f_{HB}) \cdot Res \quad (2.13)$$

Both methods have the premise that the application is only possible for energy fluxes greater than 10 W m^{-2} . The main difference between methods, is that with method (ii) secondary structures can be considered, which are mainly driven by buoyancy (Foken et al., 2011) and a larger portion of the residual Res will be allocated to the sensible heat flux. In method (i) structures with different scales should be considered (Foken, 2008b), by assuming there is a similarity between small and large scale structures, which enables a closed energy balance after Equation (1.1) in the form:

$$0 = Q_S^* - Q_G - Q_B - \langle Q_H \rangle_s - \langle Q_H \rangle_l - \langle Q_E \rangle_s - \langle Q_E \rangle_l \quad (2.14)$$

where the index s represents small-scale structures and l large scale structures. The similarity is not valid for the long-wave part of the turbulence spectra (Ruppert et al., 2006), which made an accurate distribution of the residual to the large-eddy part of the sensible and latent heat flux problematic (Foken, 2008b).

The measured net ecosystem exchange (NEE) was corrected with a ratio of corrected and uncorrected Q_E , since there is a dependency in the stomatal exchange of water vapour and CO_2 of all plants:

$$k^{EBC-Bo} = \frac{Q_E^{EBC-Bo}}{Q_E} \quad (2.15)$$

$$k^{EBC-HB} = \frac{Q_E^{EBC-HB}}{Q_E} \quad (2.16)$$

and therefore the corrected NEE is

$$NEE^{EBC-Bo} = k^{EBC-Bo} \cdot NEE \quad (2.17)$$

$$NEE^{EBC-HB} = k^{EBC-HB} \cdot NEE. \quad (2.18)$$

3. Results and discussion

In Section 3.1 a metrological assessment of the HMMS is given, comparing the HMMS measurements with fixed tower measurements at the clearing. The subsequent sections concentrate on the analysis of three ‘Golden Day’ periods (GDP) during the EGER IOP3 project in June/July 2011, namely 26 – 29 June (DOY: 177 - 180, GDP1), 4 – 8 July (DOY: 185 – 189, GDP2) and 14 – 17 July (DOY: 195 – 198, GDP3). The three periods were characterised by good to adequate weather conditions, with a high solar radiation, nearly similar radiation properties, low to moderate wind forcing and almost no precipitation, but sometimes clouds. For a more detailed description of the weather conditions see Section 2.1.3 and Serafimovich et al. (2011a). The confinement to these three periods, with nearly similar radiation forcing, and wind velocity, but shifting wind directions, facilitates the comprehensive investigation and interpretation of the heterogeneous forest, with a focus on the forest edge, or in other words, the roughness change, taking into account the objectives of this work, named in Section 1.3.

3.1. Metrological assessment of the HMMS

The newly developed Horizontal Mobile Measuring System (HMMS) was used during the EGER IOP3 project to capture horizontal gradients along a transect leading from the dense forest to the open clearing, with a focus on the forest edge. Besides the technical realisation of the system (presented in Section 2.3 and Hübner et al., 2014), the correction of dynamical errors was a major task for an exact representativeness of the measured data. The applied correction is presented in Section 2.4.1 and Hübner et al. (2014). This section sets out to assess the HMMS measurements, whether if there are discrepancies caused by the movement and/or the chosen design, the used components and the realised modifications. Therefore, a side-by-side comparison with fixed tower measurements was performed. This field-site comparison was preferred over laboratory tests because of the changing conditions caused by the movement of the HMMS, or the changing position of the sun, etc. could not be simulated adequately in the laboratory. The comparison is shown for all four radiation measurements in Figure 3.1, for the HMP155 measurements (temperature and

relative humidity) in Figure 3.2 and for the trace gas measurements (CO_2 and O_3) in Figure 3.3. The measurements of the HMMS were averaged for the last few metres of the track at the clearing (position 145 to 150 m), including the turnaround and the same distance in 'Backward Direction'. The HMMS passes this section approximately every 10 min and has a transit time of 20 s including the turnaround. This 20 s of data (a snapshot in time) was used for the comparison with 10 min averaged values from the tower measurements.

All four radiation measurements of the HMMS were compared to the fixed measurements near M4, where a Kipp & Zonen CNR4 was installed at 2 m height (see Section 2.2.4). The sensors have nearly the same accuracy, and the only difference between the two measurements is the ventilated and heated sensor housing of the CNR4, which is not available for the single sensors (2 x CMP3/2 x CGR3) used on the HMMS. Figure 3.1a shows the short-wave downwelling radiation K_{\downarrow} , where the majority of HMMS data points show a good correlation with the fixed measurements. But there is also a wide scatter of some data points with absolute deviations of 400 W m^{-2} and more observable. This is an effect caused by the mobile system, since only 20 s of data are compared with 10 min averaged data, and therefore one cloud can change the measured values of the HMMS significantly. The short-wave upwelling radiation K_{\uparrow} in Figure 3.1b shows a good correlation in the lower values (up to 60 W m^{-2}) and a systematic divergence towards the fixed tower measurements at higher values. In other words K_{\uparrow} is higher at the fixed measurements, than it is at the HMMS. Considering both short-wave radiations it can be concluded that the albedo is higher at M4 than at the HMMS. Another effect is observable for $K_{\uparrow} = 0 \text{ W m}^{-2}$ at the HMMS, where the values at M4 vary between 0 and approximately 50 W m^{-2} . This can be explained by the more easterly location of M4, where the short-wave radiation set in earlier, and the differences in the measuring height (1 m at HMMS against 2 m at M4), which especially affects the downward-looking sensor for short-wave upwelling radiation. The scatter caused by the different averaging time exists here also. The long-wave downwelling radiation L_{\downarrow} (Figure 3.1c) shows an acceptable correlation with a divergence towards the HMMS measurements. This minor overestimation illustrates the absence of ventilation and a possible thermal radiation from the HMMS housing which affects the long-wave radiation measurements. In the long-wave upwelling radiation L_{\uparrow} (Figure 3.1d) it can be observed that there is similar behaviour as seen in the short-wave upwelling radiation. The lower values (up to 400 W m^{-2}) are in good agreement, whereas the higher values also show a systematic divergence, but now towards the HMMS measurements. In other words, the surface near the HMMS is warmer (less the minor overestimation like it was found for L_{\downarrow}), than it is near M4, which coincides with the findings of the albedo. A random scatter which

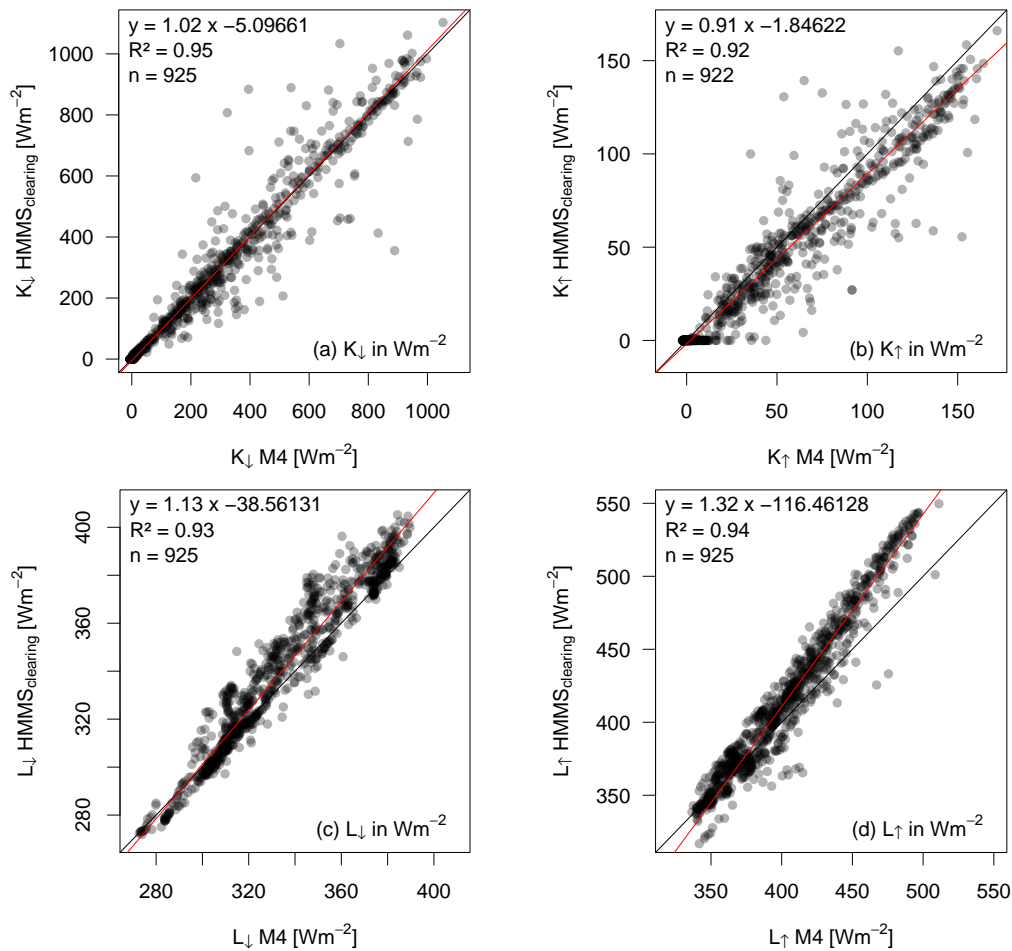


Figure 3.1. Radiation measurements of the HMMS at the clearing (position 145 to 149 m) versus tower measurements in 2 m height near M4 (see Section 2.2.4). Red line indicates the regression between the measurements, with linear equation, coefficient of determination (R^2) and amount of data points (n) given top left.

can be seen in the short-wave radiation does not exist in both long-wave radiation components, which can be explained by a smaller dependence of shadowing effects caused by clouds. All radiation measurements have a good correlation with the fixed measurements and divergences can be explained by differences in the surfaces, in the averaging time, and probably by a small influence of the HMMS housing in the long-wave radiation and by general uncertainties in the measurements, but systematic errors in the measurements can be excluded.

The HMP155 measurements (temperature and humidity) shown in Figure 3.2 were compared with the psychrometer measurements at 1.4 m at the tower for chemical measurements (CM; see Section 2.2.3). Both psychrometer at CM were also double shielded and

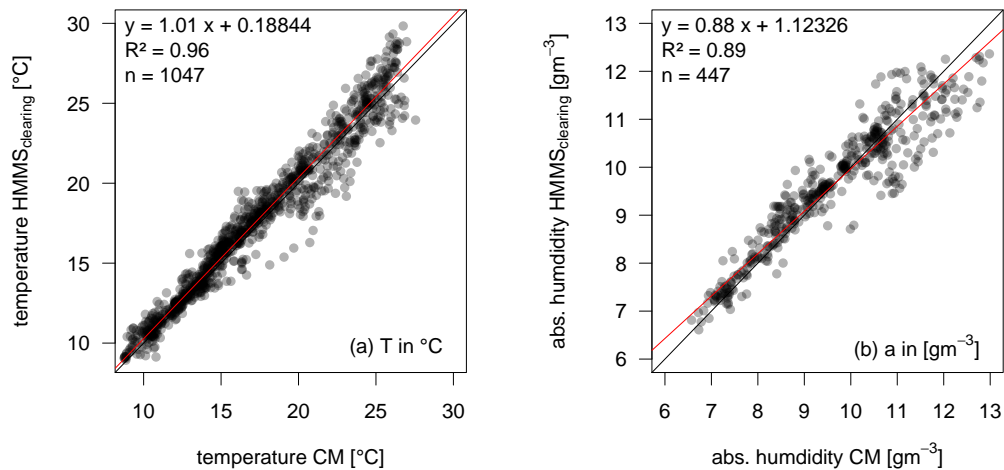


Figure 3.2. Temperature and absolute humidity measurements of the HMMS at the clearing (position 145 to 149 m) versus tower measurements in 2 m height near M4 (see Section 2.2.4). Red line indicates the regression between the measurements, with linear equation, coefficient of determination (R^2) and amount of data points (n) given top left.

ventilated. The correlation of the temperature measurements (Figure 3.2a) is very good, with a somewhat larger scatter in the higher values. This can be explained by the different surface temperatures also found in the long-wave upwelling radiation (see text above and Figure 3.1d). The humidity measurements (Figure 3.2b) have been converted to absolute values in g m^{-3} . Due to the drying out of the water reservoir (needed for the wet bulb temperature) at the psychrometer at CM at several instances, there are fewer data points than for temperature. At values below 10 g m^{-3} the correlation between the HMMS and CM is good, but at absolute humidities above 10 g m^{-3} the scatter is significant. Absolute humidity measurements correlate with temperature measurements and higher values occur mainly during daytime – caused by higher temperatures the capacity of air to absorb humidity is higher, till saturation is reached – and therefore the variations between the two locations can be explained due to the higher temperature measurements found in Figure 3.2a. In both measurements, deviations can be assigned to true differences, caused by variations between the sites and not caused by systematical errors.

The trace gas measurements (CO_2 and O_3) were compared to measurements performed directly at M4. For CO_2 comparison (Figure 3.3a) the LI-7200 in 2.25 m was used. This is a very commonly used sensor for turbulent flux measurements, with high accuracy and quality checked results (see Section 2.4.2) the significant differences between both measurements can be attributed to Gascard NG[®] used on the HMMS. This sensor has a lower accuracy compared to the LI-7200. Because of the radiation problems during daytime (see

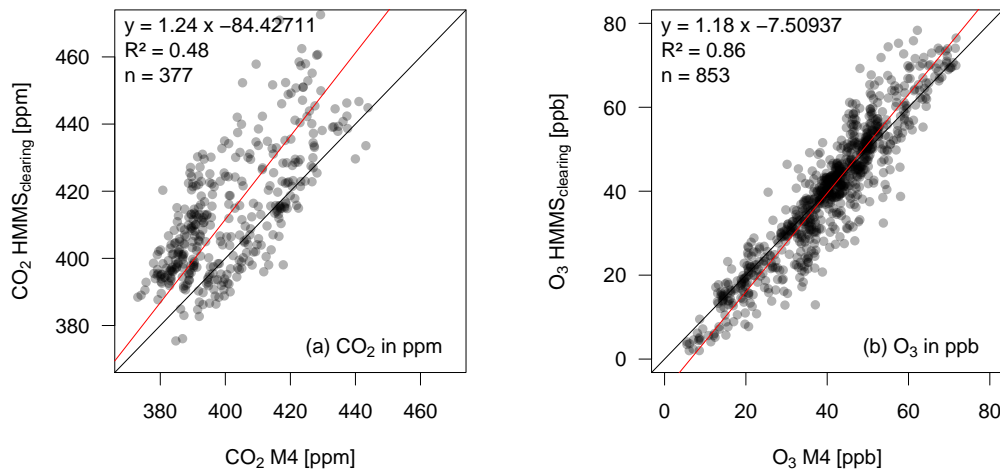


Figure 3.3. Trace gas measurements of the HMMS at the clearing (position 145 to 149 m) versus tower measurements at mast M4 and CM for all eight quantities. Red line indicates the regression between the measurements, with linear equation given top left.

Section 2.3.6), only the night-time values are shown in this plot. Due to the found deviations, a comparison between the CO_2 measurements on the HMMS and other CO_2 tower measurements performed during EGER IOP3 should be handled with care. The O_3 measurements (Figure 3.3b) show, on the other hand, a good correlation between HMMS and the O_3 monitor at 5.5 m at M4, despite the significant difference in the measuring height and the location for the performed calibration of the HMMS sensor in the forest and not at the clearing (see Section 2.3.3).

When now looking at the results of this comparison, it can be concluded, that the found discrepancies are basically caused by local differences in the surface, or rather the vegetation and soil parameters, and the different averaging times. The movement of the HMMS plays only a role for sudden changes in the input signal (as found at the forest edge) where a spatial relocation can be found, caused by the time constant τ (see Section 2.4.1). An influence at the clearing can be excluded. The design and the realised modifications of the HMMS have only a small influence on its measurements.

3.2. Characterisation of horizontal structures at the forest edge

A characterisation of the horizontal structures is given with the aid of the HMMS measurements. Comprising of gradients of typical meteorological parameters and trace gas concentrations along the transect from the dense spruce forest to the open clearing (Section 3.2.1) and turbulent flux measurements on a transect perpendicular to the forest edge

and another one parallel to the forest edge (Section 3.2.2). In addition, the horizontal distribution of coupling situations and coherent structures are presented in Section 3.2.3, and in Section 3.2.4 the ACASA modelled energy and matter fluxes are presented.

3.2.1. Horizontal gradients of typical meteorological parameters

The measurements of the HMMS gave an overview of important meteorological parameters, like radiation, air temperature and relative humidity, as well as trace gas concentrations of CO₂ and O₃ and their differences (gradients) at the forest edge. These differences are the prevailing driving forces at the forest edge (Murcia, 1995; Matlack and Litvaitis, 1999; Davies-Colley et al., 2000; Klaassen et al., 2002) and their investigation serves as the basis of the detailed characterisation of prevailing horizontal structures.

For a detailed investigation of the prevailing gradients along the HMMS measuring transect forest to clearing, the meteorological parameters were investigated at five different locations for all measurement days of the HMMS during the EGER IOP3 project (see Figure 2.3). One of the locations was situated in the forest (start of measuring transect), one at the clearing (end of transect) and three were located in the transition area. Exact positions (defined with bar codes) and their designations are given in Table 3.1. The specified endpoints differ depending on the driving direction, in order to capture in both directions the same area. Ensuing from the endpoints, an averaging over the preceding 15 s was performed. This approach was used to minimise influences caused by small-scale fluctuations, which were found in any turbulence influenced measurements (here: temperature, humidity and trace gases). Furthermore, influences of the dynamical error could be considerably minimised (averaged out) as even the sensor with the slowest adaptation (relative humidity sensor with a τ of 19 s) already has reached 60 % of the final value, the temperature sensor 73 % and the radiation sensors almost 100 %. A longer averaging period has not been applied, since the influences of spatial heterogeneities increases the longer the defined averaging period. Over the EGER IOP3 project, the distance covered during the 15 s of averaging time decreased slightly because of the variances of the HMMS speed, or in other words the increase found in the run durations (see Section 2.3.5). These variances (even if they are small) have been considered, in order to capture approximately the same distance every time. The application of the correction algorithm to avoid the influence of the dynamical error was, as already mentioned, not possible, since it could not be applied for the amount of data which was investigated here.

In Figure 3.4 the mean diurnal variations for all measurement days is shown at the five locations for the radiation measurements of the HMMS. Figure 3.5 shows the measure-

Table 3.1. Designations of the five locations for a detailed overview of the prevailing gradients along the transect forest to clearing. From the specified endpoints (distance from starting point in metre), which defer depending on the driving direction, an averaging over the preceding 15 s was performed.

Location	Forward Direction	Backward Direction
Forest	10	0
Forest (near forest edge)	70	60
Forest edge	80	70
Clearing (near forest edge)	90	80
Clearing	150	140

ments of the HMP155 (temperature and relative/absolute humidity) and the trace gas measurements (CO_2 and O_3). Here, the data were averaged over 15 s (see text above) for every single run at the five different locations and afterwards an averaging of 3 h took place. The used box-and-whisker plot shows the median (clarified by the bar in the box and the notches), the 25 % quartile and 75 % quartile (marked by lower and upper side of the box) and by the whiskers, the minimum and maximum values (1.5 times the interquartile range) are indicated. The single points above or below the whisker illustrate outliers.

The short-wave radiation components K_{\downarrow} (downwelling) and K_{\uparrow} (upwelling) are presented in Figure 3.4a, and 3.4b respectively. The short-wave radiation measurements show a significant gradient of approximately 750 W m^{-2} for downwelling and 110 W m^{-2} for upwelling radiation between clearing and forest around noon. While the values of the downwelling radiation decreases from the clearing to the forest continuously, the upwelling radiation has its maximum at the forest edge (here the gradient to the forest is 120 W m^{-2}). The influence of the forest edge (shadowing effect) is discernible in the early morning hours (03:00 to 06:00 CET) and enhanced between 06:00 to 09:00 CET, but also between 09:00 to 12:00 CET. Here, the gradient between forest edge and clearing is about 300 W m^{-2} . After noon the influence is no longer present and also during sunset, the effect of the forest edge is indiscernible. The many outliers, especially in both locations within the forest can be described by an inhomogeneous closed forest canopy (cf. sunny spots in Figure 3.21a and 3.21b). Here, the measured values are nearly as high as at the clearing. Outliers at clearing occur only during sunrise (03:00 to 06:00 CET) and sunset (18:00 to 21:00 CET), due to the presence/absence of fog, or the low position of the sun leads to a higher variation caused by (i) the movement of the HMMS and/or (ii) the cloudage.

The long-wave downwelling radiation measurements (Figure 3.4c) show also an obvi-

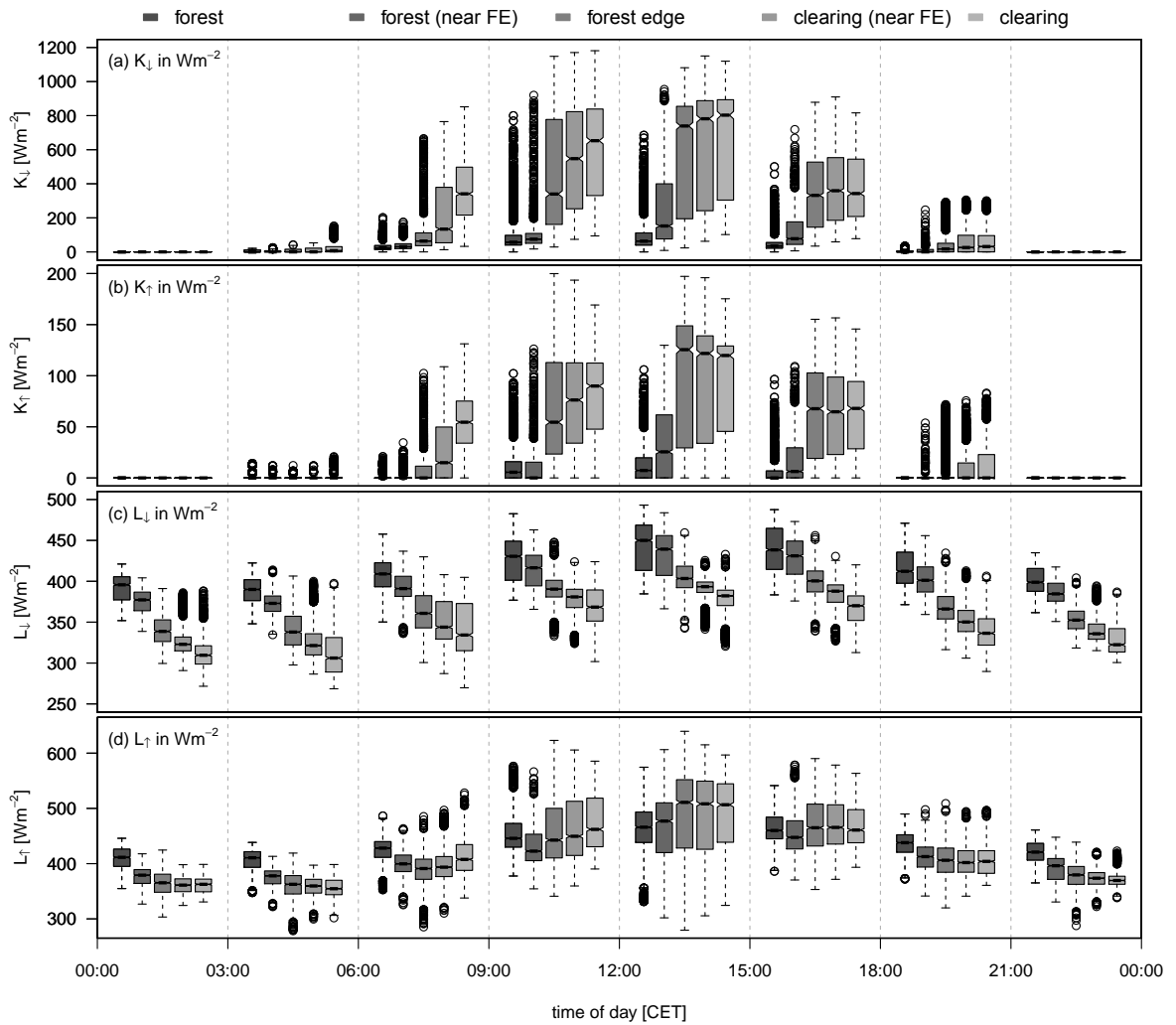


Figure 3.4. Diurnal variation of the radiation measurements; short-wave downwelling radiation K_{\downarrow} (a); short-wave upwelling radiation K_{\uparrow} (b); long-wave downwelling radiation L_{\downarrow} (c); long-wave upwelling radiation L_{\uparrow} (d); measured with the HMMS at five different locations: forest, forest (near forest edge/FE), forest edge, clearing (near FE) and clearing. Table 3.1 contains the exact bar code positions. The data was averaged at each location over 15 s per each run and afterwards these averages were averaged again in 3 h intervals. Data based on all completed runs during the three ‘Golden Day’ periods (Figure 2.3).

ous gradient between the forest and the clearing, with its maximum in the forest and its minimum at the clearing. The gradient persists all day long around 80 W m^{-2} higher in the forest than at the clearing and the values decreased continuously towards the clearing. The reason for this is the warmed forest canopy which radiates more heat than the free atmosphere. The effect of radiation can also be seen at the forest edge and weakly marked at the location near the forest edge. On the other side, the location in the forest

near the forest edge shows significantly lower values (approximately 20 W m^{-2}) than at the first location in the forest, which suggests, that near the forest edge there is also an effect of the free atmosphere measurable. In other words, the influence of the forest canopy decreases more and more towards the clearing, and the influence of the free atmosphere decreases more and more towards the forest. Outliers can mainly be found at the clearing, because of the greater influence of cloudy or sunny days on the measurements than within the forest. The long-wave upwelling radiation (Figure 3.4d) has higher variations throughout the course of the day at the clearing (350 W m^{-2} during night and 510 W m^{-2} during day), while variations in the forest are significantly smaller (410 W m^{-2} during night and 460 W m^{-2} during day). To put it another way, the clearing shows during the night an enhanced cooling compared to the forest and during day an enhanced warming. The shadowing effect of the forest edge in the morning, like it was found for the short-wave downwelling radiation (Figure 3.4a), has also an effect on the long-wave downwelling radiation. The heating of the ground starts significantly earlier at the clearing than near the forest edge. After noon, the effect is no longer discernible and the values along the transect forest edge to clearing are almost the same, with the highest variations at the forest edge. This may indicate the presence of advective conditions mainly from the clearing towards the forest edge with enlarged convective conditions directly at the forest edge, like it was found in Eder et al. (2013) for the EGER IOP3 project. Eder et al. (2013) presumed also the presence of secondary circulations. Both will be investigated in detail in Section 3.4.1.

Figure 3.5a shows the diurnal variation of the temperature measurements. The temperatures decrease during night and have their minimum in the early morning hours (03:00 to 06:00 CET; with $12.6 \text{ }^\circ\text{C}$ in the forest and $11.3 \text{ }^\circ\text{C}$ at the clearing), with a continuous decrease from the forest to the clearing. Additionally, in this time the variations are very small, but outliers indicate (i) the presence of fog during some days and (ii) the start of turbulent mixing. Caused by the earlier start of incident sunlight at the clearing, the temperature rises earliest at the clearing (06:00 to 09:00 CET) and the gradient is now reversed (highest values at clearing and lowest values in the forest). During day, the temperatures in the forest are $22.4 \text{ }^\circ\text{C}$ and at the clearing also $22.4 \text{ }^\circ\text{C}$, while the three locations in between have higher values, most of all the location at the clearing near the forest edge with temperatures of $23.9 \text{ }^\circ\text{C}$. As the location at the clearing is the least wind sheltered and in addition most humid, the lower temperatures are explainable. Aside from that, the forest line heats the area near the forest edge. During the evening (sun down), with decrease of turbulence, a relatively homogeneous temperature profile is discernible and afterwards a stronger cooling at the clearing. The relative humidity is presented in Figure 3.5b. During night the

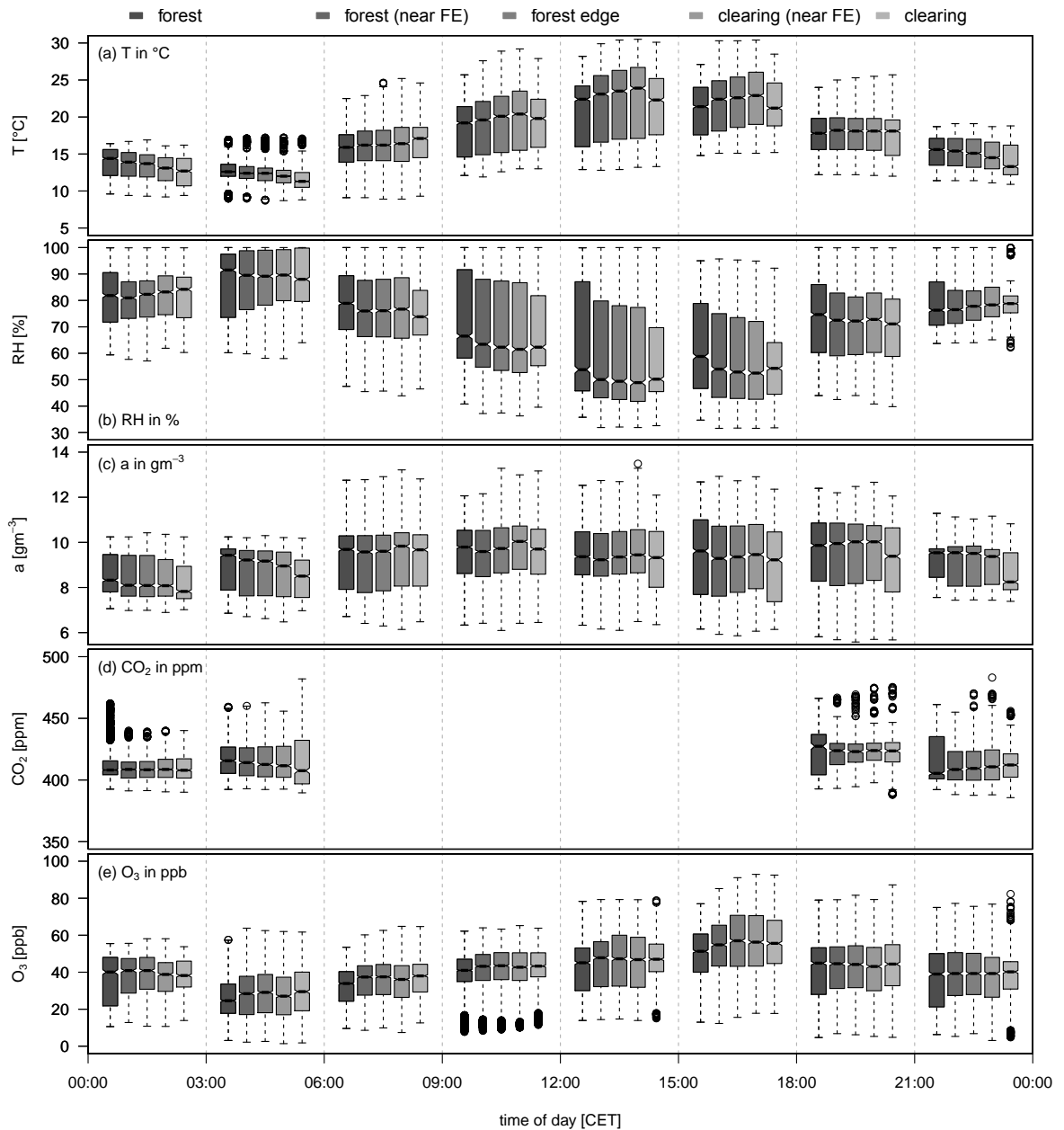


Figure 3.5. Diurnal variation of the temperature T (a) and humidity, shown as relative humidity RH (b) and absolute humidity a (c), CO_2 (d) and O_3 (e) concentrations, measured with the HMMS at five different locations: forest, forest (near forest edge/FE), forest edge, clearing (near FE) and clearing. Table 3.1 contains the exact bar code positions. The data was averaged at each location over 15 s per each run and afterwards these averages were averaged again in 3 h intervals. Data based on all completed runs during the three ‘Golden Day’ periods (Figure 2.3).

transect becomes more and more humid and reaches its maximum during the early morning with highest values in the forest (91.5 %). With sunrise the humidity starts to decrease

first at the clearing, but already during the period 09:00 to 12:00 CET, the locations near the forest edge are drier. Additionally, the absolute humidity is shown in Figure 3.5c. The profile along the five locations shows that absolute humidities are higher during night in the forest than at the clearing, caused by the more humid conditions in the forest (higher transpiration). The effect of sunrise can also be seen at first at the clearing, with an increase of the absolute humidity caused there by a higher transpiration. The highest values occur near the forest edge between 09:00 CET and 15:00 CET. Afterwards the faster cooling of the clearing is noticeable, since the absolute humidities decrease fastest at the clearing than in the forest. The findings for temperature and humidity may also, in addition to the radiation-induced higher temperatures at the forest edge, be an indication for advective conditions near the forest edge, since the highest temperatures and lowest humidities occur there during day.

Because of the radiation problems for the CO₂ concentration measurements (Figure 3.5d) named in Section 2.3.6 and 3.1, only values before sunrise and sundown were used for the analysis and because of that, no values are shown in the time between 06:00 CET and 18:00 CET. Also, between the times of 03:00 to 06:00 CET and 18:00 to 21:00 CET, the data basis is smaller compared to the other measured quantities. The found deviations (named in Section 3.1) for the comparison with fixed tower measurements calls into question how accurate the CO₂ measurements are. Nevertheless, the night time values do not show significant gradients between forest and clearing. This is attributable to stable conditions which are prevalent during evening, night and early morning, but the outliers during 00:00 to 06:00 CET mainly in the forest suggest the presence of coherent structures, where motions into the trunk space (sweeps) or motions out of the trunk space (ejections) change the CO₂ concentration. Another possibility for the decrease of CO₂ in the forest are low-level jets (LLJ; Section 3.4.2), or strong winds above the forest, leading to a decoupling situation, causing cold air drainage with CO₂ enriched air (Section 3.4.3). During 18:00 to 24:00 CET the outliers are mainly at the clearing, which indicate a later formation of a stable stratification caused by the intensity of the wind. The O₃ concentration in Figure 3.5e has, like the CO₂ concentration, only minimal deviations/gradients along the total measurement transect during the night. During daytime the concentration differences are also very small (at clearing only 3 – 4 ppm higher than in the forest). The significant gradient between forest and clearing, like it was found for the 28 June 2011 in Figure 3.21h is the result of the good weather conditions during this day. The formation of ozone is mainly a sun-induced photochemical reaction: $\text{NO}_2 + \text{O}_2 \xrightarrow{h\nu} \text{NO} + \text{O}_3$, but because ozone is a reactive gas, there also exists a back reaction: $\text{NO} + \text{O}_3 \longrightarrow \text{NO}_2 + \text{O}_2$

(Dlugi, 1993; Foken et al., 1995). During day (high radiation) and mainly in rural areas (less exhaust gases), there is a surplus of ozone possible, since the reaction times of typical chemical reactions are in the order of $10^1 - 10^4$ s and therefore in the range of the turbulent transport. A precise statement of transport and gradients arising thereof can only be made when the Damköhler numbers Da are investigated, which is the ratio between transport and reaction time (Molemaker and Vilà-Guerau de Arellano, 1998). For an exact investigation of Da , several measurements along a transect have to be made under the assumption of isotropic turbulence (Foken et al., 1995). Therefore, advective transport must be either excluded or exactly measured. Because of this difficulty, the statement drawn above is only an assumption. Figure 3.5e presents analyses, where such obvious gradients between the locations are averaged out.

Appendix C.1 contains additional averaged variations of time series of the turbulent influenced quantities (temperature, humidity and trace gases), regarding different wind directions (Appendix C.1.1), and additionally including a breakdown of different stability parameters (Appendix C.1.2) and friction velocities (Appendix C.1.3).

3.2.2. Horizontal distribution of turbulent structures

The horizontal distribution of turbulent structures is shown along two different transects. The transect perpendicular to the forest edge with the towers M1 (M2/M8) – M3 – M4. In each case the top heights were equipped with 3D sonic anemometers and with optical gas analysers, while the lowest heights (M1 was not equipped within the canopy and consequently the measurements from M2 as well as from M8 were taken) were only equipped with 3D sonic anemometers. At the transect M1 – M3 – M4, measurements of the available energy were conducted. Another transect parallel to the forest edge with the towers M6 – M3 – M7 was also equipped with 3D sonic anemometers and optical gas analysers (only in top heights), while at the towers M6 and M7 no energy measurements were available. Section 2.2.2 comprises measuring heights and used equipment for the turbulent flux measurements (sensible Q_H and latent Q_E heat flux, as well as trace gas fluxes) and Section 2.2.4 comprises the measurements of the available energy (net radiation Q_S^* and ground heat flux Q_G ; additional, for the forest the storage heat flux Q_B was calculated, Section 2.4.4). The determination of the available energy at the forest edge tower M3 was more problematic (mainly in the top height at 41 m) than at M1 (forest) and M4 (clearing), as the available energy consists of a part resulting from the forest and a part resulting from the clearing. In addition to advection, the distribution can vary here significantly depending on the prevailing wind direction and the resulting footprint. Furthermore, a stability

depending variation in the footprint, and thus, a variation in the available energy could not be taken into account since exact footprints for the forest edge were not calculated. Because of the transition from forest to clearing, the fluxes are strongly influenced by sudden changes in horizontal pressure gradients associated with changes in thermal and mechanical turbulence and consequently, common footprint models will encounter their limits (Leclerc and Foken, 2014). Only high-order closure models (e.g. large-eddy simulations) can properly quantify the effect of forest edges (roughness step-changes) on flux footprints (e.g. Leclerc et al., 1997; Sogachev et al., 2004, 2005; Klaassen and Sogachev, 2006; Belcher et al., 2008; Steinfeld et al., 2008; a comprehensive overview of footprint (models) is given in Leclerc and Foken, 2014). Because of this, the footprint, and thus, the distribution of available energy at the forest edge tower M3 at 41 m could only be estimated. Therefore, the following assumptions for the distribution of the available energy were made depending on the wind sector, which are equivalent to the four used sector-wise planar-fit sectors at the forest edge (Figure 2.9):

330 – 90° (Forest): 80 % Forest & 20 % Clearing

90 – 150° (Forest Edge Sector East): 50 % Forest & 50 % Clearing

150 – 270° (Clearing): 20 % Forest & 80 % Clearing

270 – 330° (Forest Edge Sector West): 50 % Forest & 50 % Clearing

In other words, if the prevailing wind direction comes from the forest (more or less northerly winds) the distribution of available energy lies towards the forest and when the wind comes from the clearing (more or less southerly winds), the distribution is reversed. From the sectors along the forest edge (easterly and westerly winds) an equal distribution is adopted. To calculate the available energy, the measurements at M1 (forest) and at M3-South (clearing) were taken. In Appendix C.2.1 different percentage distributions are discussed.

Figure 3.6 shows the observed energy fluxes along the transect perpendicular to the forest edge M1 (M2/M8) – M3 – M4 averaged over all three ‘Golden Days’ periods (Table 2.2). The figures on the left side (Figures 3.6a, 3.6c, 3.6e) show the top heights of the energy flux measurements, whereas the figures on the right side (Figures 3.6b, 3.6d, 3.6f) show the lowest heights. A closer look into the top heights of the flux measurements shows that the net radiation is highest above the forest and decreases towards the clearing, whereas the forest edge (Figure 3.6c) has almost identical values (on average only 2.5 % or 5 W m^{-2} smaller than in forest). There, the effect of the calculated distribution (mentioned above) is obvious, if compared to the net radiation measurements

at M3 in 2.25 m (Figure 3.6d) – for which the measurements of M3-South were taken –, which are on average 20 % or 30 W m^{-2} smaller than at 41 m. So in other words, at the forest edge top level, a greater percentage of the net radiation (and hence higher available energy) results from the forest than from the clearing. The sensible Q_H and latent Q_E heat flux, on the other hand, are during daytime highest at the forest edge, despite of the higher available energy above the forest. Mainly, the latent heat flux is significantly higher at the forest edge (max: 280 W m^{-2}), than above the forest (max: 180 W m^{-2}) and the clearing (max: 200 W m^{-2}), while the differences in the sensible heat flux are smaller (M1: 220 W m^{-2} ; M3: 230 W m^{-2} ; M4: 150 W m^{-2}). Ground heat flux Q_G and storage heat flux Q_B (only calculated for M1) are, at all locations, very small (maximum at M3-South with approximately 30 W m^{-2}). The measurements in the lowest levels (on the right side of Figure 3.6) show a comparable behaviour as the measurements at the top levels. While the measurements of sensible and latent heat flux are very small within the trunk space of the forest ($< 20 \text{ W m}^{-2}$; Figure 3.6b), they are highest at the forest edge (approximately 200 W m^{-2} both). Also the available energy is highest at the forest edge.

There is a time lag in the onset of net radiation and heat fluxes of more than 2 h between clearing (M4) and forest edge (M3), which was also found in the short-wave radiation measurements of the HMMS shown in Section 3.2.1, more precisely Figures 3.4a and 3.4b, caused by the shading of the forest edge. The shading leads to an abrupt increase of available energy at the forest edge, which results in a very fast increase of the residual Res at 2.25 m, since the onset of turbulent heat fluxes is delayed. After onset the residual at the forest edge at 2.25 m is very low. Sometimes the energy balance is closed and more than closed. The daily mean residual at the forest edge is approximately 17 % (also for 41 m), while above the clearing and the forest, a residual of 25 – 30 % was calculated, which is a typical range for residuals for such a landscape, like it is shown in Foken (2008b). The smaller residual, or respectively the better closed energy balance at the forest edge might be an indication for thermal updraft near the forest edge which contributes to higher turbulent fluxes and probably to the development of secondary circulations during the daytime, which were supposed by Eder et al. (2013) for the experimental site. A brief summary of the results found by Eder et al. (2013) is given in Section 3.2.3 for the coupling regimes and horizontal distribution of coherent structures. Section 3.4.1 contains a detailed investigation of the residual at the forest edge using all important measurements.

Figure 3.7 shows the net radiation and soil heat flux measurements conducted at M3-North. Since the measurements were located in the first metres of the forest, the heat flux measurements at M3 could not be used here. The net radiation measurements illustrates

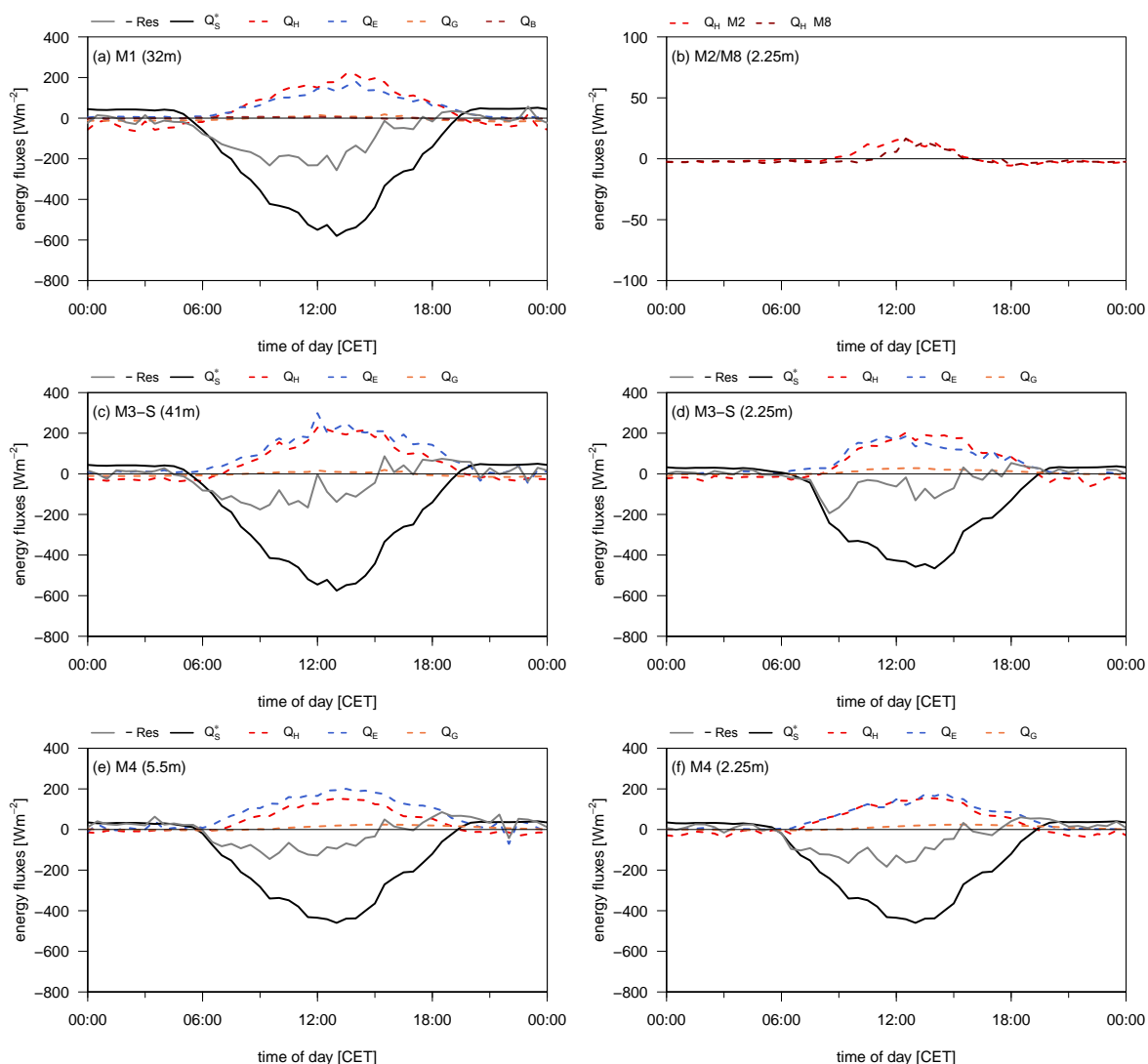


Figure 3.6. Mean diurnal cycles of the observed energy fluxes along the transect perpendicular to the forest edge for all days of the three ‘Golden Day’ periods (a total of 13 days; see Table 2.2). Measurements were performed above the forest at M1 (a), within the forest at M2/M8 (b), at the forest edge (M3 - South) at two different heights (c,d) and at the clearing (M4) at two different heights (e,f). Remark: The scaling of the y-axis in (b) is different compared to the other graphs.

the heterogeneity of the forest, which was also found in the radiation measurements of the HMMS (Section 3.2.1). The soil heat flux has a delayed reaction to the increase of the net radiation.

Figure 3.8 shows the measurements of the masts M6 (Figure 3.8a) and M7 (Figure 3.8b), which form, together with M3, the transect parallel to the forest edge. The measurements do not show notable differences along the transect and both masts have values which

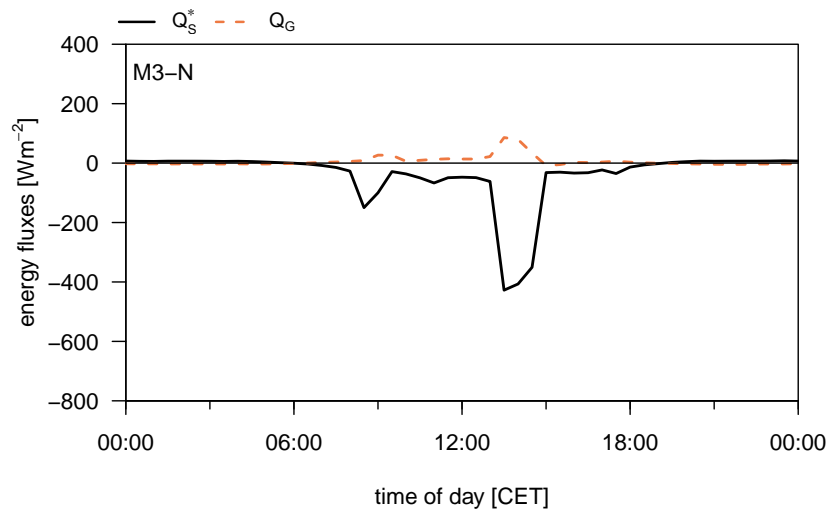


Figure 3.7. Mean diurnal cycles of the observed energy fluxes near the forest edge within the forest (M3-North) for all days of the three ‘Golden Day’ periods (a total of 13 days; see Table 2.2).

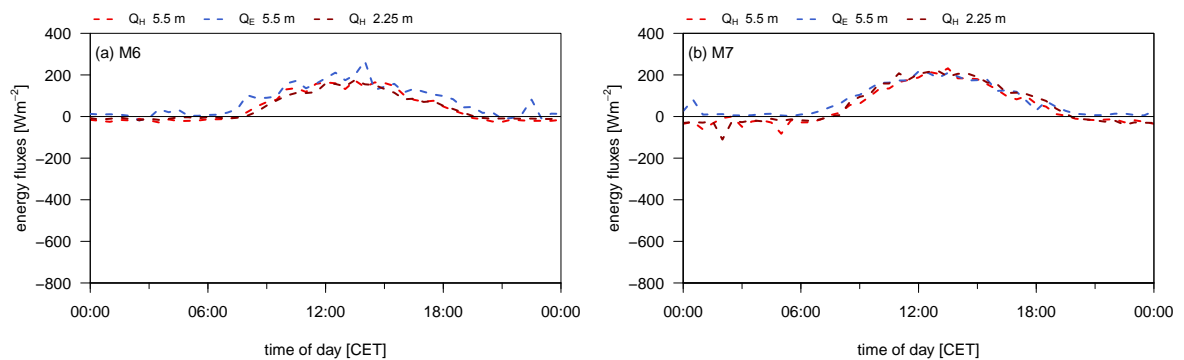


Figure 3.8. Mean diurnal cycles of the observed energy fluxes along the transect parallel to the forest edge for all days of the three ‘Golden Day’ periods (a total of 13 days; see Table 2.2). Measurements were performed at M6 (a) at two different heights and at M7 (b) at two different heights. The measurements of M3 (2.25 m) which are part of the transect are already presented in Figure 3.6d.

are comparable to the measurements at 2.25 m at tower M3 (Figure 3.6d). As for these locations no measurements of available energy exists, the transect is of more importance for the investigation of horizontal coupling regimes (Section 3.2.3) than it is for the energy fluxes. The coupling regime of this transect is, for example, a good indication of nighttime cold drainage, which was found in the HMMS measurements and investigated in detail in Section 3.4.3.

Figure 3.9 shows the net ecosystem exchange (NEE) of CO_2 for the transect perpendicular to the forest edge, with measurements at M1 above the forest, forest edge (M3) at two

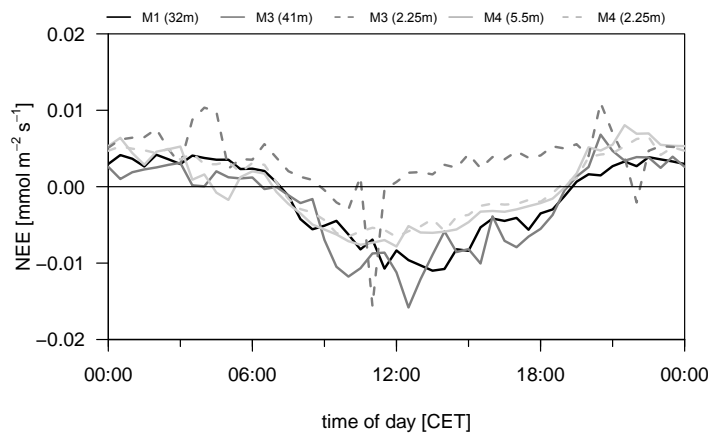


Figure 3.9. Mean diurnal cycles of observed CO₂ net ecosystem exchange (NEE) along a transect perpendicular to the forest edge with towers M1 – M3 – M4 (latter two in different heights) for all days of the three ‘Golden Day’ periods (a total of 13 days; see Table 2.2).

heights and at the clearing (M4) also at two heights. Most locations show a daily cycle, with positive fluxes in $\text{mmol m}^{-2} \text{s}^{-1}$ during nighttime (respiration) and negative fluxes during daytime (assimilation), as is normal. However, the daily cycle at M3 at 2.25 m is extremely weak compared to the other locations. While the respiration during night barely differs from the other locations, there is a significant difference during day because, for the most time the fluxes are also positive. The reason for this is the high amount of deadwood in the vicinity of M3 and the elevated wood chips to cover the forest path along the forest edge. Since the mean wind flow corresponds with the orientation of the forest edge, the footprint has therefore a high amount of non-assimilating deadwood, which in fact respire CO₂ leading to a positive flux near the ground. The flux during daytime at M3 at 41 m fluctuates the most, which is an indication for thermal updraft and secondary circulations near the forest edge, which is investigated in detail in Section 3.4.1. The transect parallel to the forest edge is neglected, since the energy fluxes in Figure 3.8 do not show much variations compared to each other and here it is the same.

3.2.3. Horizontal distribution of coherent structures and coupling regimes

Coherent structures play an important role, especially in the exchange processes of forest ecosystems (contribution to the total flux: 20 – 30 %, up to 50 % during nighttime), therefore it is absolutely essential to analyse coherent structures. The analysis of coherent structures and also of coupling regimes was performed by Eder et al. (2013) for the EGER IOP3 project.

A short illustration of the used methods and different coupling regimes is presented in Section 2.4.3. In this section the results found by Eder et al. (2013) are briefly summarised and discussed. Beside the contribution of the coherent structure flux to the total flux, the flux contribution of sweeps and ejection events was determined. Additionally, the coupling regimes (Section 2.4.3) were investigated. While in case of vertical coupling the regimes were investigated at one location at different measuring heights, in the case of horizontal coupling the regimes are investigated at different locations at the same measuring heights (along the transects perpendicular and parallel to the forest edge).

In Figure 3.10 the vertical coupling was investigated in a daily cycle for two different locations, within the forest at M2 (Figure 3.10a) and at the forest edge at M3 (Figure 3.10b). According to the coupling regime classifications, five different regimes were considered: wave motion (Wa), decoupled canopy (Dc), decoupled sub-canopy layer (Ds), coupled sub-canopy layer by sweeps (Cs), and fully coupled canopy (C); a detailed description of the regimes is given in Section 2.4.3. Since measuring data at 27 m height at M3 is only available up to 2 July 2011, the vertical coupling regimes were analysed only for the time period between 21 June and 2 July 2011 (Eder et al., 2013). At both sites there is a clear daily variation observable, with a higher amount of decoupled situations during nighttime and more frequent coupled situations during daytime. Due to low friction velocities ($u_* < 0.5 \text{ m s}^{-1}$) and stable stratification, the decoupled situations are more often during nighttime, but nevertheless, there are also coupled situations during the night. However, during daytime, the fully coupled situations (C and Cs) are more frequent at both locations. The daily cycle is typical for the forest site ‘Waldstein-Weidenbrunnen’ and was already documented by Thomas et al. (2006), Serafimovich et al. (2011b) and Foken et al. (2012b). A closer look at the differences of both sites shows in the morning and late afternoon a well coupled forest site (Figure 3.10a), while the forest edge (Figure 3.10b) is not well coupled. This indicates a more stable stratification at the forest edge caused by a higher cooling at the clearing/forest edge (M3) compared to the forest (M2). The temperature differences can be confirmed by the measurements of the HMMS (Figure 3.5a). Additionally, the later onset of radiation at the clearing, and as a consequence, later warming prevents an earlier breakup of the stable stratification, which in turn prevents coherent structures that can propagate vertically in the morning hours (Eder et al., 2013). Between 15:00 to 18:00 CET the regime Ds (decoupled sub-canopy) dominates at M2, which was also found for the former IOPs of the EGER project (Foken et al., 2012b). This is caused by an oasis effect, leading to a fast development of stable stratification. This effect could not be observed for the forest edge because of the prevailing drier conditions there and as a consequence longer lasting

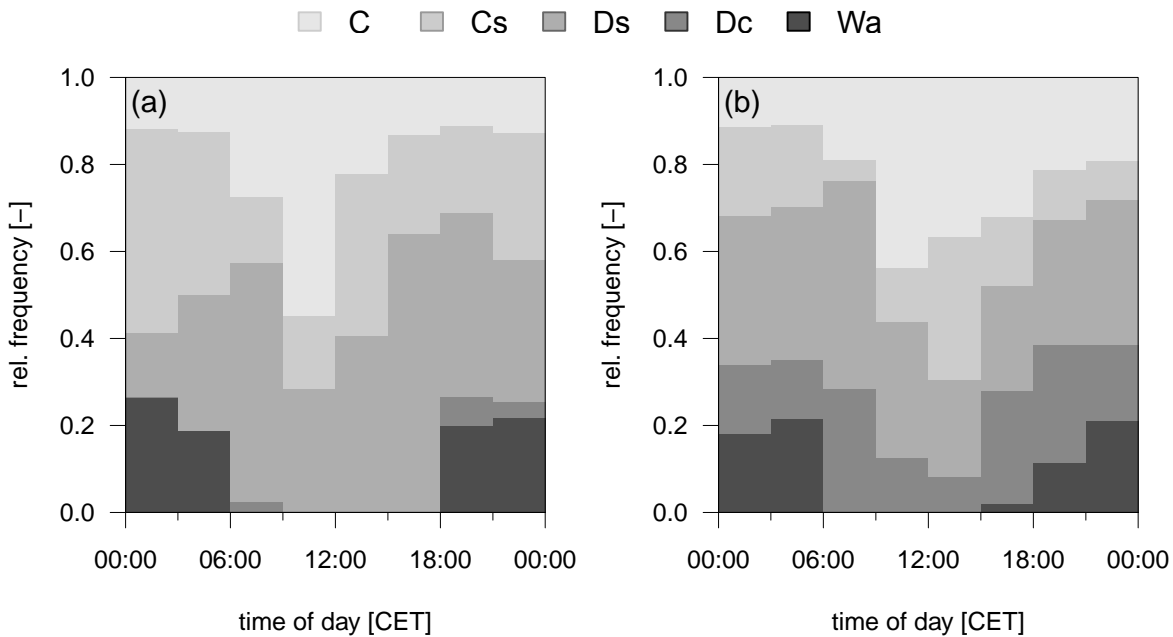


Figure 3.10. Diurnal cycle of relative frequency of vertical coupling regimes within the forest at M2 (a) and at the forest edge tower M3 (b). For this investigation only the data between 21 June 2011 and 02 July 2011 was used (modified from Eder et al., 2013).

vertical coupling. Indeed, the vertical coupling over the total profile (C and Cs) is at the forest edge (36.4%) less frequent than at the forest site (48.9%), and at M3 there is a large number of Dc situations detected, which is detected rarely within the forest. To conclude this, the vertical coupling mechanism at the forest edge is not dominated by structures that evolve from the mixing layer like in the case of the forest site (Eder et al., 2013).

The analysis of the horizontal coupling regimes according to Serafimovich et al. (2011b), with four different regimes, C_h : complete coupling, C_h/D_{c_h} : first two towers coupled but second and third tower decoupled, D_{c_h}/C_h : first two towers decoupled but second and third tower coupled, D_{c_h} : complete decoupling, was performed along the two transects (Eder et al., 2013). One transect perpendicular to the forest edge (M8 – M3 – M4) and the other parallel to the forest edge (M6 – M3 – M7) and both are shown in Figure 3.11. Except for some nighttime data, a horizontal coupling along the transect parallel to the forest edge (Figure 3.11a) was always observed (86% of all 30 min averaged data), while perpendicular to the edge (Figure 3.11b) the forest is only in a few cases coupled with the clearing (16% of all 30 min averaged data). This contribution is based upon two remarkable differences between the two transects: (i) the transect parallel to the forest edge has very few obstacles (trees), which facilitates the propagation of coherent structures, and (ii) the mean wind flow corresponds with the orientation of the transect M6 – M3 – M7. A daily

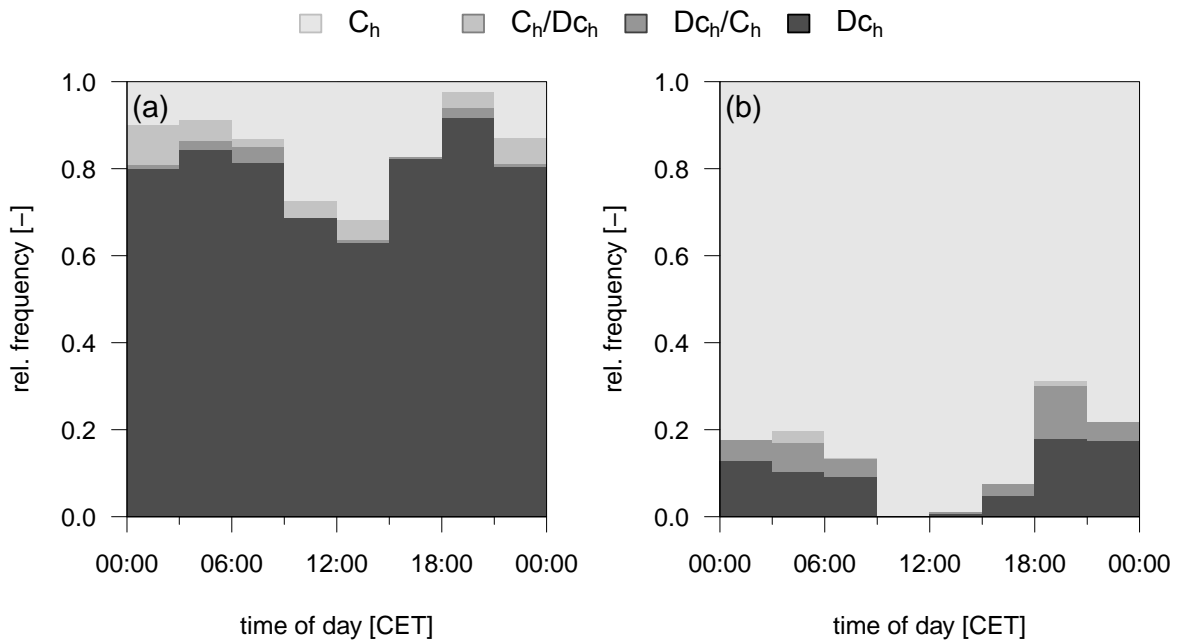


Figure 3.11. Diurnal cycle of relative frequency of horizontal coupling regimes along the transect perpendicular to the forest edge M8 – M3 – M4 (a) and parallel to the forest edge M6 – M3 – M7 (b). The measurement heights were at 2.25 m. For this investigation data from the whole measurement period (13 June 2011 till 26 July 2011) was used (modified from Eder et al., 2013).

cycle can be recognised along both transects with a larger amount of horizontally coupled situations during daytime and decoupling during nighttime. Eder et al. (2013) also found a relationship between vertical coupling at the forest edge tower and the horizontal coupling along both transects, but the wind direction has no significant influence on horizontal coupling regimes. Furthermore, they observed that the decoupling situations during night parallel to the forest edge is mainly caused by drainage flows, but this drainage is not necessarily associated with coupling along the transect perpendicular to the forest edge. Eder et al. (2013) concluded that this flow should be regarded as a quasi-laminar mass flow associated with insufficient mixing, which could be confirmed by the HMMS measurements (Section 3.2.1 and 3.4.3).

The relative flux contribution of coherent structures F_{CS} to the total turbulent fluxes F_{tot} of momentum $\overline{u'w'}$, buoyancy $\overline{w'T'_s}$, carbon dioxide $\overline{w'c'}$, and latent heat $\overline{w'q'}$ is presented in Figure 3.12. At the top heights the contribution of F_{CS}/F_{tot} decreases from the forest to the clearing (Figure 3.12a). The percentage contribution above the forest canopy is 24 – 29 % and above the clearing and the forest edge it is only 19 %. While coherent structures contribute almost the same to buoyancy, carbon dioxide and latent heat flux, the contribu-

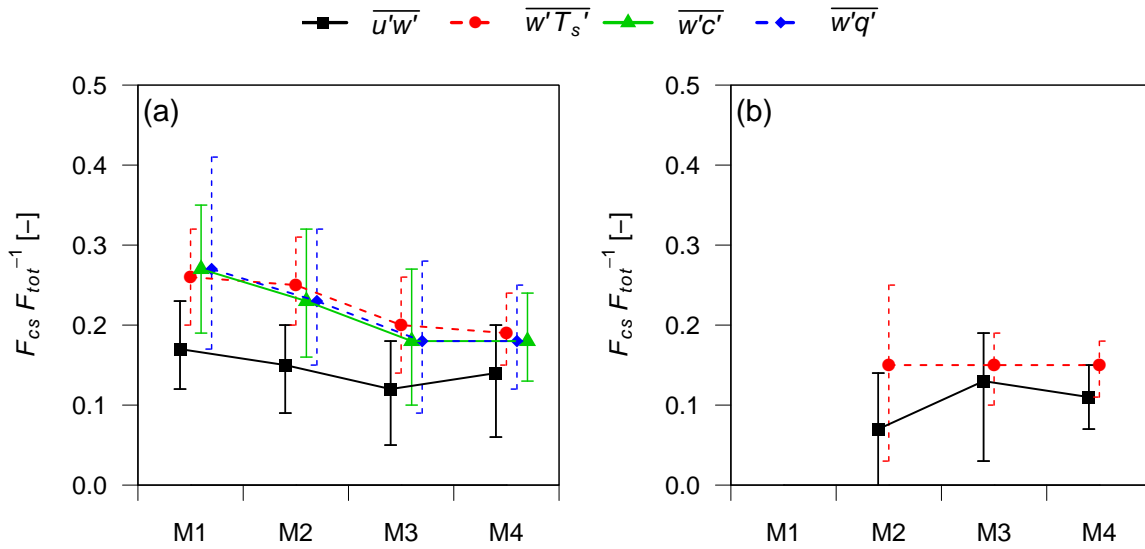


Figure 3.12. The relative flux contribution of coherent structures F_{CS} to total fluxes F_{tot} of momentum $\overline{u'w'}$, buoyancy $\overline{w'T'_s}$, carbon dioxide $\overline{w'c'}$, and latent heat $\overline{w'q'}$ along the transect perpendicular to the forest edge with towers M1 – M4. Measurements at top heights (M1: 32 m, M2: 36 m, M3: 41 m, M4: 5.5 m) are presented in (a) and in (b) the measurements were taken at 2.25 m. The symbols mark sample medians and error bars represent interquartile ranges (modified from Eder et al., 2013).

tion to momentum flux is less, which is confirmed by the results of Barthlott et al. (2007), Thomas and Foken (2007b) and Serafimovich et al. (2011b). The contribution of F_{CS}/F_{tot} is also very similar to results from former studies at the ‘Waldstein-Weidenbrunnen’ site (Thomas and Foken, 2007b; Serafimovich et al., 2011b). In general, the contribution of coherent structures to vertical exchange is smaller at the forest edge and at the clearing than above the forest. This might be explainable by the spatial distance of M3 to the forest canopy, because the maximum contribution of coherent structure is near to the canopy where most of the foliage is situated (Serafimovich et al., 2011b; Eder et al., 2013). There is every likelihood that the captured structures (originating from the mixing layer) are not the dominant transport mechanism at the forest edge, but rather the coherent flux is dominated by other mechanisms, like secondary circulations (Zhang et al., 2007). At the lowest measuring level (Figure 3.12b), the contribution of coherent structures to the turbulent fluxes is less than at the top levels of the respective measurement tower.

In Figure 3.13 the daily cycles of the ejection contribution to coherent transport F_{ej}/F_{CS} of momentum $\overline{u'w'}$, buoyancy $\overline{w'T'_s}$, carbon dioxide $\overline{w'c'}$, and latent heat $\overline{w'q'}$ are presented along the transect perpendicular to the forest edge with towers M1 – M4 at top heights. If one looks now at the daily variations, there is a discernible pattern in all four different

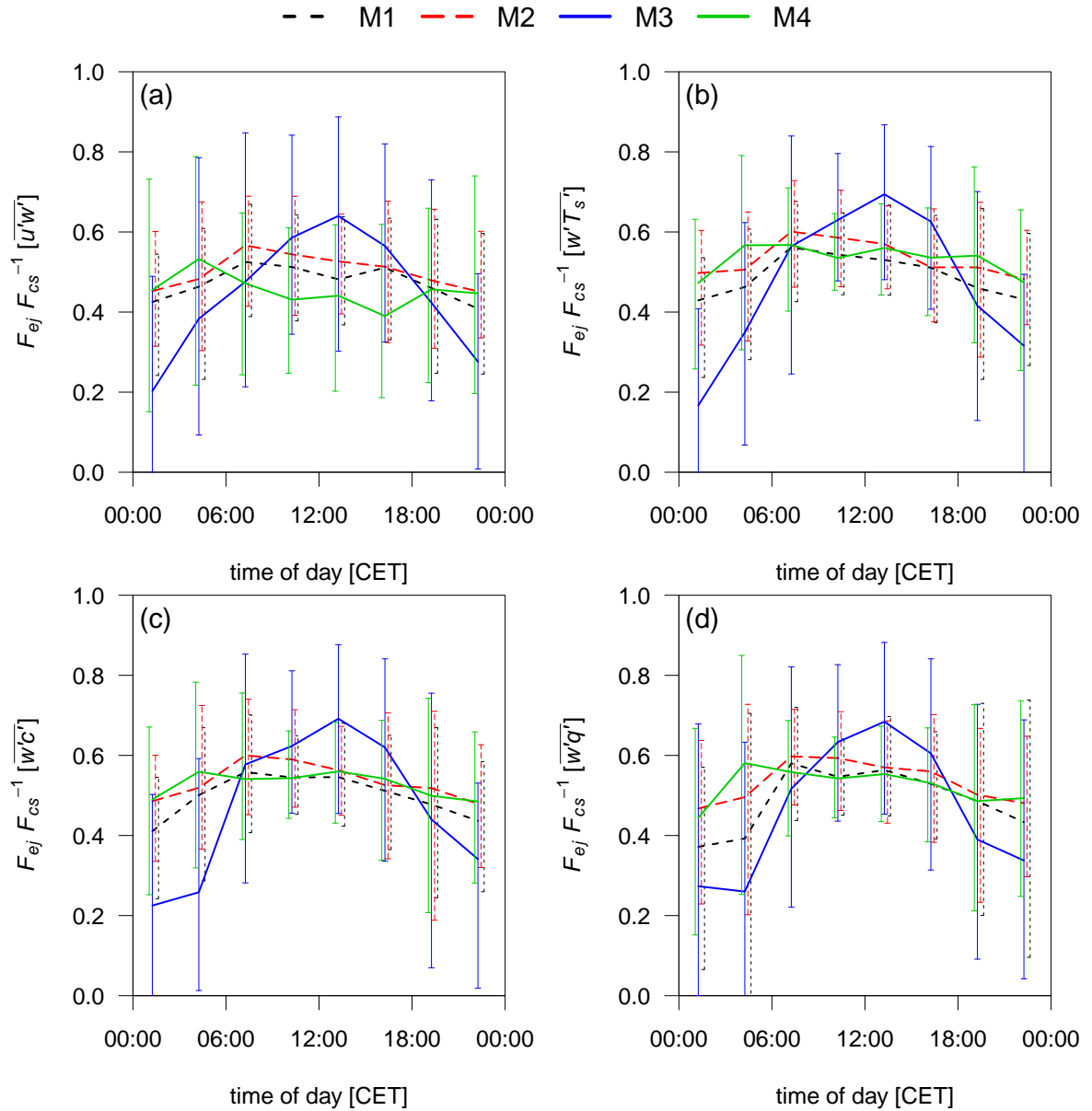


Figure 3.13. Daily cycle of the ejection contribution to coherent transport F_{ej}/F_{CS} of momentum $\overline{u'w'}$ (a), buoyancy $\overline{w'T'_s}$ (b), carbon dioxide $\overline{w'c'}$ (c), and latent heat $\overline{w'q'}$ (d) along the transect perpendicular to the forest edge with towers M1 – M4 at top heights. 3 h averages were calculated from medians of 30 min data and error bars represent interquartile ranges (modified from Eder et al., 2013).

fluxes, which attract attention: while the contribution above the forest (M1 and M2) and the clearing (M4) show a weakened variation during day, there is an obvious detectable change of the contribution only at the forest edge (M3). Here, the coherent flux is mainly dominated by sweeps during night and by ejections during day. This pattern strengthens

the assumptions of thermal updraft and the enhanced turbulent fluxes during day (made for the turbulent structures in Section 3.2.2). During night, the stronger cooling of the clearing induces an increased presence of sweeps at the forest edge. The thermal variations between the clearing and the forest is the driving force at the forest edge and the circulation modulates then again the coherent structures. Eder et al. (2013) could also show, that the daily variation is also weakened discernible in 2.25 m at the forest edge, which suggests that the secondary circulations reach the ground. This could be also reinforced by the measurements of energy fluxes in Section 3.2.2 and will therefore be studied in detail in Section 3.4.1. As this phenomena was not discernible in 5.5 m at the clearing, it can be assumed that this is restricted to the vicinity of the forest edge. Furthermore, Eder et al. (2013) investigated the structures at the forest edge, depending on different wind directions with two main results: (i) there are discernible differences of the ejection contribution to coherent transport F_{ej}/F_{CS} , depending on the wind direction, but (ii) there was no discernible dependence of the wind direction on the time of day meaning that the dominance of the ejections during day and sweeps during night are not explainable by the flow distortion and this is a further indication for a secondary circulation above the clearing.

3.2.4. Stand-scale modelling of the energy and matter exchange

The energy and matter exchange was modelled by the third-order closure model ACASA (Pyles et al., 2000), following the first investigation by Staudt et al. (2011) for IOP1 and IOP2. In Section 2.4.5 a brief summary of the model development and adaptation for EGER IOP3 is given, which was done within the scope of the master thesis of Gatzsche (2013). Additionally, both methods to close the energy balance for the measured energy fluxes is given in Section 2.4.5.

ACASA model runs were conducted the forest (M2) and the clearing (M4), both with individual forcing parameters. For the clearing, six different model runs were done for the six dominating species, which are: *Deschampsia*, *Picea abies*, *Vaccinium*, *Calamagrostis*, *Juncus* and deadwood (see Table 2.1 for ground cover and Table B.2 for model parameters). To compare modelled data with measured data, the results from the individual modelled species runs were combined by utilising a footprint-dependent tile approach. In Gatzsche (2013) a uniform distribution of the species over the clearing was assumed, neglecting a wind direction dependent change of the species composition. A subsequent consideration of the species composition depending on the wind direction on the basis of a land-use matrix and footprint analysis, performed in 2014, showed no substantial improvements in the model and therefore the results from Gatzsche (2013) for the individual species Net Eco-

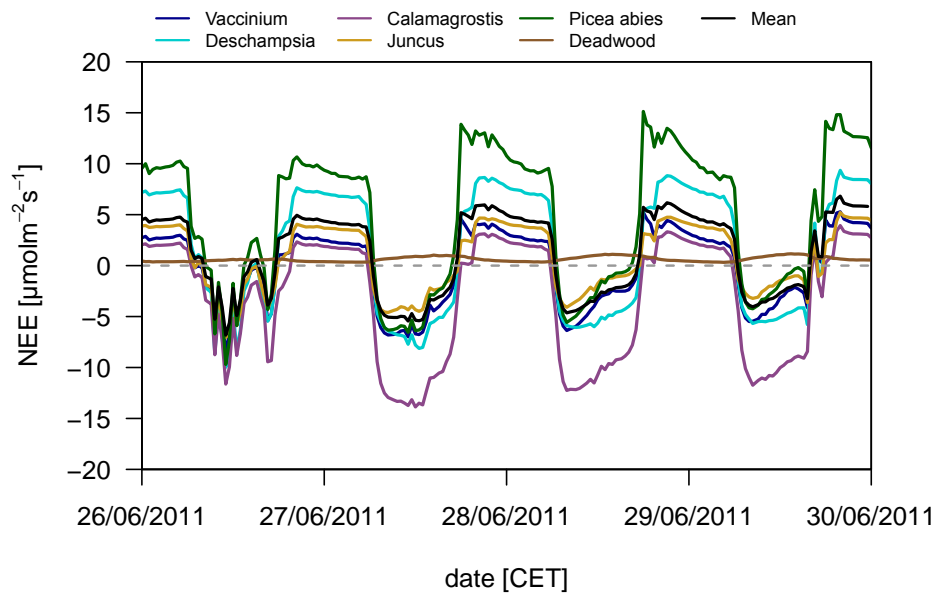


Figure 3.14. Modelled Net Ecosystem Exchange (NEE) for six different land cover types of the clearing for the first ‘Golden day’ period (GDP1; 26 to 29 June 2011). The mean is an averaged tile approach of the land cover distribution of the whole clearing (modified from Gatzsche, 2013).

system Exchange (NEE) and the combined NEE are shown in Figure 3.14. All species show a typical daily variation with positive fluxes during nighttime (respiration) and negative fluxes during daytime (assimilation). Only the deadwood respire all day long. Furthermore, it was found for the deadwood that the sensible heat flux is lowest and the latent heat flux highest compared to the other species (results not shown).

To validate the simulated sensible and latent heat fluxes, the model results are compared to measured eddy-covariance fluxes. Therefore, the measured fluxes were energy balance closure corrected according to the two methods named in Section 2.4.5. The results are shown in Figure 3.15. For both locations (forest and clearing) the modelled sensible heat flux $Q_H^{modelled}$ shows better accordance with the buoyancy flux corrected data (Q_H^{EBC-HB}) than with the Bowen ratio corrected data (Q_H^{EBC-Bo}). During nighttime both methods show similar deviations, due to the limitations of both methods (energy fluxes greater than 10 W m^{-2} , which is often not the case during nighttime). The latent heat flux (Q_E) shows a comparable behaviour to the sensible heat flux, with greater deviations during daytime, but a better accordance (smaller relative deviations) with the Bowen ratio method (Q_E^{EBC-Bo}) than the buoyancy flux method (Q_E^{EBC-HB}), and because of the method limitations during nighttime both methods have similar deviations. In general, the ACASA model shows a better accordance for Q_H than for Q_E .

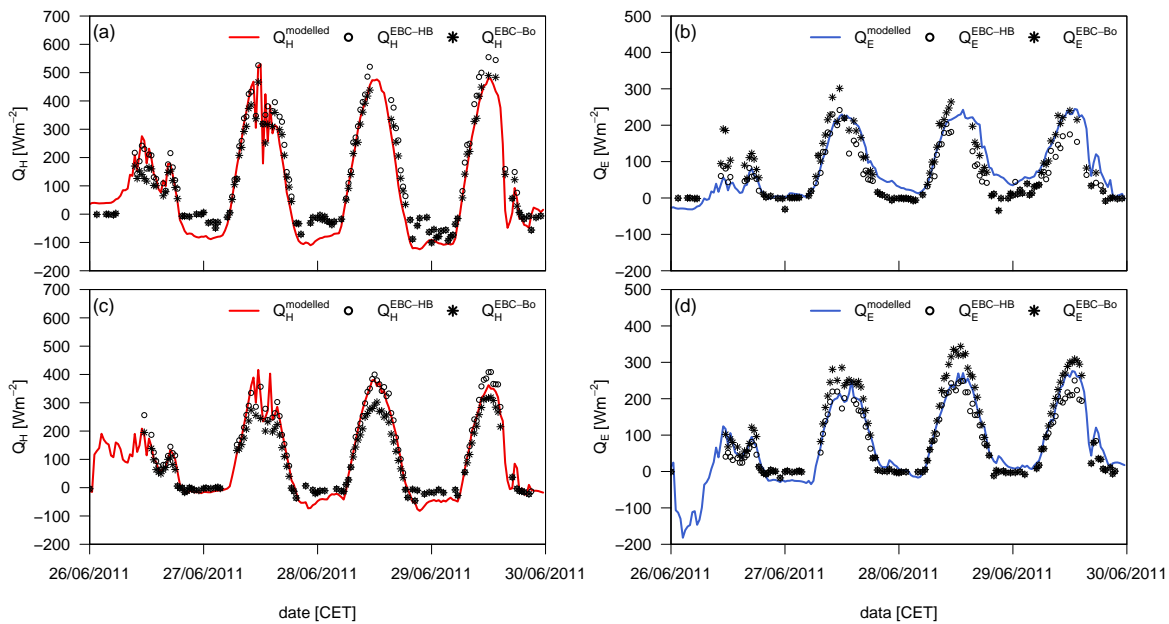


Figure 3.15. Comparison of modelled and measured sensible (a,c; left) and latent (b,d; right) heat fluxes for the first ‘Golden day’ period (GDP1; 26 to 29 June 2011). Comparison was performed above the spruce forest (a,b; M2 36 m) and at the clearing (c,d; M4 2.25 m). The measured fluxes were energy balance closure corrected according to the Bowen ratio method (EBC-Bo) and the buoyancy flux method (EBC-HB). The modelled data were simulated with a footprint dependent tile approach (modified from Gatzsche, 2013).

The net ecosystem exchange (NEE), presented in Figure 3.16, is significantly higher in the forest than at the clearing due to the high amount of deadwood and dead grass. These do not assimilate CO_2 , quite the reverse, they are a CO_2 source (see Figure 3.14). Additionally, the leaf area index (LAI) of the forest is with $5 \text{ m}^2 \text{ m}^{-2}$ significantly higher than at the clearing ($3.4 \text{ m}^2 \text{ m}^{-2}$). In comparison, the measured and simulated NEE show a better accordance at the clearing than in the forest and the Bowen ratio corrected ($NEE^{\text{EBC-Bo}}$) show smaller relative deviations than the buoyancy flux corrected results ($NEE^{\text{EBC-HB}}$). This is explainable, since the NEE was corrected by a ratio of corrected and uncorrected Q_E , and there, the Bowen ratio method has also smaller deviations.

The third-order closure of the ACASA model show a good performance regarding different coupling regimes and the representativeness of fluxes caused by coherent structures. Deviations found between measured and simulated fluxes above the forest, during night and during decoupled sub-canopy situations, as well as deviations at the clearing during day and coupled situations are also an indication for secondary circulations. Secondary circulations can not be captured adequately by the eddy-covariance method, and therefore, are not considered in the ACASA model.

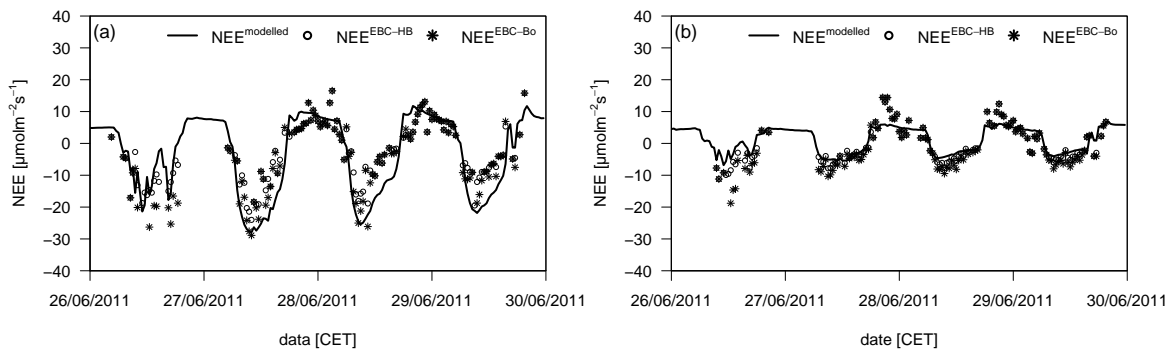


Figure 3.16. Comparison of modelled and measured NEE for the first ‘Golden day’ period (GDP1; 26 to 29 June 2011). Comparison was performed above the spruce forest (a; M2 36 m) and at the clearing (b; M4 2.25 m). The measured NEE was energy balance closure corrected according to the Bowen ratio method (EBC-Bo) and the buoyancy flux method (EBC-HB). The modelled data were simulated with a footprint dependent tile approach (modified from Gatzsche, 2013).

3.3. Characterisation of vertical structures at the forest edge

Additional to the investigation of the horizontal structures (Section 3.2), a brief characterisation of the vertical structures at the forest edge is given with the aid of the CO_2 profile measurements (Section 3.3.1) and the temperature and wind profile (Section 3.3.2) at the tower M3. The measurement heights and devices are presented in Section 2.2.3.

3.3.1. Vertical CO_2 profile

The CO_2 profile system was installed at the tower M3 at 8 different heights (Section 2.2.3) and measurements were started at 01 July 2011 up to the end of the EGER IOP3 project, with dropouts of several hours to a maximum of one day during the period. Thus, the profile is available for ‘Golden day’ period GDP2 (not for 08 July 2011) and the full GDP3, but not for GDP1 (Table 2.2). Trace gas fluxes, as well as concentrations from CO_2 but also ozone (O_3) are good ‘tracers’ for coupling regimes and larger structures.

Figure 3.17 shows the averaged vertical CO_2 profiles of GDP2 and GDP3, with a half-hour averaged contour plot in Figure 3.17a, and three hour averaged profiles in Figures 3.17b to 3.17e. The symbols in Figures 3.17b to 3.17e mark sample medians and error bars represent interquartile ranges. In Figure 3.17a a clear daily cycle is obvious, with high values during night, and low values during day. During night the highest values occur in the levels up to 5 m, with the maximum at 2.25 m. In the upper trunk-space, canopy height and above canopy height, the profile is relatively well mixed, but the line for the average interval from

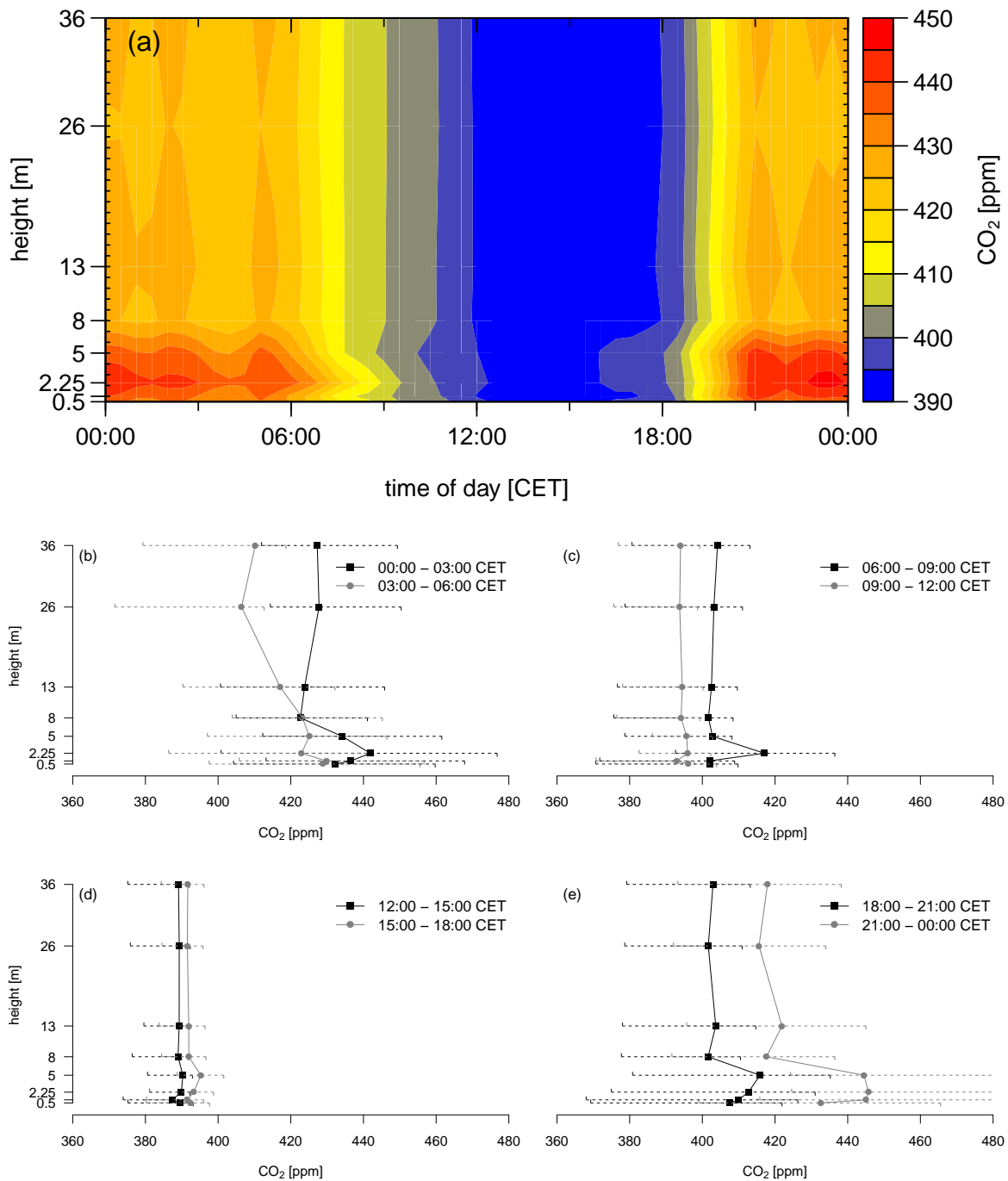


Figure 3.17. Averaged vertical CO₂ profile, installed at M3 at the stated heights (only the designation at 1 m is missed). Half-hour averaged data are presented as a contour plot (a) and three hour averaged data are presented as vertical profiles (b – e). The symbols in (b – e) mark sample medians and error bars represent interquartile ranges. Average period are the ‘Golden Day’ periods GDP2 (without 08 July 2011) and GDP3 (Table 2.2).

00:00 – 03:00 CET in Figure 3.17b shows at all heights a really high variation, with two maximum peaks. The mentioned maximum at 2.25 m and another one at canopy height (26 m). This can be explained by the highest respiration rate at canopy height and the lower maximum is caused by (i) highest biomass in the trunk-space and at the clearing with young spruces, (ii) nighttime cold-air drainage with CO₂ enriched air (in Section 3.4.3 discussed in detail) and/or (iii) a stable stratification during nighttime, which leads to an enrichment of CO₂ near the ground. The sweep dominated coherent flux found by Eder et al. (2013) (Section 3.2.3) may be the reason for a good mixing in the upper heights, but due to the stable stratification it does not reach the ground (no complete coupling situation). Later in the morning (03:00 – 06:00 CET and especially 06:00 – 09:00 CET) there is an abrupt and fast decrease of the CO₂ concentration (storage depletion), caused by the onset of radiation, turbulence and of course the onset of assimilation. This is very clear in Figure 3.17b for 03:00 – 06:00 CET, where both maximums turned into minimums. During daytime, the minimum at 2.25 m still exists, while the concentration above 8 m is perfectly mixed, since also the error bars in Figure 3.17c (09:00 – 12:00 CET) and both profiles in Figure 3.17d show a very similar range at these four heights. Looking at the time 12:00 – 15:00 CET in Figure 3.17a, a homogeneous concentration along the total profile is discernible. The very small maximum during this time lies at 5 m, the area with the lowest biomass. The well mixed profile during this time is a confirmation of the ejection dominated fluxes at the forest edge, presented in Eder et al. (2013) (Section 3.2.3), where the fluxes are dominated by high thermal updraft (good vertical coupling). After sunset and the onset of respiration, the described nighttime profile is formed again, with large gradients due to decoupled atmospheric conditions (stable stratification).

3.3.2. Vertical temperature and wind profile

Besides the CO₂ profile (Section 3.3.1), a vertical temperature and wind profile was installed at the forest edge tower M3. The dry and wet bulb temperatures were measured at five different heights and the wind at six different heights (Section 2.2.3). The systems ran from the start of the EGER IOP3 project, up to the 19 June 2011 with a lot of dropouts with durations ranging from hours up to several days, due to logger problems caused by lightning strikes and afterwards insufficiently configured replacement devices (similar loggers with old software). Because of these problems, there is no possibility to show mean temperature profiles over all or single ‘Golden day’ periods, and only one single day is presented here. Additionally, the wet bulb temperature at 36 m had unrealistic data and therefore, the HMP45 data at 41 m was taken. The data availability for the vertical wind profile is

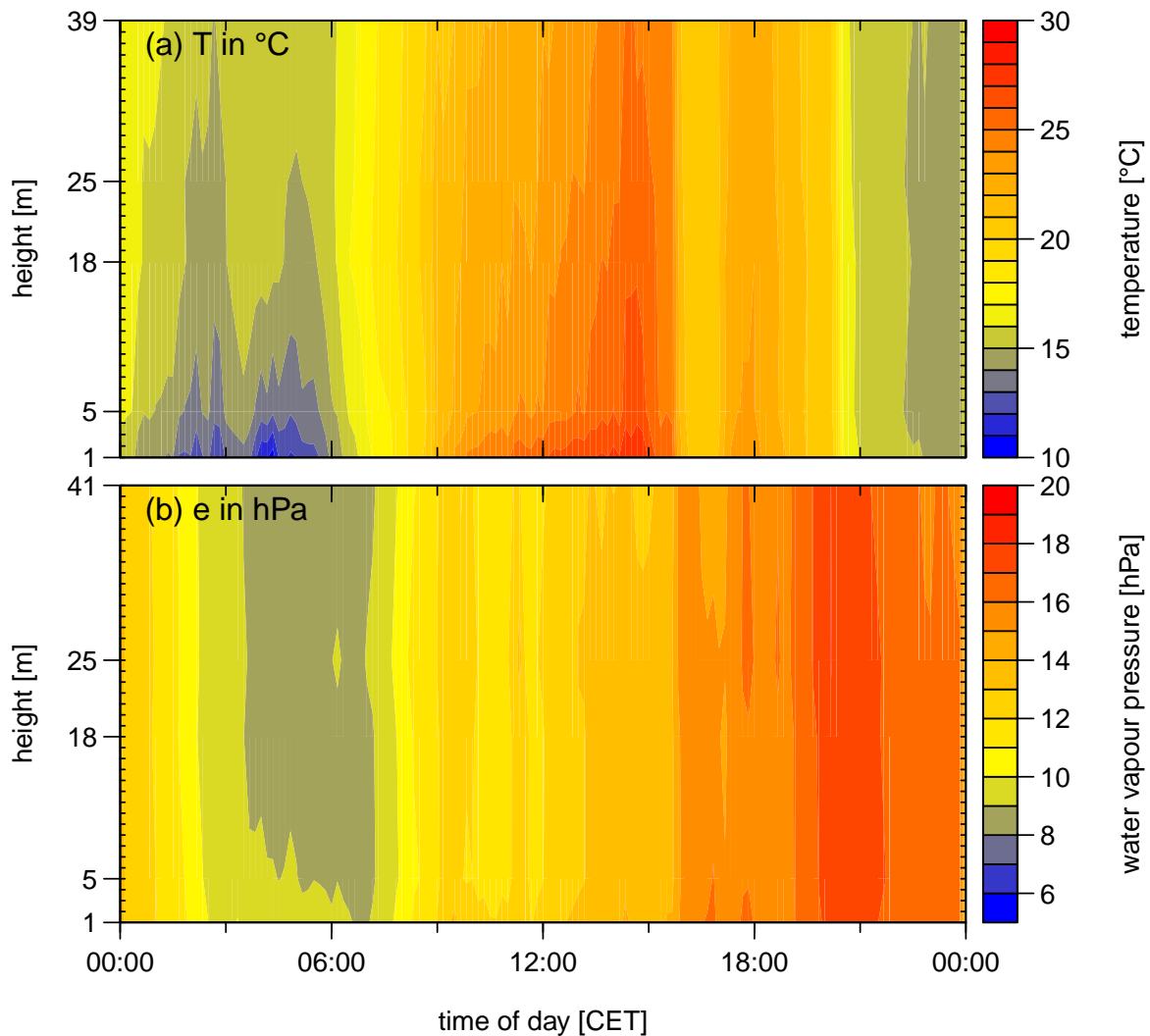


Figure 3.18. Measured vertical profiles for the 29 June 2011 for dry bulb temperature (a) and water vapour pressure e (b) measured at tower M3. Remarks: (i) The colour scaling and (ii) also the stated heights are different in the graphs.

good for GDP2 and GDP3. But the lowest heights (5 m and 13 m) show unrealistic values and have been neglected, instead, the wind velocity measured with the sonic anemometer at 2.25 m has been taken.

In Figure 3.18 the vertical temperature profile for the 29 June 2011 is shown. Figure 3.18a shows the dry bulb temperature T and Figure 3.18b shows the water vapour pressure e . Both show a typical daily variation with lowest values during night and highest during day. An obvious minimum and maximum occur for the dry bulb temperature near ground at the lowest height (1 m), and the maximum of the water vapour pressure is also located there. The minimum during night is not very pronounced. Looking into the vertical pro-

file after sundown, no expected profile developed, like in the night before sunrise. The reason for this behaviour is the passage of a cold front over Germany. The convergence line crossed the site around 09:00 CET and the cold front with rain reached the site in the evening (started around 21:00 CET), which can be seen in both profiles, by a homogeneous profile over the total height. First indication for the cold front is the wind change from south-east to west at 09:00 CET and the cloud band which crossed the experimental site around 16:00 CET to 17:00 CET leading to a decrease in downwelling short-wave radiation, and therefore to a decrease of the dry bulb temperature and an increase of the water vapour pressure. Both profiles show a more or less homogeneous profile during this cloud band. Before the increasing cloudiness, there is for the most part of day a good coupled vertical profile (between 1 m and 39 m, respectively 41 m) at the tower M3. The night is dominated by a coherent structure flux with a higher fraction of sweeps, while the day is dominated by ejections. This corresponds with the findings of Eder et al. (2013) for M3 for the total EGER IOP3 project (Section 3.2.3). In the night from 28 to 29 June high wind velocities (up to 5 m s^{-1}) were measured, coming along with south-easterly winds and a low-level jet (LLJ) above the site (discussed in detail in Section 3.4.2). LLJs from this direction were already found by Foken et al. (2012b) for the site, which corresponds to the anabatic wind from the 'Lehstenbach' valley mentioned in Section 2.1. This LLJ stands in contrast to the discussed findings in Section 3.4.3, where a strong wind situation with westerly winds (alternating to south-west, but also to north-west) cause a long time decoupled situation with wave motions above the forest and a nocturnal drainage of cold air, enriched with CO_2 and depleted with O_3 . Here, only short periods (30-min average) show fully decoupled situations, coming along with weakened wind velocities and resulting in an increase of temperature and decrease of humidity around 03:00 CET and also around 06:00 CET. At the same time, the CO_2 concentration increases (Section 3.4.2) like it was found for the long time decoupled situation in Section 3.4.3. The temperature decrease is also weakly observable in the vertical profile at M1 (also not presented). During day the forest edge is well coupled, associated by an ejection dominated coherent flux, due to convective conditions at the forest edge. This leads to a better mixed vertical profile, but highest temperatures still occur near ground, and above the forest canopy, a poor mixing is observable, due to higher wind velocities.

The vertical wind profile is averaged for the GDP2 and GDP3 and is presented in Figure 3.19, with a 10-min averaged contour plot in Figure 3.19a and three hour averaged profiles in Figure 3.19b to 3.19e. The symbols in Figure 3.19b to 3.19e mark sample medians and error bars represent interquartile ranges. In the contour plot (Figure 3.19a) a

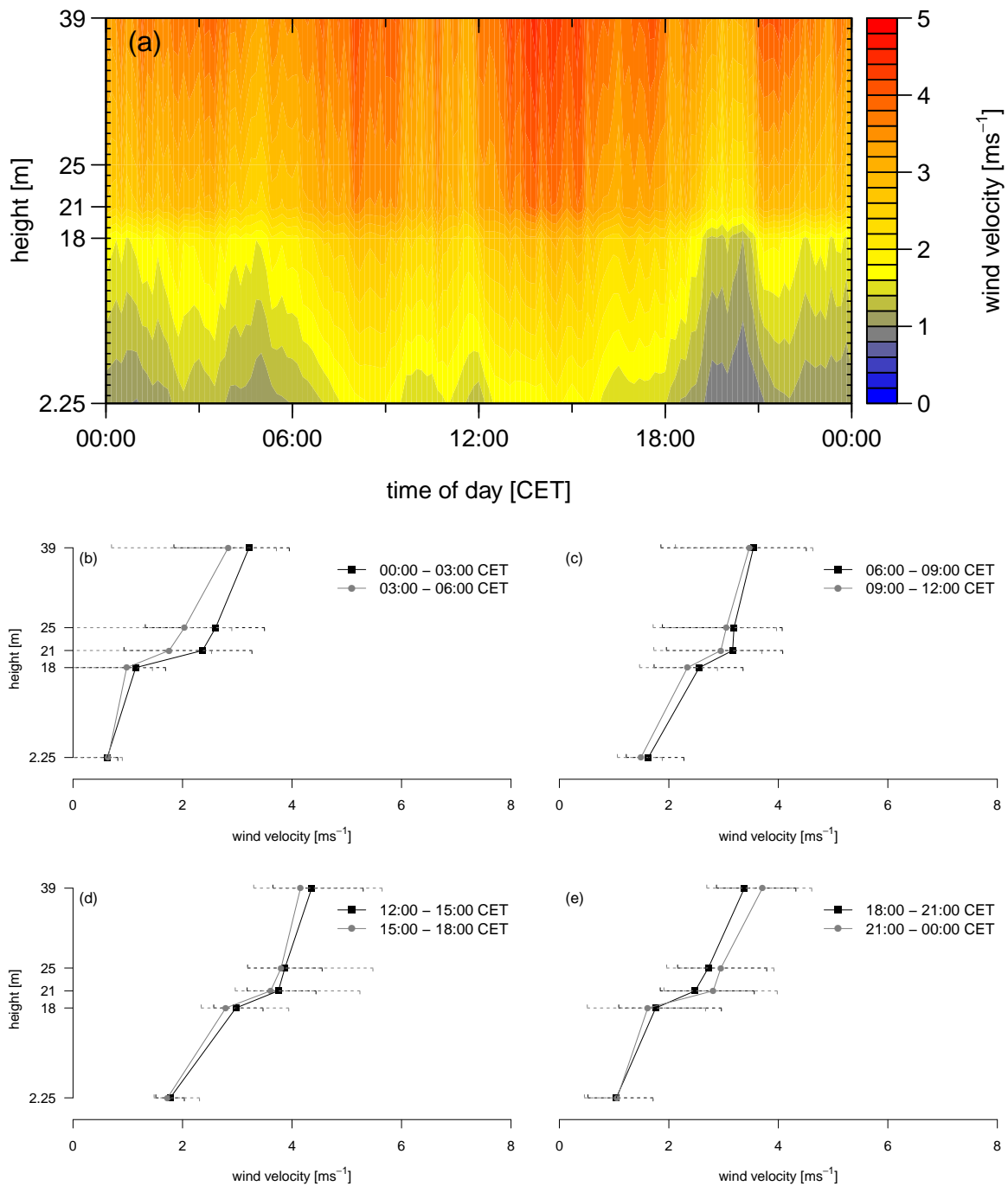


Figure 3.19. Averaged vertical wind profile installed at M3 at the stated heights. 10-min averaged data are presented as a contour plot (a) and three hour averaged data are presented as vertical profiles (b – e). The symbols in (b – e) mark sample medians and error bars represent interquartile ranges. Average period are the ‘Golden Day’ periods GDP2 (without 04 & 08 July 2011) and GDP3 (Table 2.2).

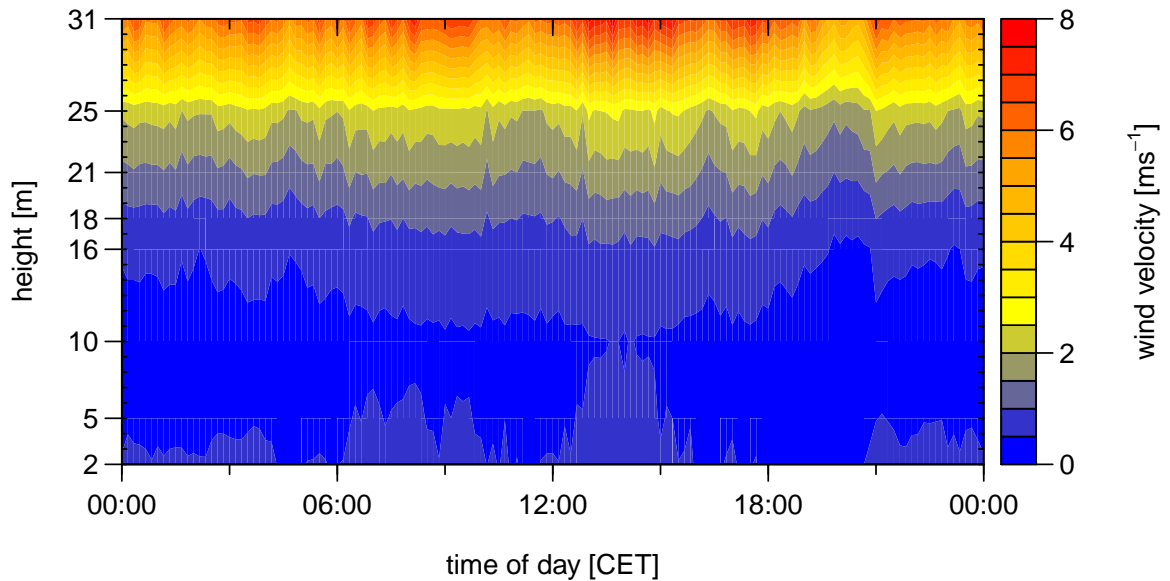


Figure 3.20. Averaged vertical wind profile measured at M1 at the stated heights. Average period are the ‘Golden Day’ periods GDP2 (without 04 & 08 July 2011) and GDP3 (Table 2.2).

continuous increase of the wind velocity with height is observable, with a clear jump from 18 m (within forest canopy) to 21 m and 25 m (top and above forest canopy). This jump was already been shown by Foken et al. (2012b) for the homogeneous part of the forest, but more pronounced at the canopy top. This can be confirmed by the measurements at M1 in Figure 3.20, which shows the same average period and a more precise distinction between canopy and above canopy. The wind velocity at M1 at the top height is significantly higher than at M3 even though the measurements are 8 m lower. This is mainly caused by different anemometer types and differences in bearing. The differences in Figure 3.19a between 18 m and 25 m is on average 1.5 m s^{-1} during day and 2 m s^{-1} during night. A daily variation of the wind velocity is evident with differences of approximately 1 m s^{-1} between night and daytime. Additionally, there are three observable aspects in the contour plot: a decrease in wind velocity over the total profile around 04:00 – 06:00 CET, 10:00 – 12:00 CET and 19:00 – 21:00 CET, where the wind velocity is before and afterwards higher than during these periods. The first situation is caused by the stable stratification and calm wind situation, normal for nighttime and early morning. With sunrise and the increase of the turbulence, the wind velocity increases, too. The last situation is caused by the sunset and the decrease of turbulence and the resulting changes in the boundary layer. The second situation before noon is caused by the full development of the mixing layer. All three situations, mainly the low velocities at 19:00 – 21:00 CET can also be seen in the vertical wind profile within and above the forest at M1 (Figure 3.20). The three hour

averaged vertical profiles in Figures 3.19b to 3.19e show the highest variations near the roughness change from the forest canopy to atmosphere above the canopy and the upper height. The lowest velocities along with the smallest variations are measured the whole day at 2.25 m. In Figure 3.19b, 3.19c, 3.19e the three situations with lower wind velocities can also be clearly seen. As the three situations were measured at the forest edge (M3) as well as within the forest (M1), it can be concluded that the situations are caused by changes in stratification and turbulent mixing and they can not be described by the influences of the forest edge.

3.4. Linkage of vertical structures and horizontal fields

After a general discussion of horizontal structures around the forest edge in Section 3.2 and the vertical structures at the forest edge in Section 3.3, the found results there are now combined in the following sections to obtain a detailed overview of exchange processes near the forest edge. For this purpose, the results found by Foken et al. (2012b) for EGER IOP1 and IOP2 (Section 2.1.2) are summarised and connected to the results of EGER IOP3 found in the work of Eder et al. (2013) and in the framework of this thesis.

3.4.1. Energy balance closure and secondary circulations

To sum up the results found for energy balance closure and the indication for secondary circulations near the forest edge the following statements can be drawn:

- i. Section 3.2.1 demonstrates that the highest variations in temperature, humidity, as well as trace gases occur near the forest edge and additionally, the highest available energy is located at the clearing, but close to the forest edge.
- ii. Section 3.2.2 has shown an approximately 10 % better closed energy balance at the forest edge (Residual $Res = 17\%$), than above the forest and the clearing (Residual $Res = 25 - 30\%$).
- iii. The highest fluctuation in CO_2 fluxes can be found at the forest edge (M3), especially at 41 m (Section 3.2.2).
- iv. Section 3.2.3 shows daily variations in the ejection contribution to coherent transport F_{ej}/F_{CS} solely at the forest edge. The structures there are different from those above the forest.

- v. The ACASA model shows a better agreement with the buoyancy flux corrected turbulent fluxes than with the Bowen ratio method.
- vi. Vertical CO₂ and temperature profiles show a good mixing during the day (Section 3.3).

These findings suggest a higher rate of advective and convective conditions near the forest edge and the presence of secondary circulations above the site, like it was presumed by Foken (2008b) for investigation sites with a roughness change. To connect all the found characteristics, a detailed consideration follows on the basis of an individual event. Considered here was the 28 June 2011. This was the day with the best weather conditions, with an almost cloudless sky and, due to preceding dry weather conditions high air temperatures and low humidities also prevailed. There was no early morning fog and dew. Additionally south-easterly wind was prevailing till 10:00 CET, than it changed to north and after sundown (21:00 CET) again to south-east. This is typical for such high pressure weather conditions at this site, with calm wind velocities during day. More detailed information about the weather conditions can be found in Serafimovich et al. (2011a).

In Figure 3.21, the horizontal meteorological fields along the complete HMMS measuring track (distance of 150 m, starting in the forest and ending at the clearing, with the forest edge in the middle indicated by a green dotted line) are presented. White areas in the profiles (on the time axis) are stops of the HMMS and thus, gaps in the measurement of all quantities. Bigger gaps in the concentration measurements of CO₂ and O₃ are discussed below. Here, the profiles show the data as measured, without the application of the correction algorithm named in Section 2.4.1. All four radiation measurements (short-wave down- and upwelling in Figure 3.21a/3.21b and long-wave down- and upwelling in Figures 3.21c/3.21d) have a clear gradient at or close to the forest edge, like it was shown already in Figure 3.4. In the forest, the short-wave components are low (except at some sunny spots) and at the clearing a nearly undisturbed diurnal variation can be observed, with highest values around noon. Only in the morning (5:30 to 9:00 CET) shadowing effects are observed, caused by the forest edge and the HMMS itself. Due to the low short-wave radiation within the forest during daytime, the long-wave upwelling radiation is lower than it is at the clearing. But the downwelling radiation is, as a consequence of a warm forest canopy, higher in the forest than at the clearing. During night both values are higher in the forest. At the clearing, especially near the forest edge is the highest available energy, because both long-wave radiation components are high and the short-wave radiation components are undisturbed (after 09:00 CET). The temperature profile (Figure 3.21e) shows

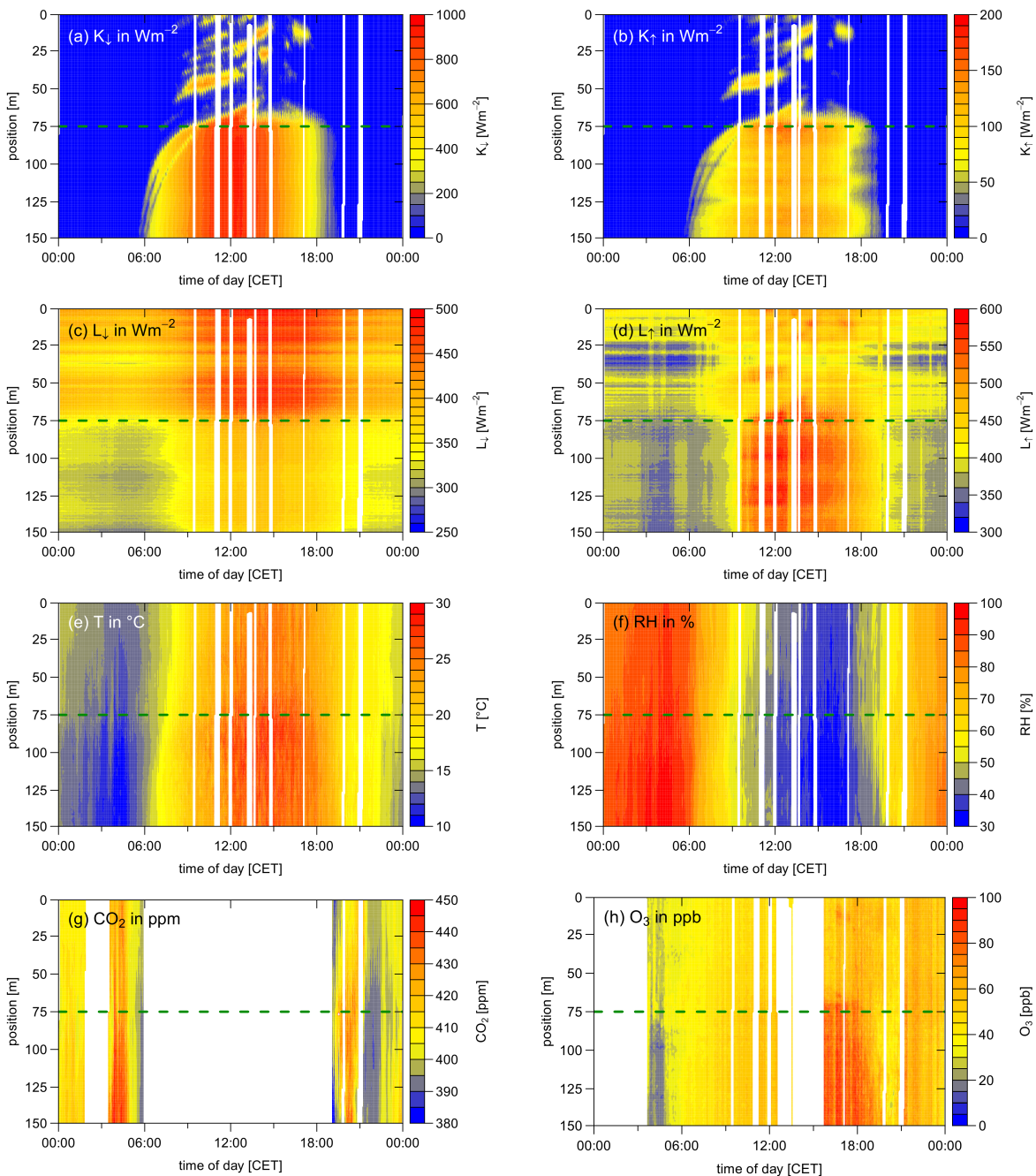


Figure 3.21. Measured horizontal profiles for the 28 June 2011 for all HMMS measurements. Short-wave down/upwelling radiation K_{\downarrow} , K_{\uparrow} (a, b), Long-wave down/upwelling radiation L_{\downarrow} , L_{\uparrow} (c, d), temperature T (e), relative humidity RH (f), CO_2 concentration (g) and O_3 concentration (h). Position shows distance from starting point in metres, with starting point in the forest (0 m), forest edge (75 m, horizontal green dotted line) and endpoint at the clearing (150 m). Remark: The colour scaling is different in all graphs.

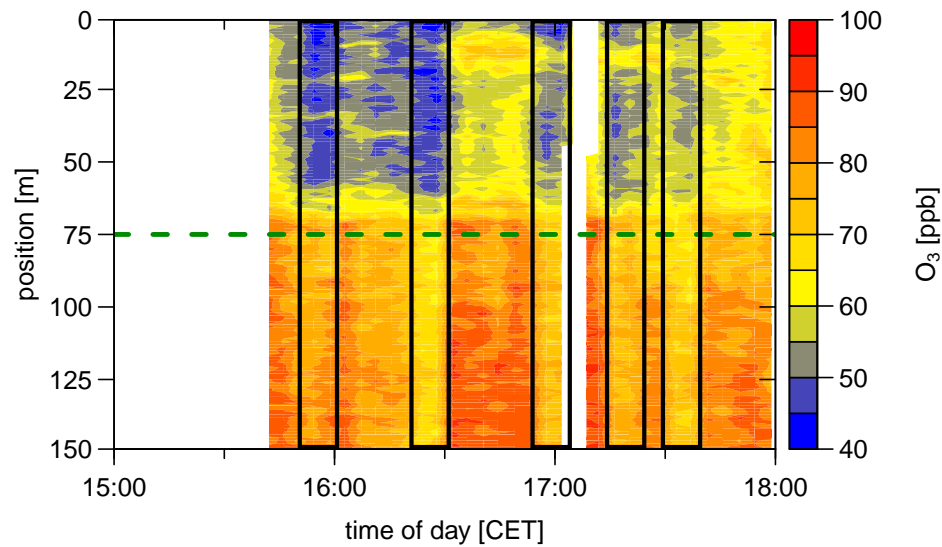


Figure 3.22. Horizontal profile for the 28 June 2011 from 15:00 CET to 18:00 CET for the O_3 concentration, measured with the HMMS. Position shows distance from starting point in metres, with starting point in the forest (0 m), forest edge (75 m, horizontal green dotted line) and endpoint at the clearing (150 m). Black rectangles within the profile show periods with a horizontal coupled regime.

a greater variation at the clearing, with values of about 10 °C during nighttime and about 30 °C during daytime, with an earlier increase in the morning as well as a decrease in the evening. Here, the shadowing effect of the forest edge can also be observed, but not for as long as with the short-wave radiation measurements, suggesting the onset of turbulence causing a better mixing. The temperature rise and fall starts later in the forest compared to the clearing and the daily variation is also lower. A similar observation can be made for the relative humidity (Figure 3.21f), with highest and lowest values, as well as the earlier decrease and increase, occurring at the clearing. Figure 3.21g shows the CO_2 concentration, where a concentration maximum can be observed in the early morning and early evening under stable situations, with higher values at the clearing. This is in accordance with the findings of Foken et al. (2012b) and Serafimovich et al. (2011b). They found a concentration accumulation during uncoupled situations. Because of radiation-induced errors in the CO_2 sensor (Section 2.3.6), the daytime measurements have to be discarded. The O_3 concentration (Figure 3.21h; bigger gaps are caused by connection problems of the sensor) has highest values in the afternoon and lowest values during night-time at the clearing. There is an obvious gradient during daytime near the forest edge, suggesting a sun-induced production at the clearing, with low transport into the forest, like it was discussed in Section 3.2.1. But as Foken et al. (2012b) noted, trace gases are good indicators for coupling

regimes and if now looking in the O_3 concentrations (Figure 3.21h) there is a variation along the total transect during the afternoon discernible, with a sudden decrease of the concentration, and afterwards an increase again. To make this clear, Figure 3.22 shows the variation of O_3 along the horizontal profile for the period from 15:00 to 18:00 CET. The black rectangles illustrate the points in time where, over the entire profile, a decrease in O_3 concentration of approximately 20 ppb was measured. This decrease persists each time for around 10 min (1 to 2 runs of the HMMS) and subsequently the O_3 concentration increases back to the concentration before. Since the concentration decreases along the total profile, and increases shortly thereafter, the following conclusions can be drawn: (i) the profile is fully horizontally coupled, which is shown and discussed in the following text, with the aid of the variations in the energy fluxes and coherent transport, as well as in the horizontal coupling regimes and (ii) this strongly suggests a (secondary) circulation system above the investigation site.

Looking now at the diurnal cycles of the energy fluxes in Figure 3.23 there are obvious differences in the turbulent fluxes. Despite of the highest available energy Q_S^* above the forest (available energy at forest edge is almost similar), the energy fluxes, especially the latent heat flux Q_E are much smaller than at the forest edge. The available energy and thus also the energy fluxes are, at the clearing, about 200 W m^{-2} , and 100 W m^{-2} smaller, respectively. Resulting in a high residual Res above the forest, which is in the range of 40 % (Figure 3.23a), compared to the Res of the clearing (Figure 3.23c) and the forest edge (Figure 3.23b), which are both in the range of 25 %. This stands in contrast to the overall results found for the residuals in Section 3.2.2, where the Res for the forest edge is 17 %. But a conspicuousness can be observed, mainly between the forest edge and the clearing, but also between the forest and the forest edge. There are discernibly high fluctuations in the residuals of the forest edge and the clearing and each time, the residual at the forest edge decreases, the residual at the clearing increases, and vice versa. In other words, there is a significant exchange of available energy discernible, which is transported towards, or away from the forest edge. This is very clear at 11:00 CET (simultaneous with the wind direction change to north), but also between 14:00 and 18:00 CET (stable wind direction). The change in the available energy of the forest and the forest edge reacts consistently, with significantly lower changes above the forest. When taking into account the different coupling regimes presented in Figure 3.24, it is clear that the different sites are occasionally coupled, corresponding to times, where the exchange of available energy is measurable. This is indicated by C_h for a full coupling situation along the total transect M8 – M3 – M4, and D_{C_h}/C_h for coupling along M3 – M4 in Figure 3.24b. As said above, it was also pos-

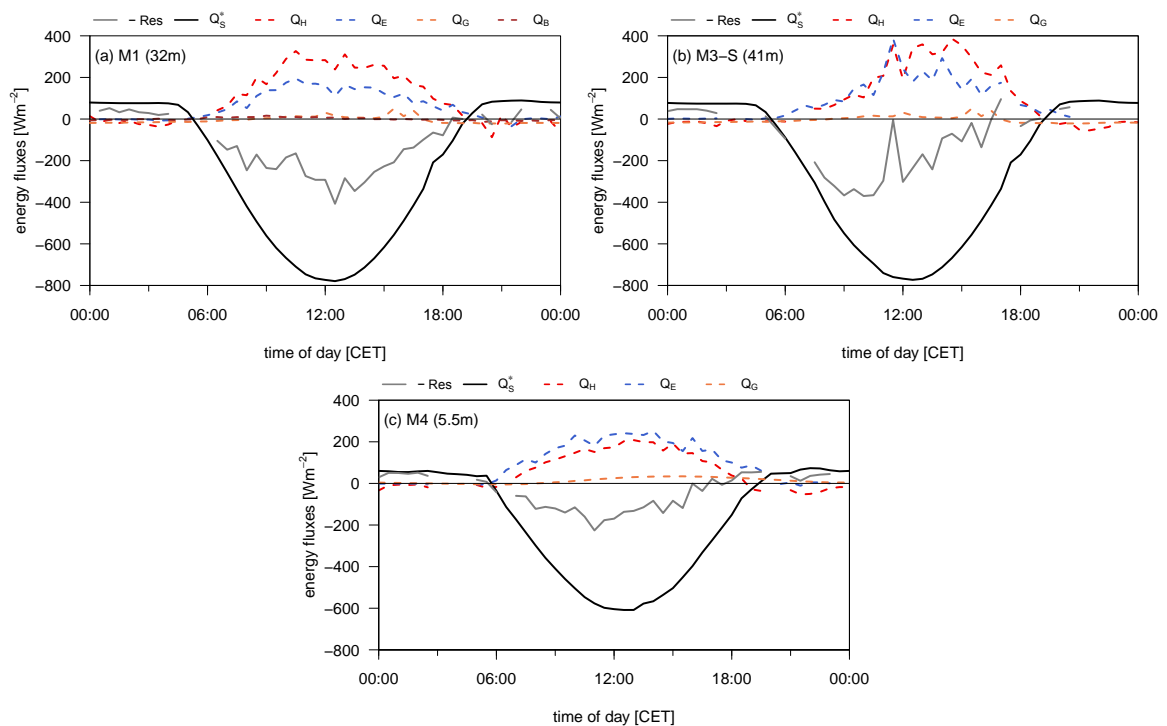


Figure 3.23. Diurnal cycles of the observed energy fluxes for the 28 June 2011 along the transect perpendicular to the forest edge. Measurements were performed above the forest at M1 (a), at the forest edge (M3 - South) at 41 m (b) and at the clearing (M4) at 5.5 m (c).

sible to establish a connection between horizontal coupling and the horizontal O_3 profile measured with the HMMS (Figure 3.22). Indeed, the coupling regimes are presented in 30-min conditional sampled and averaged data (Collineau and Brunet, 1993b; Thomas and Foken, 2007b), and also the energy fluxes show 30-min averaged data, while the HMMS measurements show continuous time series with a temporal resolution of 1 s. This means that half an hour marked as fully horizontal coupled must not necessarily mean that the horizontal O_3 profile is coupled for the total half hour. Nevertheless, during the coupled periods 15:00 to 15:30, 15:30 to 16:00 and 17:00 to 17:30 CET, variations with enrichment and temporarily depletion of O_3 could be measured (black rectangles in Figure 3.22 show depletion). However, not every variation in the O_3 concentration was captured adequately by the horizontal coupling regimes, but yet O_3 is a good tracer for coupling regimes as already mentioned in Foken et al. (2012b). In the moments of good horizontal coupling, the vertical coupling at the forest edge tower M3 (Figure 3.24a) shows no well coupled regime. This is due to the big differences in the turbulent fluxes, especially for sensible heat Q_H , between the top level (41 m) and lowest level (2.25 m) with differences in Q_H of 200 W m^{-2} , which indicates a different circulation system in the higher levels, with a

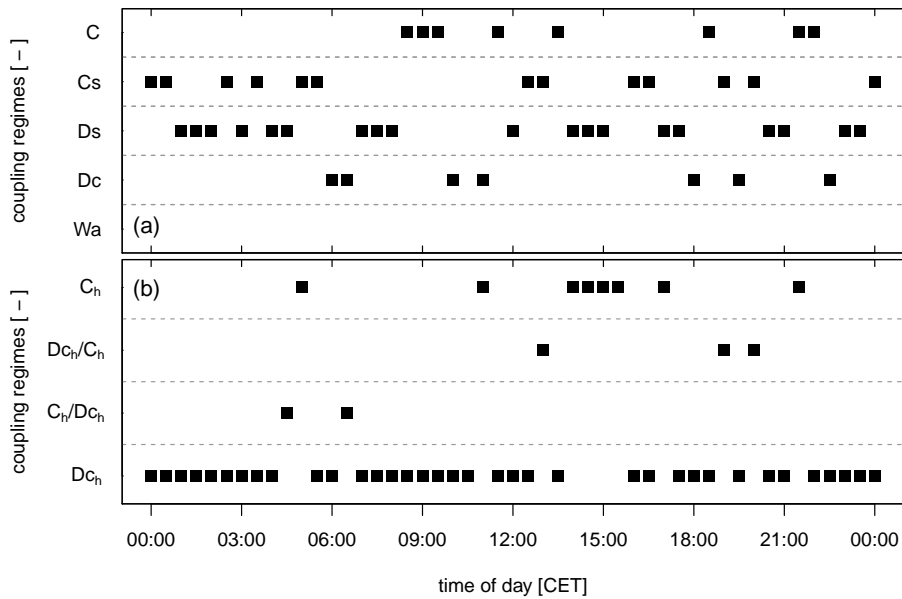


Figure 3.24. Diurnal variation in vertical coupling regimes at M3 (a) and horizontal coupling regimes (b) along the transect perpendicular to the forest edge (M8 – M3 – M4) on 28 June 2011. The different coupling regimes are described in Section 2.4.3.

heightened amount of advectively transported energy towards the forest edge and a convective updraft there. This is also illustrated by the consideration of coherent transport (Figure 3.25). While the contribution of coherent transport F_{CS} to total fluxes F_{tot} is very stable over the day (Figure 3.25a), there is a daily variation in the relative contribution of ejections to the total coherent transport F_{ej}/F_{CS} (Figure 3.25b). Like it was found for the total days of the EGER IOP3 project (Figure 3.13) the ejections dominate during day and the sweeps during the night. When the contribution of ejections is extremely high, the residual at the forest edge decreases and when the contribution is less the residual increases. Eder et al. (2013) had investigated the dependency of different wind directions and flow distortions at the project site and found an extremely high contribution of ejections with northerly winds, but nevertheless, there was a daily cycle of the contribution of ejections and sweeps measurable, independent of the wind direction. They assumed that the found behaviour is caused by secondary circulations above the clearing. Furthermore, they pointed out that the circulations reach the ground but only in the vicinity of the forest edge. The investigations made here confirm the assumption of Eder et al. (2013) that secondary circulations could be found above the clearing, since (i) there is an (advective) transport between the forest edge and the clearing and weakened to the forest, which could be measured in the horizontal profiles of the HMMS (especially in O_3 concentration) and confirmed

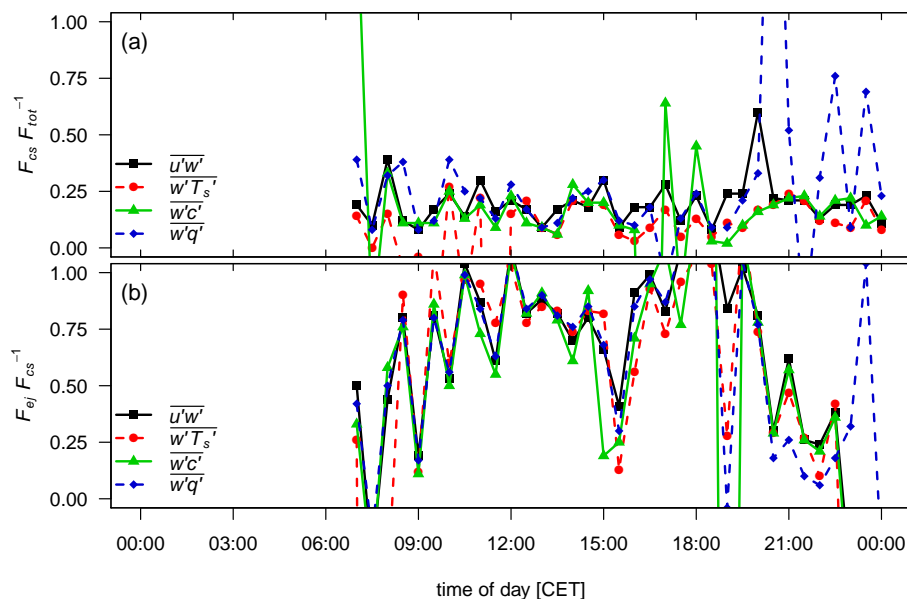


Figure 3.25. The relative flux contribution of coherent structures F_{CS} to total fluxes F_{tot} (a) and of the ejection contribution to coherent transport F_{ej}/F_{CS} (b) of momentum $\overline{u'w'}$, buoyancy $\overline{w'T_s'}$, carbon dioxide $\overline{w'c'}$, and latent heat $\overline{w'q'}$ at the forest edge tower M3 at 41 m on 28 June 2011.

by the horizontal coupling regimes, (ii) a heightened amount of ejections and convective updraft leads to the decrease of the residual at the forest edge, while (iii) the clearing has at the same time less energy available, resulting in a decrease of the turbulent fluxes and an increase of the residual. However, (iv) there also exists the reversed case that the clearing has a sudden increase in the energy fluxes, linked with a decrease at the forest edge.

3.4.2. Influence on horizontal profiles by low-level jet

Foken et al. (2012b) have already investigated the influence of coupling regimes on trace gases at the EGER site. They found a strong increase of CO_2 fluxes and low nighttime CO_2 accumulation during low-level jet events, which corresponds with the findings of Karipot et al. (2006, 2008). The LLJ at the site originates usually from south/south-east, coming along with negative vertical winds (downward), a well coupled system and good mixing. Only during weakened LLJ events and/or the formation of gravity waves above the forest canopy there is an accumulation of CO_2 within the trunk space observable. In Section 3.4.3 a nocturnal drainage with enriched CO_2 air is presented, caused by gravity waves above the site and the resulting long time decoupling.

As mentioned in Section 3.3.2 there was a LLJ event in the night from 28 to 29 June 2011

after midnight, but an even more pronounced LLJ event was the night before, from 27 June 22:00 CET to 28 June 08:00 CET. In Section 3.4.1 the energy balance for the 28 June was examined, since this day was the day with the best and most stable weather conditions. This favours the formation of LLJ events in the night. Looking at the vertical profiles in Figure 3.26 of wind direction (above), wind velocity (middle) and vertical wind velocity (below), which are shown for the windprofiler, the SODAR/RASS, and the miniSODAR, it can be noted that the maximum wind velocities up to $12 - 15 \text{ m s}^{-1}$ occur between the heights of 200 – 250 m from 00:00 to 03:00 CET. A second maximum is around 06:00 CET. The vertical winds are over the total time of LLJ negative (downward) with a maximum of -1 m s^{-1} and the typical south to south-easterly winds are prevailing. Above the LLJ the wind direction is north with significantly lower wind velocities.

Regarding the enhanced CO_2 fluxes during LLJ events found by Karipot et al. (2006, 2008) up to $9 - 15 \mu\text{mol m}^{-2} \text{ s}^{-1}$ and the increase of 100 % found by Foken et al. (2012b) from 4 to $8 \mu\text{mol m}^{-2} \text{ s}^{-1}$, there are also comparable increases measurable during this LLJ event. Here, the maximum CO_2 flux at M3 at 2.25 m was measured during this night as $7 - 12 \mu\text{mol m}^{-2} \text{ s}^{-1}$, while the mean flux (of all ‘Golden Day’ periods) for the same night time period is $6 \mu\text{mol m}^{-2} \text{ s}^{-1}$. At the clearing (M4) the fluxes remain almost unchanged. The high fluxes during this night come along with a good mixing, indicated by the almost always vertically coupled system (Figure 3.27a). The horizontal coupling along the transect parallel to the forest edge (Figure 3.27b) is well coupled. Only in the periods before and after the LLJ, as well as during the weakened LLJ situation between 03:00 to 04:30 CET, there is an uncoupled or partially coupled system. In all three cases northerly winds are prevailing (wind from the forest), and supposedly structures which are formed at the forest edge change the transport locally in such a way so that there is no coupling between the masts. The transect perpendicular to the forest edge (Figure 3.27c) shows the reversed behaviour. During the LLJ, the system is uncoupled. Before, after, and during the weakened LLJ event with northerly winds the system is partially or fully coupled.

As said above, there is no CO_2 concentration accumulation during LLJ events recognised by Foken et al. (2012b), and this could be confirmed by the horizontal profile of CO_2 , measured with the HMMS during this night (Figure 3.28c). Besides the CO_2 concentration, there are profiles of temperature (Figure 3.28a), relative humidity (Figure 3.28b) and O_3 concentration (Figure 3.28d). In all profiles there is a change visible with the formation of the LLJ, but most evident in the CO_2 concentration. During the northerly winds from 20:00 to 22:00 CET, there is a concentration maximum near the forest edge, which confirms the assumption of changed turbulent structures caused by the forest edge. Also temperat-

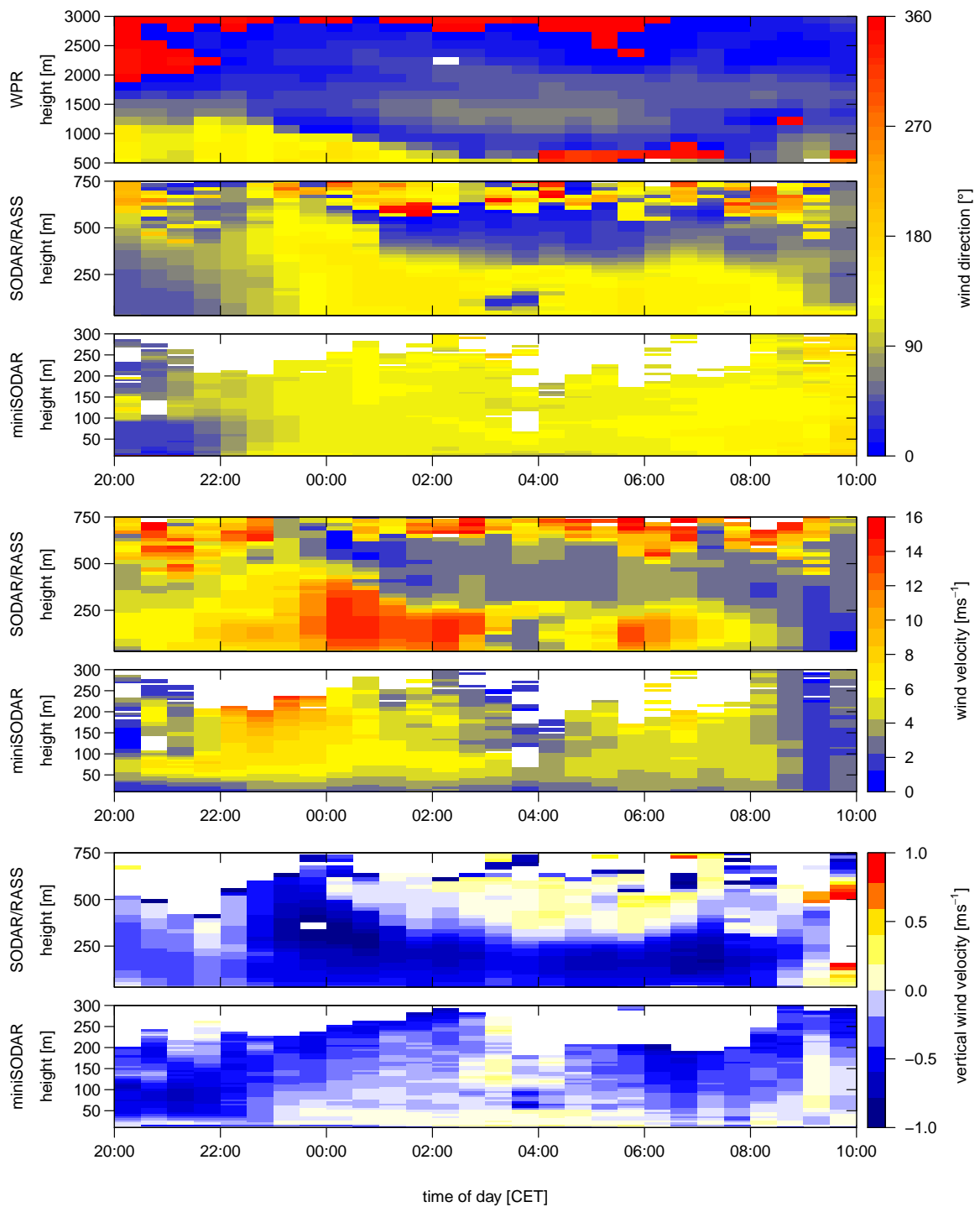


Figure 3.26. Vertical profiles from windprofiler (WPR), SODAR/RASS, and miniSODAR of the wind direction (above), wind velocity (middle), and vertical wind velocity (below) in the night from 27 June 20:00 CET to 28 June 2011 10:00 CET.

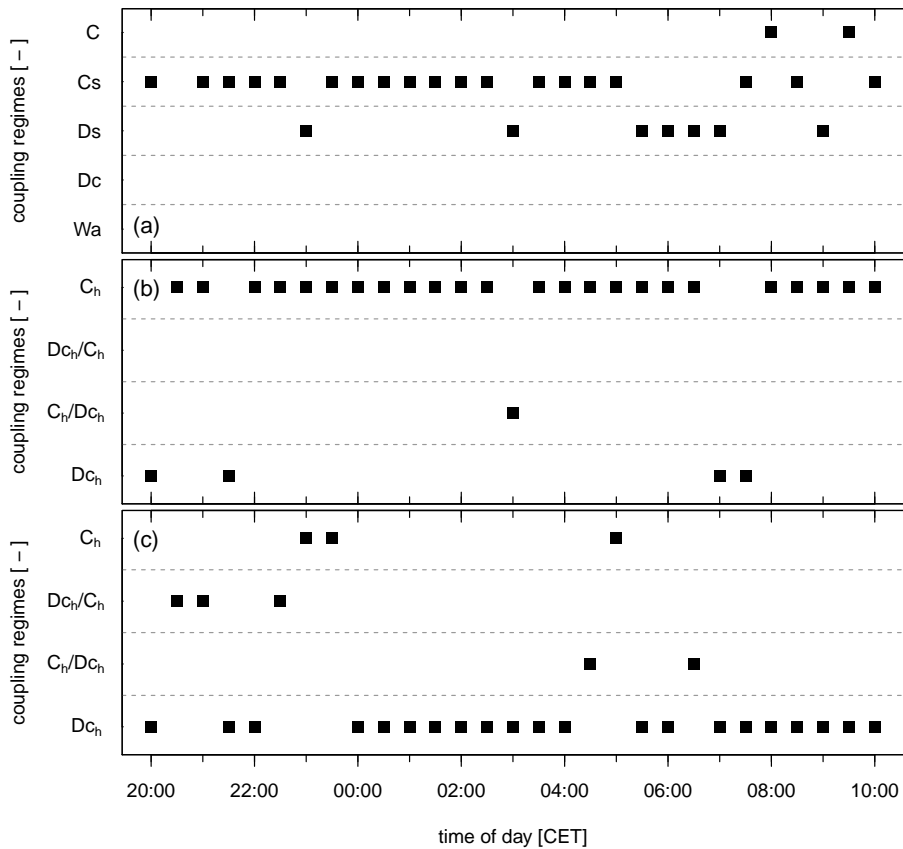


Figure 3.27. Vertical coupling regimes at tower M2 (a) at three different measuring heights (2 m, 26 m, 36 m), horizontal regimes parallel to the forest edge (M6 – M3 – M7; b) and perpendicular to the forest edge (M8 – M3 – M4; c) from 27 June 2011 20:00 CET to 28 June 2011 10:00 CET. The different coupling regimes are named in Section 2.4.3.

ure is lower near the edge, and humidity higher. At the clearing the concentration is equal to the atmospheric concentration of around 380 ppm. Between 22:00 and 00:00 CET, the conditions at the site changes, and the LLJ with southerly winds and higher wind velocities prevails (Figure 3.26). First the lower CO₂ concentrations are blown into the forest and the horizontal profile is nearly mixed, and after 00:00 CET with the high wind velocities, and the resulting bigger footprint, there is an inflow of CO₂ from the southern located forest. Highest concentrations can be observed at the clearing, and lowest in the forest. Around 01:30 CET there is an inflow of colder, CO₂-depleted air measurable, which can not be seen in the SODAR measurements, but there is a short increase in the wind velocity at 2.25 m at M3. During the weakened LLJ, from 03:00 to 04:30 CET, the wind direction changes in the height of 200 – 250 m of the SODAR/RASS to north, while above and below the wind direction is still south. The wind velocity is very low (smaller than 2 m s⁻¹). The temperature

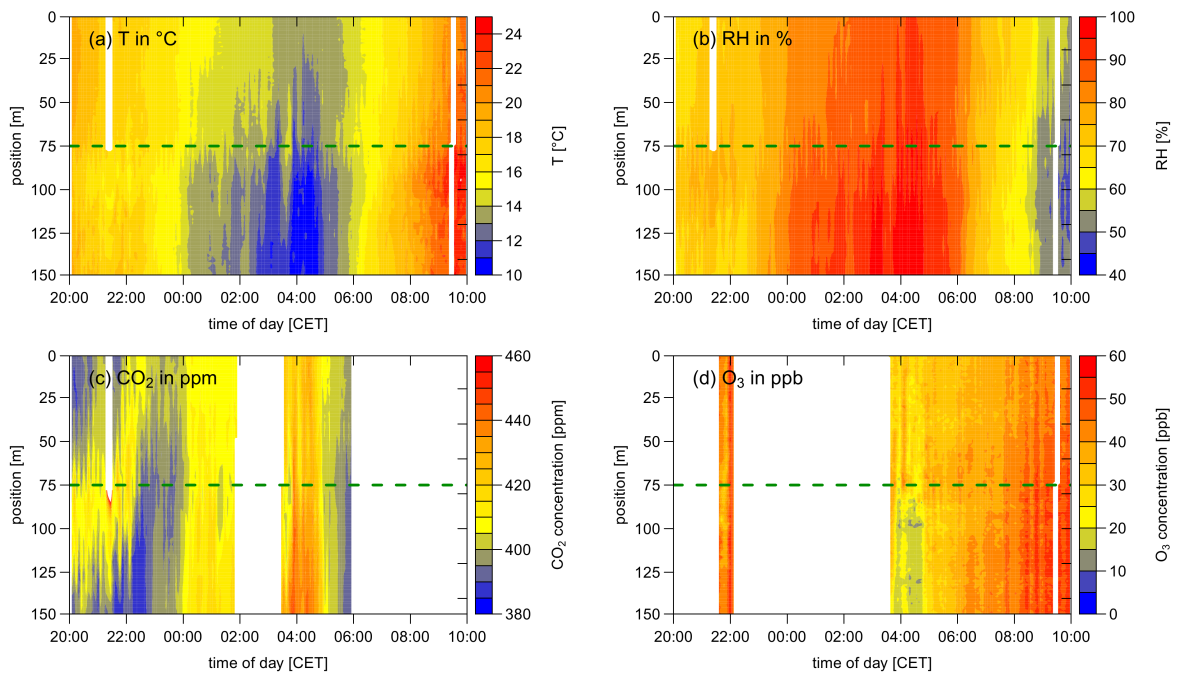


Figure 3.28. Measured horizontal profiles from 27 June 20:00 CET to 28 June 2011 10:00 CET for temperature T (a), relative humidity RH (b), CO_2 concentration (c) and O_3 concentration (d), measured with the HMMS. Position shows distance from starting point in metres, with starting point in the forest (0 m), forest edge (75 m, horizontal green dotted line) and endpoint at the clearing (150 m). Remark: The colour scaling is different in all graphs.

decreases and the humidity increases during this situation. The CO_2 concentration measurements are at this time not available, because of a connection failure. But at 03:30 CET there is another observed concentration minimum near the forest edge. After 04:00 CET the wind velocity increases to $4 - 6 \text{ m s}^{-1}$ and the wind direction is again southerly along the total vertical profile. But because of the still weakened LLJ at this time, an accumulation of CO_2 and a depletion of O_3 can be observed. After 05:00 CET, the wind velocity is again higher than 10 m s^{-1} and the system is well mixed. After the end of the LLJ the typical high pressure weather situation with calm northerly winds is prevalent at the site.

3.4.3. Nocturnal drainage caused by a long decoupling situation

In Sections 3.2 and 3.3 high variations during nighttime were recognised. Especially in the CO_2 and O_3 concentration, which are an indication for an enrichment, or respectively depletion caused by different coupling regimes. In detail it was observed:

- i. High variations in the CO_2 and O_3 nighttime concentrations of the HMMS measurements (Section 3.2.1).

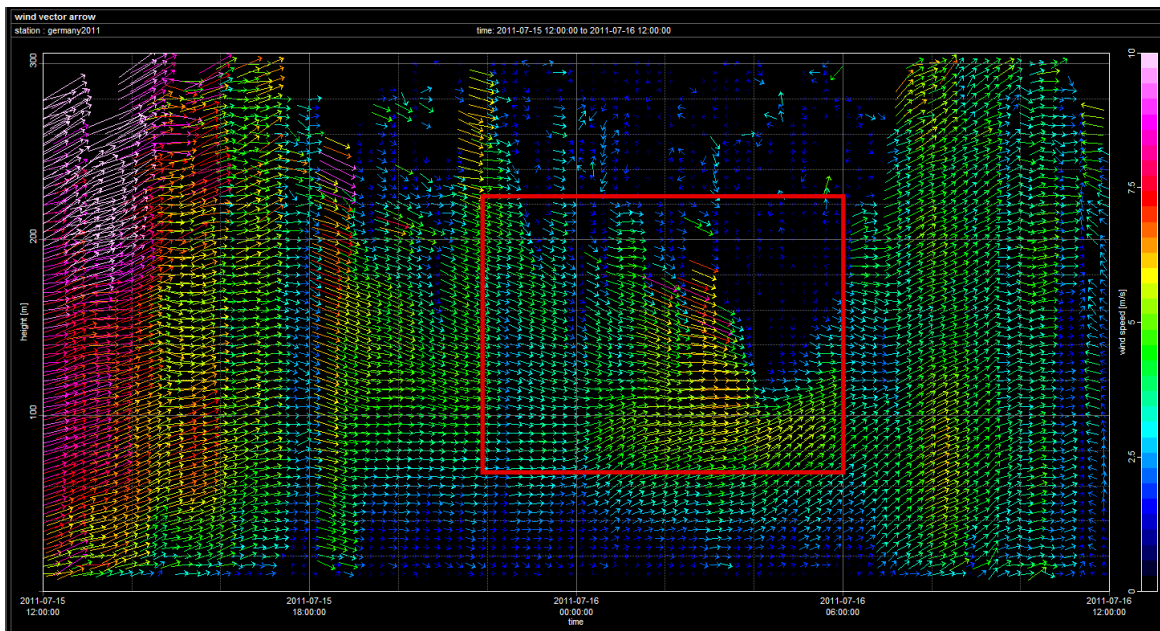


Figure 3.29. Sodargram of the MiniSODAR (location at clearing ‘Köhlerloh’; see Figure 2.2) from 15 July 2011 12:00 CET to 16 July 2011 12:00 CET. Direction of the arrows show the two-dimensional direction of the wind and the colour scale indicates the wind velocity. Red rectangle marks the strong wind situation with westerly winds in the night of 16 July with wind velocities up to 7.5 m s^{-1} at a height of 100 – 200 m.

- ii. Nighttime horizontal decoupling situations in the transect parallel to the forest edge, which are an indication of drainage events (Section 3.2.3).
- iii. Nighttime maximum in the vertical CO_2 profile at 2.25 m with variations of about 100 ppm (Section 3.3.1)

All these findings have been observed, for example, during the night from 15 to 16 July 2011, but mainly in the second half of the night. Compared to described findings in Section 3.4.2 and Foken et al. (2012b), in this night no LLJ was prevailing. There was a situation with strong nighttime winds from the west (alternating to south-west, but also to north-west) at a height of 100 – 200 m above ground with wind velocities from 3.0 m s^{-1} up to 7.5 m s^{-1} (Figure 3.29, red rectangle marks event). This situation was caused by a temperature inversion, where strong wind shears often occur above the inversion layer.

As a result, wave motions (Wa) exist above the forest canopy (see Section 2.4.3 for detailed description of the different coupling regimes). The sub-canopy and canopy layer of the forest are mostly decoupled from the layer above the canopy during this event. The coupling regimes are shown in Figure 3.30 for the period of the 15 June 2011, 12:00 CET to 16 June 2011, 12:00 CET, where a red rectangle marks the event. Those are presented in the

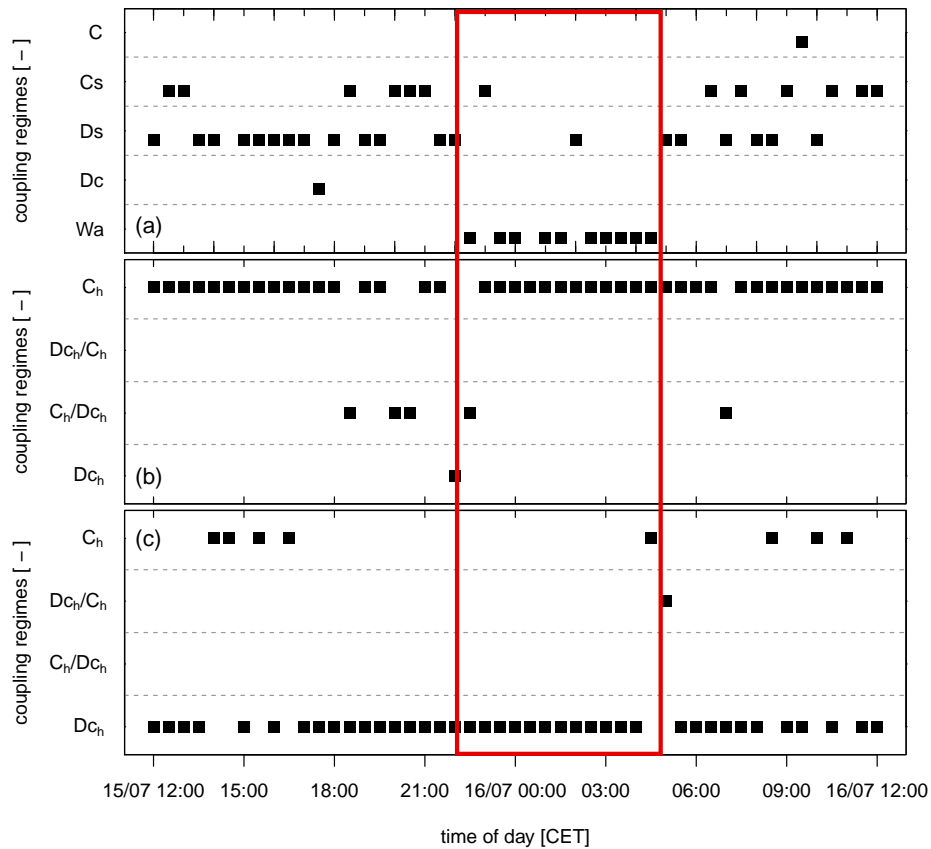


Figure 3.30. Vertical coupling regimes at tower M2 (a) in three different measuring heights (2 m, 26 m, 36 m), horizontal regimes parallel to the forest edge (M6 – M3 – M7; b) and perpendicular to the forest edge (M8 – M3 – M4; c) from 15 July 2011 12:00 CET to 16 July 2011 12:00 CET. The different coupling regimes are named in Section 2.4.3. Red rectangle marks the strong wind situation with westerly winds in the night of 16 July.

vertical regimes for the tower M2 (Figure 3.30a) at all three measuring heights (2 m, 26 m and 32 m). Additionally, the horizontal regimes parallel to the forest edge at 2.25 m (M6 – M3 – M7) are presented in Figure 3.30b and the horizontal profile perpendicular to the forest edge at 2.25 m (M8 – M3 – M4) in Figure 3.30c. While the obviously decoupled situation in the vertical profile is between 15 July 2011, 22:30 CET till 16 July 2011, 04:30 CET, with short discontinuities, or other coupling regimes, there are no or only a few changes in the horizontal coupling regimes. This is an indication of near-ground advective transport, or katabatic drainage following the terrain slope from north-east to south-west (perpendicular to forest edge), which can not be adequately captured by the routines for coupling regimes as there is no turbulent transport prevalent.

The strong wind situation with the wave motions above the forest has also an effect on fluxes of coherent structures. Figure 3.31 shows fluxes of momentum $\overline{u'w'}$, buoyancy

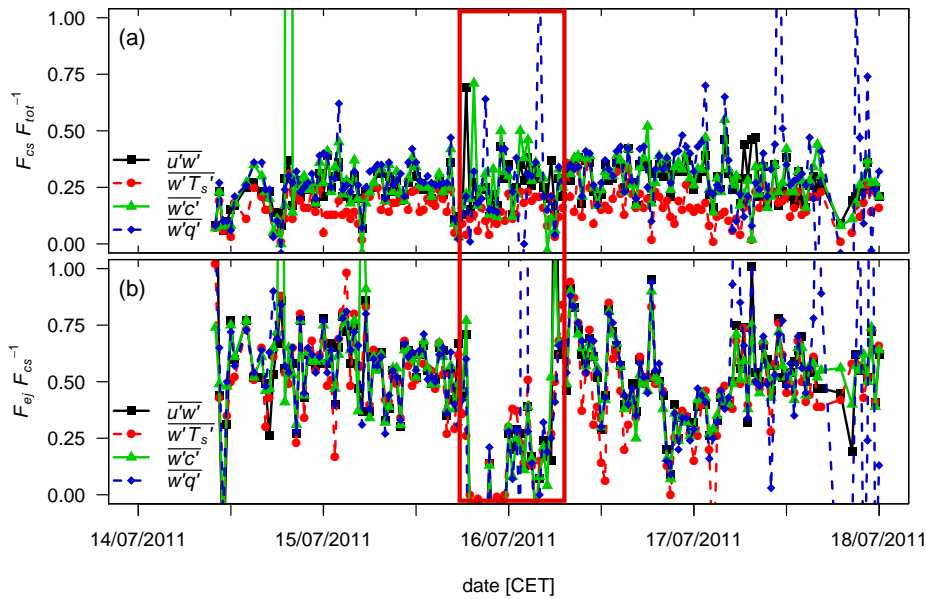


Figure 3.31. The relative flux contribution of coherent structures F_{CS} to total fluxes F_{tot} (a) and of the ejection contribution to coherent transport F_{ej}/F_{CS} (b) of momentum $\overline{u'w'}$, buoyancy $\overline{w'T'_s}$, carbon dioxide $\overline{w'c'}$, and latent heat $\overline{w'q'}$ at the main tower M1 at 32 m from 14 July to 18 July 2011. Red rectangle marks the strong wind situation with westerly winds in the night of 16 July.

$\overline{w'T'_s}$, carbon dioxide $\overline{w'c'}$, and latent heat $\overline{w'q'}$ exemplary for the tower M1 at 32 m. The presented period from 14 July 00:00 CET to 18 July 2011 00:00 CET was chosen to have a comparison to nights before and after the event. The event itself is marked by a red rectangle, where the relative flux contribution of coherent structures F_{CS} to total flux F_{tot} (Figure 3.31a) decreases significantly from approximately 25 % to approximately 15 % with high fluctuations. This indicates less vertical transport, which is largely dominated by sweeps. This is presented as the ejection contribution to coherent transport F_{ej}/F_{CS} in Figure 3.31b, which drops almost to zero. This stands in contrast to nights before and after the event. So in other words, the sweeps are predominant during the event above the canopy and the turbulent transport out of the forest caused by ejections is very low.

This small vertical transport affiliated to the long decoupling situation leads to an enrichment of CO_2 and a depletion of O_3 in the trunk space of the forest, but also at the clearing there are changes due to this event. These are (i) a lower exchange with the atmosphere above and (ii) cold air drainage (shown below). This is presented by the horizontal profiles measured with the HMMS in Figure 3.32. Because of the non continuous measurements and the radiation-induced problems in the CO_2 measurements with the Gascard[®] NG (Section 2.3.6) there are big gaps in the CO_2 time series (Figure 3.32a), but also in O_3 (Fig-

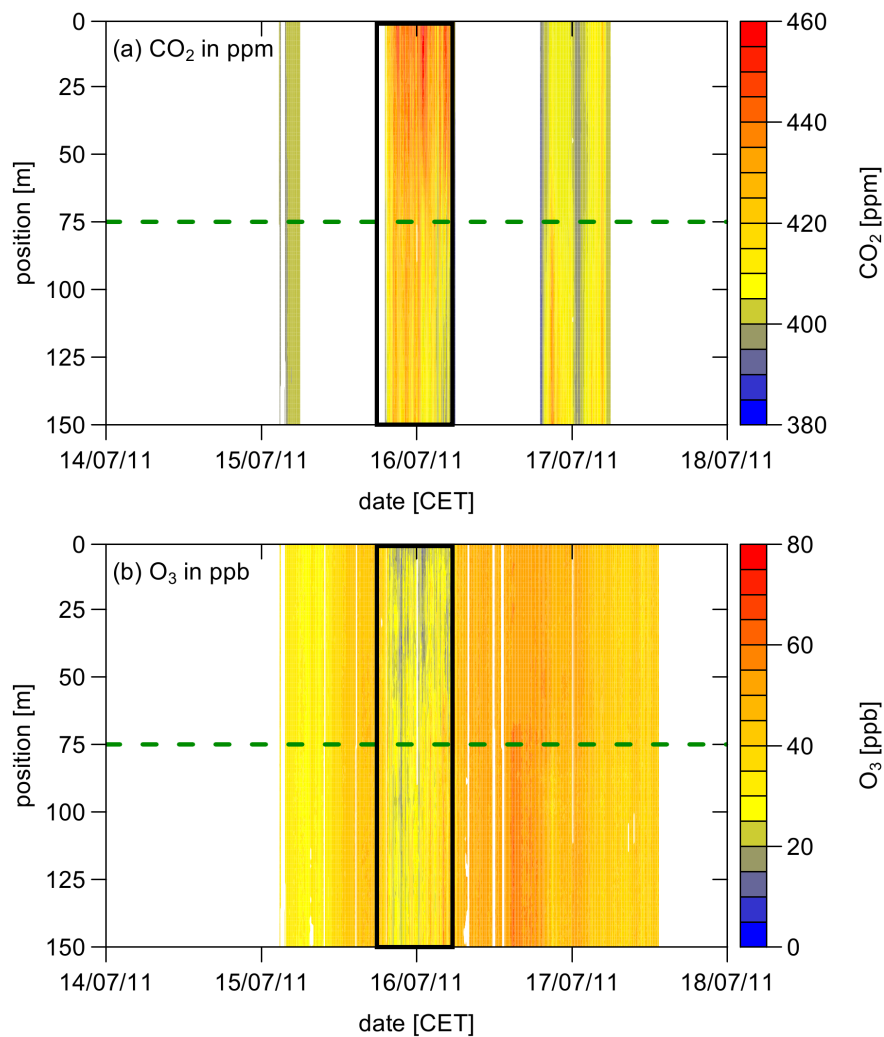


Figure 3.32. Horizontal profiles of CO₂ (a) and O₃ (b) concentration measured with the HMMS from 14 July to 18 July 2011. Position shows distance from the starting point in metres, with starting point in the forest (0 m), forest edge (75 m, horizontal green dotted line) and endpoint at the clearing (150 m). Black rectangles mark in both figures the strong wind situation with westerly winds in the night of 16 July. Remark: The colour scaling is different in all graphs.

ure 3.32b). However, the nighttime values of 15/16 July (night with strong wind situation) and 16/17 July can be presented. The CO₂ concentration is in the forest approximately 40 – 60 ppm higher than in the subsequent night, whereas the CO₂ concentration has not changed significantly at the clearing. The O₃ concentration is approximately 10 – 20 ppb lower within the forest, compared to nights before and after the strong wind situation. The strong wind event is less remarkable at the clearing (decrease of approximately 5 – 10 ppb). Additionally, there is a katabatic (cold air) drainage observable, which is caused by the

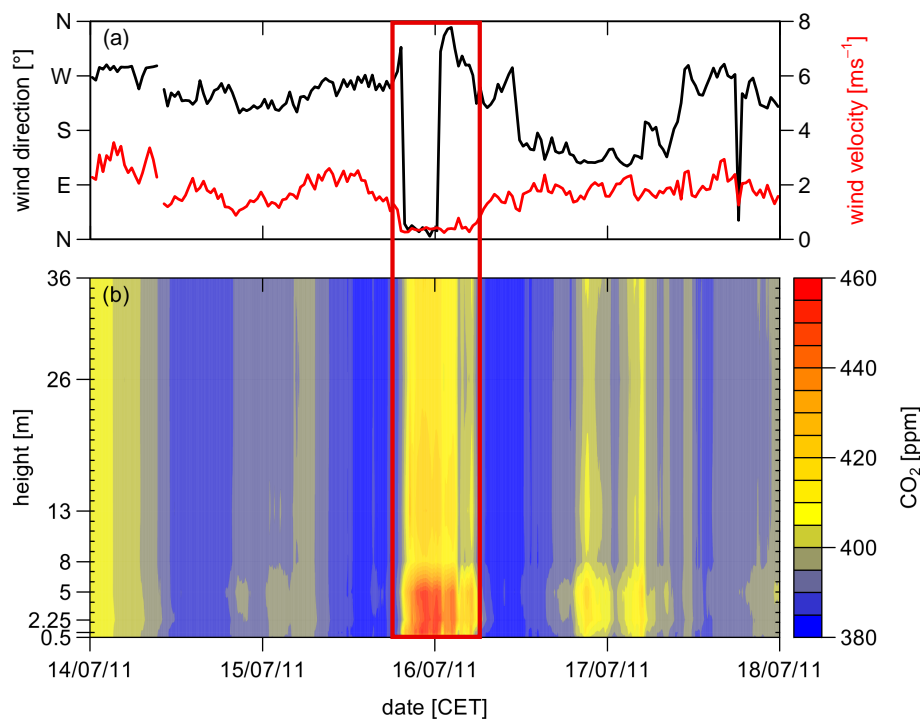


Figure 3.33. Wind direction and velocity (a) measured with the 3D sonic anemometer at 2.5 m at the forest edge tower M3. Vertical CO_2 profile (b) at 8 heights (0.5, 1, 2.25, 5, 8, 13, 26 and 36 m; see Table 2.4) also at M3. Both measurements are presented from 14 July to 18 July 2011. Red rectangle marks the strong wind situation with westerly winds in the night of 16 July.

slope of the investigation area, sloping from north-east to south-west and consequently, the CO_2 -enriched and O_3 -depleted air drains over the course of the night out of the forest and onto the clearing. In both profiles the highest (in case of CO_2) or lowest (in case of O_3) values occur in the forest and the drainage is discernible over the complete horizontal profile (0 – 150 m). In nights before and after the strong wind situation there is no comparable drainage.

The drainage was also measured in the lower metres of the forest edge tower M3. Here, at the moment the drainage starts, the wind direction (measured in 2.5 m with the sonic anemometer) changes from westerly to northerly, with a very low wind velocity ($< 0.5 \text{ m s}^{-1}$). Both measured quantities are shown in Figure 3.33a. The vertical CO_2 profile (Figure 3.33b), also installed at M3 at eight different levels (0.5, 1, 2.25, 5, 8, 13, 26 and 36 m; see Section 2.2.3 for a more detailed description), shows the drainage at the lower four heights (up to 5 m), with concentration maximums up to 460 ppm. Compared to nights before and after the drainage, the concentration is 40 up to 60 ppm higher. The height up to 5 m

at M3 is explainable by a small embankment (near the last line of trees), which acts like a ‘jumping platform’ for the drained cold air. There is also an effect of the strong wind situation measurable in the heights above (8 – 36 m). Here, the CO₂ concentration is approximately 20 ppm higher than in the nights before and after.

In Section 3.4.2 the increased CO₂ fluxes are described during LLJ events, but in the case of the strong wind situation, coming along with gravity waves and long decoupled situations, the CO₂ accumulates within the trunk space of the forest, and regarding the CO₂ fluxes, they are only 2 to 4 μmol m⁻² s⁻¹ during this situation and therefore significantly smaller than during the other nights, or particularly during LLJ events. Towards the forest edge, the fluxes are less affected (30 – 50 % less) and the reduction at the clearing is marginal (10 – 20 % less).

3.4.4. Inflow of fresh air caused by convergence line

Besides low-level jets (LLJ; Section 3.4.2) and the strong wind situation (Section 3.4.3), which both occur mainly in the second half of the night, there are further influences of the atmospheric boundary layer. As Foken et al. (2012b) observed on the night with a LLJ (after midnight), a prior inflow of fresh air with low NO₂ and high O₃ concentrations between 22:00 to 24:00 CET, with the occurrence of gravity waves above the forest. An inflow of fresh air was also observed during EGER IOP3, late on 7 July 2011 between 21:00 and 22:00 CET caused by the transition of a convergence line across the investigation area. The vertical wind profiles in Figure 3.34 show corresponding to the crossing (first red rectangle), a wind direction change from south to west and a wind velocity increase from smaller than 3 m s⁻¹ to 8 – 15 m s⁻¹. The vertical wind velocity changes from weakly negative (downward) to positive (upward). After 23:00 CET there is at heights below 250 m a wind change to north, while in heights above 500 m the west wind remains unchanged after 21:00 CET. Around 01:00 CET on the 8 July there are again southerly winds with low wind velocities and after 02:30 CET there is a westerly flow again (second red rectangle).

Of interest here is how the fresh air distributes in the investigation site, and if there are differences between the dense forest and the open clearing. Figure 3.35 shows the vertical profiles of wind velocity, temperature, water vapour pressure, and CO₂ concentration from 07 July 2011 18:00 CET to 08 July 2011 06:00 CET. The wind velocity (Figure 3.35a) increases during the crossing of the convergence line (first red rectangle) above the forest canopy at 39 m to 8 m s⁻¹, and decreases towards the ground. Near the ground there are measured velocities of 2 m s⁻¹, while before and after the inflow the velocities are < 1 m s⁻¹. With the wind direction change to west again after 02:30 CET, the wind velocity is again higher. The

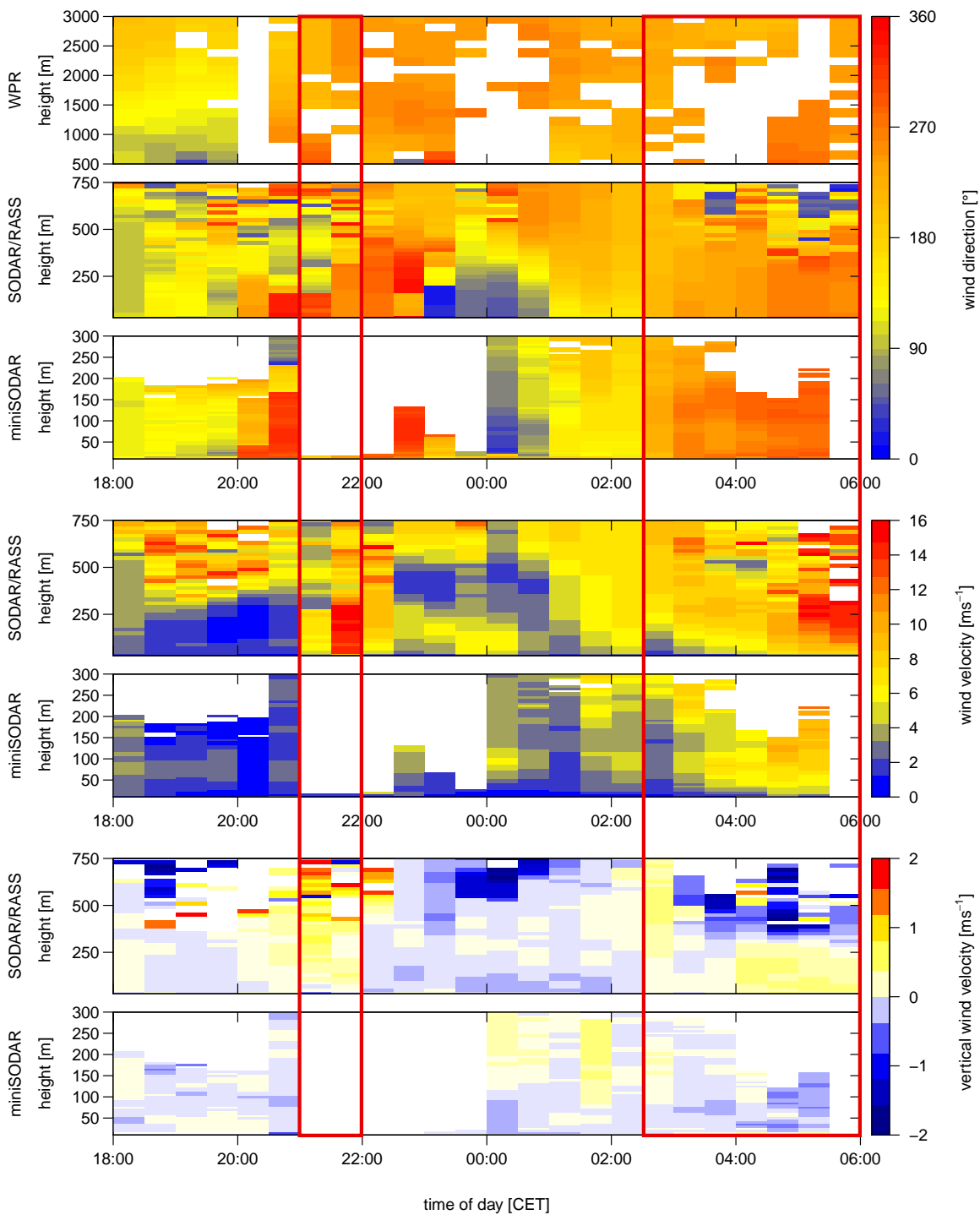


Figure 3.34. Vertical profiles from windprofiler (WPR), SODAR/RASS, and miniSODAR of the wind direction (above), wind velocity (middle), and vertical wind velocity (below) from 07 July 18:00 to 08 July 2011 06:00 CET. First red rectangle marks the inflow of fresh air between 21:00 to 22:00 CET and the second the west wind situation after 02:30 CET.

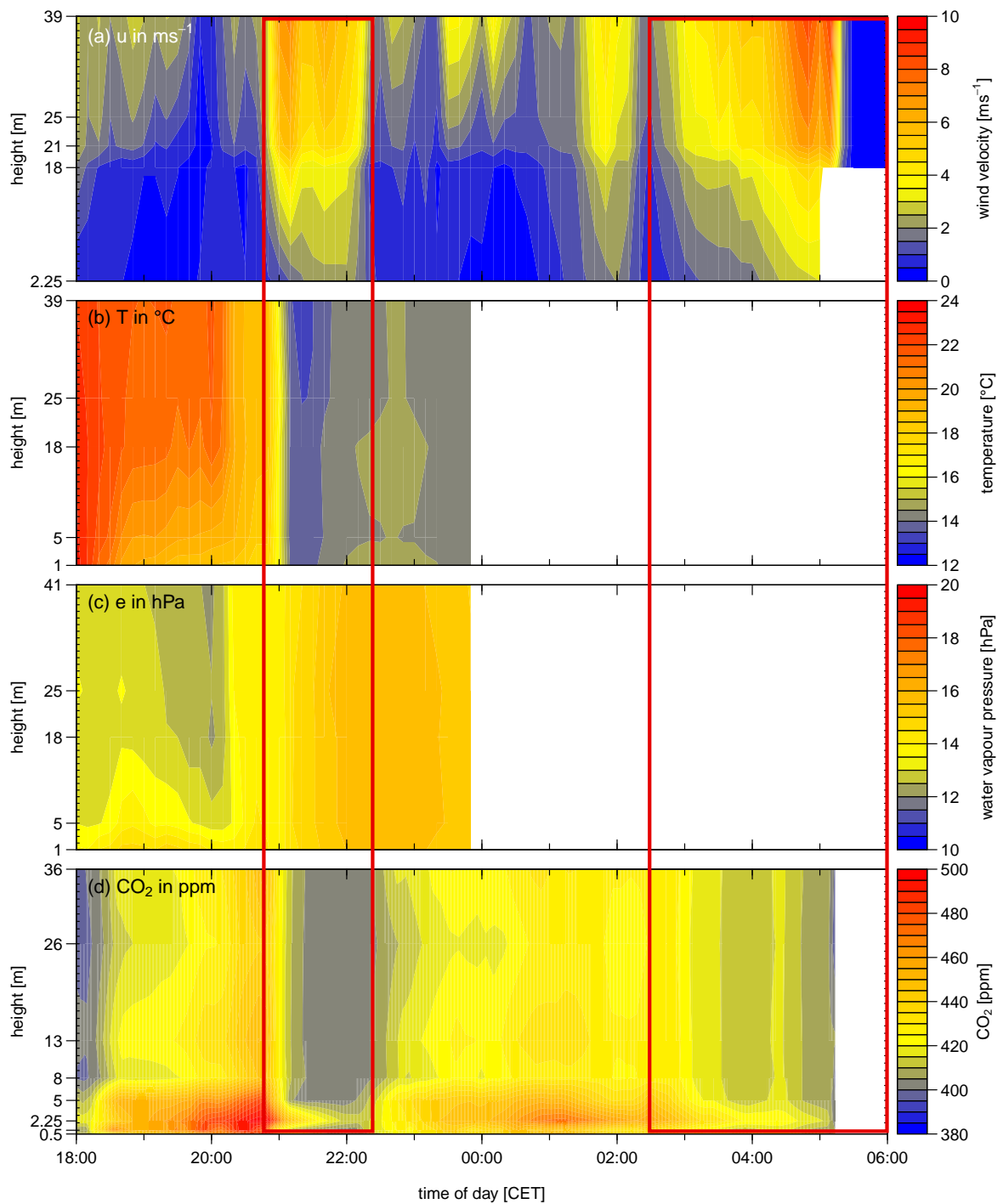


Figure 3.35. Vertical profiles of wind velocity u (a), temperature T (b), water vapour pressure e (c) and CO_2 concentration (d) measured at tower M3 at the stated heights from 07 July 2011, 18:00 to 24:00 CET. Red rectangle marks the inflow of fresh air between 21:00 to 22:00 CET and the second the west wind situation after 02:30 CET. Remarks: (i) The colour scaling and (ii) also the stated heights are different in the graphs.

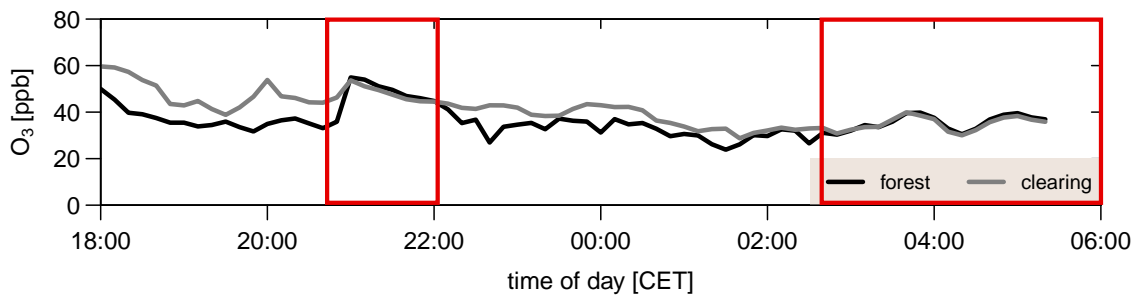


Figure 3.36. O_3 concentration within the forest measured with the monitor ‘49i’ and at the clearing measured with the monitor at the tower M4 from 07 July 18:00 to 08 July 2011 06:00 CET. First red rectangle marks the inflow of fresh air between 21:00 to 22:00 CET and the second the west wind situation after 02:30 CET. Figure 2.2 shows the location of the measurements.

inflow causes also significant changes in the temperature (Figure 3.35b) and water vapour profile (Figure 3.35c). There is a temperature gradient before the inflow, with maximum near the canopy and the strongest cooling near the ground. During the inflow there is a decrease of more than 4 K observable, with a well mixed profile. After the inflow, the temperature increases slightly. The water vapour pressure in Figure 3.35c has before the inflow its maximum also near ground. With the inflow there is also a well mixed profile, with an obvious increase. After midnight there are no data available. The effect of the inflow on temperature, as well as on water vapour pressure is slightly delayed, compared to the increase of wind velocity, but with the maximum of the wind velocity, the influence of the inflow starts as well. This behaviour was also measured in the CO_2 concentration (Figure 3.35d), which has before the inflow a profile, as described in Section 3.4.3, with maximum near ground at 2.25 m. In this night there is also a nocturnal drainage observable, which is almost interrupted by the inflow of the fresh, CO_2 -depleted air. But there is still a concentration maximum at 2.25 m visible and it looks like there is still a discernible outflow of CO_2 , even though the wind direction at 2.25 m at M3 turns from north to west (not presented). The CO_2 fluxes increases at all locations during this event. After the inflow, the concentration increases along the total profile again, but not to an equal level like before the inflow. So it can be presumed from the CO_2 measurements at M3, that the fresh air also distributes into the forest. But there were no HMMS measurements during this event conducted and also the coherent structures and coupling regimes are not available in order to verify this assumption.

The O_3 concentration presented in Figure 3.36, is the only indication for a horizontal distribution of the inflow, since the measurements were conducted within the forest (monitor ‘49i’), and at the clearing (monitor at M4). The deviations between both locations are obvi-

ous and the monitor at the clearing always shows 5 – 15 ppb higher concentrations before the inflow. But during the inflow, marked by the first red rectangle, the concentrations are almost identical (< 2 ppb) and afterwards, the concentrations differ again. The second red rectangle shows the west wind situation after 02:30 CET and here, the horizontal profile is also well mixed.

4. Conclusions

The comprehensive goal of this study was to obtain better knowledge about exchange processes, in a heterogeneous forest ecosystems in the temperate climate of Central Europe with a focus on horizontal structures. Therefore, measurements were conducted in the vicinity of a forest edge (transect from a dense spruce forest to an open clearing) during the third intensive observation period of the EGER project (EGER IOP3, Section 2.1) in the 'Fichtelgebirge Mountains' (northeastern Bavaria, Germany). Beside common static tower measurements (Section 2.2), a novel Horizontal Mobile Measuring System (HMMS; Section 2.3; Hübner et al., 2011, 2014) was developed and for the first time, measurements with a mobile system were conducted at an obvious forest edge, with a focus on horizontal structures influenced by the forest edge. Despite the limited payload and dimension restrictions, eight quantities could be measured with the HMMS, and for the first time the ozone concentration on such a small system. Foken et al. (2012b) designated trace gases as 'passive tracers' for different coupling regimes, and therefore, the carriage of such an analyser on a mobile system is an innovation in near ground atmospheric observation. Dynamical errors caused by the individual response times of the sensors have been considered to obtain the exact location of the HMMS' measurements. Therefore, a linear correction algorithm was applied for the first time in near-ground horizontal mobile measuring systems. The following conclusions for the HMMS can be drawn:

- To assess the technical side of the HMMS, it should be pointed out that the system development and the desired measuring procedure worked like anticipated, with some limitations. These include: (i) the wearing process of the engines was high, due to the total weight of the HMMS (17 kg), and therefore, a change of the engines after the EGER IOP3 project was necessary. (ii) Additionally, the HMMS stopped or faltered because of the high coefficient of thermal expansion of the rails' material (brass). Both problems and their consequences are discussed in more detail in Section 2.3.5. During a subsequent project (EVENT II; Jentsch and Beierkuhnlein, 2010; Babel et al., 2013) with the HMMS, which was conducted in summer 2012, modified rail connectors were used between the 2 m long rail segments, which res-

ulted in a significant improvement in the rail system. Thus, problem (ii) could be completely eliminated. A more robust drive system, like for example Örländer and Langvall (1993) and Oncley et al. (2009) used with cables and steel wheels is certainly more uncomplicated in terms of consistency, durability, and has in addition a broader range of usability (variation in height, or respectively measurements in heights above few metres are possible), but on the other side the development effort and financial input is substantially larger.

- The set of devices, used for the control of the HMMS, as well as the data acquisition were nearly unproblematic. The HMMS software was, together with the DAQ device, a perfect interface between the sensors and the data acquisition and also between the determination of position (bar codes) and the HMMS speed and driving direction system. The flexibility and usability could not be achieved by common used data loggers, and size and weight of for example a CR3000 (Campbell Scientific Inc., Logan, Utah, USA) and our set of devices is not much different. Only the bar code scanner had during humid conditions (morning fog) intermediately some failed readings, because of dew on the codes and the sensor's glass. During sunny days the scanner had to be shaded to avoid fail readings.
- In case of the sensor system on the HMMS, most sensors (CMP3/CGR3, HMP155, O₃ analyser) are frequently used in (micro-)meteorological measurements and consequently, application was quite simple and the results were adequate (Section 3.1). The HMMS design and the realised modifications to some sensors (named in Section 2.3.3) do not have an influence overall. Only because of the low accuracy (± 40 ppm) and the radiation induced errors in the CO₂ concentration measurements, a change to a more accurate sensor should be considered. Since larger spatial differences in CO₂ measurements occur mainly during nighttime, this is not a significant limitation in the applicability of the HMMS. Another possibility could be the protection of the sensor with a housing and cooling system. This could in turn lead to high demands being placed on the power supply of the HMMS. Here, maybe the change from a transparent to a non-transparent Makrolon® cover could already be the remedy. We chose the transparent cover only for an easy view into the HMMS.
- The horizontal profiles measured with the HMMS show a gradient near the forest edge, with a spatial relocation caused by the individual sensor response times τ . The application of the correction algorithm shows a more significant gradient within a shorter distance (see Section 2.4.1). So the before-and-after comparisons illustrate

the need of a correction, especially for slow responding sensors. The results of the correction algorithm (first-order) are, for most cases, absolutely sufficient. An improvement could be a second-order system (Brock and Richardson, 2001), which requires the function of the non-steady-state conditions, but this is unknown. Therefore, an approximation would be necessary with the derivation of a parabola-like transfer function with the consideration of local heterogeneities (combination of first and second-order systems). Another possible way can be an approximation with many overlaid linear functions. However, both algorithms are very work-intensive for an insignificant advantage. Regardless of which kind of algorithm, an approximation is only possible for every single run (one direction) and not for the entire time series, or parts thereof. The reason is that the transition from the forest to the clearing is (except for radiation) greatly influenced by turbulent/coherent structures, rapidly changing the conditions there. Due to the high effort necessary for the application of the correction algorithm, it can only be applied for short events (few runs of HMMS), where a detailed investigation of gradients near the edge is required.

- The limited application of the correction algorithm over the entire time series or even parts (e.g. daily time series), resulted in the use of uncorrected profiles, which are absolutely sufficient for the interpretation of daily variations (e.g. Figure 3.21 in Section 3.4.1). Another approach for the detailed investigation of horizontal gradients was performed by averaging over a well-defined preceding time (Section 3.2.1) and was also adopted in the supervised bachelor thesis of Schaller (2012). This approach minimises the influence of small-scale fluctuations and the dynamical errors in an acceptable manner and can be easily applied for the entire time series.

Combined with tower measurements (especially eddy-covariance measurements), the HMMS is a good tool for a better understanding of the exchange processes near the forest edge and the investigations went during this study into three directions: (i) the investigation of the heterogeneity of scalars in combination with the results found in Foken et al. (2012b) for EGER IOP1/IOP2, (ii) the influence of coherent structures and coupling regimes on horizontal structures according to the findings by Eder et al. (2013) for EGER IOP3 and (iii) the influences of atmospheric boundary layer phenomena (occurring mainly during nighttime). Additionally, the results of Gatzsche (2013) were considered. The main results and findings can be concluded as follows:

- Significant differences in meteorological quantities could be observed along the transect perpendicular to the forest edge, with highest changes/gradients occurring near

the forest edge within short distance (Section 3.2.1). Additionally, the investigations of single runs of the HMMS showed that especially in the turbulence influenced quantities (temperature, humidity and trace gas concentrations), significant changes in the gradients could be found at the forest edge within a short period of time, while the influence decreased both into the forest and onto the clearing. It could, for instance, be shown that during night (Figure 3.13; 20:00 – 22:00 CET, before the LLJ event) an inflow of colder, more humid and CO₂ enriched air could be seen only at the forest edge. The inflow propagated into the forest approximately 25 m and onto the clearing 50 m. Further away, the concentrations were significantly lower and the temperatures higher. This is a phenomenon caused by the forest edge and the prevailing structures there and could be visualised by the HMMS measurements. This observation could be confirmed by the coherent transport, where only at the forest edge a daily cycle in the contribution of ejections/sweeps was observable (Figure 3.13; Eder et al., 2013).

- Highest temperatures (and lowest humidities) occurred in the vicinity of the forest edge during daytime and these conditions facilitate a thermal updraft. This is caused by (i) highest radiation forcing (long-wave upwelling radiation from the clearing and down-welling from the forest), (ii) highest amount of deadwood (low albedo), (iii) low wind velocities and (iv) the advective transport of energy towards the forest edge. Eder et al. (2013) found an ejection dominated coherent transport during daytime only at the forest edge. The vertical CO₂ profile (Section 3.3.1) showed a well mixed profile during daytime, as well as the highest variation in the CO₂ fluxes occurred at 41 m at the forest edge. A similar behaviour can be expected for O₃ fluxes and for certain also for other trace gases. But variations in CO₂ fluxes were also found during nighttime. Therefore, the impact on the net ecosystem exchange by the forest edge should be investigated by long-term flux measurements, considering the footprint and advection terms (e.g. Baldocchi et al., 2000; Sogachev et al., 2005; Klaassen and Sogachev, 2006; Yi et al., 2008; Leclerc and Foken, 2014).
- Besides the ‘typical’ small-scale turbulent and coherent transport, there are large-scale quasi-stationary secondary circulations above the clearing, which could be visualised by the HMMS measurements and horizontal coupling regimes. The circulations showed horizontal advective transport and up-/downdrafts at different locations at different times (but mainly at the forest edge). This is due to: (i) the mean energy fluxes (mainly the latent heat) are increased at the forest edge, despite of the

higher available energy above the forest, which verifies the findings of enhanced heat fluxes and advective transport towards the forest edge by Klaassen et al. (2002) and Leclerc et al. (2003). And, (ii) the ejection dominated coherent transport during daytime (updrafts) and sweep dominated during nighttime (inflow of fresh air), which was found by Eder et al. (2013) only at the forest edge and independent from the prevailing wind direction. This leads (iii) on average to a better energy balance closure at the forest edge (17 %), compared to the clearing and the forest (25 – 30 %), with highest variation in energy fluxes observed in the diurnal cycle at the forest edge, and therefore also in the energy balance closure. The variations in the fluxes and hence the available energy are in particular affected by the contribution of ejections. Consequently, (iv) if there is a change in the energy fluxes at the forest edge, there is also a weakened change in the fluxes above the forest and at the clearing (Section 3.4.1). This implies a transport towards the forest edge and weakened transport to the forest, but also off the forest edge towards the clearing, where one location is fed with energy, while from the other location energy is extracted. This transport can not be only described by horizontal advection, but rather by a circulation above the clearing. (v) This circulations could be confirmed by changes in the horizontal coupling regimes along the transect perpendicular to the forest edge, as well as in the horizontal profile of the O_3 concentration, measured with the HMMS. At times of energy exchange between the locations, there is a horizontal coupling along the transect (or at least between forest edge and clearing), and it has to be considered that this secondary circulation influences the coherent transport along the total transect, and also within the forest. This could be confirmed by an inflow of O_3 -depleted air, with slightly lower temperatures. This air originates from above the clearing and is distributed over the total 150 m long HMMS profile and it should be assumed that the spatial distribution of secondary circulations is larger.

- The ACASA model (Gatzsche, 2013) has in general a better agreement with the buoyancy corrected measured data (Charuchittipan et al., 2014), which implies also the formation of quasi-stationary secondary circulations, since those are mainly driven by differences in thermal heating (buoyancy-driven). Additionally, the third-order closure of the ACASA model showed, in general, good agreement regarding coherent structures and changing coupling regimes. However, significant deviations in the model results were found during nighttime with a decoupled sub-canopy (Ds), indicating horizontal advective transport (nocturnal drainage), but also secondary circulations, which can not be captured adequately by the ACASA model.

- Boundary layer dynamics play an important role in the exchange processes of (heterogeneous) forest ecosystems, and therefore vertical profile measurements of the boundary layer (SODAR), as well as the investigation of coherent transport and coupling regimes should be investigated, if exchange processes want to be described correctly. It could be shown that (i) during low-level jets (LLJ) increased CO₂ fluxes can be observed (like in e.g. Karipot et al., 2006, 2008; Foken et al., 2012b), due to high friction velocity u_* and good mixing with coupled situations (C/Cs). While the CO₂ fluxes increase significantly above the forest and at the forest edge, the fluxes at the clearing increase only marginally. This could be visualised by different concentrations, where lowest concentrations occurred in the forest and slightly higher at the forest edge, and even higher at the clearing. During weak-LLJ events, a decrease of the fluxes could be observed, coming along with an accumulation of CO₂ and a depletion of O₃, but during extremely weak-LLJ events, there are possible inflows by sweeps at the forest edge. (ii) If atmospheric inversion layers occur below the altitude of the site (and thus: only relevant for forest ecosystems in higher altitudes), strong wind shears often exist across the inversion layer, causing a long decoupled situation (Wa), and an enormous reduction of CO₂ fluxes. Here, the strongest reduction was found above the forest and the least at the clearing, which coincide with the observations of found flux increases during LLJ events. The different fluxes led to a different accumulation of CO₂, but because of the sloping area, the high CO₂ concentrations drained out of the forest onto the clearing. (iii) Passing of convergence lines or widened strong wind situations during coupled regimes lead to an inflow of fresh, CO₂-depleted air, which is distributed over the total transect.
- Due to found differences in the fluxes along the transect perpendicular to the forest edge, during various boundary layer dynamics, it can be assumed that the contribution and the scale of coherent structures plays an important role for the exchange processes. And both are largest above the forest and decreasing towards the clearing (Eder et al., 2013). This makes it necessary to investigate and interpret the different locations separately, regardless of which kind of heterogeneous ecosystem. In so doing, horizontal as well as vertical gradient measurements of CO₂, O₃, but also temperature measurements are, beside of flux measurements important tools to realise different coupling regimes, as well as inflows and outflows. To which extent the small size of the clearing plays a role, and if and how the other forest edges (mainly south due to the prevailing wind direction during LLJ events) may effect the measurements at the clearing, could be investigated at a forest edge not within

a clearing, or within a larger clearing. Alternatively, large eddy simulations should be considered. This could provide ultimate certainty.

Finally, it should be said, that the continuous horizontal gradient measurements of the HMMS provide an enhanced overview of the horizontal structures in the transition from the dense spruce forest to the open clearing, which is in this range absolutely new for the community. Additionally, the measurements and presentation of temporal dynamics of prevailing structures relating to inflows, outflows, but also accumulations, and depletions is also new along such a transect. This gained knowledge provides together with the used standard tower/profile measurements (in horizontal and vertical transects) a better understanding of exchange processes of heterogeneous forest ecosystems. The results found by Eder et al. (2013) could be confirmed and the appearance of coherent/turbulent transport and coupling regimes could be visualised in spatial and temporal terms without exception. The knowledge about coupling regimes, coherent and turbulent transport of trace gases, gained by Foken et al. (2012b) for the homogenous part of the heterogeneous forest ecosystem could be confirmed, but also extended to the heterogeneity. Additionally, secondary circulations could be confirmed to some extent by the visualisation of an O₃-depleted inflow of fresh air over the total profile, and the horizontal transport of energy (indicated by horizontal coupling). Such an overview of prevailing gradients, inflows, outflows, accumulations, depletions, as well as insights on coherent/turbulent transport, coupling regimes and secondary circulations over spatial and temporal terms would have not been possible if only static tower measurements were used instead in combination with the HMMS. It must be emphasised that, as with every mobile measuring system, the HMMS has the limitation that it can not measure at every location simultaneously. So the HMMS or another mobile measuring system can never replace tower measurements, otherwise small-scale and short-time events could not be captured adequately.

The focus of further investigations should now be the time scales of the found secondary circulations and their spatial extension, as well as the contribution of coherent structures and their influence on long-term fluxes in such a heterogeneous forest ecosystem. Here, large eddy simulations of this heterogeneous site are now of great interest, in order to verify the measured observations (Kanani et al., 2014). A further approach of experimental measurements can be described as follows: (i) High frequency horizontal and vertical O₃/CO₂ profile in 2D/3D arrangement, and/or (ii) high frequency fibre-optic temperature measurements (Thomas et al., 2012), in combination with the HMMS measurements. In all aspects, the role of clearing sizes, as well as the bias of forest edges with regard to the main wind flow should be considered.

References

- Antonia, R. A. (1981). Conditional Sampling in Turbulence Measurement. *Annu. Rev. Fluid Mech.*, 13 (1), pp. 131–156. DOI: 10.1146/annurev.fl.13.010181.001023.
- Assmann, R. (1887). Das Aspirationspsychrometer, ein neuer Apparat zur Ermittlung der wahren Temperatur und Feuchtigkeit der Luft. *Das Wetter*, 4, pp. 245–286.
- Assmann, R. (1888). Das Aspirationspsychrometer, ein neuer Apparat zur Ermittlung der wahren Temperatur und Feuchtigkeit der Luft. *Das Wetter*, 5, pp. 1–22.
- Aubinet, M., Grelle, A., Ibrom, A., Rannik, Ü., Moncrieff, J., Foken, T., Kowalski, A. S., Martin, P. H., Berbigier, P., Bernhofer, C., Clement, R., Elbers, J., Granier, A., Grünwald, T. H., Morgenstern, K., Pilegaard, K., Rebmann, C., Snijders, W., Valentini, R., and Vesala, T. (2000). Estimates of the Annual Net Carbon and Water Exchange of Forests: The EUROFLUX Methodology. *Adv. Ecol. Res.*, 30, pp. 113–175. DOI: 10.1016/S0065-2504(08)60018-5.
- Aubinet, M., Heinesch, B., and Yernaux, M. (2003). Horizontal and vertical CO₂ advection in a sloping forest. *Bound.-Lay. Meteorol.*, 108 (3), pp. 397–417. DOI: 10.1023/A:1024168428135.
- Babel, W., Schaller, C., Eigenmann, R., Foken, T., Hübner, J., Jentsch, A., Kreyling, J., Sultana, F., and Zhao, P. (2013). Documentation of the EVENT-HMMS Experiment 2012 – Microclimatological effects of rain-out shelters within EVENT II. Work Report, University of Bayreuth, Dept. of Micrometeorology, ISSN: 1614-8916, 55, p. 43.
- Baldocchi, D. (2014). Measuring fluxes of trace gases and energy between ecosystems and the atmosphere - the state and future of the eddy covariance method. *Glob. Change Biol.* DOI: 10.1111/gcb.12649.
- Baldocchi, D. D., Matt, D. R., Hutchison, B. A., and McMillen, R. T. (1984a). Solar radiation within an oak-hickory forest: an evaluation of the extinction coefficients for several radiation components during fully-leafed and leafless periods. *Agr. For. Meteorol.*, 32 (3), pp. 307–322. DOI: 10.1016/0168-1923(84)90056-X.

- Baldocchi, D., Hutchison, B., Matt, D., and McMillen, R. (1984b). Seasonal variations in the radiation regime within an oak-hickory forest. *Agr. For. Meteorol.*, 33 (2), pp. 177–191. DOI: 10.1016/0168-1923(84)90069-8.
- Baldocchi, D., Finnigan, J. F., Wilson, K., Paw U, K. T., and Falge, E. (2000). On Measuring Net Ecosystem Carbon Exchange Over Tall Vegetation on Complex Terrain. *Bound.-Lay. Meteorol.*, 96 (1), pp. 257–291. DOI: 10.1023/A:1002497616547.
- Baldocchi, D., Falge, E., Gu, L., Olson, R., Hollinger, D., Running, S., Anthoni, P., Bernhofer, C., Davis, K., Evans, R., Fuentes, J., Goldstein, A., Katul, G., Law, B., Lee, X., Malhi, Y., Meyers, T., Munger, W., Oechel, W., Paw U, K. T., Pilegaard, K., Schmid, H. P., Valentini, R., Verma, S., Vesala, T., Wilson, K., and Wofsy, S. (2001). FLUXNET: A new tool to study the temporal and spatial variability of ecosystem-scale carbon dioxide, water vapor, and energy flux densities. *B. Am. Meteorol. Soc.*, 82 (11), pp. 2415–2434. DOI: 10.1175/1520-0477(2001)082<2415:FANTTS>2.3.CO;2.
- Ballantyne, A. P., Alden, C. B., Miller, J. B., Tans, P. P., and White, J. W. C. (2012). Increase in observed net carbon dioxide uptake by land and oceans during the past 50 years. *Nature*, 488 (7409), pp. 70–72. DOI: 10.1038/nature11299.
- Balsley, B. B., Baisley, C. L., Williams, J. B., and Tyrrell, G. W. (1992). Atmospheric Research Using Kites: Here We Go Again!. *B. Am. Meteorol. Soc.*, 73 (1), pp. 17–29. DOI: 10.1175/1520-0477(1992)073<0017:ARUKHW>2.0.CO;2.
- Balsley, B. B., Jensen, M. L., and Frehlich, R. G. (1998). The Use of State-of-the-Art Kites for Profiling the Lower Atmosphere. *Bound.-Lay. Meteorol.*, 87 (1), pp. 1–25. DOI: 10.1023/A:1000812511429.
- Barthlott, C., Drobinski, P., Fesquet, C., Dubos, T., and Pietras, C. (2007). Long-term study of coherent structures in the atmospheric surface layer. *Bound.-Lay. Meteorol.*, 125 (1), pp. 1–24. DOI: 10.1007/s10546-007-9190-9.
- Belcher, S. E., Finnigan, J. J., and Harman, I. N. (2008). Flows through forest canopies in complex terrain. *Ecol. Appl.*, 18 (6), pp. 1436–1453. DOI: 10.1890/06-1894.1.
- Belcher, S. E., Harman, I. N., and Finnigan, J. J. (2012). The Wind in the Willows: Flows in Forest Canopies in Complex Terrain. *Annu. Rev. Fluid Mech.*, 44 (1), pp. 479–504. DOI: 10.1146/annurev-fluid-120710-101036.
- Bentley, J. P. (2005). *Principles of measurement systems*. Pearson Prentice Hall, Harlow. p. 528.

- Bergström, H. and Högström, U. (1989). Turbulent exchange above a pine forest II. Organized structures. *Bound.-Lay. Meteorol.*, 49 (3), pp. 231–263. DOI: 10.1007/BF00120972.
- Blanken, P. D., Black, T. A., Neumann, H. H., den Hartog, G., Yang, P. C., Nestic, Z., and Lee, X. (2001). The seasonal water and energy exchange above and within a boreal aspen forest. *J. Hydrol.*, 245 (1), pp. 118–136. DOI: 10.1016/S0022-1694(01)00343-2.
- Brock, F. V. and Richardson, S. J. (2001). *Meteorological measurement systems*. New York: Oxford University Press.
- Brown, G. W. (1973). Measuring Transmitted Global Radiation with Fixed and Moving Sensors. *Agr. Meteorol.*, 11 (1), pp. 115–121. DOI: 10.1016/0002-1571(73)90055-1.
- Cantwell, B. J. (1981). Organized Motion in Turbulent Flow. *Annu. Rev. Fluid Mech.*, 13 (1), pp. 457–515. DOI: 10.1146/annurev.fl.13.010181.002325.
- Cassiani, M., Katul, G. G., and Albertson, J. D. (2008). The Effects of Canopy Leaf Area Index on Airflow Across Forest Edges: Large-eddy Simulation and Analytical Results. *Bound.-Lay. Meteorol.*, 126 (3), pp. 433–460. DOI: 10.1007/s10546-007-9242-1.
- Cava, D., Giostra, U., Siqueira, M., and Katul, G. (2004). Organised Motion and Radiative Perturbations in the Nocturnal Canopy Sublayer above an Even-Aged Pine Forest. *Bound.-Lay. Meteorol.*, 112 (1), pp. 129–157. DOI: 10.1023/B:BOUN.0000020160.28184.a0.
- Cellier, P. and Brunet, Y. (1992). Flux-gradient relationships above tall plant canopies. *Agr. For. Meteorol.*, 58 (1), pp. 93–117. DOI: 10.1016/0168-1923(92)90113-I.
- Charuchittipan, D., Babel, W., Mauder, M., Leps, J.-P., and Foken, T. (2014). Extension of the Averaging Time in Eddy-Covariance Measurements and Its Effect on the Energy Balance Closure. *Bound.-Lay. Meteorol.*, 152 (3), pp. 303–327. DOI: 10.1007/s10546-014-9922-6.
- Chen, J. M., Blanken, P. D., Black, T. A., Guilbeault, M., and Chen, S. (1997). Radiation regime and canopy architecture in a boreal aspen forest. *Agr. For. Meteorol.*, 86 (1), pp. 107–125. DOI: 10.1016/S0168-1923(96)02402-1.
- Chen, J., Franklin, J. F., and Spies, T. A. (1993). Contrasting microclimates among clearcut, edge, and interior of old-growth Douglas-fir forest. *Agr. For. Meteorol.*, 63 (3), pp. 219–237. DOI: 10.1016/0168-1923(93)90061-L.
- Chen, J., Franklin, J. F., and Spies, T. A. (1995). Growing-Season Microclimatic Gradients from Clearcut Edges into Old-Growth Douglas-Fir Forests. *Ecol. Appl.*, 5 (1), pp. 74–86. DOI: 10.2307/1942053.

- Collatz, G., Ball, J., Grivet, C., and Berry, J. A. (1991). Physiological and environmental regulation of stomatal conductance, photosynthesis and transpiration: a model that includes a laminar boundary layer. *Agr. For. Meteorol.*, 54 (2), pp. 107–136. DOI: 10.1016/0168-1923(91)90002-8.
- Collineau, S. and Brunet, Y. (1993a). Detection of turbulent coherent motions in a forest canopy part I: Wavelet analysis. *Bound.-Lay. Meteorol.*, 65 (4), pp. 357–379. DOI: 10.1007/BF00707033.
- Collineau, S. and Brunet, Y. (1993b). Detection of turbulent coherent motions in a forest canopy part II: Time-scales and conditional averages. *Bound.-Lay. Meteorol.*, 66 (1), pp. 49–73. DOI: 10.1007/BF00705459.
- Culf, A. D., Foken, T., and Gash, J. H. C. (2004). The Energy Balance Closure Problem. In: *Vegetation, Water, Humans and the Climate. A new perspective on an interactive system*. Ed. by P. Kabat, M. Claussen, P. A. Dirmeyer, J. H. C. Gash, L. B. Guenni, M. Meybeck, R. A. Pielke, C. I. Vörösmarty, R. W. A. Hutjes, and S. Lütkeemeier. Springer, Berlin/Heidelberg, pp. 159–166.
- Dabberdt, W. F. (1968). Tower-Induced Errors in Wind Profile Measurements. *J. Appl. Meteorol.*, 7 (3), pp. 359–366. DOI: 10.1175/1520-0450(1968)007<0359:TIEIWP>2.0.CO;2.
- Davies-Colley, R. J., Payne, G. W., and van Elswijk, M. (2000). Microclimate gradients across a forest edge. *New Zeal. J. Ecol.*, 24 (2), pp. 111–121.
- Dawson, J. W. and Sneddon, B. V. (1969). The New Zealand lowland rainforest. A comparison with tropical rainforest. *Pac. Sci.*, 23, pp. 131–147.
- Denmead, O. T. and Bradley, E. F. (1985). Flux-Gradient Relationships in a Forest Canopy. In: *The forest-atmosphere interaction. Proceedings of the Forest Environmental Measurements Conference held at Oak Ridge, Tennessee, October 23-28, 1983*. Ed. by B. A. Hutchison and B. B. Hicks. D. Reidel Publishing Company, Dordrecht, pp. 421–442.
- Denmead, O. T. and Bradley, E. F. (1987). On Scalar Transport in Plant Canopies. *Irrig. Sci.*, 8 (2), pp. 131–149. DOI: 10.1007/BF00259477.
- Dlugi, R. (1993). Interaction of NO_x and VOC's within vegetation. In: *Proceedings EURO-TRAC Symposium '92*. Ed. by P. W. Borrell. SPB Acad. Publ., The Hague, pp. 682–688.
- Duarte, H. F., Leclerc, M. Y., and Zhang, G. (2012). Assessing the shear-sheltering theory applied to low-level jets in the nocturnal stable boundary layer. *Theor. Appl. Climatol.*, 110 (3), pp. 359–371. DOI: 10.1007/s00704-012-0621-2.

- Dupont, S. and Brunet, Y. (2008). Edge Flow and Canopy Structure: A Large-Eddy Simulation Study. *Bound.-Lay. Meteorol.*, 126 (1), pp. 51–71. DOI: 10.1007/s10546-007-9216-3.
- Dupont, S. and Brunet, Y. (2009). Coherent structures in canopy edge flow: a large-eddy simulation study. *J. Fluid Mech.*, 630, pp. 93–128. DOI: 10.1017/S0022112009006739.
- Dupont, S., Irvine, M. R., Bonnefond, J.-M., Lamaud, E., and Brunet, Y. (2012). Turbulent Structures in a Pine Forest with a Deep and Sparse Trunk Space: Stand and Edge Regions. *Bound.-Lay. Meteorol.*, pp. 1–28. DOI: 10.1007/s10546-012-9695-8.
- Eder, F., Serafimovich, A., and Foken, T. (2013). Coherent structures at a forest edge: Properties, coupling and impact of secondary circulations. *Bound.-Lay. Meteorol.*, 148 (2), pp. 285–308. DOI: 10.1007/s10546-013-9815-0.
- FAO (2010). *Global Forest Resources Assessment 2010*. FAO Forestry Paper, 163, p. 378.
- Farquhar, G. D. and von Caemmerer, S. (1982). Modelling of Photosynthetic Response to Environmental Conditions. In: *Physiological Plant Ecology II - Encyclopedia of Plant Physiology - Volume 12 / B*. Ed. by O. L. Lange, P. S. Nobel, C. B. Osmond, and H. Ziegler. Springer Berlin, pp. 549–587.
- Fazu, C. and Schwerdtfeger, P. (1989). Flux-gradient relationships for momentum and heat over a rough natural surface. *Q. J. Roy. Meteor. Soc.*, 115 (486), pp. 335–352. DOI: 10.1002/qj.49711548607.
- Finnigan, J. (2000). Turbulence in Plant Canopies. *Annu. Rev. Fluid Mech.*, 32 (1), pp. 519–571. DOI: 10.1146/annurev.fluid.32.1.519.
- Finnigan, J. J. (1979). Turbulence in waving wheat. *Bound.-Lay. Meteorol.*, 16 (2), pp. 213–236. DOI: 10.1007/BF02350512.
- Finnigan, J. J., Clement, R., Malhi, Y., Leuning, R., and Cleugh, H. A. (2003). A Re-Evaluation of Long-Term Flux Measurement Techniques Part I: Averaging and Coordinate Rotation. *Bound.-Lay. Meteorol.*, 107 (1), pp. 1–48. DOI: 10.1023/A:1021554900225.
- Finnigan, J. J., Shaw, R. H., and Patton, E. G. (2009). Turbulence structure above a vegetation canopy. *J. Fluid Mech.*, 637, pp. 387–424. DOI: 10.1017/S0022112009990589.
- Foken, T. (2003). Lufthygienisch-bioklimatische Kennzeichnung des oberen Egertales (Fichtelgebirge bis Karlovy Vary). *Bayreuther Forum Ökologie*, ISSN: 0944-4122, 100, p. 69+XLVIII.

- Foken, T. (2004). Climate Change in the Lehstenbach Region. In: *Biogeochemistry of Forested Catchments in a Changing Environment, A German Gase Study*. Ecological Studies. Ed. by E. Matzner. Springer, Heidelberg, pp. 59–66.
- Foken, T. (2008a). *Micrometeorology*. Springer-Verlag Heidelberg, XX, p. 308.
- Foken, T. (2008b). The energy balance closure problem: An overview. *Ecol. Appl.*, 18 (6), pp. 1351–1367. DOI: 10.1890/06-0922.1.
- Foken, T. and Wichura, B. (1996). Tools for quality assessment of surface-based flux measurements. *Agr. Meteorol.*, 78 (1), pp. 83–105. DOI: 10.1016/0168-1923(95)02248-1.
- Foken, T., Dlugi, R., and Kramm, G. (1995). On the determination of dry deposition and emission of gaseous compounds at the biosphere-atmosphere interface. *Meteorol. Z.*, 4, pp. 91–118.
- Foken, T., Göckede, M., Mauder, M., Mahrt, L., Amiro, B., and Munger, W. (2004). Post-Field Data Quality Control. In: *Handbook of Micrometeorology*. Ed. by X. Lee, W. Massman, and B. E. Law. Vol. 29. Kluwer, Dordrecht, pp. 181–208.
- Foken, T., Wimmer, F., Mauder, M., Thomas, C., and Liebethal, C. (2006). Some aspects of the energy balance closure problem. *Atmos. Chem. Phys.*, 6 (12), pp. 4395–4402. DOI: 10.5194/acp-6-4395-2006.
- Foken, T., Mauder, M., Liebethal, C., Wimmer, F., Beyrich, F., Leps, J.-P., Raasch, S., DeBruin, H. A. R., Meijninger, W. M. L., and Bange, J. (2010). Energy balance closure for the LITFASS-2003 experiment. *Theor. Appl. Climatol.*, 101 (1), pp. 149–160. DOI: 10.1007/s00704-009-0216-8.
- Foken, T., Leuning, R., Oncley, S. P., Mauder, M., and Aubinet, M. (2012a). Corrections and data quality. In: *Eddy covariance: A practical guide to measurement and data analysis*. Ed. by M. Aubinet, T. Vesala, and D. Papale. Springer, Dordrecht, Heidelberg, London, New York, pp. 85–131.
- Foken, T., Meixner, F. X., Falge, E., Zetzsch, C., Serafimovich, A., Bargsten, A., Behrendt, T., Biermann, T., Breuninger, C., Dix, S., Gerken, T., Hunner, M., Lehmann-Pape, L., Hens, K., Jocher, G., Kesselmeier, J., Lüers, J., Mayer, J.-C., Moravek, A., Plake, D., Riederer, M., Rütz, F., Scheibe, M., Siebicke, L., Sörgel, M., Staudt, K., Trebs, I., Tsokankunku, A., Welling, M., Wolff, V., and Zhu, Z. (2012b). Coupling processes and exchange of energy and reactive and non-reactive trace gases at a forest site – results of the EGER experiment. *Atmos. Chem. Phys.*, 12 (4), pp. 1923–1950. DOI: 10.5194/acp-12-1923-2012.

- Foken, T., Aubinet, M., Finnigan, J. J., Leclerc, M. Y., Mauder, M., and Paw U, K. T. (2011). Results Of A Panel Discussion About The Energy Balance Closure Correction For Trace Gases. *Bull. Amer. Meteor. Soc.*, 92 (4), ES13–ES18. DOI: 10.1175/2011BAMS3130.1.
- Frankenberger, E. (1951). Untersuchungen über den Vertikalaustausch in den unteren Dekametern der Atmosphäre. *Ann. Meteor.*, 4, pp. 358–374.
- Friehe, C. A. and Khelif, D. (1992). Fast-Response Aircraft Temperature Sensors. *J. Atmos. Ocean. Tech.*, 9 (6), pp. 784–795. DOI: 10.1175/1520-0426(1992)009<0784:FRATS>2.0.CO;2.
- Gamon, J. A., Cheng, Y., Claudio, H., Mackinney, L., and Sims, D. A. (2006). A mobile tram system for systematic sampling of ecosystem optical properties. *Remote Sens. Environ.*, 103 (3), pp. 246–254. DOI: 10.1016/j.rse.2006.04.006.
- Gao, W., Shaw, R. H., and Paw U, K. T. (1989). Observation of organized structure in turbulent flow within and above a forest canopy. *Bound.-Lay. Meteorol.*, 47 (1), pp. 349–377. DOI: 10.1007/BF00122339.
- Garratt, J. R. (1978). Flux profile relations above tall vegetation. *Q. J. Roy. Meteor. Soc.*, 104 (439), pp. 199–211. DOI: 10.1002/qj.49710443915.
- Garratt, J. R. (1980). Surface influence upon vertical profiles in the atmospheric near-surface layer. *Q. J. Roy. Meteor. Soc.*, 106 (450), pp. 803–819. DOI: 10.1002/qj.49710645011.
- Gatzsche, K. (2013). Modellierung des Energie- und Stoffaustausch im Grenzbereich Wald–Lichtung unter besonderer Berücksichtigung des Einflusses kohärenter Strukturen. University of Leipzig. p. 137.
- Gerstberger, P., Foken, T., and Kalbitz, K. (2004). The Lehstenbach and Steinkreuz catchments in NE Bavaria, Germany. In: *Biogeochemistry of Forested Catchments in a Changing Environment, A German Gase Study*. Ecological Studies. Ed. by E. Matzner. Springer, Heidelberg, pp. 15–41.
- Glickman, T. S. (2000). *Glossary of meteorology*. 2nd edn. Am. Meteorol. Soc., Boston, MA, USA. p. 855.
- Güsten, H. and Heinrich, G. (1996). On-line measurements of ozone surface fluxes: Part I. Methodology and instrumentation. *Atmos. Environ.*, 30 (6), pp. 897–909. DOI: 10.1016/1352-2310(95)00269-3.
- Harman, I. N. and Finnigan, J. J. (2007). A simple unified theory for flow in the canopy and roughness sublayer. *Bound.-Lay. Meteorol.*, 123 (2), pp. 339–363. DOI: 10.1007/s10546-006-9145-6.

- Harman, I. N. and Finnigan, J. J. (2008). Scalar Concentration Profiles in the Canopy and Roughness Sublayer. *Bound.-Lay. Meteorol.*, 129 (3), pp. 323–351. DOI: 10.1007/s10546-008-9328-4.
- Haverd, V., Cuntz, M., Leuning, R., and Keith, H. (2007). Air and biomass heat storage fluxes in a forest canopy: Calculation within a soil vegetation atmosphere transfer model. *Agr. For. Meteorol.*, 147 (3), pp. 125–139. DOI: 10.1016/j.agrformet.2007.07.006.
- Hendl, M. (1991). Globale Klimaklassifikation. In: *Das Klimasystem der Erde. Diagnose und Modellierung, Schwankungen und Wirkungen*. Ed. by P. Hupfer. Akad.-Verl., Berlin, pp. 218–266.
- Heusinkveld, B., Jacobs, A., Holtslag, A., and Berkowicz, S. (2004). Surface energy balance closure in an arid region: role of soil heat flux. *Agr. For. Meteorol.*, 122 (1), pp. 21–37. DOI: 10.1016/j.agrformet.2003.09.005.
- Holmes, O., Lumley, J. L., Berkooz, G., and Rowley, C. W. (2012). *Turbulence, coherent structures, dynamical systems and symmetry*, 2nd Edition. Cambridge University Press, Cambridge, UK. p. 386.
- Houghton, R. A. (2003). Why are estimates of the terrestrial carbon balance so different?. *Glob. Change Biol.*, 9 (4), pp. 500–509. DOI: 10.1046/j.1365-2486.2003.00620.x.
- House, J. I., Prentice, I. C., Ramanakutty, N., Houghton, R. A., and Heimann, M. (2003). Reconciling apparent inconsistencies in estimates of terrestrial CO₂ sources and sinks. *Tellus B*, 55 (2), pp. 345–363. DOI: 10.1034/j.1600-0889.2003.00037.x.
- Huang, J., Cassiani, M., and Albertson, J. D. (2011). Coherent Turbulent Structures Across a Vegetation Discontinuity. *Bound.-Lay. Meteorol.*, 140 (1), pp. 1–22. DOI: 10.1007/s10546-011-9600-x.
- Hübner, J., Olesch, J., Falke, H., Meixner, F. X., and Foken, T. (2011). Documentation and Instruction Manual for the Horizontal Mobile Measuring System (HMMS). Work Report, University of Bayreuth, Dept. of Micrometeorology, ISSN: 1614-8916, 48, p. 88.
- Hübner, J., Olesch, J., Falke, H., Meixner, F. X., and Foken, T. (2014). A horizontal mobile measuring system for atmospheric quantities. *Atmos. Meas. Tech.*, 7 (9), pp. 2967–2980. DOI: 10.5194/amt-7-2967-2014.
- Inagaki, A., Letzel, M. O., Raasch, S., and Kanda, M. (2006). Impact of Surface Heterogeneity on Energy Imbalance: A Study Using LES. *J. Meteorol. Soc. Japan*, 84 (1), pp. 187–198. DOI: 10.2151/jmsj.84.187.

- Inagaki, A., Castillo, M. C. L., Yamashita, Y., Kanda, M., and Takimoto, H. (2012). Large-Eddy Simulation of Coherent Flow Structures within a Cubical Canopy. *Bound.-Lay. Meteorol.*, 142 (2), pp. 207–222. DOI: 10.1007/s10546-011-9671-8.
- Inverarity, G. W. (2000). Correcting Airborne Temperature Data for Lags Introduced by Instruments with Two-Time-Constant Responses. *J. Atmos. Ocean. Tech.*, 17 (2), pp. 176–184. DOI: 10.1175/1520-0426(2000)017<0176:CATDFL>2.0.CO;2.
- IPCC (2013). *Climate Change 2013: The physical science basis. Contribution of Working Group I to the Fifth Assessment Report of the Intergovernmental Panel on Climate Change*. Ed. by T. F. Stocker, D. Qin, G.-K. Plattner, M. Tignor, S. K. Allen, J. Boschung, A. Nauels, Y. Xia, V. Bex, and P. M. Midgley. Cambridge University Press, Cambridge, United Kingdom and New York, NY, USA. p. 1535.
- Jentsch, A. and Beierkuhnlein, C. (2010). Simulating the Future - Responses of Ecosystems, Key Species, and European Provenances to Expected Climatic Trends and Events. *Nova Acta Leopoldina NF*, 112 (384), pp. 89–98.
- Kaimal, J. C., Wyngaard, J. C., Haugen, D. A., Coté, O. R., Izumi, Y., Caughey, S. J., and Readings, C. J. (1976). Turbulence Structure in the Convective Boundary Layer. *J. Atmos. Sci.*, 33 (11), pp. 2152–2169. DOI: 10.1175/1520-0469(1976)033<2152:TSITCB>2.0.CO;2.
- Kanani, F., Träumner, K., Ruck, B., and Raasch, S. (2014). What determines the differences found in forest edge flow between physical models and atmospheric measurements? – An LES study. *Meteorol. Z.*, 23 (1), pp. 33–49. DOI: 10.1127/0941-2948/2014/0542.
- Kanda, M., Inagaki, A., Letzel, M. O., Raasch, S., and Watanabe, T. (2004). LES Study of the Energy Imbalance Problem with Eddy Covariance Fluxes. *Bound.-Lay. Meteorol.*, 110 (3), pp. 381–404. DOI: 10.1023/B:BOUN.0000007225.45548.7a.
- Karipot, A., Leclerc, M. Y., Zhang, G., Martin, T., Starr, G., Hollinger, D., McCaughey, J. H., and Hendrey, G. R. (2006). Nocturnal CO₂ exchange over a tall forest canopy associated with intermittent low-level jet activity. *Theor. Appl. Climatol.*, 85 (3), pp. 243–248. DOI: 10.1007/s00704-005-0183-7.
- Karipot, A., Leclerc, M. Y., Zhang, G., Lewin, K. F., Nagy, J., Hendrey, G. R., and Starr, G. (2008). Influence of nocturnal low-level jet on turbulence structure and CO₂ flux measurements over a forest canopy. *J. Geophys. Res.*, 113 (D10102). DOI: 10.1029/2007JD009149.

- Katul, G., Poggi, D., Cava, D., and Finnigan, J. (2006). The relative importance of ejections and sweeps to momentum transfer in the atmospheric boundary layer. *Bound.-Lay. Meteorol.*, 120 (3), pp. 367–375. DOI: 10.1007/s10546-006-9064-6.
- Klaassen, W. and Sogachev, A. (2006). Flux Footprint Simulation Downwind of a Forest Edge. *Bound.-Lay. Meteorol.*, 121 (3), pp. 459–473. DOI: 10.1007/s10546-006-9078-0.
- Klaassen, W., van Breugel, P. B., Moors, E. J., and Nieveen, J. P. (2002). Increased heat fluxes near a forest edge. *Theor. Appl. Climatol.*, 72 (3), pp. 231–243. DOI: 10.1007/s00704-002-0682-8.
- Kline, S. J., Reynolds, W. C., Schraub, F. A., and Runstadler, P. W. (1967). The structure of turbulent boundary layers. *J. Fluid Mech.*, 30 (4), pp. 741–773. DOI: 10.1017/S0022112067001740.
- Knohl, A., Kolle, O., Minayeva, T. Y., Milyukova, I. M., Vygorskaya, N. N., Foken, T., and Schulze, E.-D. (2002). Carbon dioxide exchange of a Russian boreal forest after disturbance by wind throw. *Glob. Change Biol.*, 8 (3), pp. 231–246. DOI: 10.1046/j.1365-2486.2002.00475.x.
- Langvall, O. and Löfvenius, M. O. (2002). Effect of shelterwood density on nocturnal near-ground temperature, frost injury risk and budburst date of Norway spruce. *Forest Ecol. Manag.*, 168 (1), pp. 149–161. DOI: 10.1016/S0378-1127(01)00754-X.
- Le Quéré, C., Aumont, O., Bopp, L., Bousquet, P., Ciais, P., Francey, R., Heimann, M., Keeling, C. D., Keeling, R. F., Kheshgi, H., Peylin, P., Piper, S. C., Prentice, I. C., and Rayner, P. J. (2003). Two decades of ocean CO₂ sink and variability. *Tellus B*, 55 (2), pp. 649–656. DOI: 10.1034/j.1600-0889.2003.00043.x.
- Leclerc, M. Y. and Foken, T. (2014). *Footprints in Micrometeorology and Ecology*. Springer, Heidelberg, XIX, p. 239.
- Leclerc, M. Y., Shen, S., and Lamb, B. (1997). Observations and large-eddy simulation modeling of footprints in the lower convective boundary layer. *J. Geophys. Res.*, 102 (D8), pp. 9323–9334. DOI: 10.1029/96JD03984.
- Leclerc, M. Y., Karipot, A., Prabha, T., Allwine, G., Lamb, B., and Gholz, H. L. (2003). Impact of non-local advection on flux footprints over a tall forest canopy: a tracer flux experiment. *Agr. For. Meteorol.*, 115 (1), pp. 19–30. DOI: 10.1016/S0168-1923(02)00168-5.
- Lee, X. and Black, T. A. (1993). Atmospheric turbulence within and above a douglas-fir stand. Part II: Eddy fluxes of sensible heat and water vapour. *Bound.-Lay. Meteorol.*, 64, pp. 369–389. DOI: 10.1007/BF00711706.

- Lenschow, D. H. (1972). The Measurement of Air Velocity and Temperature Using the NCAR Buffalo Aircraft Measuring System. NCAR-TN/EDD-74, National Center for Atmospheric Research, Boulder, Colorado, p. 39. DOI: 10.5065/D6C8277W.
- Leonard, R. E. and Eschner, A. R. (1968). A treetop tramway system for meteorological studies. Northeastern Forest Experiment Station, Forest Service, U.S. Dept. of Agriculture, U.S. Forest Service Research Paper, NE-92, p. 10.
- Leuning, R. (1990). Modelling Stomatal Behaviour and Photosynthesis of *Eucalyptus grandis*. Austr. J. Plant Physiol., 17 (2), pp. 159–175. DOI: 10.1071/PP9900159.
- Liebenthal, C. and Foken, T. (2007). Evaluation of six parameterization approaches for the ground heat flux. Theor. Appl. Climatol., 88 (1), pp. 43–56. DOI: 10.1007/s00704-005-0234-0.
- Lindroth, A., Mölder, M., and Lagergren, F. (2010). Heat storage in forest biomass improves energy balance closure. Biogeosciences, 7 (1), pp. 301–313. DOI: 10.5194/bg-7-301-2010.
- Lu, S. S. and Willmarth, W. W. (1973). Measurements of the structure of the Reynolds stress in a turbulent boundary layer. J. Fluid Mech., 60 (3), pp. 481–511. DOI: 10.1017/S0022112073000315.
- Luyssaert, S., Ciais, P., Piao, S. L., Schulze, E.-D., Jung, M., Zaehle, S., Schelhaas, M. J., Reichstein, M., Churkina, G., Papale, D., Abril, G., Beer, C., Grace, J., Loustau, D., Matteucci, G., Magnani, F., Nabuurs, G. J., Verbeeck, H., Sulkava, M., van der WERF, G. R., Janssens, I. A., and members of the CARBOEUROPE-IP SYNTHESIS TEAM (2010). The European carbon balance. Part 3: forests. Glob. Change Biol., 16 (5), pp. 1429–1450. DOI: 10.1111/j.1365-2486.2009.02056.x.
- Mahrt, L. (2010). Computing turbulent fluxes near the surface: Needed improvements. Agr. For. Meteorol., 150 (4), pp. 501–509. DOI: 10.1016/j.agrformet.2010.01.015.
- Mahrt, L., Sun, J., Vickers, D., MacPherson, J. I., Pederson, J. R., and Desjardins, R. L. (1994). Observations of Fluxes and Inland Breezes over a Heterogeneous Surface. J. Atmos. Sci., 51 (17), pp. 2484–2499. DOI: 10.1175/1520-0469(1994)051<2484:OOFAIB>2.0.CO;2.
- Maitani, T. and Ohtaki, E. (1987). Turbulent transport processes of momentum and sensible heat in the surface layer over a paddy field. Bound.-Lay. Meteorol., 40 (3), pp. 283–293. DOI: 10.1007/BF00117452.
- Malhi, Y., McNaughton, K., and Randow, C. (2005). Low Frequency Atmospheric Transport and Surface Flux Measurements. In: Handbook of Micrometeorology. Ed. by X. Lee, W. Massman, and B. E. Law. Vol. 29. Dordrecht: Kluwer Academic Publishers, pp. 101–118.

- Matlack, G. R. and Litvaitis, J. A. (1999). Forest edges. In: *Maintaining biodiversity in forest ecosystems*. Ed. by M. L. Hunter Jr. Cambridge University Press, Cambridge, U. K., pp. 210–233.
- Mauder, M. and Foken, T. (2006). Impact of post-field data processing on eddy covariance flux estimates and energy balance closure. *Meteorol. Z.*, 15 (6), pp. 597–609. DOI: 10.1127/0941-2948/2006/0167.
- Mauder, M. and Foken, T. (2011). Documentation and Instruction Manual of the Eddy-Covariance Software Package TK3. Work Report, University of Bayreuth, Dept. of Micrometeorology, ISSN: 1614-8916, 46, p. 44.
- Mauder, M., Liebethal, C., Göckede, M., Leps, J.-P., Beyrich, F., and Foken, T. (2006). Processing and quality control of flux data during LITFASS-2003. *Bound.-Lay. Meteorol.*, 121 (1), pp. 67–88. DOI: 10.1007/s10546-006-9094-0.
- Mauder, M., Jegede, O. O., Okogbue, E. C., Wimmer, F., and Foken, T. (2007a). Surface energy balance measurements at a tropical site in West Africa during the transition from dry to wet season. *Theor. Appl. Climatol.*, 89 (3), pp. 171–183. DOI: 10.1007/s00704-006-0252-6.
- Mauder, M., Oncley, S. P., Vogt, R., Weidinger, T., Ribeiro, L., Bernhofer, C., Foken, T., Kohsiek, W., De Bruin, H. A. R., and Liu, H. (2007b). The energy balance experiment EBEX-2000. Part II: Intercomparison of eddy-covariance sensors and post-field data processing methods. *Bound.-Lay. Meteorol.*, 123 (1), pp. 29–54. DOI: 10.1007/s10546-006-9139-4.
- Mauder, M., Foken, T., Clement, R., Elbers, J. A., Eugster, W., Grünwald, T., Heusinkveld, B., and Kolle, O. (2008). Quality control of CarboEurope flux data - Part 2: Inter-comparison of eddy-covariance software. *Biogeosciences*, 5 (2), pp. 451–462. DOI: 10.5194/bg-5-451-2008.
- Mauder, M., Cuntz, M., Drüe, C., Graf, A., Rebmann, C., Schmid, H. P., Schmidt, M., and Steinbrecher, R. (2013). A strategy for quality and uncertainty assessment of long-term eddy-covariance measurements. *Agr. For. Meteorol.*, 169, pp. 122–135. DOI: 10.1016/j.agrformet.2012.09.006.
- Mayer, J.-C., Hens, K., Rummel, U., Meixner, F. X., and Foken, T. (2009). Moving measurement platforms - specific challenges and corrections. *Meteorol. Z.*, 18, pp. 1–12. DOI: 10.1127/0941-2948/2009/0401.

- McCarthy, J. (1973). A Method for Correcting Airborne Temperature Data for Sensor Response Time. *J. Appl. Meteorol.*, 12 (1), pp. 211–214. doi: 10.1175/1520-0450(1973)012<0211:AMFCAT>2.0.CO;2.
- McDonald, D. and David, A. N. (1992). Light environments in temperate New Zealand podocarp rainforests. *New Zeal. J. Ecol.*, 16, pp. 15–22.
- Meyers, T. P. (1985). A simulation of the canopy microenvironment using higher order closure principles. PhD thesis. Ph. D. thesis, Purdue University, Purdue, Indiana, USA. p. 153.
- Meyers, T. P. and Paw U, K. T. (1986). Testing of a higher-order closure model for modeling airflow within and above plant canopies. *Bound.-Lay. Meteorol.*, 37 (3), pp. 297–311. doi: 10.1007/BF00122991.
- Meyers, T. P. and Paw U, K. T. (1987). Modelling the plant canopy micrometeorology with higher-order closure principles. *Agr. For. Meteorol.*, 41 (1), pp. 143–163. doi: 10.1016/0168-1923(87)90075-X.
- Miloshevich, L. M., Paukkunen, A., Vömel, H., and Oltmans, S. J. (2004). Development and Validation of a Time-Lag Correction for Vaisala Radiosonde Humidity Measurements. *J. Atmos. Ocean. Tech.*, 21 (9), pp. 1305–1327. doi: 10.1175/1520-0426(2004)021<1305:DAVOAT>2.0.CO;2.
- Molemaker, M. J. and Vilà-Guerau de Arellano, J. (1998). Control of Chemical Reactions by Convective Turbulence in the Boundary Layer. *J. Atmos. Sci.*, 55 (4), pp. 568–579. doi: 10.1175/1520-0469(1998)055<0568:COCRBC>2.0.CO;2.
- Moncrieff, J. (2004). Surface Turbulent Fluxes. In: *Vegetation, Water, Humans and the Climate. A new perspective on an interactive system.* Ed. by P. Kabat, M. Claussen, P. A. Dirmeyer, J. H. C. Gash, L. B. Guenni, M. Meybeck, R. A. Pielke, C. I. Vörösmarty, R. W. A. Hutjes, and S. Lütke-meier. Springer, Berlin/Heidelberg, pp. 173–182.
- Mukammal, E. I. (1971). Some aspects of radiant energy in a pine forest. *Theor. Appl. Climatol.*, 19, pp. 29–52. doi: 10.1007/BF02243401.
- Mund, M., Kummerow, E., Hein, M., Bauer, G., and Schulze, E.-D. (2002). Growth and carbon stocks of a spruce forest chronosequence in central Europe. *Forest Ecol. Manag.*, 171 (3), pp. 275–296. doi: 10.1016/S0378-1127(01)00788-5.
- Murcia, C. (1995). Edge effects in fragmented forests: implications for conservation. *Trends Ecol. Evol.*, 10 (2), pp. 58–62. doi: 10.1016/S0169-5347(00)88977-6.

- Muschinski, A., Frehlich, R., Jensen, M., Hugo, R., Hoff, A., Eaton, F., and Balsley, B. (2001). Fine-Scale Measurements of Turbulence in the Lower Troposphere: An Intercomparison between a Kite- and Balloon-Borne, and a Helicopter-Borne Measurement System. *Bound.-Lay. Meteorol.*, 98 (2), pp. 219–250. DOI: 10.1023/A:1026520618624.
- Newmark, W. D. (2001). Tanzanian Forest Edge Microclimatic Gradients: Dynamic Patterns. *Biotropica*, 33 (1), pp. 2–11. DOI: 10.1646/0006-3606(2001)033[0002:TFEMGD]2.0.CO;2.
- Ogawa, Y. and Ohara, T. (1982). Observation of the Turbulent Structure in the Planetary Boundary Layer with a Kytoon-Mounted Ultrasonic Anemometer System. *Bound.-Lay. Meteorol.*, 22 (1), pp. 123–131. DOI: 10.1007/BF00128060.
- Oncley, S. P., Foken, T., Vogt, R., Kohsiek, W., DeBruin, H. A. R., Bernhofer, C., Christen, A., Gorsel, E., Grantz, D., Feigenwinter, C., Lehner, I., Liebenthal, C., Liu, H., Mauder, M., Pitacco, A., Ribeiro, L., and Weidinger, T. (2007). The Energy Balance Experiment EBEX-2000. Part I: overview and energy balance. *Bound.-Lay. Meteorol.*, 123 (1), pp. 1–28. DOI: 10.1007/s10546-007-9161-1.
- Oncley, S. P., Schwenz, K., Burns, S. P., Sun, J., and Monson, R. K. (2009). A Cable-Borne Tram for Atmospheric Measurements along Transects. *J. Atmos. Ocean. Tech.*, 26 (3), pp. 462–473. DOI: 10.1175/2008JTECHA1158.1.
- Örlander, G. and Langvall, O. (1993). The Asa Shuttle - A System for Mobile Sampling of Air Temperature and Radiation. *Scand. J. Forest Res.*, 8 (3), pp. 359–372. DOI: 10.1080/02827589309382783.
- Paw U, K. T. and Gao, W. (1988). Applications of solutions to non-linear energy budget equations. *Agr. For. Meteorol.*, 43 (2), pp. 121–145. DOI: 10.1016/0168-1923(88)90087-1.
- Paw U, K. T., Baldocchi, D. D., Meyers, T. P., and Wilson, K. B. (2000). Correction Of Eddy-Covariance Measurements Incorporating Both Advective Effects And Density Fluxes. *Boundary-Layer Meteorology*, 97 (3), pp. 487–511. DOI: 10.1023/A:1002786702909.
- Péché, G. (1986). Mobile Sampling of Solar Radiation Under Conifers. *Agr. For. Meteorol.*, 37 (1), pp. 15–28. DOI: 10.1016/0168-1923(86)90025-0.
- Poggi, D., Porporato, A., Ridolfi, L., Albertson, J. D., and Katul, G. G. (2004). The Effect of Vegetation Density on Canopy Sub-Layer Turbulence. *Bound.-Lay. Meteorol.*, 111 (3), pp. 565–587. DOI: 10.1023/B:BOUN.0000016576.05621.73.

- Prentice, I. C., Farquhar, G. D., Fasham, M. J. R., Goulden, M. L., Heimann, M., Jaramillo, V. J., Kheshgi, H. S., Le Quéré, C., Scholes, R. J., and Wallace, D. W. R. (2001). The carbon cycle and atmospheric carbon dioxide. In: *Climate Change 2001: The Scientific Basis*. Ed. by J. T. Houghton, Y. Ding, D. J. Griggs, M. Noguer, P. J. van der Linden, X. Dai, K. Maskell, and C. A. Johnson, pp. 183–237.
- Privette, J. L., Eck, T. F., and Deering, D. W. (1997). Estimating spectral albedo and nadir reflectance through inversion of simple BRDF models with AVHRR/MODIS-like data. *J. Geophys. Res. D: Atmos.*, 102 (D24), pp. 29529–29542. DOI: 10.1029/97JD01215.
- Pyles, R. D. (2000). The development and testing of the UCD advanced canopy-atmosphere-soil algorithm (ACASA) for use in climate prediction and field studies. PhD thesis. Ph. D. thesis, University of California, Davis, California, USA. p. 194.
- Pyles, R. D., Weare, B. C., and Paw U, K. T. (2000). The UCD Advanced Canopy-Atmosphere-Soil Algorithm: Comparisons with observations from different climate and vegetation regimes. *Q. J. Roy. Meteor. Soc.*, 126 (569), pp. 2951–2980. DOI: 10.1002/qj.49712656917.
- Raupach, M. R. (1981). Conditional statistics of Reynolds stress in rough-wall and smooth-wall turbulent boundary layers. *J. Fluid Mech.*, 108 (1), pp. 363–382. DOI: 10.1017/S0022112081002164.
- Raupach, M. R., Finnigan, J. J., and Brunei, Y. (1996). Coherent eddies and turbulence in vegetation canopies: The mixing-layer analogy. *Bound.-Lay. Meteorol.*, 78 (3), pp. 351–382. DOI: 10.1007/BF00120941.
- Rebmann, C., Kolle, O., Heinesch, B., Queck, R., Ibrom, A., and Aubinet, M. (2012). Data Acquisition and Flux Calculations. In: *Eddy covariance: A practical guide to measurement and data analysis*. Ed. by M. Aubinet, T. Vesala, and D. Papale. Springer, Dordrecht, Heidelberg, London, New York, pp. 59–83.
- Rodi, A. R. and Spyers-Duran, P. A. (1972). Analysis of Time Response of Airborne Temperature Sensors. *J. Appl. Meteorol.*, 11 (3), pp. 554–556. DOI: 10.1175/1520-0450(1972)011<0554:AOTROA>2.0.CO;2.
- Rodskjer, N. and Kornher, A. (1967). Eine Methode zur Registrierung der räumlichen Verteilung der Globalstrahlung in einem Pflanzenbestand. *Theor. Appl. Climatol.*, 15, pp. 186–190. DOI: 10.1007/BF02319119.
- Rodskjer, N. and Kornher, A. (1971). Über die Bestimmung der Strahlungsenergie im Wellenlängenbereich von 0,3–0,7 μ in Pflanzenbeständen. *Agr. Meteorol.*, 8, pp. 139–150. DOI: 10.1016/0002-1571(71)90103-8.

- Rummel, U., Ammann, C., Gut, A., Meixner, F. X., and Andreae, M. O. (2002). Eddy covariance measurements of nitric oxide flux within an Amazonian rain forest. *J. Geophys. Res.*, 107 (D20). DOI: 10.1029/2001JD000520.
- Ruppert, J. (2005). ATEM software for atmospheric turbulent exchange measurements using eddy covariance and relaxed eddy accumulation systems + Bayreuth whole-air REA system setup. Work Report, University of Bayreuth, Dept. of Micrometeorology, ISSN: 1614-8916, 28, p. 29.
- Ruppert, J., Thomas, C., and Foken, T. (2006). Scalar similarity for relaxed eddy accumulation methods. *Bound.-Lay. Meteorol.*, 120 (1), pp. 39–63. DOI: 10.1007/s10546-005-9043-3.
- Saggin, B., Debei, S., and Zaccariotto, M. (2001). Dynamic error correction of a thermometer for atmospheric measurements. *Measurement*, 30 (3), pp. 223–230. DOI: 10.1016/S0263-2241(01)00015-X.
- Sakai, R. K., Fitzjarrald, D. R., and Moore, K. E. (2001). Importance of Low-Frequency Contributions to Eddy Fluxes Observed over Rough Surfaces. *J. Appl. Meteorol.*, 40 (12), pp. 2178–2192. DOI: 10.1175/1520-0450(2001)040<2178:IOLFCT>2.0.CO;2.
- Schaller, C. (2012). Untersuchung des Mikroklimas des EVENT-Experimentes mittels eines horizontal beweglichen Messsystems. University of Bayreuth. p. 75.
- Schimel, D. S., House, J. I., Hibbard, K. A., Bousquet, P., Ciais, P., Peylin, P., Braswell, B. H., Apps, M. J., Baker, D., Bondeau, A., Canadell, J., Churkina, G., Cramer, W., Denning, A. S., Field, C. B., Friedlingstein, P., Goodale, C., Heimann, M., Houghton, R. A., Melillo, J. M., Moore, B., Murdiyarso, D., Noble, I., Pacala, S. W., Prentice, I. C., Raupach, M. R., Rayner, P. J., Scholes, R. J., Steffen, W. L., and Wirth, C. (2001). Recent patterns and mechanisms of carbon exchange by terrestrial ecosystems. *Nature*, 414 (6860), pp. 169–172. DOI: 10.1038/35102500.
- Schlegel, F., Stiller, J., Bienert, A., Maas, H.-G., Queck, R., and Bernhofer, C. (2012). Large-Eddy Simulation of Inhomogeneous Canopy Flows Using High Resolution Terrestrial Laser Scanning Data. *Bound.-Lay. Meteorol.*, 142 (2), pp. 223–243. DOI: 10.1007/s10546-011-9678-1.
- Schulze, E.-D. (2006). Biological control of the terrestrial carbon sink. *Biogeosciences*, 3 (2), pp. 147–166. DOI: 10.5194/bg-3-147-2006.

- Serafimovich, A., Siebicke, L., Staudt, K., Lüers, J., Biermann, T., Schier, S., and Mayer, J.-C. (2008a). ExchanGE processes in mountainous Regions (EGER) - Documentation of the Intensive Observation Period (IOP1) September, 6th to October, 7th 2007. Work Report, University of Bayreuth, Dept. of Micrometeorology, ISSN: 1614-8916, 36, p. 147.
- Serafimovich, A., Siebicke, L., Staudt, K., Lüers, J., Biermann, T., Schier, S., and Mayer, J.-C. (2008b). ExchanGE processes in mountainous Regions (EGER) - Documentation of the Intensive Observation Period (IOP2) June, 1st to July, 15th 2008. Work Report, University of Bayreuth, Dept. of Micrometeorology, ISSN: 1614-8916, 37, p. 180.
- Serafimovich, A., Eder, F., Hübner, J., Falge, E., Voß, L., Sörgel, M., Held, A., Liu, Q., Eigenmann, R., Huber, K., Duarte, H. F., Werle, P., Gast, E., Cieslik, S., Heping, L., and Foken, T. (2011a). ExchanGE processes in mountainous Regions (EGER): Documentation of the Intensive Observation Period (IOP3) June, 13th to July, 26th 2011. Work Report, University of Bayreuth, Dept. of Micrometeorology, ISSN: 1614-8916, 47, p. 137.
- Serafimovich, A., Thomas, C., and Foken, T. (2011b). Vertical and horizontal transport of energy and matter by coherent motions in a tall spruce canopy. *Bound.-Lay. Meteorol.*, 140, pp. 429–451. DOI: 10.1007/s10546-011-9619-z.
- Shaw, R. H., Tavangar, J., and Ward, D. P. (1983). Structure of the Reynolds Stress in a Canopy Layer. *J. Clim. Appl. Meteorol.*, 22 (11), pp. 1922–1931. DOI: 10.1175/1520-0450(1983)022<1922:SOTRSI>2.0.CO;2.
- Siebicke, L. (2008). Footprint synthesis for the FLUXNET site Waldstein/Weidenbrunnen (DE-Bay) during the EGER experiment. Work Report, University of Bayreuth, Dept. of Micrometeorology, ISSN: 1614-8916, 38, p. 49.
- Siebicke, L., Hunner, M., and Foken, T. (2012). Aspects of CO₂ advection measurements. *Theor. Appl. Climatol.*, 109 (1), pp. 109–131. DOI: 10.1007/s00704-011-0552-3.
- Singh, A., Batalin, M. A., Stealey, M., Chen, V., Hansen, M. H., Harmon, T. C., Sukhatme, G. S., and Kaiser, W. J. (2008). Mobile Robot Sensing for Environmental Applications. In: *Field and Service Robotics*. Ed. by C. Laugier and R. Siegwart. Vol. 42. Springer, Berlin, Heidelberg, pp. 125–135.
- Smirnova, T. G., Brown, J. M., and Benjamin, S. G. (1997). Performance of Different Soil Model Configurations in Simulating Ground Surface Temperature and Surface Fluxes. *Mon. Weather Rev.*, 125 (8), pp. 1870–1884. DOI: 10.1175/1520-0493(1997)125<1870:PODSMC>2.0.CO;2.

- Smirnova, T. G., Brown, J. M., Benjamin, S. G., and Kim, D. (2000). Parameterization of cold-season processes in the MAPS land-surface scheme. *J. Geophys. Res.*, 105 (D3), pp. 4077–4086. DOI: 10.1029/1999JD901047.
- Sogachev, A., Rannik, Ü., and Vesala, T. (2004). Flux footprints over complex terrain covered by heterogeneous forest. *Agr. For. Meteorol.*, 127 (3), pp. 143–158. DOI: 10.1016/j.agrformet.2004.07.010.
- Sogachev, A., Leclerc, M. Y., Karipot, A., Zhang, G., and Vesala, T. (2005). Effect of clearcuts on footprints and flux measurements above a forest canopy. *Agr. For. Meteorol.*, 133 (1), pp. 182–196. DOI: 10.1016/j.agrformet.2005.09.008.
- Sogachev, A., Leclerc, M. Y., Zhang, G., Rannik, Ü., and Vesala, T. (2008). CO₂ fluxes near a forest edge: A numerical study. *Ecol. Appl.*, 18 (6), pp. 1454–1469. DOI: 10.1890/06-1119.1.
- Staudt, K. and Foken, T. (2007). Documentation of reference data for the experimental areas of the Bayreuth Center for Ecology and Environmental Research (BayCEER) at the Waldstein site. Work Report, University of Bayreuth, Dept. of Micrometeorology, ISSN: 1614-8916, 35, p. 35.
- Staudt, K., Falge, E., Pyles, R. D., Paw U, K. T., and Foken, T. (2010). Sensitivity and predictive uncertainty of the ACASA model at a spruce forest site. *Biogeosciences*, 7 (11), pp. 3685–3705. DOI: 10.5194/bg-7-3685-2010.
- Staudt, K., Serafimovich, A., Siebicke, L., Pyles, R. D., and Falge, E. (2011). Vertical structure of evapotranspiration at a forest site (a case study). *Agr. For. Meteorol.*, 151 (6), pp. 709–729. DOI: 10.1016/j.agrformet.2010.10.009.
- Steiner, A. L., Pressley, S. N., Botros, A., Jones, E., Chung, S. H., and Edburg, S. L. (2011). Analysis of coherent structures and atmosphere-canopy coupling strength during the CABINEX field campaign. *Atmos. Chem. Phys.*, 11 (23), pp. 11921–11936. DOI: 10.5194/acp-11-11921-2011.
- Steinfeld, G., Letzel, M. O., Raasch, S., Kanda, M., and Inagaki, A. (2007). Spatial representativeness of single tower measurements and the imbalance problem with eddy-covariance fluxes: results of a large-eddy simulation study. *Bound.-Lay. Meteorol.*, 123 (1), pp. 77–98. DOI: 10.1007/s10546-006-9133-x.
- Steinfeld, G., Raasch, S., and Markkanen, T. (2008). Footprints in Homogeneously and Heterogeneously Driven Boundary Layers Derived from a Lagrangian Stochastic Particle Model Embedded into Large-Eddy Simulation. *Bound.-Lay. Meteorol.*, 129 (2), pp. 225–248. DOI: 10.1007/s10546-008-9317-7.

- Stoy, P. C., Mauder, M., Foken, T., Marcolla, B., Boegh, E., Ibrom, A., Arain, M. A., Arneeth, A., Aurela, M., Bernhofer, C., Cescatti, A., Dellwik, E., Duce, P., Gianelle, D., van Gorsel, E., Kiely, G., Knohl, A., Margolis, H., McCaughey, H., Merbold, L., Montagnani, L., Papale, D., Reichstein, M., Saunders, M., Serrano-Ortiz, P., Sottocornola, M., Spano, D., Vaccari, F., and Varlagin, A. (2013). A data-driven analysis of energy balance closure across FLUXNET research sites: The role of landscape scale heterogeneity. *Agr. For. Meteorol.*, 171-172, pp. 137–152. DOI: 10.1016/j.agrformet.2012.11.004.
- Su, H.-B., Paw U, K. T., and Shaw, R. H. (1996). Development of a Coupled Leaf and Canopy Model for the Simulation of Plant-Atmosphere Interaction. *J. Appl. Meteorol.*, 35 (5), pp. 733–748. DOI: 10.1175/1520-0450(1996)035<0733:DOACLA>2.0.CO;2.
- Taconet, O. and Weill, A. (1982). Vertical velocity field in the convective boundary layer as observed with an acoustic Doppler sodar. *Bound.-Lay. Meteorol.*, 23 (2), pp. 133–151. DOI: 10.1007/BF00123292.
- Taconet, O. and Weill, A. (1983). Convective plumes in the atmospheric boundary layer as observed with an acoustic Doppler sodar. *Bound.-Lay. Meteorol.*, 25 (2), pp. 143–158. DOI: 10.1007/BF00123971.
- Thomas, C. K., Kennedy, A. M., Selker, J. S., Moretti, A., Schroth, M. H., Smoot, A. R., Tuffillaro, N. B., and Zeeman, M. J. (2012). High-Resolution Fibre-Optic Temperature Sensing: A New Tool to Study the Two-Dimensional Structure of Atmospheric Surface-Layer Flow. *Bound.-Lay. Meteorol.*, 142 (2), pp. 177–192. DOI: 10.1007/s10546-011-9672-7.
- Thomas, C. K., Martin, J. G., Law, B. E., and Davis, K. (2013). Toward biologically meaningful net carbon exchange estimates for tall, dense canopies: Multi-level eddy covariance observations and canopy coupling regimes in a mature Douglas-fir forest in Oregon. *Agr. For. Meteorol.*, 173, pp. 14–27. DOI: 10.1016/j.agrformet.2013.01.001.
- Thomas, C. and Foken, T. (2005). Detection of long-term coherent exchange over spruce forest using wavelet analysis. *Theor. Appl. Climatol.*, 80 (2), pp. 91–104. DOI: 10.1007/s00704-004-0093-0.
- Thomas, C. and Foken, T. (2007a). Organised Motion in a Tall Spruce Canopy: Temporal Scales, Structure Spacing and Terrain Effects. *Bound.-Lay. Meteorol.*, 122, pp. 123–147. DOI: 10.1007/s10546-006-9087-z.
- Thomas, C. and Foken, T. (2007b). Flux contribution of coherent structures and its implications for the exchange of energy and matter in a tall spruce canopy. *Bound.-Lay. Meteorol.*, 123 (2), pp. 317–337. DOI: 10.1007/s10546-006-9144-7.

- Thomas, C., Mayer, J.-C., Meixner, F. X., and Foken, T. (2006). Analysis of Low-Frequency Turbulence Above Tall Vegetation Using a Doppler Sodar. *Bound.-Lay. Meteorol.*, 119 (3), pp. 563–587. DOI: 10.1007/s10546-005-9038-0.
- Twine, T., Kustas, W., Norman, J., Cook, D., Houser, P., Meyers, T., Prueger, J., Starks, P., and Wesely, M. (2000). Correcting eddy-covariance flux underestimates over a grassland. *Agr. For. Meteorol.*, 103 (3), pp. 279–300. DOI: 10.1016/S0168-1923(00)00123-4.
- Wallace, J. M., Eckelmann, H., and Brodkey, R. S. (1972). The wall region in turbulent shear flow. *J. Fluid Mech.*, 54 (1), pp. 39–48. DOI: 10.1017/S0022112072000515.
- Weaver, C. P. and Avissar, R. (2001). Atmospheric Disturbances Caused by Human Modification of the Landscape. *Bull. Amer. Meteor. Soc.*, 82 (2), pp. 269–281. DOI: 10.1175/1520-0477(2001)082<0269:ADCBHM>2.3.CO;2.
- Wilczak, J. M., Oncley, S. P., and Stage, S. A. (2001). Sonic anemometer tilt correction algorithms. *Bound.-Lay. Meteorol.*, 99 (1), pp. 127–150. DOI: 10.1023/A:1018966204465.
- Wilson, K., Goldstein, A., Falge, E., Aubinet, M., Baldocchi, D., Berbigier, P., Bernhofer, C., Ceulemans, R., Dolman, H., Field, C., Grelle, A., Ibrom, A., Law, B. E., Kowalski, A., Meyers, T., Moncrieff, J., Monson, R., Oechel, W., Tenhunen, J., Valentini, R., and Verma, S. (2002). Energy balance closure at FLUXNET sites. *Agr. For. Meteorol.*, 113 (1), pp. 223–243. DOI: 10.1016/S0168-1923(02)00109-0.
- Wolf, A. (2008). Die Kohlenstoff-Senkenkapazität des Schweizer Waldes | Carbon sink capacity of Swiss forests. *Schweiz. Z. Forstwes.*, 159 (9), pp. 273–280. DOI: 10.3188/szf.2008.0273.
- Yang, B., Raupach, M. R., Shaw, R. H., Paw U, K. T., and Morse, A. P. (2006a). Large-eddy Simulation of Turbulent Flow Across a Forest Edge. Part I: Flow Statistics. *Bound.-Lay. Meteorol.*, 120 (3), pp. 377–412. DOI: 10.1007/s10546-006-9057-5.
- Yang, B., Shaw, R. H., and Paw U, K. T. (2006b). Wind loading on trees across a forest edge: A large eddy simulation. *Agr. For. Meteorol.*, 141 (2), pp. 133–146. DOI: 10.1016/j.agrformet.2006.09.006.
- Yi, C., Anderson, D. E., Turnipseed, A. A., Burns, S. P., Sparks, J. P., Stannard, D. I., and Monson, R. K. (2008). The contribution of advective fluxes to net ecosystem exchange in a high-elevation, subalpine forest. *Ecol. Appl.*, 18 (6), pp. 1379–1390. DOI: 10.1890/06-0908.1.

- Zahn, A., Weppner, J., Widmann, H., Schlote-Holubek, K., Burger, B., Kühner, T., and Franke, H. (2012). A fast and precise chemiluminescence ozone detector for eddy flux and airborne application. *Atmos. Meas. Tech.*, 5 (2), pp. 363–375. DOI: 10.5194/amt-5-363-2012.
- Zeeman, M. J., Eugster, W., and Thomas, C. K. (2013). Concurrency of Coherent Structures and Conditionally Sampled Daytime Sub-canopy Respiration. *Bound.-Lay. Meteorol.*, 146 (1), pp. 1–15. DOI: 10.1007/s10546-012-9745-2.
- Zhang, G., Thomas, C., Leclerc, M. Y., Karipot, A., Gholz, H. L., Binford, M., and Foken, T. (2007). On the effect of clearcuts on turbulence structure above a forest canopy. *Theor. Appl. Climatol.*, 88 (1), pp. 133–137. DOI: 10.1007/s00704-006-0250-8.

A. Analysis of vertical wind velocity

According to Siebicke et al. (2012), sector-wise planar fit is recommended for the complex terrain of the EGER IOP3 site. It was therefore conducted for most mast/tower measurements where the eddy-covariance technique was used. The sector-wise planar fit rotation was performed due to the proposal by Foken et al. (2004). Section 2.4.2 contains all information about the used method and the chosen sectors (in case of sector-wise) are summarised in Table 2.10. The figures (A.1 till A.7) presented here show the vertical wind velocity w versus wind direction for all towers named in Table 2.10. In each case, (a) shows the data before coordinate rotation, (b) after standard planar fit rotation and (c) after sector-wise planar fit rotation. (c) is only shown, when sector-wise planar fit rotation is conducted and only then, the sector limits are indicated by dashed-vertical lines in all plots.

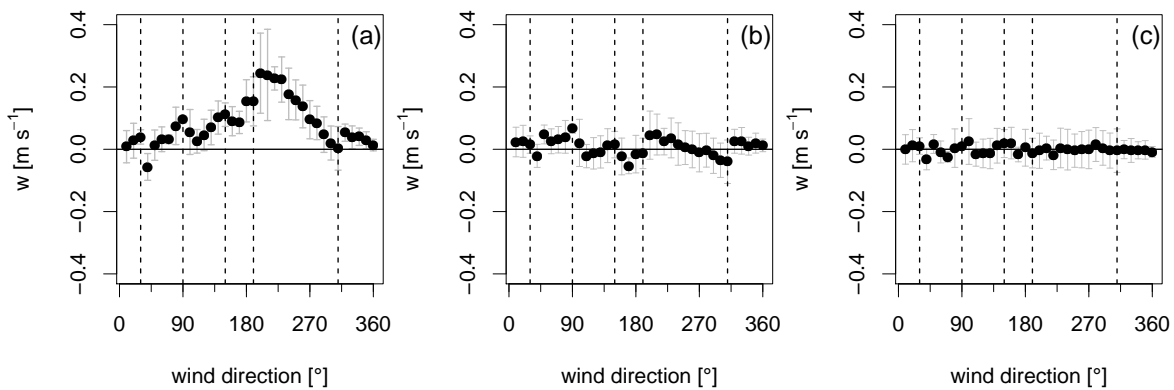
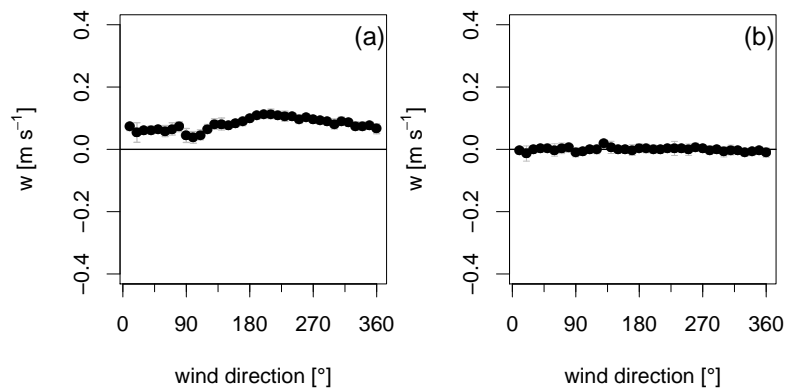
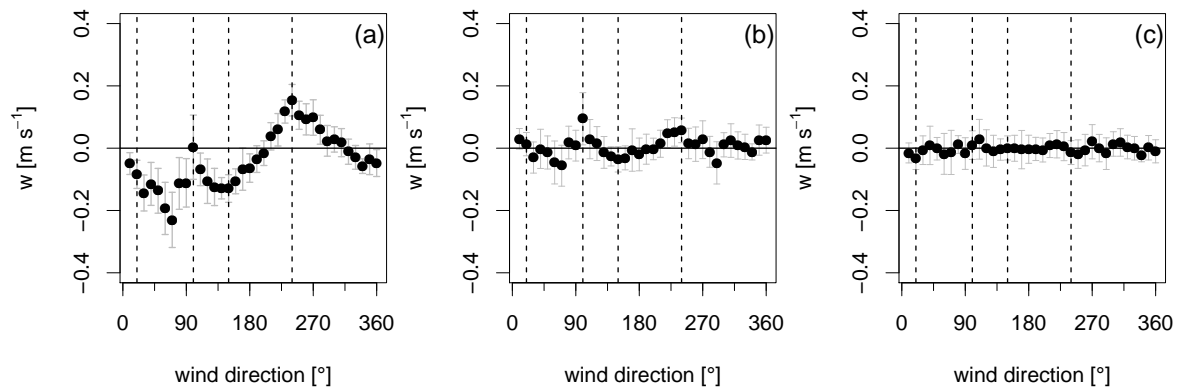


Figure A.1. Vertical wind velocity w versus wind direction for tower M1 ($z = 32$ m): (a) before coordinate rotation, (b) after standard planar-fit rotation and (c) after sector-wise planar fit rotation. Sector limits are indicated by dashed vertical lines in all plots. Data is averaged in 10° wind direction bins. Gray arrows indicates $w \pm$ standard deviation.

M2 ($z = 2.25$ m):



M2 ($z = 26$ m):



M2 ($z = 36$ m):

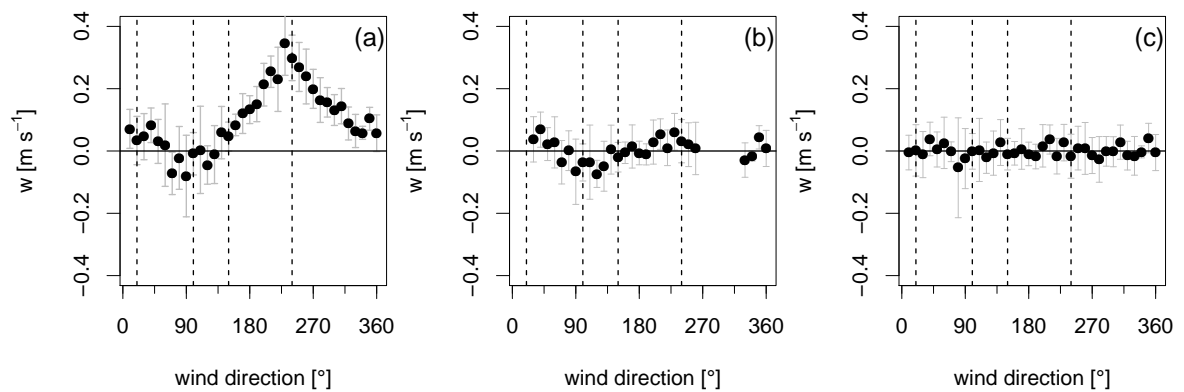
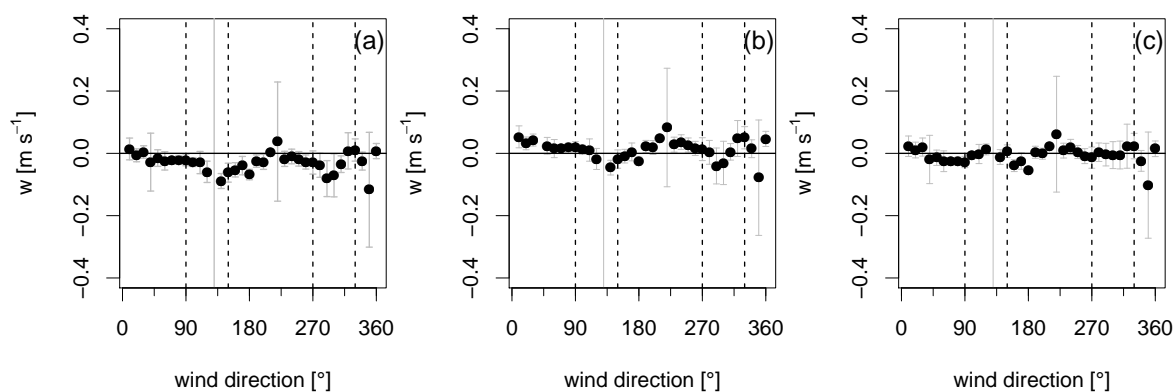


Figure A.2. Vertical wind velocity w versus wind direction for tower M2 ($z = 2.25$ m, $z = 26$ m, $z = 36$ m): (a) before coordinate rotation, (b) after standard planar-fit rotation and (c) sector-wise planar fit rotation. For $z = 2.25$ m no sector-wise planar-fit was performed. For $z = 26$ m, $z = 36$ m sector limits are indicated by dashed vertical lines in all plots. Data is averaged in 10° wind direction bins. Gray arrows indicates $w \pm$ standard deviation.

M3 ($z = 2.25$ m):



M3 ($z = 41$ m):

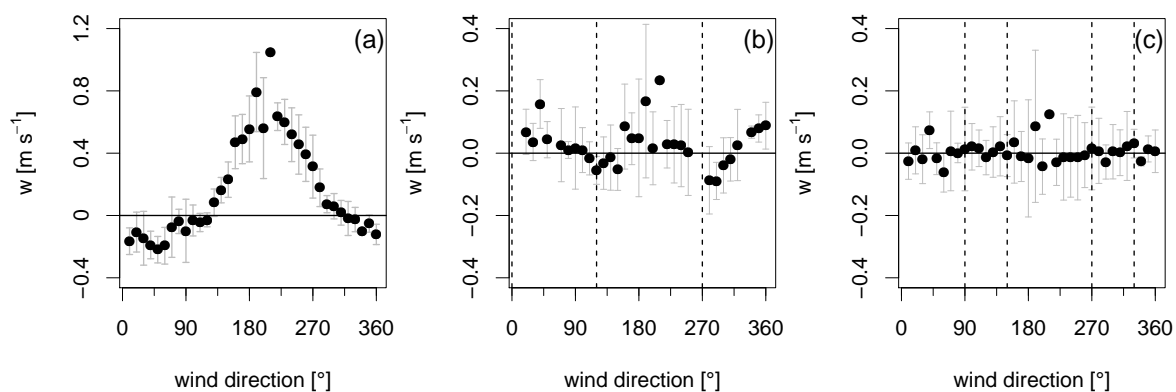
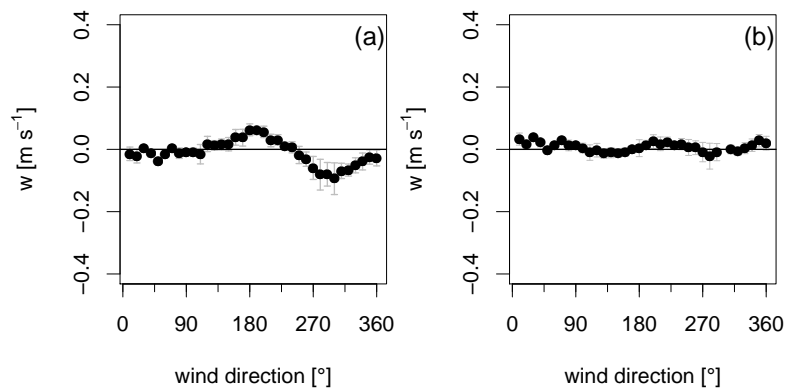


Figure A.3. Vertical wind velocity w versus wind direction for tower M3 ($z = 2.25$ m, $z = 26$ m, $z = 41$ m): (a) before coordinate rotation, (b) after standard planar-fit rotation and (c) sector-wise planar fit rotation. Sector limits are indicated by dashed vertical lines in all plots. Data is averaged in 10° wind direction bins. Gray arrows indicates $w \pm$ standard deviation. Note different y-scales in $z = 41$ m between (a) and (b,c).

M4 ($z = 2.25$ m):



M4 ($z = 5.5$ m):

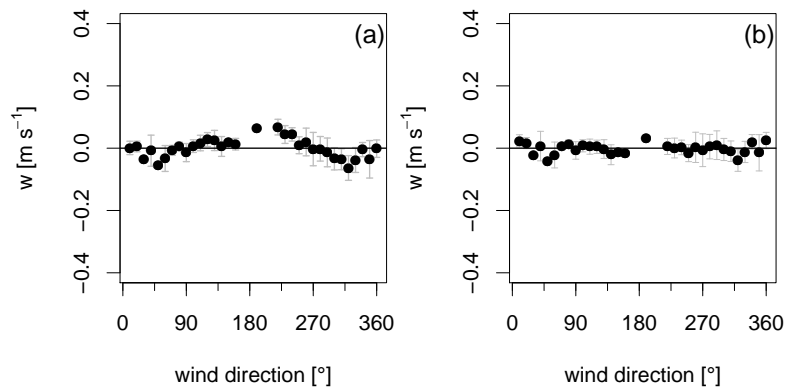
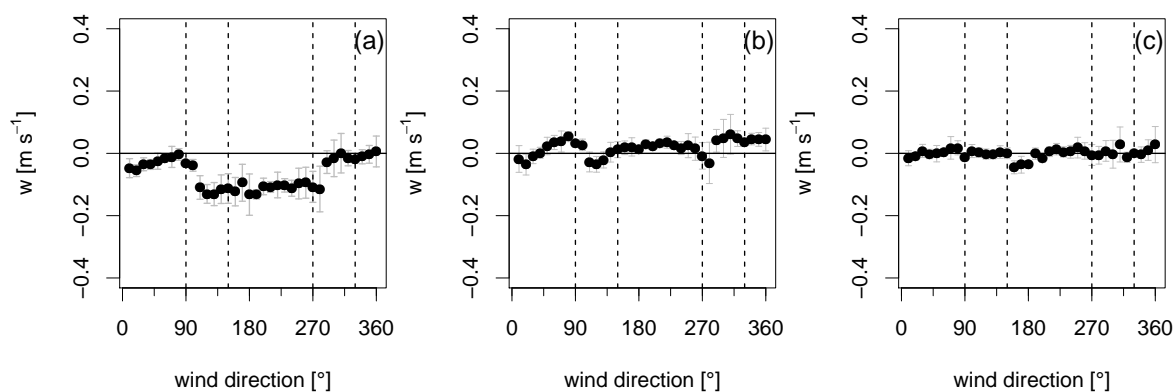


Figure A.4. Vertical wind velocity w versus wind direction for mast M4 ($z = 2.25$ m, $z = 5.5$ m): (a) before coordinate rotation, (b) after standard planar-fit rotation and (c) sector-wise planar fit rotation. Sector limits are indicated by dashed vertical lines in all plots. Data is averaged in 10° wind direction bins. Gray arrows indicates $w \pm$ standard deviation.

M6 ($z = 2.25$ m):



M6 ($z = 5.5$ m):

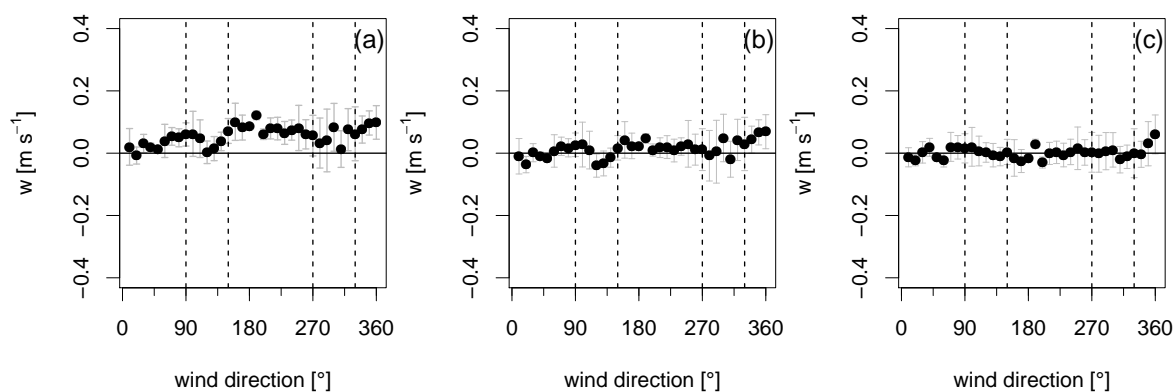
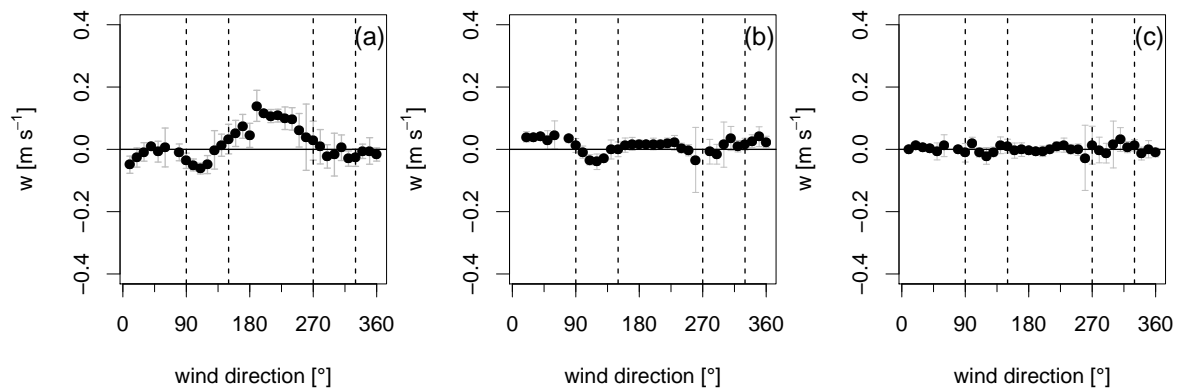


Figure A.5. Vertical wind velocity w versus wind direction for mast M6 ($z = 2.25$ m, $z = 5.5$ m): (a) before coordinate rotation, (b) after standard planar-fit rotation and (c) sector-wise planar fit rotation. Sector limits are indicated by dashed vertical lines in all plots. Data is averaged in 10° wind direction bins. Gray arrows indicates $w \pm$ standard deviation.

M7 ($z = 2.25$ m):



M7 ($z = 5.5$ m):

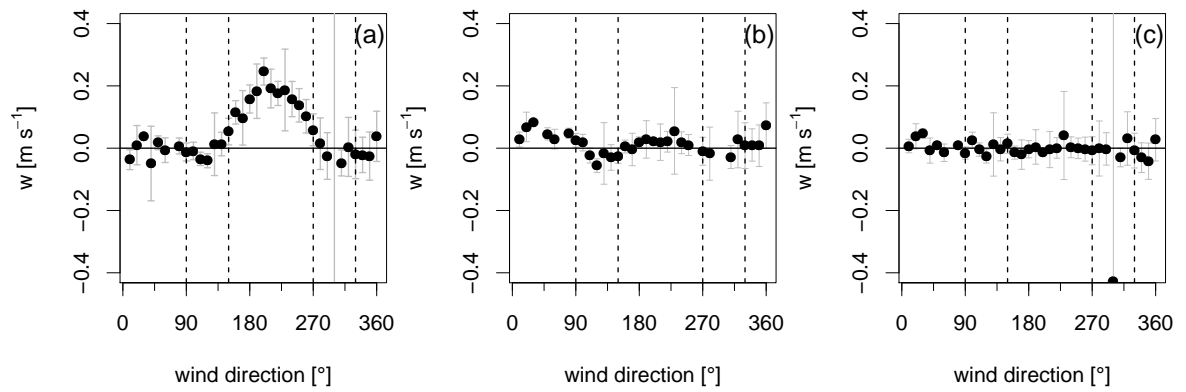


Figure A.6. Vertical wind velocity w versus wind direction for mast M7 ($z = 2.25$ m, $z = 5.5$ m): (a) before coordinate rotation, (b) after standard planar-fit rotation and (c) sector-wise planar fit rotation. Sector limits are indicated by dashed vertical lines in all plots. Data is averaged in 10° wind direction bins. Gray arrows indicates $w \pm$ standard deviation.

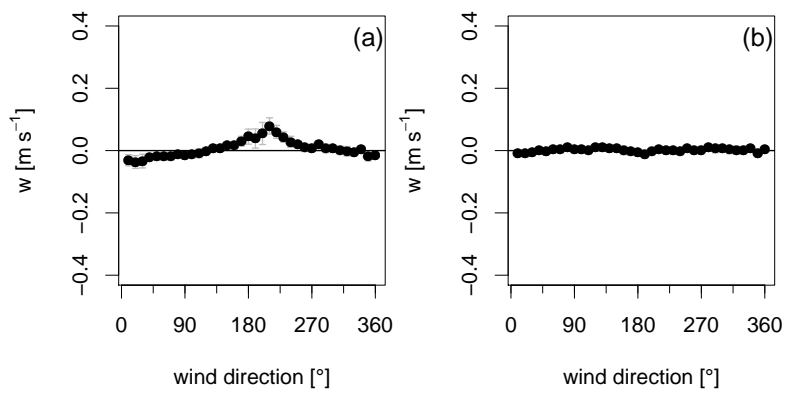


Figure A.7. Vertical wind velocity w versus wind direction for mast M8 ($z = 2.25$ m): (a) before coordinate rotation and (b) after standard planar-fit rotation. A sector-wise planar fit rotation was not performed. Data is averaged in 10° wind direction bins. Gray arrows indicates $w \pm$ standard deviation.

B. Parameter for ACASA Tile Approach

The ACASA model (Pyles, 2000; Pyles et al., 2000) was performed to model the energy and matter exchange (Section 2.4.5 Gatzsche, 2013). Therefore plant physiological parameters are necessary, which are given in Table B.1. And as mentioned in Section 3.2.4, six different model runs were conducted at the clearing for the six dominating species. The used parameters for each species is given in Table B.2.

Table B.1. List of plant physiological input parameters for the ACASA model (Gatzsche, 2013).

Parameter	Definition	Dimension
V_{cmax25}	Maximum rate of carboxylation at 25 °C*	$\mu\text{mol m}^{-2} \text{s}^{-1}$
$eavc$	Activation energy ΔH_a^*	J mol^{-1}
$hdvc$	Deactivation energy ΔH_d^*	J mol^{-1}
$dsvc$	Entropy	$\text{J mol}^{-1} \text{K}^{-1}$
$ejmax$	Activation energy for RuBP regeneration†	J mol^{-1}
$smax$	Term entropy for RuBP regeneration†	J mol^{-1}
$hjmax$	Deactivation energy for RuBP regeneration†	J mol^{-1}
J_{max25}	Potential rate of electron transport at 25 °C	$\mu\text{mol m}^{-2} \text{s}^{-1}$
cm	Slope of Ball-Berry formula	–
cb	Intercept of Ball-Berry formula	$\text{mol m}^{-2} \text{s}^{-1}$
oi	Percentage of O ₂ within cells (Michaelis–Menten kinetic)	mmol mol^{-1}
iqe	Quantum efficiency	–
$r0$	Leaf basal respiration rate at 0 °C	$\mu\text{mol m}^{-2} \text{s}^{-1}$
$q10$	Q_{10} temperature coefficient for leaves	–
$xldiam$	Mean leaf diameter	m

* Used for the calculation of V_{cmax}

† Ribulose-1,5-bisphosphate

Table B.2. Plant physiological parameters for the ACASA model for the representative vegetation species at the clearing ‘Köhlerloh’ during EGER IOP3 (Gatzsche, 2013). For dimensions of the individual parameters cf. Table B.1.

Parameter	Vaccinium	Deschampsia	Calamagrostis	Juncus	Picea abies
<i>vcmax25</i>	26.61	29.53	45.57	30.39	31.78
<i>eavc</i>	46 986	34 030	37 211	41 226	29 487
<i>hdvc</i>	200 000	200 000	200 000	200 000	200 000
<i>dsvc</i>	238.8	254.4	243.2	240.1	245.0
<i>ejmax</i>	52 642	48 000	137 205	16 745	36 185
<i>smax</i>	488.2	511.4	468.7	492.4	486.2
<i>hjmax</i>	200 000	200 000	200 000	200 000	200 000
<i>jmax25</i>	86.12	157.46	198.32	128.92	123.98
<i>cm</i>	10.09	10.58	10.68	8.17	9.40
<i>cb</i>	0.050	0.127	0.049	0.002	0.054
<i>oi</i>	0.21	0.21	0.21	0.21	0.21
<i>iqe</i>	0.0626	0.1223	0.0809	0.1215	0.0851
<i>r0</i>	0.1154	0.9174	0.0817	0.6815	0.5413
<i>q10</i>	2.7316	1.4226	2.7167	1.4632	1.8653
<i>xldiam</i>	0.130	0.004	0.050	0.050	0.010
Percentage [%]	17.5	21.7	9.0	3.1	21.4

C. Detailed overview of horizontal structures

C.1. Meteorological gradients measured with the HMMS

The following sections are an extension of Section 3.2.1 and include the investigation of the turbulence influenced quantities (temperature, humidity and trace gases), regarding four different wind directions (Appendix C.1.1). Additionally considering different stability parameters (Appendix C.1.2). Table C.1 contains the three different stability classes. Appendix C.1.3 investigates, in addition to the different wind directions, regarding different friction velocities (threshold $u_* = 0.4 \text{ m s}^{-1}$). The four chosen wind sectors are equivalent to the four used sector-wise planar fit sectors at the forest edge (Figure 2.9). The designations indicated in Figure 2.9 have not been adopted here. Instead, the following designations have been used:

North: 330 – 90° (supersedes designation ‘Forest’)

East: 90 – 150° (supersedes designation ‘Forest Edge Sector East’)

South: 150 – 270° (supersedes designation ‘Clearing’)

West: 270 – 330° (supersedes designation ‘Forest Edge Sector West’)

Table C.1. Stability classes used for the investigation of the five locations named in Table 3.1.

Stability class	$\zeta = z/L$
unstable	$-0.033 > \zeta$
neutral	$-0.033 < \zeta < 0.04$
stable	$0.04 < \zeta$

C.1.1. Variation regarding different wind directions

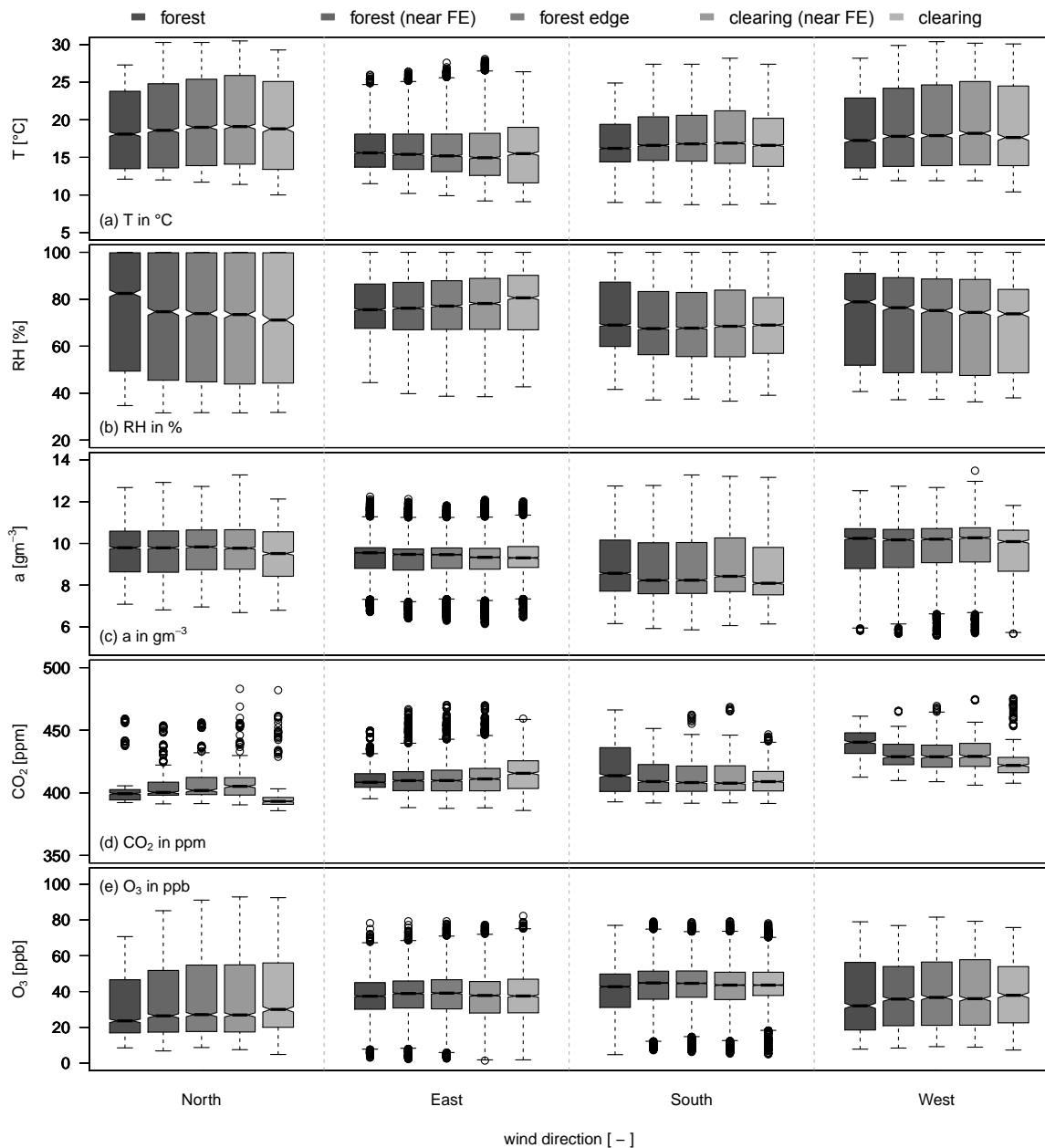


Figure C.1. Variation of the temperature T (a) and humidity, shown as relative humidity RH (b) and absolute humidity a (c), as well as CO_2 (d) and O_3 (e) concentration, regarding different wind directions (see Section C.1) at five different locations: forest, forest (near forest edge/FE), forest edge, clearing (near FE) and clearing. Table 3.1 contains the exact bar code positions. The data were averaged at each location over 15s per each run. Data based on all completed runs during the three ‘Golden Day’ periods (Figure 2.3)

C.1.2. Variation regarding different wind directions and stability parameters

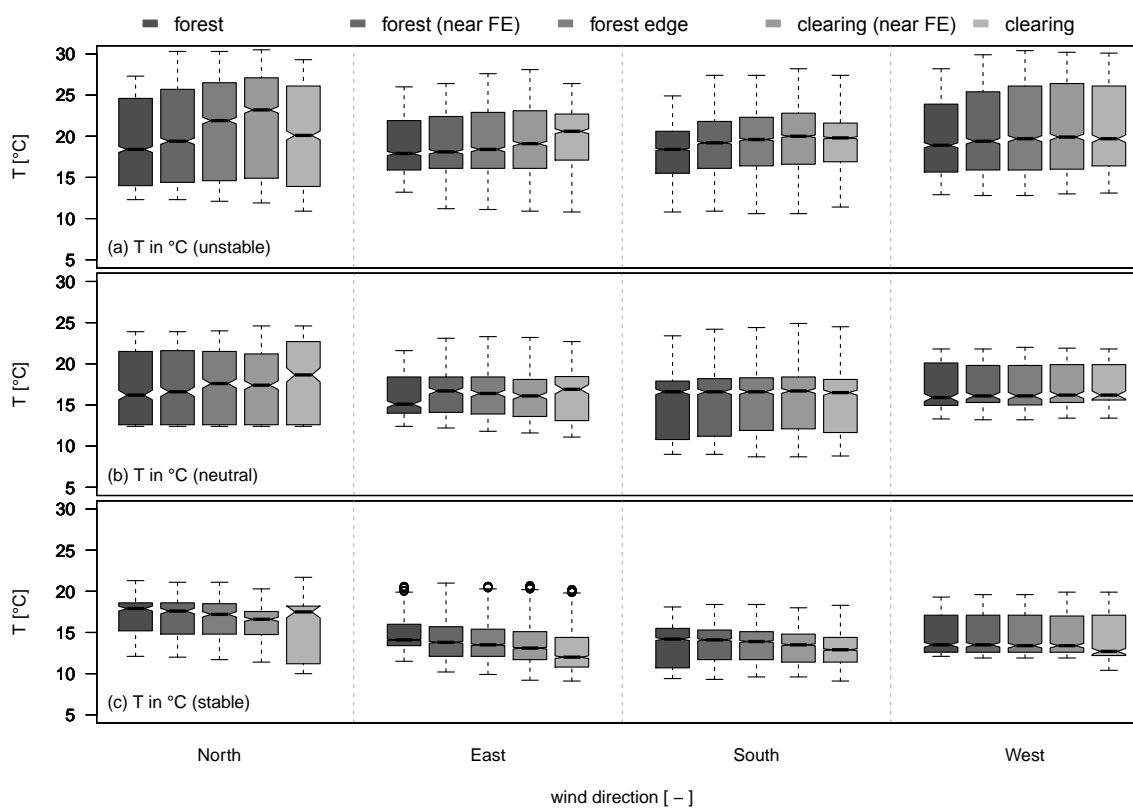


Figure C.2. Variation of the temperature T regarding different stabilities and wind directions (see Section C.1). Unstable stratification is shown in (a), neutral in (b) and stable in (c). Data were measured with the HMMS at five different locations: forest, forest (near forest edge/FE), forest edge, clearing (near FE) and clearing. Table 3.1 contains the exact bar code positions. The data were averaged at each location over 15s per each run. Data based on all completed runs during the three ‘Golden Day’ periods (Figure 2.3)

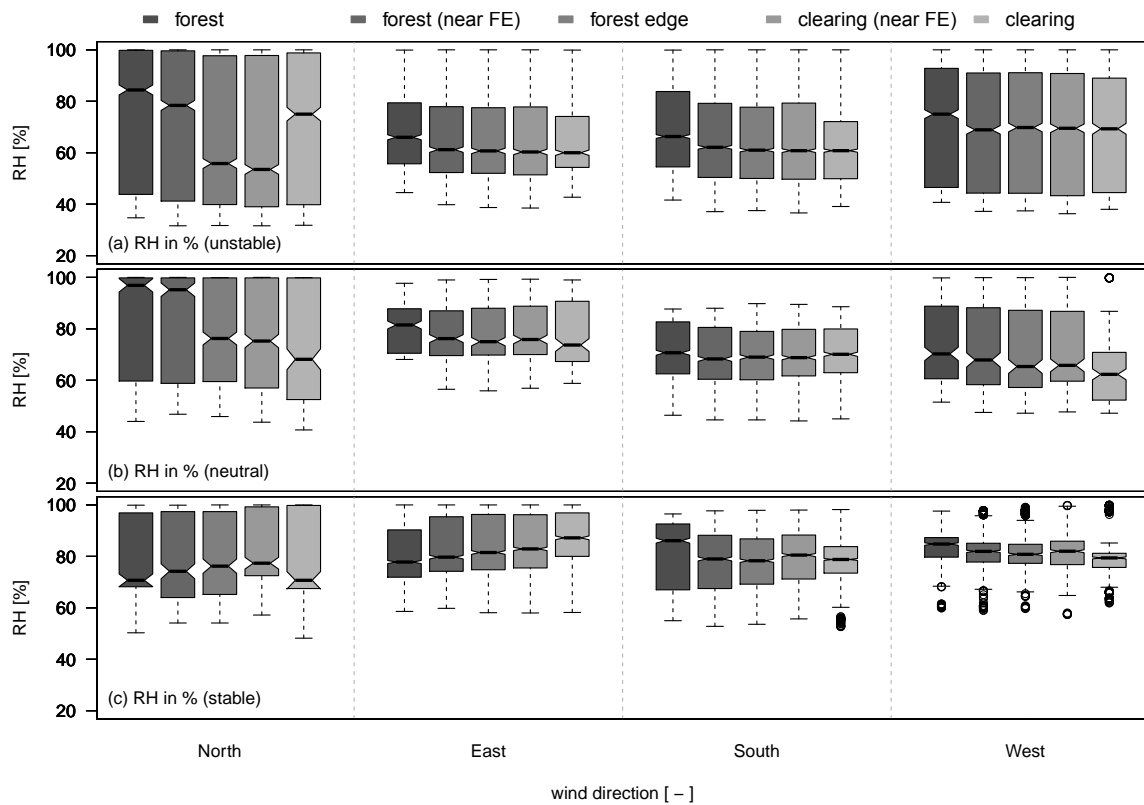


Figure C.3. Variation of the relative humidity RH regarding different stabilities and wind directions (see Section C.1). Unstable stratification is shown in (a), neutral in (b) and stable in (c). Data were measured with the HMMS at five different locations: forest, forest (near forest edge/FE), forest edge, clearing (near FE) and clearing. Table 3.1 contains the exact bar code positions. The data were averaged at each location over 15s per each run. Data based on all completed runs during the three ‘Golden Day’ periods (Figure 2.3)

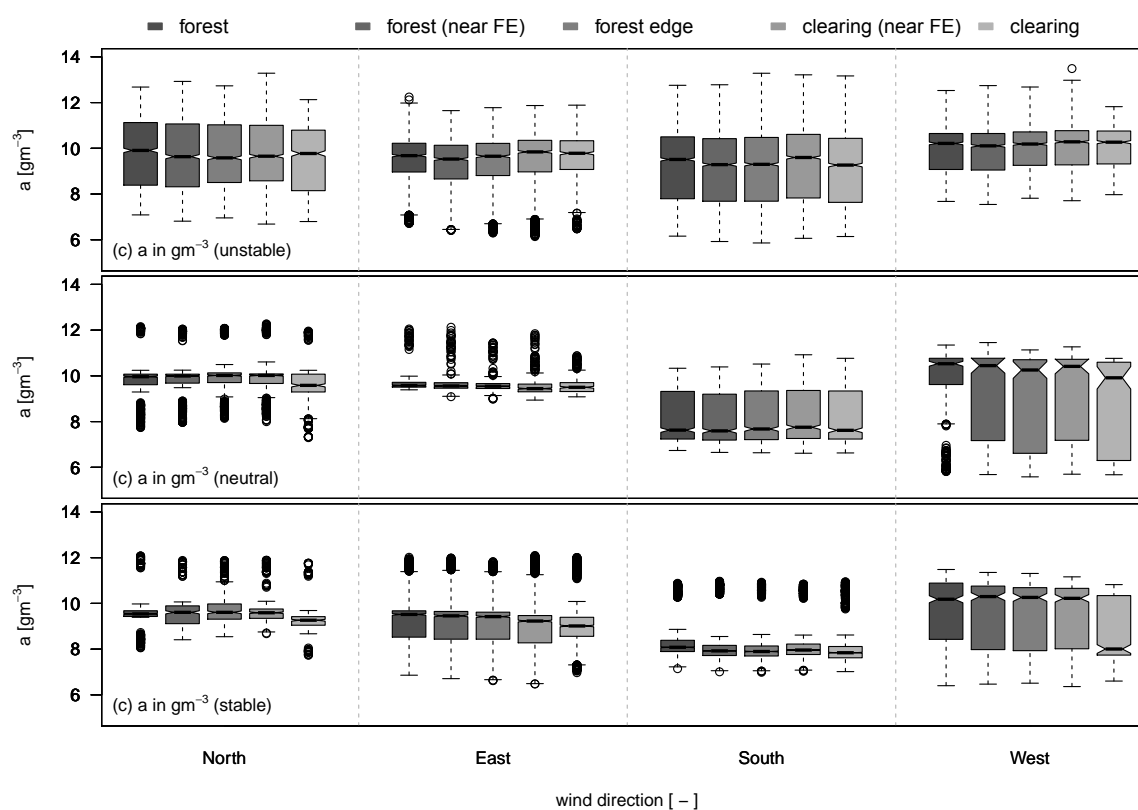


Figure C.4. Variation of the absolute humidity a regarding different stabilities and wind directions (see Section C.1). Unstable stratification is shown in (a), neutral in (b) and stable in (c). Data were measured with the HMMS at five different locations: forest, forest (near forest edge/FE), forest edge, clearing (near FE) and clearing. Table 3.1 contains the exact bar code positions. The data were averaged at each location over 15s per each run. Data based on all completed runs during the three ‘Golden Day’ periods (Figure 2.3)

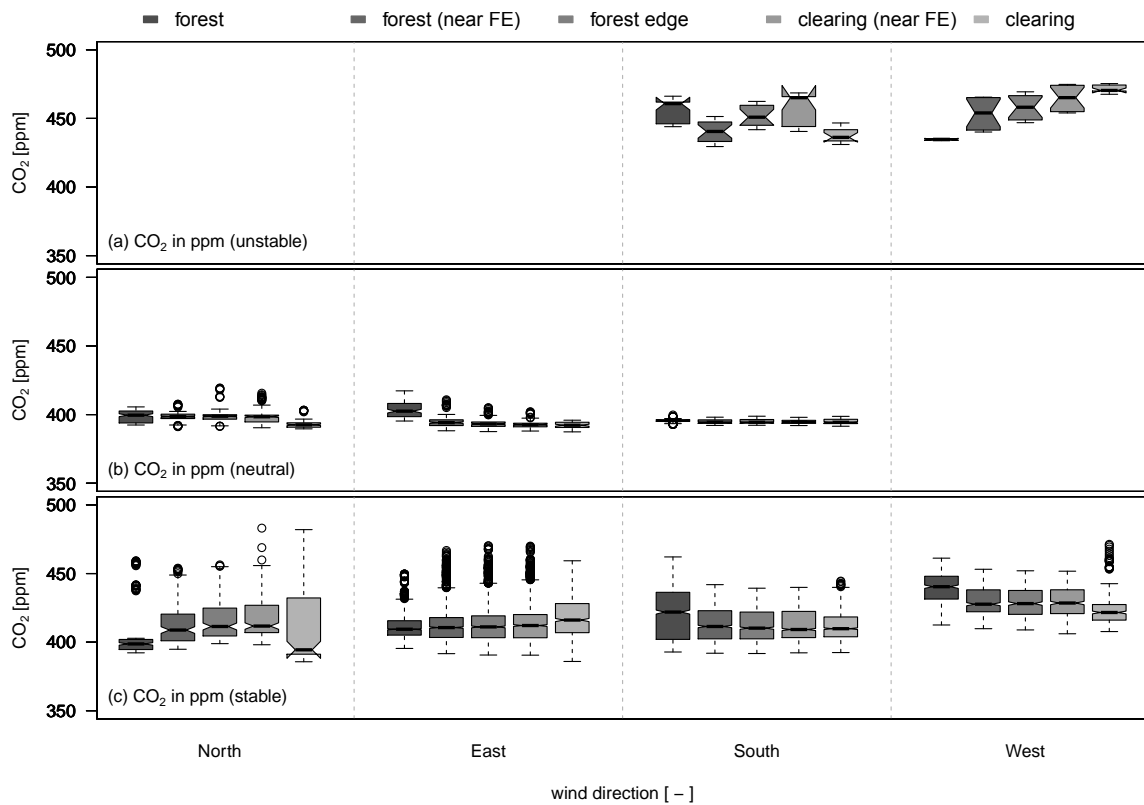


Figure C.5. Variation of the CO₂ concentration regarding different stabilities and wind directions (see Section C.1). Unstable stratification is shown in (a), neutral in (b) and stable in (c). Data were measured with the HMMS at five different locations: forest, forest (near forest edge/FE), forest edge, clearing (near FE) and clearing. Table 3.1 contains the exact bar code positions. The data were averaged at each location over 15s per each run. Data based on all completed runs during the three ‘Golden Day’ periods (Figure 2.3)

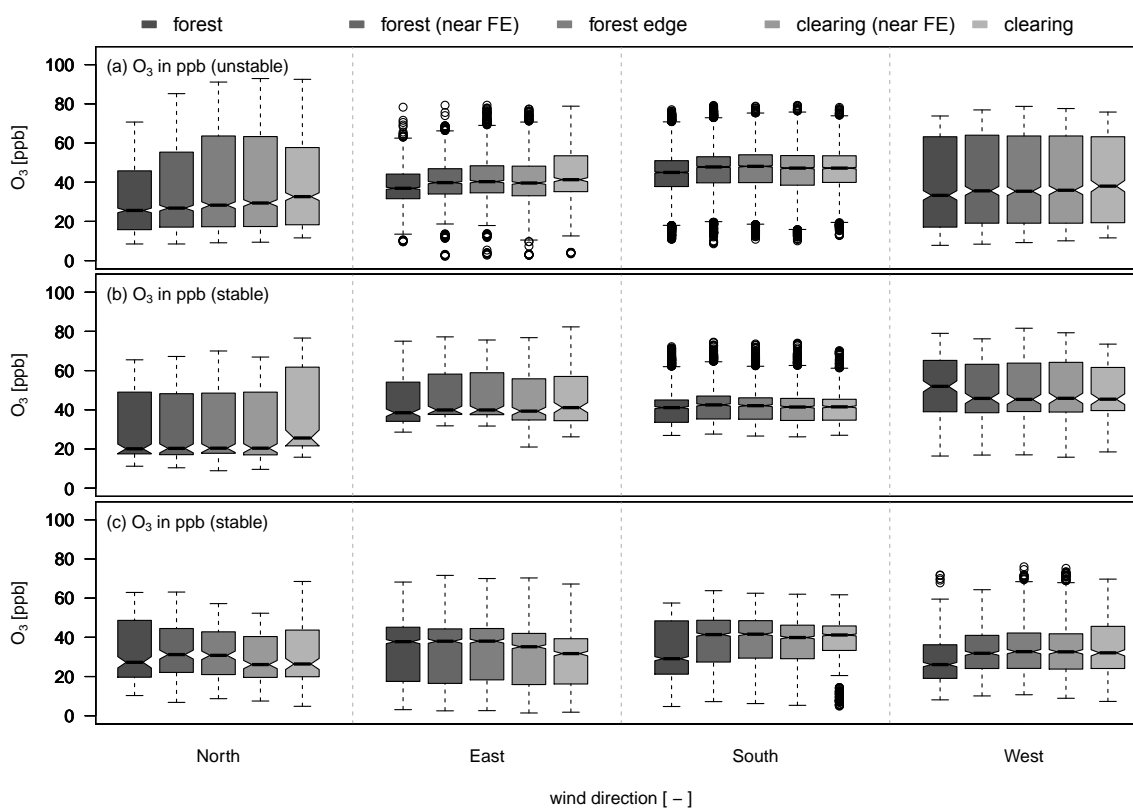


Figure C.6. Variation of the O_3 concentration regarding different stabilities and wind directions (see Section C.1). Unstable stratification is shown in (a), neutral in (b) and stable in (c). Data were measured with the HMMS at five different locations: forest, forest (near forest edge/FE), forest edge, clearing (near FE) and clearing. Table 3.1 contains the exact bar code positions. The data were averaged at each location over 15s per each run. Data based on all completed runs during the three ‘Golden Day’ periods (Figure 2.3)

C.1.3. Variation regarding different wind directions and friction velocities

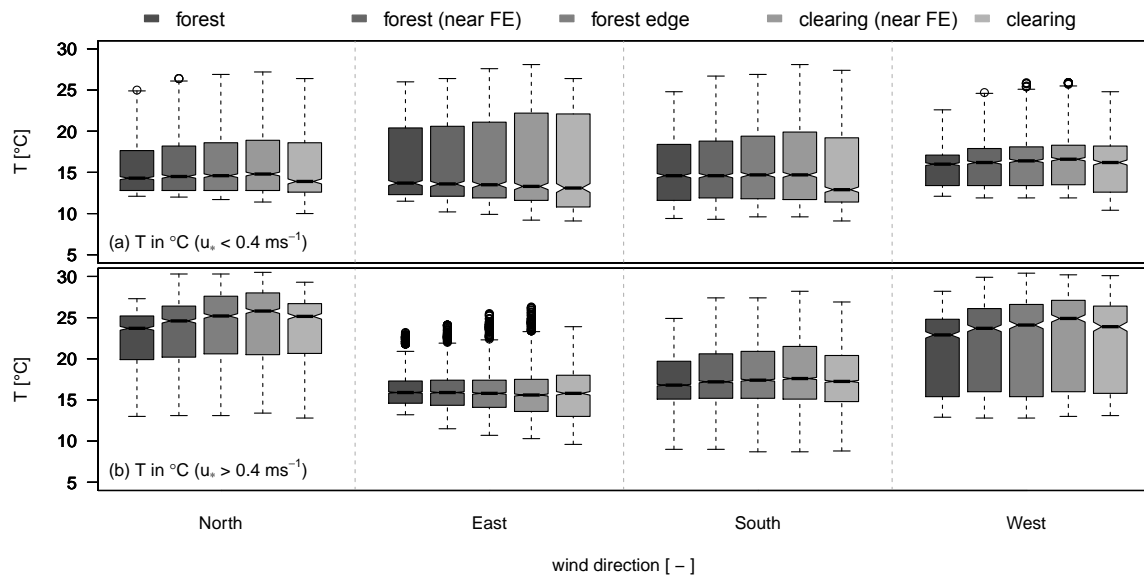


Figure C.7. Variation of the temperature T regarding different friction velocities u_* and wind directions (see Section C.1). $u_* < 0.4 \text{ m s}^{-1}$ is shown in (a) and $u_* > 0.4 \text{ m s}^{-1}$ in (b). Data were measured with the HMMS at five different locations: forest, forest (near forest edge/FE), forest edge, clearing (near FE) and clearing. Table 3.1 contains the exact bar code positions. The data were averaged at each location over 15s per each run. Data based on all completed runs during the three ‘Golden Day’ periods (Figure 2.3)

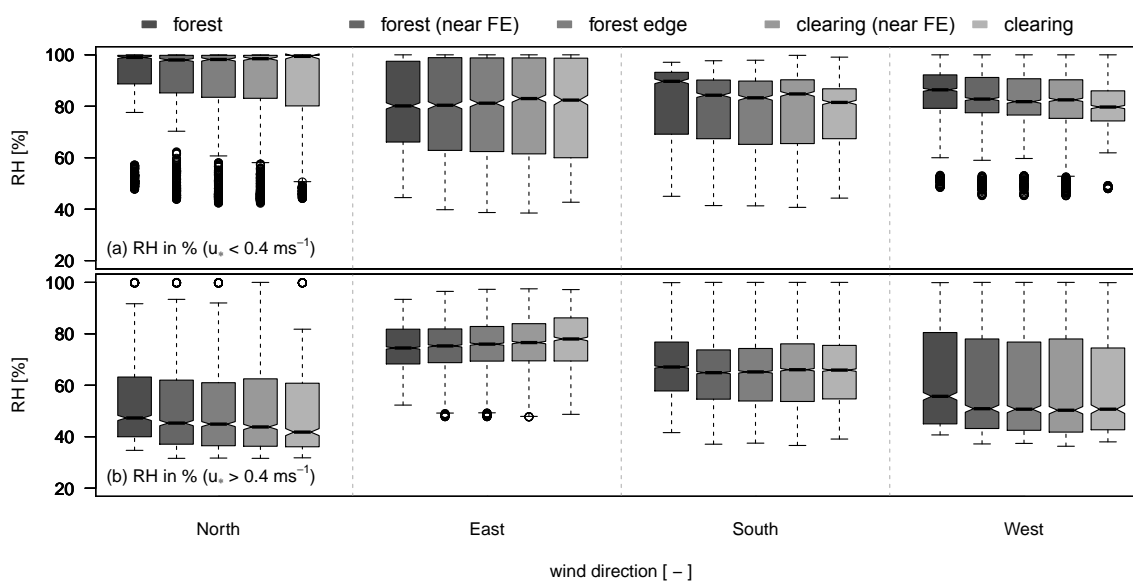


Figure C.8. Variation of the relative humidity RH regarding different friction velocities u_* and wind directions (see Section C.1). $u_* < 0.4 \text{ m s}^{-1}$ is shown in (a) and $u_* > 0.4 \text{ m s}^{-1}$ in (b). Data were measured with the HMMS at five different locations: forest, forest (near forest edge/FE), forest edge, clearing (near FE) and clearing. Table 3.1 contains the exact bar code positions. The data were averaged at each location over 15s per each run. Data based on all completed runs during the three ‘Golden Day’ periods (Figure 2.3)

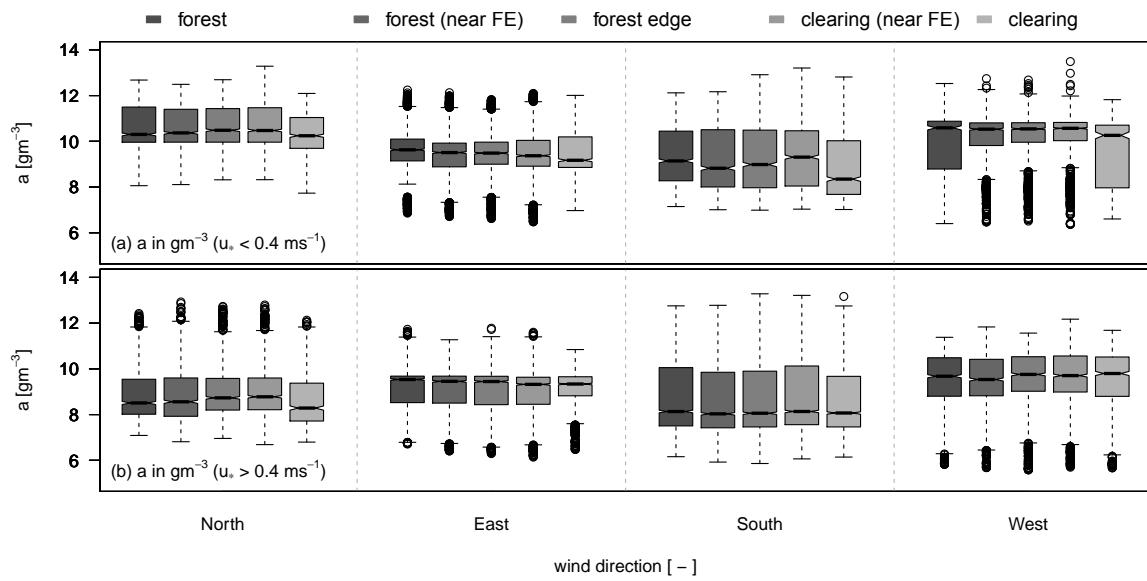


Figure C.9. Variation of the absolute humidity a regarding different friction velocities u_* and wind directions (see Section C.1). $u_* < 0.4 \text{ m s}^{-1}$ is shown in (a) and $u_* > 0.4 \text{ m s}^{-1}$ in (b). Data were measured with the HMMS at five different locations: forest, forest (near forest edge/FE), forest edge, clearing (near FE) and clearing. Table 3.1 contains the exact bar code positions. The data were averaged at each location over 15s per each run. Data based on all completed runs during the three ‘Golden Day’ periods (Figure 2.3)

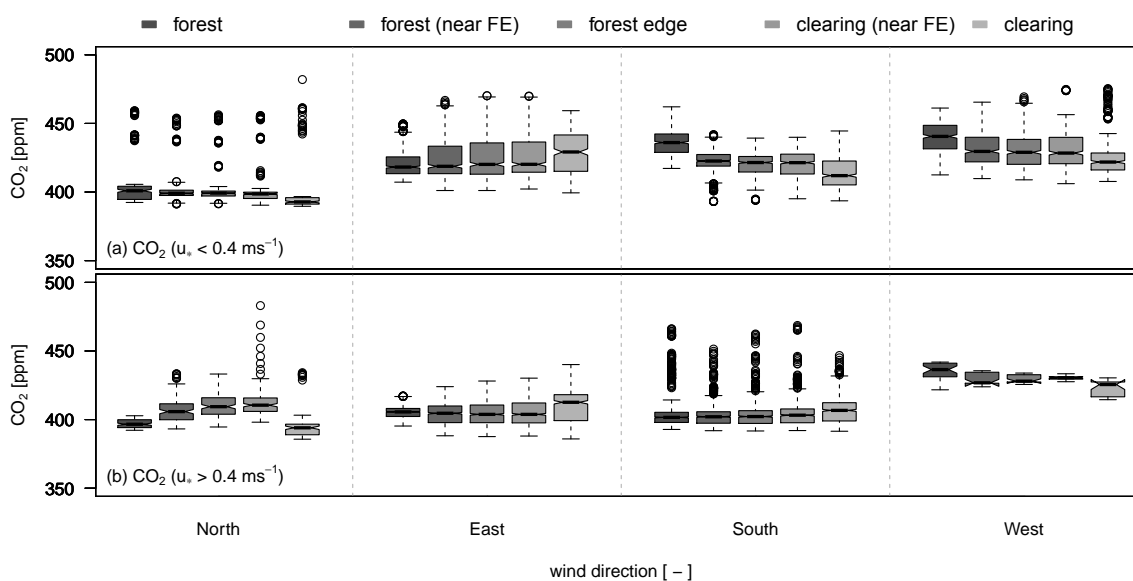


Figure C.10. Variation of the CO₂ concentration regarding different friction velocities u_* and wind directions (see Section C.1). $u_* < 0.4 \text{ m s}^{-1}$ is shown in (a) and $u_* > 0.4 \text{ m s}^{-1}$ in (b). Data were measured with the HMMS at five different locations: forest, forest (near forest edge/FE), forest edge, clearing (near FE) and clearing. Table 3.1 contains the exact bar code positions. The data were averaged at each location over 15s per each run. Data based on all completed runs during the three ‘Golden Day’ periods (Figure 2.3)

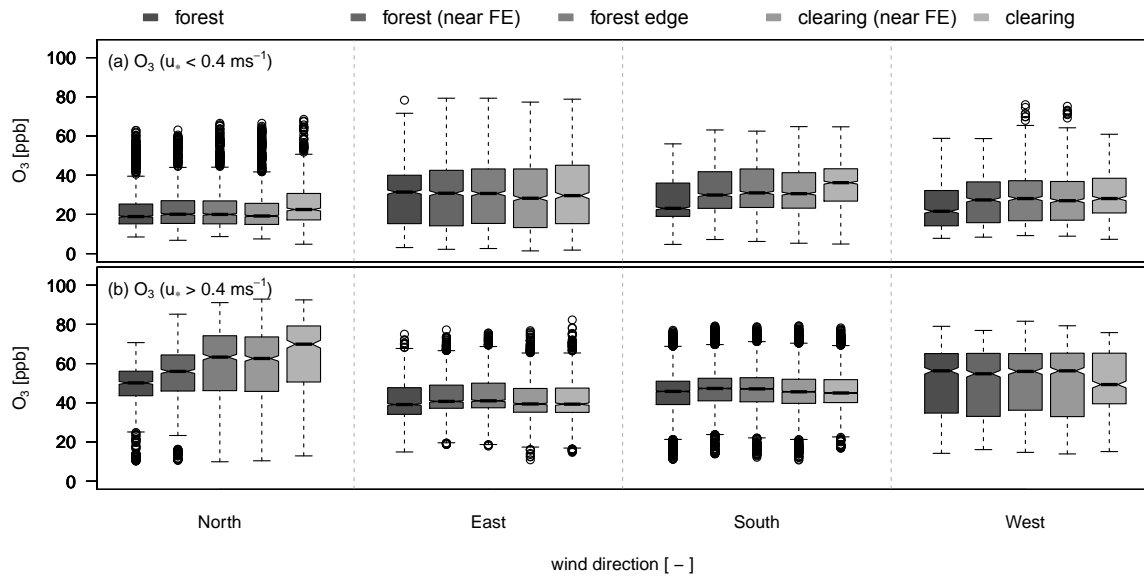


Figure C.11. Variation of the O_3 concentration regarding different friction velocities u_* and wind directions (see Section C.1). $u_* < 0.4 \text{ m s}^{-1}$ is shown in (a) and $u_* > 0.4 \text{ m s}^{-1}$ in (b). Data were measured with the HMMS at five different locations: forest, forest (near forest edge/FE), forest edge, clearing (near FE) and clearing. Table 3.1 contains the exact bar code positions. The data were averaged at each location over 15s per each run. Data based on all completed runs during the three ‘Golden Day’ periods (Figure 2.3)

C.2. Energy and trace gas fluxes measured with the eddy-covariance method

C.2.1. Percentage distribution of energy fluxes at the forest edge

As discussed in Section 3.2.2 the determination of the available energy at the forest edge tower M3 is more problematic than above the clearing and the forest, because the footprint at the forest edge consists of both landscape types, whereas the footprint above the clearing and the forest are more or less homogeneous. Furthermore a higher amount of advection should be considered. Since the distribution of the available energy at the forest edge tower M3 at 41 m can only be estimated, a percentage distribution of the available energy was considered, depending on the wind sector, which are equivalent to the four used sector-wise planar fit sectors at the forest edge (Figure 2.9). While both sectors parallel to the forest edge were kept constant at an equal contribution of 50 % forest : 50 % clearing, the percentage distribution from the forest sector and the clearing sector were varied in 10 % steps. The aim is to minimise the residual for the forest edge tower M3 at 41 m. The results of this variation is presented in Figure C.12. The distribution is shown as a relative

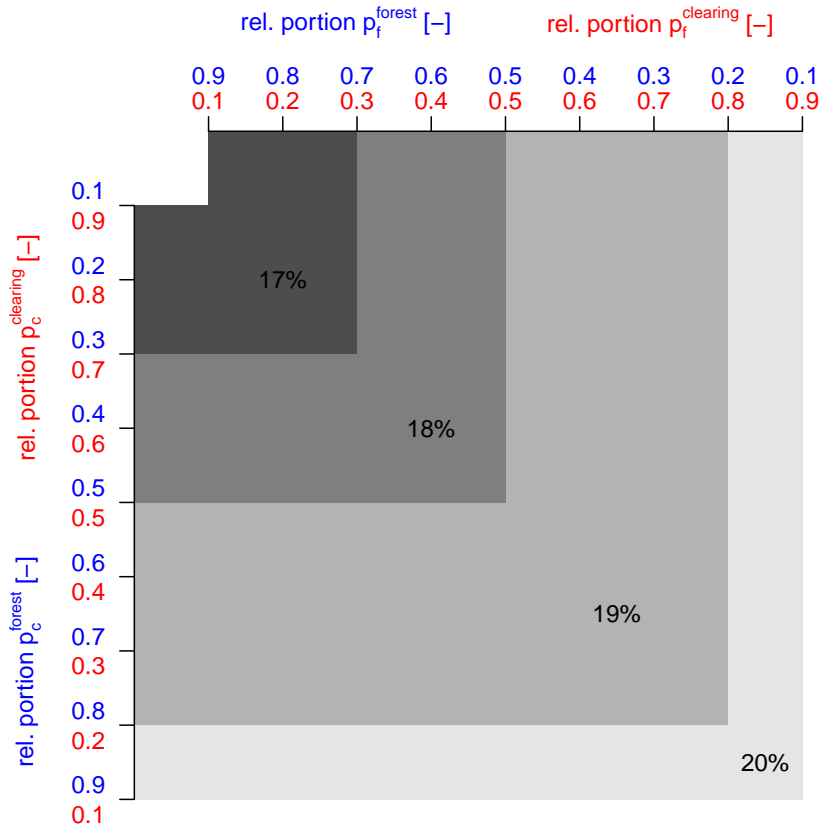


Figure C.12. Residual of the energy balance calculated for the forest edge tower M3 at 41 m, depending on a varying distribution of available energy. The available energy is divided in a part resulting from the forest p_f and a part resulting from the clearing p_c . Additionally the distribution considers two different wind sectors, one from the ‘forest’ (blue axis and numbers) and one from the ‘clearing’ (red axis and numbers). Equations (C.1) and (C.2) show the composition.

portion for the available energy for the forest p_f and for the clearing p_c , but the portion has to be considered depending on the two wind sectors ‘forest’ and ‘clearing’. Therefore four different variables has been defined: p_f^{forest} and $p_f^{clearing}$ for the portion of the available energy above the forest for both sectors and respectively p_c^{forest} and $p_c^{clearing}$ for the portions above the clearing. The sum of portions with the same wind sector is always:

$$p_f^{forest} + p_c^{forest} = 1 \quad (C.1)$$

$$p_f^{clearing} + p_c^{clearing} = 1. \quad (C.2)$$

The result of Figure C.12 is that the smallest residual with 17% can be found for a portion 70 – 90% forest : 30 – 10% clearing for wind sector ‘forest’ and 10 – 30% forest : 90 – 70% clearing for wind sector ‘clearing’. The following portions are defined for all calculations of the energy balance:

$$p_f^{forest} = 0.8$$

$$p_c^{forest} = 0.2$$

$$p_f^{clearing} = 0.2$$

$$p_c^{clearing} = 0.8.$$

D. List of publications

The following list summarises publications by myself, which were written during the production of this dissertation. These are split up in two parts: Publications which are applicable to this thesis and other publications. Two master theses and one bachelor thesis are included as well, which were supported, or supervised by myself.

Publications with reference to this thesis

Manuscripts accepted

Hübner, J., Olesch, J., Falke, H., Meixner, F. X., and Foken, T. (2014a). A horizontal mobile measuring system for atmospheric quantities. *Atmos. Meas. Tech.*, 7 (9), pp. 2967–2980. DOI: 10.5194/amt-7-2967-2014.*

Non peer-reviewed publications

Hübner, J., Olesch, J., Falke, H., Meixner, F. X., and Foken, T. (2014b). A horizontal mobile measuring system for atmospheric quantities. *Atmos. Meas. Tech. Discuss.*, 7 (5), pp. 4551–4588. DOI: 10.5194/amtd-7-4551-2014.

Hübner, J., Olesch, J., Falke, H., Meixner, F. X., and Foken, T. (2011). Documentation and Instruction Manual for the Horizontal Mobile Measuring System (HMMS). Work Report, University of Bayreuth, Dept. of Micrometeorology, ISSN: 1614-8916, 48, p. 88.

Serafimovich, A., Eder, F., Hübner, J., Falge, E., Voß, L., Sörgel, M., Held, A., Liu, Q., Eigenmann, R., Huber, K., Duarte, H. F., Werle, P., Gast, E., Cieslik, S., Heping, L., and Foken, T. (2011). ExchanGE processes in mountainous Regions (EGER): Documentation of the Intensive Observation Period (IOP3) June, 13th to July, 26th 2011. Work Report, University of Bayreuth, Dept. of Micrometeorology, ISSN: 1614-8916, 47, p. 137.

*The individual contribution for this manuscript is presented in Appendix E.

Master thesis supported by myself

- Eder, F. (2012). Influence of a clear cut on properties and vertical coupling of coherent structures. University of Bayreuth. p. 96.^{†,‡}
- Gatzsche, K. (2013). Modellierung des Energie- und Stoffaustausch im Grenzbereich Wald–Lichtung unter besonderer Berücksichtigung des Einflusses kohärenter Strukturen. University of Leipzig. p. 137.[‡]

Other publications with no reference to this thesis

Manuscripts accepted

- Riederer, M., Hübner, J., Ruppert, J., Brand, W. A., and Foken, T. (2014b). Prerequisites for application of hyperbolic relaxed eddy accumulation on managed grasslands and alternative net ecosystem exchange flux partitioning. *Atmos. Meas. Tech.*, 7 (12), pp. 4237–4250. DOI: 10.5194/amt-7-4237-2014.

Non peer-reviewed publications

- Babel, W., Schaller, C., Eigenmann, R., Foken, T., Hübner, J., Jentsch, A., Kreyling, J., Sultana, F., and Zhao, P. (2013). Documentation of the EVENT-HMMS Experiment 2012 – Microclimatological effects of rain-out shelters within EVENT II. Work Report, University of Bayreuth, Dept. of Micrometeorology, ISSN: 1614-8916, 55, p. 43.
- Riederer, M., Hübner, J., Ruppert, J., Brand, W. A., and Foken, T. (2014a). Application of relaxed eddy accumulation (REA) on managed grassland. *Atmos. Meas. Tech. Discuss.*, 7 (5), pp. 4987–5026. DOI: 10.5194/amtd-7-4987-2014.

Bachelor thesis supervised by myself

- Schaller, C. (2012). Untersuchung des Mikroklimas des EVENT-Experimentes mittels eines horizontal beweglichen Messsystems. University of Bayreuth. p. 75.

[†]Both master theses were supported by myself, mainly by data collection and data preparation. The preparation of both was closely followed, since the results found were very helpful for the right interpretation of this thesis' objectives (Section 1.3). Therefore results and discussions from both manuscripts have been included in this dissertation.

[‡]In the meantime, there is also a peer-reviewed manuscript available:

Eder, F., Serafimovich, A., and Foken, T. (2013). Coherent structures at a forest edge: Properties, coupling and impact of secondary circulations. *Bound.-Lay. Meteorol.*, 148 (2), pp. 285–308. DOI: 10.1007/s10546-013-9815-0.

E. Individual contribution to the joint publication

Hübner, J., Olesch, J., Falke, H., Meixner, F. X., and Foken, T. (2014a). A horizontal mobile measuring system for atmospheric quantities. *Atmos. Meas. Tech.*, 7 (9), pp. 2967–2980. DOI: 10.5194/amt-7-2967-2014.

- I mainly developed the idea of this manuscript. I conducted the whole data analysis, wrote the text and act as the corresponding author of the manuscript.
- Johannes Olesch developed and constructed together with me the Horizontal Mobile Measuring System (HMMS)
- Hubert Falke was the software engineer, who developed the HMMS software according to my ideas
- Franz X. Meixner and Thomas Foken contributed to the manuscript at various stages with fruitful discussions. Furthermore, they initiated the project related to the manuscript and funded both the HMMS by overhead money.

List of Figures

2.1.	Location of the investigation site of the EGER project	12
2.2.	Aerial view of the investigation site of the EGER IOP3 project in summer 2011 with all measuring points and their exact positions.	16
2.3.	Operating time of the HMMS during EGER IOP3.	23
2.4.	Front and lateral view on the HMMS.	24
2.5.	Laboratory tests for HMMS sensors to determine time constant τ_{63}	33
2.6.	Mean run duration of the HMMS.	35
2.7.	Uncorrected and dynamical error corrected time series of temperature T and relative humidity RH measured with HMMS.	37
2.8.	Uncorrected and dynamical error corrected horizontal profiles for long- wave and short-wave radiation measured with HMMS.	38
2.9.	Schematic drawing of used sectors for sector-wise planar-fit rotation	40
3.1.	Radiation measurements of HMMS versus tower measurements.	49
3.2.	Temperature and humidity measurements of HMMS versus tower meas- urements.	50
3.3.	Trace gas measurements of HMMS versus tower measurements.	51
3.4.	Diurnal variation of the HMMS radiation measurements at five locations.	54
3.5.	Diurnal variation of the HMMS temperature, humidity and trace gas meas- urements at five locations.	56
3.6.	Mean diurnal cycles of the observed energy fluxes along transect perpen- dicular to the forest edge.	61
3.7.	Mean diurnal cycles of the observed energy fluxes at location M3-North.	62
3.8.	Mean diurnal cycles of the observed energy fluxes along transect parallel to the forest edge.	62
3.9.	Mean diurnal cycles of observed CO_2 net ecosystem exchange (NEE) along transect perpendicular to the forest edge.	63
3.10.	Diurnal cycle of relative frequency of vertical coupling regimes.	65

3.11. Diurnal cycle of relative frequency of horizontal coupling regimes.	66
3.12. The relative flux contribution of coherent structures F_{CS} to total fluxes F_{tot} along transect perpendicular to the forest edge.	67
3.13. Daily cycle of the ejection contribution to coherent transport F_{ej}/F_{CS} along transect perpendicular to the forest edge.	68
3.14. Modelled Net Ecosystem Exchange (NEE) for six different land cover types of the clearing.	70
3.15. Comparison of modelled and measured sensible and latent heat fluxes for the first ‘Golden day’ period.	71
3.16. Comparison of modelled and measured NEE for the first ‘Golden day’ period.	72
3.17. Averaged vertical CO_2 profile, installed at M3.	73
3.18. Measured vertical profiles for dry bulb temperature and water vapour pressure e installed at M3.	75
3.19. Averaged vertical wind profile installed at M3.	77
3.20. Averaged vertical wind profile measured at M1.	78
3.21. Horizontal profiles for the 28 June 2011 for all HMMS measurements.	81
3.22. Horizontal profile for the 28 June 2011 from 15:00 CET to 18:00 CET for the O_3 concentration, measured with the HMMS.	82
3.23. Diurnal cycles of the observed energy fluxes for the 28 June 2011 along transect perpendicular to the forest edge.	84
3.24. Diurnal variation in vertical and horizontal coupling regimes for 28 June 2011.	85
3.25. The relative flux contribution of coherent structures F_{CS} to total fluxes F_{tot} for 28 June 2011 at the forest edge.	86
3.26. Vertical profiles from windprofiler (WPR), SODAR/RASS, and miniSODAR from 27 June 20:00 CET to 28 June 2011 10:00 CET.	88
3.27. Vertical and horizontal coupling regimes from 27 June 2011 20:00 CET to 28 June 2011 10:00 CET.	89
3.28. Measured horizontal profiles from 27 June 20:00 CET to 28 June 2011 10:00 CET for temperature, relative humidity, CO_2 and O_3 concentration, measured with the HMMS.	90
3.29. Sodargram of the MiniSODAR from 15 July 2011 12:00 CET to 16 July 2011 12:00 CET.	91
3.30. Vertical and horizontal coupling regimes from 15 July 2011 12:00 CET to 16 July 2011 12:00 CET.	92

3.31.	The relative flux contribution of coherent structures F_{CS} to total fluxes F_{tot} from 14 July to 18 July 2011 at main tower M1.	93
3.32.	Horizontal profiles of CO_2 and O_3 concentration measured with the HMMS from 14 July to 18 July 2011.	94
3.33.	Wind direction and velocity, as well as vertical CO_2 profile at M3 from 14 July to 18 July 2011.	95
3.34.	Vertical profiles from windprofiler (WPR), SODAR/RASS, and miniSODAR from 07 July 18:00 to 08 July 2011 06:00 CET.	97
3.35.	Vertical profiles of wind velocity, temperature, water vapour pressure and CO_2 concentration measured at tower M3 from 07 July 2011, 18:00 to 24:00 CET.	98
3.36.	O_3 concentration ('49i') within the forest and at the clearing (M4) from 07 July 18:00 to 08 July 2011 06:00 CET.	99
A.1.	Vertical wind velocity w versus wind direction for tower M1.	131
A.2.	Vertical wind velocity w versus wind direction for tower M2.	132
A.3.	Vertical wind velocity w versus wind direction for tower M3.	133
A.4.	Vertical wind velocity w versus wind direction for mast M4.	134
A.5.	Vertical wind velocity w versus wind direction for mast M6.	135
A.6.	Vertical wind velocity w versus wind direction for mast M7.	136
A.7.	Vertical wind velocity w versus wind direction for mast M8.	137
C.1.	Variation of HMMS temperature, humidity and trace gas concentration measurements, regarding different wind directions at five locations.	142
C.2.	Variation of HMMS temperature measurements, regarding different stability parameters and wind directions at five locations.	143
C.3.	Variation of HMMS relative humidity measurements, regarding different stability parameters and wind directions at five locations.	144
C.4.	Variation of HMMS absolute humidity measurements, regarding different stability parameters and wind directions at five locations.	145
C.5.	Variation of HMMS CO_2 concentration measurements, regarding different stability parameters and wind directions at five locations.	146
C.6.	Variation of HMMS O_3 concentration measurements, regarding different stability parameters and wind directions at five locations.	147
C.7.	Variation of HMMS temperature measurements, regarding different friction velocities and wind directions at five locations.	148

C.8. Variation of HMMS relative humidity measurements, regarding different friction velocities and wind directions at five locations.	149
C.9. Variation of HMMS absolute humidity measurements, regarding different friction velocities and wind directions at five locations.	150
C.10. Variation of HMMS CO ₂ concentration measurements, regarding different friction velocities and wind directions at five locations.	151
C.11. Variation of HMMS O ₃ concentration measurements, regarding different friction velocities and wind directions at five locations.	152
C.12. Residual of the energy balance calculated for the forest edge tower M3 at 41 m.	153

List of Tables

2.1.	Representativeness of the vegetation at the clearing ‘Köhlerloh’	12
2.2.	‘Golden Day’ periods and corresponding weather conditions during EGER IOP3 in June/July 2011.	14
2.3.	Turbulent flux measuring instrumentation of towers/masts M1 – M4 and M6 – M8 during EGER IOP3.	18
2.4.	Instrumentation of vertical profile measurements at towers M1, M3 and CM during EGER IOP3.	20
2.5.	Instrumentation of net radiation measurements, soil temperature, soil moisture, and ground heat flux measurements at towers M1, M3 and M4 during EGER IOP3.	21
2.6.	Specification of numbers from Figure 2.4.	24
2.7.	HMMS speed and direction control system.	26
2.8.	Sensors mounted on the HMMS.	29
2.9.	Calculated spatial relocation of HMMS measurements caused mainly by sensor response time.	32
2.10.	Angles of sectors used for (sector-wise) planar-fit rotation at towers/masts M1 – M4 and M6 – M8 during EGER IOP3.	40
3.1.	Designations of the five locations used for a detailed overview of the prevailing gradients, measured with the HMMS along the transect forest to clearing.	53
B.1.	List of plant physiological input parameters for the ACASA model.	139
B.2.	Plant physiological parameters for the ACASA model for the representative vegetation species at the clearing ‘Köhlerloh’ during EGER IOP3.	140
C.1.	Stability classes used for the investigation of the five locations named in Table 3.1.	141

List of abbreviations and symbols

Abbreviations

ABL	Atmospheric boundary layer
ACASA	Advanced Canopy-Atmosphere-Soil Algorithm
A/D	Analogue to digital converter
AmeriFlux	America-wide CO ₂ , water, energy and momentum measurements
a.s.l.	Above sea level
BayCEER	Bayreuth Center of Ecology and Environmental Research
BD	Backward Direction (driving direction of the HMMS)
C	Vertical coupling regime: Fully coupled canopy
C _h	Horizontal coupling regime: Locations are horizontally coupled
CET	Central European Time
CFC	Chlorofluorocarbon
CH ₄	Methane
CO ₂	Carbon dioxide
Cs	Vertical coupling regime: Cupled sub-canopy layer by sweeps
DAQ	Data acquisition
DC	Direct current
Dc	Temperate continental climate (Classification by Köppen according to Hendl, 1991)
Dc	Vertical coupling regime: Decoupled canopy
Dc _h	Horizontal coupling regime: Locations are horizontally decoupled
DFG	Deutsche Forschungsgemeinschaft (German Research Foundation)
DOY	Day of year (1 st January = 1)
Ds	Vertical coupling regime: Decoupled sub-canopy layer
DWD	Deutscher Wetterdienst (German Meteorological Service)
EGER	ExchanGE processes in moutaineous Regions
EUROFLUX	Europe-wide CO ₂ , water, energy and momentum measurements
FAO	Food and Agriculture Organization

FD	Forward Direction (driving direction of the HMMS)
FLUXNET	Worldwide CO ₂ , water, energy and momentum measurements
GDP	'Golden day' period
H ₂ O	Water
HDD	Hard disk drive
HMMS	Horizontal Mobile Measuring System
HONO	Nitrous acid
IOP	Intensive observation period
IPCC	Intergovernmental Panel on Climate Change
ITC	Integral turbulence characteristics
LES	Large-eddy simulation
LGB	Lehmann-Groß-Bahn
LLJ	Low-level jets
LP	Low pass filter
MAPS	Mesoscale Analysis and Prediction System
MUX	Multiplexer
N ₂ O	Nitrous oxide
O ₃	Ozone
PTFE	Polytetrafluoroethylene
QA	Quality assessments
QC	Quality control
RASS	Radio Acoustic Sounding System
RSL	Roughness sublayer
RuBP	Ribulose-1,5-bisphosphate
SH	Sample and hold circuit
SODAR	Sound/Sonic Detecting And Ranging
TK3b	Comprehensive software package (Version 3b) to calculate and correct eddy-covariance data (Mauder and Foken, 2011)
Wa	Vertical coupling regime: Wavemotions

Latin symbols

<i>a</i>	Absolute humidity	g m ⁻³
<i>a</i>	Scalar (general)	*
<i>Bo</i>	Bowen ratio	–

c	Carbon dioxide concentration	*
cb	Intercept of Ball-Berry formula	$\text{mol m}^{-2} \text{s}^{-1}$
cm	Slope of Ball-Berry formula	–
c_p	Specific heat at constant pressure	$\text{J kg}^{-1} \text{K}^{-1}$
Da	Dammköhler number	–
D_e	Event duration of coherent structures	s
$dsvc$	Entropy	$\text{J mol}^{-1} \text{K}^{-1}$
e	Water vapour pressure	hPa
$eavc$	Activation energy ΔH_a	J mol^{-1}
$ejmax$	Activation energy for RuBP regeneration	J mol^{-1}
F	Turbulent Flux (general)	*
f_{HB}	Portion of sensible heat flux on buoyancy flux	–
F_{CS}	Turbulent flux contribution due to coherent structures (general)	*
F_{ej}	Turbulent flux contribution due to ejection motion coherent structures (general)	*
F_{sw}	Turbulent flux contribution due to sweep motion coherent structures (general)	*
F_{tot}	Total turbulent flux (general)	*
h_c	Canopy height	m
$hdvc$	Deactivation energy ΔH_d	J mol^{-1}
$hjmax$	Deactivation energy for RuBP regeneration	J mol^{-1}
I_{\downarrow}	Long-wave downwelling radiation	W m^{-2}
I_{\uparrow}	Long-wave upwelling radiation	W m^{-2}
iqe	Quantum efficiency	–
J_{max25}	Potential rate of electron transport at 25 °C	$\mu\text{mol m}^{-2} \text{s}^{-1}$
K_{\downarrow}	Short-wave downwelling radiation (global radiation)	W m^{-2}
K_{\uparrow}	Short-wave upwelling radiation (reflected radiation)	W m^{-2}
k^{EBC-Bo}	Correction factor for the net ecosystem exchange after Bowen ratio method	–
k^{EBC-HB}	Correction factor for the net ecosystem exchange after buoyancy flux method	–
L	Obukhov length	m
LAI	Leaf area index	$\text{m}^2 \text{m}^{-2}$
NEE	Net Ecosystem Exchange	$\mu\text{mol m}^{-2} \text{s}^{-1}$

oi	Percentage of O_2 within cells (Michaelis–Menten kinetic)	mmol mol^{-1}
PAI	Plant area index	$\text{m}^2 \text{m}^{-2}$
p_c^{clearing}	rel. portion of available energy measured above the clearing for wind sector ‘clearing’, used at M3	–
p_c^{forest}	rel. portion of available energy measured above the clearing for wind sector ‘forest’, used at M3	–
p_f^{clearing}	rel. portion of available energy measured above the forest for wind sector ‘clearing’, used at M3	–
p_f^{forest}	rel. portion of available energy measured above the forest for wind sector ‘forest’, used at M3	–
q	Water vapour concentration	*
q_{10}	Q_{10} temperature coefficient for leaves	–
Q_B	Storage heat flux	W m^{-2}
Q_E	Latent heat flux	W m^{-2}
$Q_E^{\text{EBC-Bo}}$	Latent heat flux as corrected by the Bowen ratio approach	W m^{-2}
$Q_E^{\text{EBC-HB}}$	Latent heat flux as corrected by the buoyancy flux ratio approach	W m^{-2}
Q_G	Ground heat flux	W m^{-2}
Q_H	Sensible heat flux	W m^{-2}
$Q_H^{\text{EBC-Bo}}$	Sensible heat flux as corrected by the Bowen ratio approach	W m^{-2}
$Q_H^{\text{EBC-HB}}$	Sensible heat flux as corrected by the buoyancy flux ratio approach	W m^{-2}
Q_{HB}	Buoyancy flux	W m^{-2}
Q_S^*	Net radiation	W m^{-2}
r_0	Leaf basal respiration rate at 0°C	$\mu\text{mol m}^{-2} \text{s}^{-1}$
Res	Residual of the energy balance	W m^{-2}
RH	Relative humidity	%
s_{max}	Term entropy for RuBP regeneration	J mol^{-1}
t	Time	s
t_d	Delay time (here caused by inlet tube length)	s
T	Air temperature	K, $^\circ\text{C}$
T_0	Surface temperature	K, $^\circ\text{C}$
T_s	Sonic temperature	K, $^\circ\text{C}$
T'_s	Fluctuation of the sonic temperature	K, $^\circ\text{C}$
u	Wind velocity	m s^{-1}

u	Longitudinal component of the wind velocity	m s^{-1}
u_*	Friction velocity	m s^{-1}
v	Lateral component of the wind velocity	m s^{-1}
V_{cmax25}	Maximum rate of carboxylation at 25 °C	$\mu\text{mol m}^{-2} \text{s}^{-1}$
w	Vertical component of the wind velocity	m s^{-1}
w'	Fluctuation of the vertical component of the wind velocity	m s^{-1}
X	Measuring variable (general)	*
$xldiam$	Mean leaf diameter	m
z	Measuring height	m

Greek symbols

ΔH_a	Activation energy	J mol^{-1}
ΔH_d	Deactivation energy	J mol^{-1}
ΔX	Signal difference in measuring variable (general)	*
ζ	Dimensionless height z/L	–
λ	Heat of evaporation for water	J kg^{-1}
τ	Time constant	s

Remark:

- * dimension according to the use of the parameter
- dimensionless quantity

Versicherungen und Erklärungen

(§ 5 Nr. 4 PromO)

Hiermit erkläre ich, dass keine Tatsachen vorliegen, die mich nach den gesetzlichen Bestimmungen über die Führung akademischer Grade zur Führung eines Doktorgrades unwürdig erscheinen lassen.

(§ 8 S. 2 Nr. 5 PromO)

Hiermit erkläre ich mich damit einverstanden, dass die elektronische Fassung meiner Dissertation unter Wahrung meiner Urheberrechte und des Datenschutzes einer gesonderten Überprüfung hinsichtlich der eigenständigen Anfertigung der Dissertation unterzogen werden kann.

(§ 8 S. 2 Nr. 7 PromO)

Hiermit erkläre ich eidesstattlich, dass ich die Dissertation selbständig verfasst und keine anderen als die von mir angegebenen Quellen und Hilfsmittel benutzt habe.

(§ 8 S. 2 Nr. 8 PromO)

Ich habe die Dissertation nicht bereits zur Erlangung eines akademischen Grades anderweitig eingereicht und habe auch nicht bereits diese oder eine gleichartige Doktorprüfung endgültig nicht bestanden.

(§ 8 S. 2 Nr. 9 PromO)

Hiermit erkläre ich, dass ich keine Hilfe von gewerbliche Promotionsberatern bzw. -vermittlern in Anspruch genommen habe und auch künftig nicht nehmen werde.

Bayreuth, _____

Jörg Hübner